Universidade de Aveiro Departamento de Engenharia Civil
2012

Catarina Alexandra Louro Fernandes

COMPORTAMENTO CÍCLICO DE ELEMENTOS DE BETÃO ARMADO COM ARMADURA LISA

CYCLIC BEHAVIOUR OF RC ELEMENTS WITH PLAIN REINFORCING BARS

Universidade de Aveiro Departamento de Engenharia Civil
2012

Catarina Alexandra Louro Fernandes

COMPORTAMENTO CÍCLICO DE ELEMENTOS DE BETÃO ARMADO COM ARMADURA LISA

CYCLIC BEHAVIOUR OF RC ELEMENTS WITH PLAIN REINFORCING BARS

Dissertação apresentada à Universidade de Aveiro para cumprimento dos requisitos necessários à obtenção do grau de Doutor em Engenharia Civil, realizada sob a orientação científica do Prof. Doutor Humberto Salazar Amorim Varum, Professor Associado com Agregação do Departamento de Engenharia Civil da Universidade de Aveiro, e coorientação do Prof. Doutor Aníbal Guimarães da Costa, Professor Catedrático do Departamento de Engenharia Civil da Universidade de Aveiro.

Apoio financeiro da FCT e do FSE no âmbito do III Quadro Comunitário de Apoio.

the jury

president

Prof. Doutor António Carlos Matias Correia
professor catedrático da Universidade de Aveiro

Prof. Doutor Aníbal Guimarães da Costa
professor catedrático da Universidade de Aveiro

Prof. Doutor Daniel Vitorino de Castro Oliveira
professor associado da Escola de Engenharia da Universidade do Minho

Prof. Doutor Humberto Salazar Amorim Varum
professor associado com agregação da Universidade de Aveiro

Prof. Doutor Nelson Saraiva Vila Pouca
professor auxiliar da Faculdade de Engenharia da Universidade do Porto

Prof. Doutor Pedro da Silva Delgado
professor adjunto da Escola Superior de Tecnologias e Gestão do Instituto Politécnico de Viana do Castelo

acknowledgements

To Professor Humberto Varum, supervisor of this thesis, for his excellent guidance and advice, encouragement and dedication.

To Professor Aníbal Costa, co-supervisor of this thesis, for his invaluable guidance and advice, namely in the development of the experimental programme.

To Eng. Hugo Rodrigues and Eng. José Melo, for their friendship, and their assistance in the experimental programme and numerical modelling of the tested specimens.

To Eng. António Figueiredo and Eng. Henrique Pereira, for their assistance in the experimental programme.

To Professor Romeu Vicente, for his assistance in the experimental testing of the RC beam.

To Eng. Randolph Borg, for his assistance in the numerical modelling of the beam-column joint specimens.

To Professor António Arêde, Eng. Alexandre Costa, Mr. Valdemar Luís and Mr. André Martins, from the LESE laboratory of the Faculty of Engineering of University of Porto, for their invaluable assistance in the experimental testing of the RC beam.

To Civilria Construções S.A, Somague, Grupo Meneses, Silva Tavares & Bastos Almeida, Paviútil, and Arlindo Correia & Filhos S.A, for the construction and transportation of the test specimens, and construction of the structural reaction systems used in the experimental programme.

To the Santa Joana Museum, in Aveiro, for giving access to the building from where the RC beam was collected.

To my fellow PhD students in room 28.02.05, for their friendship, patience and encouragement.

To Fundação para a Ciência e a Tecnologia, for the financial support provided in the form of the PhD grant with reference SFRH/BD/27406/2006.

To my parents and grandparents, for their unconditional support, patience and encouragement.

palavras-chave

edifícios existentes de betão armado, armadura lisa, escorregamento, ensaios cíclicos, modelação numérica.

resumo

O comportamento cíclico das estruturas de betão armado é fortemente condicionado pelo mecanismo de aderência entre o betão e o aço. O escorregamento relativo entre os dois materiais, resultante da degradação progressiva da aderência em elementos solicitados por ações cíclicas, é uma causa frequente de danos graves e até do colapso de estruturas devido à ocorrência de sismos. Entre as estruturas existentes de betão armado que foram dimensionadas e construídas antes da entrada em vigor dos regulamentos sísmicos atuais, muitas foram construídas com armadura lisa, e portanto, possuem fracas propriedades de aderência. A informação disponível na literatura sobre o comportamento cíclico de elementos estruturais de betão armado com armadura lisa é reduzida e a influência das propriedades da aderência associadas a este tipo de armadura no comportamento cíclico das estruturas existentes não se encontra ainda devidamente estudada.

O objectivo principal desta tese foi estudar a influência do escorregamento na resposta cíclica de elementos estruturais de betão armado com armadura lisa. Foram realizados ensaios cíclicos em elementos do tipo nó viga-pilar, construídos à escala real, representativos de ligações interiores em edifícios existentes sem pormenorização específica para resistir às ações sísmicas. Para comparação, foi realizado o ensaio de um nó construído com armadura nervurada. Foi ainda realizado o ensaio cíclico de uma viga de betão armado recolhida de uma estrutura antiga.

Foram elaborados modelos numéricos não-lineares para simular a resposta dos elementos ensaiados, concentrando especial atenção no mecanismo do escorregamento.

Os resultados obtidos no âmbito desta tese contribuem para o avanço do conhecimento sobre o comportamento cíclico de elementos estruturais de betão armado com armadura lisa. As análises numéricas realizadas comprovam a necessidade de incluir os efeitos do escorregamento na modelação numérica deste tipo de estruturas de forma a representar com rigor a sua resposta às ações cíclicas.

keywords

existing RC building structures, plain reinforcing bars, bond-slip, cyclic testing, numerical modelling.

abstract

The hysteretic behaviour of reinforced concrete structures is highly dependent on the interaction between concrete and steel. The relative slippage between the steel reinforcing bars and the surrounding concrete, resulting from bond degradation under cyclic loading, is a common cause of severe damage and even collapse of reinforced concrete building structures due to earthquakes. Among the significant number of existing reinforced concrete buildings that were designed and built prior to the enforcement of the modern seismic-oriented design philosophies, many were built with plain reinforcing bars, thus with poor bond properties.

The available data about the cyclic behaviour of reinforced concrete structural elements with plain reinforcing bars is scarce. As a consequence, the influence of the bond properties on the hysteretic behaviour of existing reinforced concrete structures containing this type of steel reinforcement is not yet comprehensively understood.

The main objective of this thesis was to investigate the influence of the bond-slip mechanism on the cyclic behaviour of reinforced concrete structural elements with plain bars. Cyclic tests were carried out on full-scale joint specimens representative of interior beam-column connections in existing reinforced concrete buildings without specific detailing for seismic demands. An additional joint specimen, with deformed bars, was also tested for comparison. A cyclic test was also performed on a two-span beam with plain bars that was collected from an ancient structure.

Nonlinear numerical models were built to simulate the response of the tested elements, giving particular attention to the bond-slip mechanism.

The tests results obtained in the framework of this thesis contribute to the advance of knowledge on the cyclic behaviour of reinforced concrete elements with plain reinforcing bars. The numerical analyses developed confirm the need of taking into account the effects of the bond-slip mechanism in the numerical modelling of this type of structures, in order to represent more accurately their cyclic response.

TABLE OF CONTENTS

CHAPTER 3 – CYCLIC TESTING OF INTERIOR RC BEAM-COLUMN JOINTS

CHAPTER 4 – NUMERICAL MODELLING OF THE BEAM-COLUMN JOINTS

TABLE OF FIGURES

CHAPTER 2 – SEISMIC VULNERABILITY OF EXISTING RC BUILDING STRUCTURES WITH PLAIN REINFORCING BARS: STATE OF THE ART

CHAPTER 3 – CYCLIC TESTING OF INTERIOR RC BEAM-COLUMN JOINTS

CHAPTER 4 – NUMERICAL MODELLING OF THE BEAM-COLUMN JOINTS

CHAPTER 5 – CYCLIC TESTING OF A RC BEAM COLLECTED FROM AN EXISTING BUILDING STRUCTURE

CHAPTER 6 – NUMERICAL MODELLING OF THE BEAM

TABLE OF TABLES

CHAPTER 2 – SEISMIC VULNERABILITY OF EXISTING RC BUILDING STRUCTURES WITH PLAIN REINFORCING BARS: STATE OF THE ART

CHAPTER 3 – CYCLIC TESTING OF INTERIOR RC BEAM-COLUMN JOINTS

CHAPTER 4 – NUMERICAL MODELLING OF THE BEAM-COLUMN JOINTS

CHAPTER 5 – CYCLIC TESTING OF A RC BEAM COLLECTED FROM AN EXISTING BUILDING STRUCTURE

CHAPTER 6 – NUMERICAL MODELLING OF THE BEAM

CHAPTER 1

INTRODUCTION, MAIN OBJECTIVES AND PLAN OF THE THESIS

1.1 - INTRODUCTION

The hysteretic behaviour of reinforced concrete (RC) structures is strongly dependent on the interaction between the concrete and the steel reinforcement.

Cyclic load reversals, like those induced by earthquakes, lead to progressive bond degradation. The resulting relative slippage between the reinforcing bars and the surrounding concrete, which is commonly addressed as bond-slip, is one of the common causes of severe damage and even collapse of RC structures due to earthquakes.

A significant number of existing RC building structures located in seismic-prone countries all over the world was designed and built before the 1970s, prior to the enforcement of the modern seismic-oriented design philosophies, thus lacking adequate ductility and specific detailing for seismic demands. Many of these structures were built with plain reinforcing bars, to which are associated poor concrete-steel bond properties. Premature bond degradation and significant bar slippage are expected to occur in RC structural elements with plain bars subjected to moderate to severe cyclic loading, making this type of structures particularly sensitive to the bond-slip mechanism.

In critical regions, like base of columns and beam-column joints, the bond-slip mechanism can have a significant contribution to the elements' lateral deformation hence to the overall response of the structures. Reduction in stiffness and in energy dissipation capacity are also commonly associated with the occurrence of bar slippage. The complex behaviour of beam-column joints, for example, is highly influenced by the concrete-steel bond

properties, and bond degradation can dramatically alter the force transfer mechanisms within the joint region, with consequent load redistribution and impact on the joint strength. However, bond-slip is typically neglected in the numerical analysis of RC structures. Also, the specifications of the modern design codes were developed under the assumption of perfect bond between concrete and steel. In this way, the seismic response of RC structures with plain reinforcing bars can be significantly different from the theoretical predictions.

Despite the increasing number of research work devoted to the analysis of the cyclic behaviour of RC structural elements representative of non-seismic resisting structures, there is still a recognised lack of information about the performance of substandard elements with plain reinforcing bars.

When compared to the amount of information provided in the literature for elements with deformed bars, namely in terms of experimental data, the information available for elements with plain bars is scarce. The same can be said about the concrete-steel bond behaviour. In fact, a comprehensive model for describing the cyclic bond stress-slip relationship has not yet been established for this type of steel reinforcement.

It should be noted that an extensive experimental database (covering a wide range of loading conditions, typical geometrical and structural detailing characteristics, and materials mechanical properties) is fundamental to calibrate and upgrade numerical models for the adequate simulation of the cyclic behaviour of this type of elements. The development of simple modelling strategies, which take into account the influence of the bond-slip mechanism on the elements' response, is also highly dependent on the extension of the available experimental database. Various modelling strategies for simulating the bar slippage effects are proposed in the literature, but the majority is limited to the analysis of specific types of elements or, in some cases, quite complex to implement. As a consequence of the lack of experimental data and of general and reliable models for simulating the bond-slip mechanism, the influence of the bond properties of plain reinforcing bars on the hysteretic behaviour of existing RC structures built with this type of steel reinforcement is not yet completely understood.

1.2 - MAIN OBJECTIVES OF THE THESIS

The main objective of this thesis was to study the influence of the bond-slip mechanism on the cyclic behaviour of RC structural elements with plain reinforcing bars. More specifically, this research aimed to:

i) Collect and analyse relevant information provided in the scientific literature about the cyclic behaviour of RC structural elements with plain reinforcing bars, identifying needs for future research and limitations;

ii) Contribute to the characterization of the cyclic behaviour of RC structural elements with plain reinforcing bars, by analysing the influence of various parameters, with focus placed on the bond properties, and establishing the comparison with the major findings from similar research work provided in the literature;

iii) Contribute to enlarge the available experimental database on the cyclic behaviour of RC structural elements with plain reinforcing bars, which can be used to calibrate and upgrade numerical models for the adequate simulation of the cyclic response of this type of elements.

In order to achieve these objectives, the work was developed in three main parts:

i) Literature review on the main sources of seismic vulnerability of existing RC building structures designed and built before the enforcement of the modern seismic-oriented design philosophies, and on the available data about the cyclic behaviour of RC structural elements with plain reinforcing bars.

ii) Cyclic tests on full-scale RC structural elements with plain reinforcing bars and structural detailing similar to that typically adopted in RC building structures designed and built before the 1970s, namely a set of joint specimens representative of interior beam-column connections, and a two-span RC beam that was collected from an existing structure.

iii) Numerical modelling of the experimental response of the tested specimens using nonlinear fibre-based models and paying particular attention to the bond-slip mechanism.

1.3 - PLAN OF THE THESIS

This thesis is organized in seven chapters. Following the introduction, Chapter 2 presents a review on the main sources of seismic vulnerability in existing RC building structures designed and built before the enforcement of the modern seismic-oriented design philosophies. The structural deficiencies typically found in these structures, and the main causes of damage and collapse due to earthquakes are summarized. Focus is placed on the effects of the bond-slip mechanism and on the vulnerability of beam-column joints. Focusing on RC structural elements with plain reinforcing bars, a discussion about the bond performance of plain bars, and a review on recent experimental campaigns carried out for assessing the cyclic behaviour of this type of elements are presented. The chapter highlights the key role of the concrete-steel bond properties in the performance of RC elements with plain reinforcing bars and also the lack of information and need for more investigation work on the subject.

Chapter 3 addresses the cyclic testing of the RC beam-column joints. The specimens' properties, and the test setup and testing programme are described. The main experimental results are presented and analysed. The influence of various parameters on the joints performance is investigated, paying particular attention to the effects of the bond properties.

Chapter 4 is devoted to the numerical modelling of the beam-column joint specimens. The adopted modelling strategies and assumptions are presented, and comparisons are established between the numerical and experimental results. Particular focus is placed on the influence of the bond-slip mechanism on the joint specimens' response.

Chapter 5 reports the cyclic testing of the RC beam. The beam properties, and the test setup and procedure are described, and the main experimental results are presented.

Chapter 6 addresses the numerical modelling of the RC beam. The adopted modelling strategy and assumptions are presented. Comparison is established between the numerical and experimental results. Particular attention is paid to the influence of the bond-slip mechanism on the beam response.

Finally, Chapter 7 summarizes the main conclusions resulting from the research work, identifying the main contributions, as well as the limitations, and gives suggestions for further developments and possible research directions.

The references of the papers published in journals and articles presented in conferences, in the framework of the PhD thesis, are listed in the Appendix.

CHAPTER 2

SEISMIC VULNERABILITY OF EXISTING RC BUILDING STRUCTURES WITH PLAIN REINFORCING BARS: STATE OF THE ART

2.1 - INTRODUCTION

The incorporation of seismic design procedures in building design was first adopted in a general sense in the 1920s and 1930s. Lateral forces corresponding to a fraction of the building weight and elastic design to permissible stress levels were in force, what later was verified to be not an adequate design strategy [1].

As stated by Varum [2], until the 1950s in the US and the 1960s in Europe, there were essentially no formal seismic design provisions in design codes. It was only in the mid-1970s that provisions for design and detailing of members and structures came out in the US standards. Yet, it was not before the mid-1980s that these provisions were included in the European national codes. Until then, only seismic equivalent lateral loading was considered in seismic design. For example, in Portugal, the first provisions for seismic design appeared in 1958 (RSCCS [3]), but rules resembling those of modern codes were only introduced in 1983 (RSA [4]). In Greece, which is one of the most earthquake-prone countries in Europe, the first modern earthquake resistant design code was only introduced in 1992, becoming mandatory in 1995 [2]. In Italy, before the current design codes came into force, only in 1975 did the dynamic properties of the structures became considered in the Italian regulations [5]. Nowadays, together with the remaining Eurocodes (like Eurocode 2 (EC2, [6]) for RC structural design), Eurocode 8 [7] is the reference standard for seismic design in many European countries.

In general, the 1970s were a turning point in the design and construction practice all around the world. In particular, capacity design principles were introduced, highlighting the key role of ductility, instead of lateral strength, in preventing structural collapse and excessive damage during seismic events. Selection of a suitable structural configuration for inelastic response, selection of a suitable and appropriately detailed location (plastic hinges) for inelastic deformations to be concentrated, and insurance (through suitable strength differentials) that inelastic deformation does not occur in undesirable locations or by undesirable structural modes, are the basis for the capacity design philosophy [1]. For instance, a beam sway mechanism instead of a column sway mechanism (soft-storey) is more desirable, and failures due to shear (implying large degradation of strength and stiffness) and loss of reinforcement anchorage should be prevented.

A significant number of existing RC structures, located in seismic-prone countries all over the world, was built before the 1970s [2] hence prior to the enforcement of the modern seismic-oriented design philosophies. As a consequence of the absence of capacity design principles in design and poor reinforcement detailing, a significant lack of ductility, at both local and global levels, is expected for these structures, resulting in inadequate structural performance even under moderate seismic excitations [8]. This type of structures is referred to herein as old-type structures. Damage and collapse of building structures observed in recent severe earthquakes, confirm the important source of risk that old-type RC buildings represent to society, in both human and economic terms. In Portugal, for example, the survey [9] on the Portuguese residential park that was conducted in 1991 revealed the predominance of RC buildings, indicating that, by that year, 56% of the total residential buildings had been constructed between 1961 and 1991 [2].

Deformed reinforcing bars are currently used in the RC construction. However, the use of plain bars as longitudinal (and transverse) steel reinforcement in RC building structures was quite common until the mid-1960 (in the US) up to the mid-1980s (in some European countries) [10]. For example, in Italy and in the whole Mediterranean area, the use of plain reinforcing bars was widely spread up to 1970 [11]. Thus, a significant number of existing old-type RC buildings around the world has plain bars as steel reinforcement.

In the next sections, the main structural deficiencies commonly found in old-type RC building structures are briefly described, as well as the most common causes of damage

and collapse of buildings due to earthquakes. Particular attention is given to the influence of the concrete-steel bond properties and to the cyclic behaviour of beam-column joints. Focusing on RC elements with plain reinforcing bars, a discussion on the bond mechanism, and a review of the experimental work reported in the available literature aimed at the investigation of the cyclic behaviour of this type of elements, are presented.

2.2 - TYPICAL STRUCTURAL DEFICIENCIES AND COMMON CAUSES OF DAMAGE AND COLLAPSE DUE TO EARTHQUAKES

2.2.1 - Introduction

Typical structural deficiencies found in old-type RC building structures, that constitute recognised sources of seismic vulnerability, are [2, 8, 12]: i) lack of appropriate confinement through transverse reinforcement in the plastic hinge regions; ii) lack or absence of joint transverse reinforcement; iii) moment capacity of the columns lower than the moment capacity of the beams (weak column-strong beam mechanism); iv) inadequate anchorage solutions; v) lapped splices located in potential plastic hinge regions; vi) lower quality of materials when compared to current practice, in particular the use of plain reinforcing bars as longitudinal reinforcement and of low-strength concrete; and, vii) presence of masonry infill walls with complex interaction with the bare frame. Causes of damage and collapse of old-type RC building structures due to earthquakes are also frequently associated with vertical and horizontal irregularities.

Shear failure can occur in beams due to both insufficient steel reinforcement and the increase in loads during the earthquake [13]. Shear forces in columns resulting from typical gravity and wind load designs can be significantly lower than those developed during seismic loading. Shear failure in columns is frequently observed (Figure 2.1). Poor confinement (associated with inadequate spacing of stirrups or presence of ties) can result in flexural crisis at the base of columns located at low levels (Figure 2.2), with instability of the compressive reinforcement, slippage of the tensile reinforcing bars and crushing of the unconfined concrete [13]. Soft-storey mechanisms are one of the most common causes of building collapse due to earthquakes (Figure 2.3).

(a)

(b)

Figure 2.1 - Column shear failure: a) 1999 Izmit, Turkey earthquake (photo by Halil Sezen, courtesy of the National Information Service for Earthquake Engineering, EERC, University of California, Berkeley [14]); b) 1985 Mexico City earthquake [2].

Figure 2.2 - Inadequate lap-splices and lack of stirrups (1999 Izmit, Turkey earthquake) [2].

(a)

(b)

Figure 2.3 - Building collapse due to soft-storey mechanism in the: a) 2009 L'Aquila, Italy earthquake [15]; b) 1999 Izmit, Turkey earthquake (photo by Halil Sezen, courtesy of the National Information Service for Earthquake Engineering, EERC, University of California, Berkeley [14]).

The risk of collapse of RC building structures due to seismic events is often associated with the brittle failure of beam-column joints (Figure 2.4). The type of joint damage or failure mechanism is mainly dependent on the joint typology (exterior or interior joint), adopted structural details (such as the amount of joint transverse reinforcement and anchorage solution), and concrete-steel bond properties (see Section 2.2.3). Beam-column joints in old-type RC building structures typically lack appropriate joint transverse reinforcement (sometimes only one stirrup was used, but it was common the absence of transverse reinforcement), as well as appropriate anchorage and bond properties.

(a) (b)

Figure 2.4 - Failure of beam-column joints lacking proper design: a) 2011 Lorca, Spain earthquake; b) 1999 Izmit, Turkey earthquake) [2].

2.2.2 - The bond-slip mechanism

Concrete-steel bond is the mechanism that allows the force transfer between the steel reinforcing bars and the surrounding concrete in RC structures. It is a combination of [16]: i) adhesion, which is related to the shear strength of the steel-concrete interface and results primarily from chemical bonding; ii) bearing forces perpendicular to the lug faces, which arise as the bar is loaded and tries to slide; and, iii) friction, which is produced by bearing force on the concrete-steel surface and by shearing off the concrete between the lugs on the cylindrical concrete surface at the tip of the lugs. Detailed explanation about the different stages that characterise the interaction between concrete and steel can be found in [17].

Bond action is not only necessary to ensure an adequate level of safety by allowing the concrete and steel to work together, but also to control the structural behaviour by providing an adequate level of ductility. While safety requires bond to have good mechanical properties at the local level, ductility requires bond to withstand large steel strains along the embedded reinforcement in order to let the strains spread between two continuous bending cracks, and to favour the formation of densely-spaced secondary cracks in the concrete [17].

The hysteretic behaviour of RC structures is highly dependent on the concrete-steel interactional mechanisms. Cyclic load reversals (like those induced by earthquakes) lead to progressive bond degradation, resulting in significant relative slippage between the reinforcing bars and the surrounding concrete, which is commonly addressed as bond-slip. The sudden loss of bond, and consequent bar slippage, is acknowledged as one of the

sources of brittle failure in RC structural elements, and is reported to have been the cause of severe local damage and even collapse of many structures due to earthquakes [2]. In RC structural elements subjected to cyclic loading, the concrete-steel bond can deteriorate even before the stress state has attained the yield stress of the steel and the stress strength of the concrete [2, 18].

Bond failure can occur due to [16]: i) direct pullout of the reinforcing bar, if ample confinement is provided for the reinforcing bars (observed as fixed-end rotations at the elements ends, like in column bases and beam-column joints); or, ii) splitting of the concrete cover along the bar, if the concrete cover or confinement is insufficient to obtain a pullout failure. The failure modes under monotonic loading and cyclic loading are similar. However, particularly under reversed cyclic loading, bond failure may occur at cyclic bond stress levels lower than the ultimate stress under monotonic loading [17].

Plain reinforcing bars exhibit poor bond properties when compared to deformed bars (see Section 2.3) hence being particularly sensitive to bond degradation under cyclic loading. Plain reinforcement does not possess lugs or other surface deformations and therefore cannot transfer bond forces by mechanical interlock. Instead, bond is transferred by adhesion between the concrete and the reinforcing bar before slip occurs, and by the wedging action of small particles that break free from the concrete during slip [19, 20]. Appropriate anchoring details are necessary to ensure a satisfactory interaction between the concrete and the longitudinal steel reinforcement. Anchorage of plain bars in old-type RC building structures was typically provided by end-hooks which may not be effective in preventing the bars from slipping. The effectiveness of different end details on plain reinforcing bars was investigated, among others, by Fabbrocino *et al.* [21, 22].

Fixed-end rotations due to bar slippage in critical regions like column bases and beam-column joints are additive to the rotation calculated from flexural analysis in the elements and for this reason should be taken into account when determining the response of RC structures subjected to seismic loading. Experimental results concerning RC columns with deformed bars tested by Sezen [23] indicate that, in some cases, the deformations due to reinforcement slip may be as large as column flexural deformations. Regarding the tested columns, the slip deformation contributed 25% to 40% to the total lateral displacement. In elements with plain reinforcing bars, the deformation component associated with the fixed-

end rotation effect can be considerably increased, and may represent up to 80% to 90% of the elements' overall deformability [11, 24, 25]. Therefore, ignoring the bond-slip effects, particularly in the presence of plain bars, may lead to predicted lateral deformation significantly smaller than the real deformation or to predicted lateral stiffness larger than the existing element stiffness [26], and also to overestimation of the hysteretic energy dissipated during cyclic loading [27, 28]. For example, the results of the numerical analyses concerning a RC frame, carried out by Fabbrocino *et al.* [22], illustrate the important effect of bond and fixed-end rotation on the base shear-top drift response, particularly in the presence of plain bars (Figure 2.5).

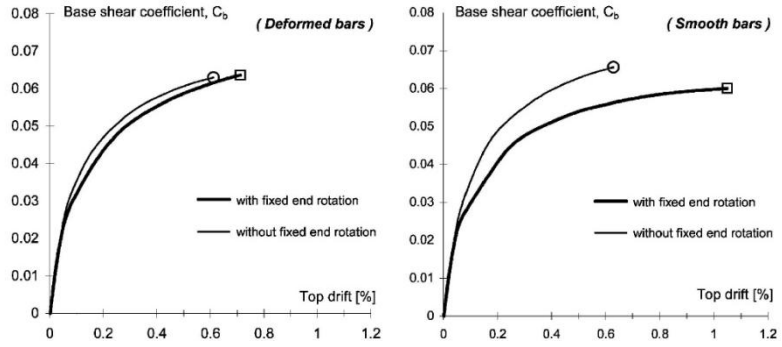

Figure 2.5 - Comparative results on effect of type of reinforcement on drift capacity [22].

Poor bond properties also have a direct influence on the bending and shear deformation mechanisms. Fewer and wider cracks are generally observed (see Section 2.4), increasing the deformation component due to bending and reducing the deformation component associated with shear [11, 24, 25]. Also, it should be noted that the provisions of the modern design codes (like EC2) were developed under the assumption of perfect bond between concrete and steel. Therefore, the use of plain bars as steel reinforcement may lead to a structural performance that is very different from that predicted by the design codes.

In this way, it is clear that the accurate modelling of the bond-slip behaviour and its inclusion in the numerical models of structural analysis is fundamental to achieve a more realistic simulation of the hysteretic behaviour of RC structures, in particular of those built with plain reinforcing bars. However, perfect bond is a common assumption in the numerical analysis of RC structures. Also, a model for describing the cyclic bond-slip behaviour for plain reinforcing bars has not yet been established (see Section 2.3.2).

Modelling strategies for including bond-slip effects in the nonlinear analysis of RC structural elements

Several proposals of analytical models that include bond-slip effects in the response of RC structures can be found in the published literature. According to Limkatanyu and Spacone [28], the simplest way to account for the bond-slip effects in frame elements is to add nonlinear springs at the element ends. Examples of this type of modelling strategy applied to beam-column joints are mentioned in Section 2.2.3. Following other approaches: i) Filippou and Issa [29] and Filippou *et al.* [30] proposed a so-called sub-element frame element model in which the different sources of material nonlinearities (such as bending deformations, shear deformations, and bond-slip) are represented by separate sub-elements; ii) Manfredi and Pecce [31] proposed a refined fibre model for the analysis of RC beams that includes an explicit formulation of the bond stress-slip relationship; iv) Monti and Spacone [32] combined the force-based fibre beam element proposed by Spacone *et al.* [33] with the reinforcing bar element with bond-slip proposed by Monti *et al.* [34]; v) Limkatanyu and Spacone [27] proposed a frame element in which the bond-slip is computed directly as the difference in the steel and the concrete displacements at the bar level. Limkatanyu and Spacone [28] used two models that were developed by the authors to investigate how bond-slip affects the cyclic response of one interior RC beam-column joint and of a two-storey one-bay RC frame that had been tested under cyclic loading. One was the previously mentioned model [27], and the other was a rigid-panel joint element with bond-slip [35]. In both cases, the analytical results were shown to correlate better with the experimental results when bond-slip effects were taken into account, namely in terms of strength, displacement demands and energy dissipation (Figure 2.6).

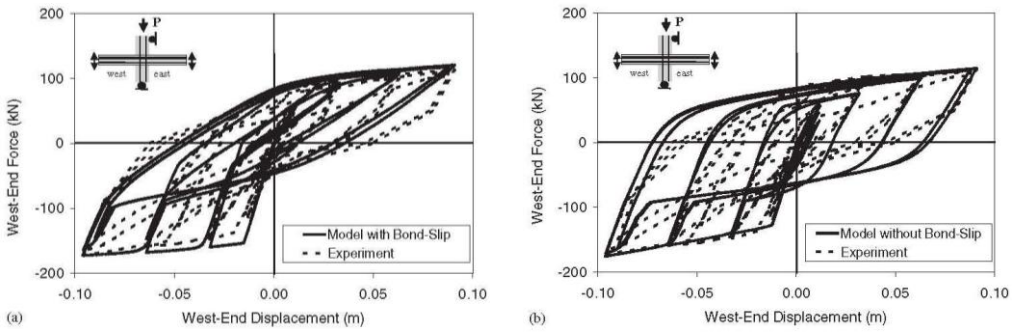

(a) (b)

Figure 2.6 - Experimental and numerical responses of the beam-column joint analysed by Limkatanyu and Spacone [28]: a) model with bond-slip; b) model without bond-slip.

Varum [2] proposed a simple method for including bond-slip in the numerical analysis of a RC frame structure that had been pseudo-dynamically tested. Bond-slip was modelled explicitly using a correction of the steel reinforcement constitutive law (slippage factor, λ) that expresses the lack of compatibility between concrete and steel strains (ε_c and ε_s, respectively) due to bond-slip. The corrected constitutive law is depicted in Figure 2.7. Considering that steel hardening strain in not reached, the steel constitutive law is assumed bi-linear with an elastic perfect plastic behaviour [2]. In the numerical analyses, it was assumed for each element (beam or column) a constant value of λ in accordance to the maximum deformation experimentally observed at this element during the pseudo-dynamic tests. The comparison established between the numerical (with and without bond-slip) and the experimental results shows that it was only possible to reproduce the experimental results well with the inclusion of the bond-slip effects in the numerical model (see Figure 2.8) [2, 36]. However, Varum [2] states the need for the improvement of the proposed model. Namely, it is presumed that a more precise numerical simulation can be achieved with a bond-slip model that provides full bond at the beginning of loading being increased the slippage factor with the maximum steel strain observed at each element.

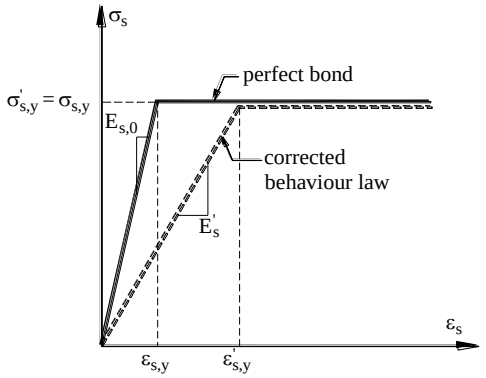

$$\lambda = \frac{\varepsilon_C}{\varepsilon_S} \qquad \varepsilon'_{s,y} = \lambda \cdot \varepsilon_{s,y} \qquad \sigma'_{s,y} = \sigma_{s,y} \qquad E'_s = \frac{1}{\lambda} \cdot E_{s,0}$$

$$\sigma_s(\varepsilon_s) = \begin{cases} \text{if perfect bond} \begin{cases} \varepsilon_s < \varepsilon_{s,y} \leftarrow \sigma_s(\varepsilon_s) = E_{s,0} \cdot \varepsilon_s \\ \varepsilon_s \geq \varepsilon_{s,y} \leftarrow \sigma_s(\varepsilon_s) = \sigma_{s,y} \end{cases} \\ \text{if not (not yielding steel occurs)} \leftarrow \sigma_s(\varepsilon_s) = \frac{1}{\lambda} \cdot E_{s,o} \cdot \varepsilon_s \end{cases}$$

Figure 2.7 - Correction of the steel reinforcement constitutive law for taking into account bond-slip, as proposed by Varum [2].

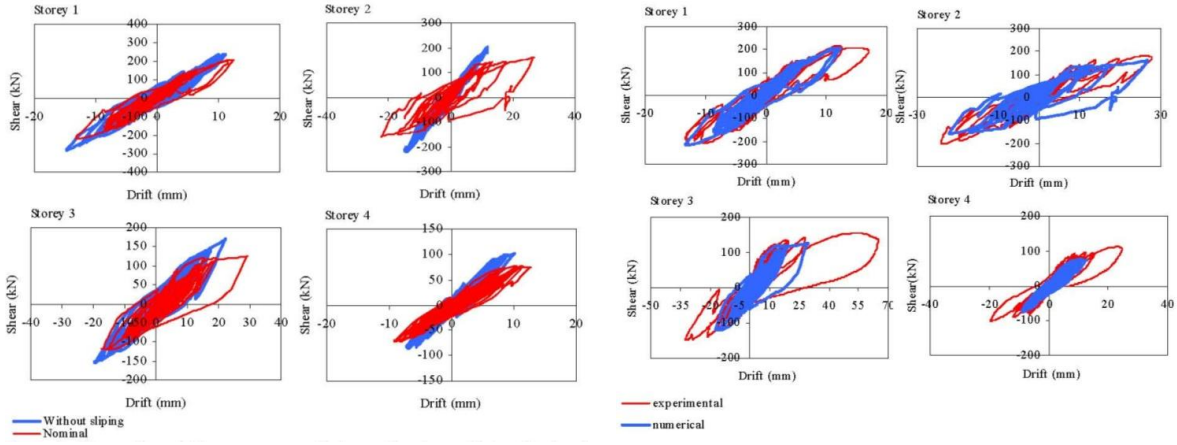

(a) (b)

Figure 2.8 - Storey shear-drift response of a RC frame with plain reinforcing bars (pseudo-dynamic test) [36]: a) numerical results considering and not considering bond-slip; b) comparison between experimental results and numerical results considering bond-slip.

In terms of available software for nonlinear structural analysis, only a few provide specific tools for including bond-slip. For example:

i) The CASTEM 2000 software [37] provides the *acier-ancrage* model, which is based on the bond stress-slip relationship proposed by CEB-FIP Model Code 90 [38] for deformed bars.

ii) OpenSees [39] provides a steel material model (*Bond_SP01*) described by the bar stress-slip relationship proposed by Zhao and Sritharan [40] for simulating the slip between steel and concrete, in particular that resulting from strain penetration. The model was calibrated for elements with deformed bars. In OpenSees is also implemented the joint model proposed by Lowes and Altoontash [41], which takes into account the effects of bar slippage (see Section 2.2.3).

iii) The ATENA finite element package [42] provides two models to account for the effects of bond-slip [42]: one model based on the bond stress-slip relationship proposed by the CEB-FIP Model Code 90 [38] for deformed bars, and the other model based on the bond-slip law by Bigaj [43]. A new model implemented in ATENA that allows considering an arbitrary bond-slip relationship is described in [44].

2.2.3 - Beam-column joints

There is a vast amount of literature about the cyclic behaviour of RC beam-column joints, the majority of which was derived from data collected from investigation work carried out on joint specimens designed according to the specifications of modern design codes. The focus is mainly placed on the improvement of joint performance through new design concepts and improved details, such as joint hoops and improved anchorage [45]. In comparison, there is a considerably lesser amount of similar data available for joint elements representative of beam-column connections in existing old-type RC building structures lacking proper detailing. Data referring to beam-column joints with plain reinforcing bars is particularly scarce (see Section 2.4.3).

Beam-column joint regions are characterised by complex mechanical interactions. Frame member loads may be idealised as tension, compression, and shear resultants acting on the joint, with tension carried by the frame members' longitudinal steel, compression carried by longitudinal steel and concrete, and shear carried by concrete (Figure 2.9). The load carried in the frame members' longitudinal steel is transferred into the joint core concrete through bond. The load carried in the frame members' concrete is transferred directly into the joint core concrete. The shear transfer from the frame members into the joint core at the perimeter of the joint is assumed to occur across closed concrete cracks in the vicinity of the frame (member flexural compression zones) [41]. Joint failure is conventionally assumed when one of the force transfer mechanisms fails.

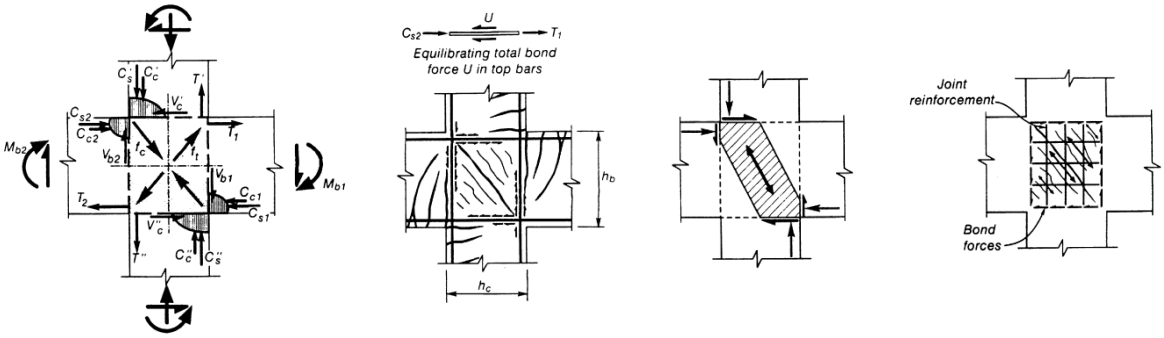

forces from beams an columns acting on the joint

crack pattern and bond forces after diagonal tension cracking initiates in the joint core

concrete diagonal strut mechanism, equilibrating concrete compression forces in beams and columns and some bond forces in the compression zones

truss mechanism of concrete diagonal compression field and horizontal and vertical reinforcement needed for equilibrium after diagonal tension cracking

Figure 2.9 - Interior beam-column joint subjected to seismic loading [46].

Diagonal tension cracking of the joint core takes place when the principal tensile stress acting under the combination of the stress and of the mean vertical compressive stress in the joint exceeds the concrete tensile strength [10]. If bond deterioration occurs at an early stage (as expected in the presence of plain reinforcing bars), the majority of the forces are transferred into the joint core by the compression strut (Figure 2.9-c), and therefore diagonal tension cracking is less likely to occur [46]. In this case, shear failure is not observed, but the connection is not able to develop its maximum nominal capacity. If diagonal cracking occurs, the joint is assumed to resist shear via the combination of the diagonal compression strut mechanism and a truss mechanism (Figure 2.9-d), the efficiency of which is highly dependent on the bond properties and also on the joint transverse reinforcement [46]: i) if bond is poor, the truss mechanism will not function; ii) if bond is good, the truss mechanism cannot transfer the joint shear without transverse reinforcement in the joint core and the joint shear will be mainly carried by the diagonal compression strut. The efficiency of the diagonal compression strut is strongly related to the anchorage solution adopted for the longitudinal reinforcement. Detailed information on the joint force transfer and shear resistance mechanisms can be found, for example, in [10, 46, 47].

As previously stated, beam-column joints in old-type RC building structures typically lack appropriate joint transverse reinforcement. Moreover, bond properties are typically poor, namely when plain bars are used as longitudinal reinforcement. In this case, the shear transfer from the elements framing into the joint to the joint core will have to mainly rely on the compression strut mechanism. Therefore, the joint behaviour will be highly dependent on the anchorage solution adopted for the longitudinal bars, the role of which has been observed to be particularly relevant on the response of exterior beam-column joints [8, 48, 49].

Detailed discussion on the effects of bond deterioration in beam-column joints on the local hierarchy of strength and sequence of events was provided by Calvi *et al.* [50]. Analysis of the influence of bond properties, namely the use of plain bars versus deformed bars, and its effects on the damage distribution can be found in Section 2.4.3.

Reference to reports of experimental work containing investigation about the influence of other parameters on the cyclic behaviour of beam-column joints (like column axial load, joint transverse reinforcement, amount of longitudinal and transverse reinforcement in the elements framing into the joint, alternative anchorage solutions, presence of slabs and transverse beams, among others) can be found in [12, 45, 51], and also in Section 2.4.3 for the particular case of joints with plain reinforcing bars.

Modelling strategies for beam-column joints

In the seismic analysis of RC frame structures, beam-column joints are commonly assumed rigid [52, 53]. However, recent analytical investigations [52, 54, 55] show that in most cases the rigid joint assumption is inadequate, and highlight the importance of accounting for shear and bond-slip. Only when joint shear deformations are negligible may the rigid joint assumption be considered an adequate modelling approach [28]. Many modelling strategies have been proposed for simulating the cyclic behaviour of beam-column joints, ranging from empirical methods to finite element models (see [12, 27, 35, 41, 50, 52, 54-67]). For example (Figure 2.10):

i) Youssef and Ghobarah [60] proposed a joint model in which the joint region is represented by four rigid elements, and beams and columns are idealised using elastic elements (Figure 2.10-a). The connection between the joint and each element idealises bond-slip and concrete crushing by using three steel springs and three concrete springs. Two diagonal translational springs connecting the opposite corners of the panel zone are used to simulate shear deformation.

ii) Shin and LaFave [63] proposed a model in which the joint is represented by four rigid link elements located along the joint edges and three nonlinear rotational springs embedded in one of the four hinges connecting the adjacent rigid elements. Rotational springs, two at each beam-joint interface, placed in series, separately simulate the fixed-end rotations due to slip of the beam longitudinal reinforcement and plastic hinge rotations due to inelastic behaviour of the beam (Figure 2.10-b). The model is particularly intended for the analysis of RC beam-column joints of ductile moment frames designed and detailed according to the provisions of modern seismic design codes.

iii) Lowes and Altoontash [41] proposed a joint element composed by one shear panel, eight bar-slip springs and four interface-shear spring elements (Figure 2.10-c). The model takes into account various inelastic response mechanisms such as the shear failure of the joint core, the loss of shear load transfer due to cracking at the beam-column interfaces, and the failure of bond on the longitudinal reinforcement. Modifications to the model were proposed by Mitra and Lowes [54, 61]. A simplified version of the model was proposed by Altoontash [62], consisting of a panel zone with a rotational spring to simulate the shear deformation of the joint and four zero-length rotational springs located at the beam-joint and column-joint interfaces to simulate the fixed-end rotations due to bar slippage (Figure 2.10-d).

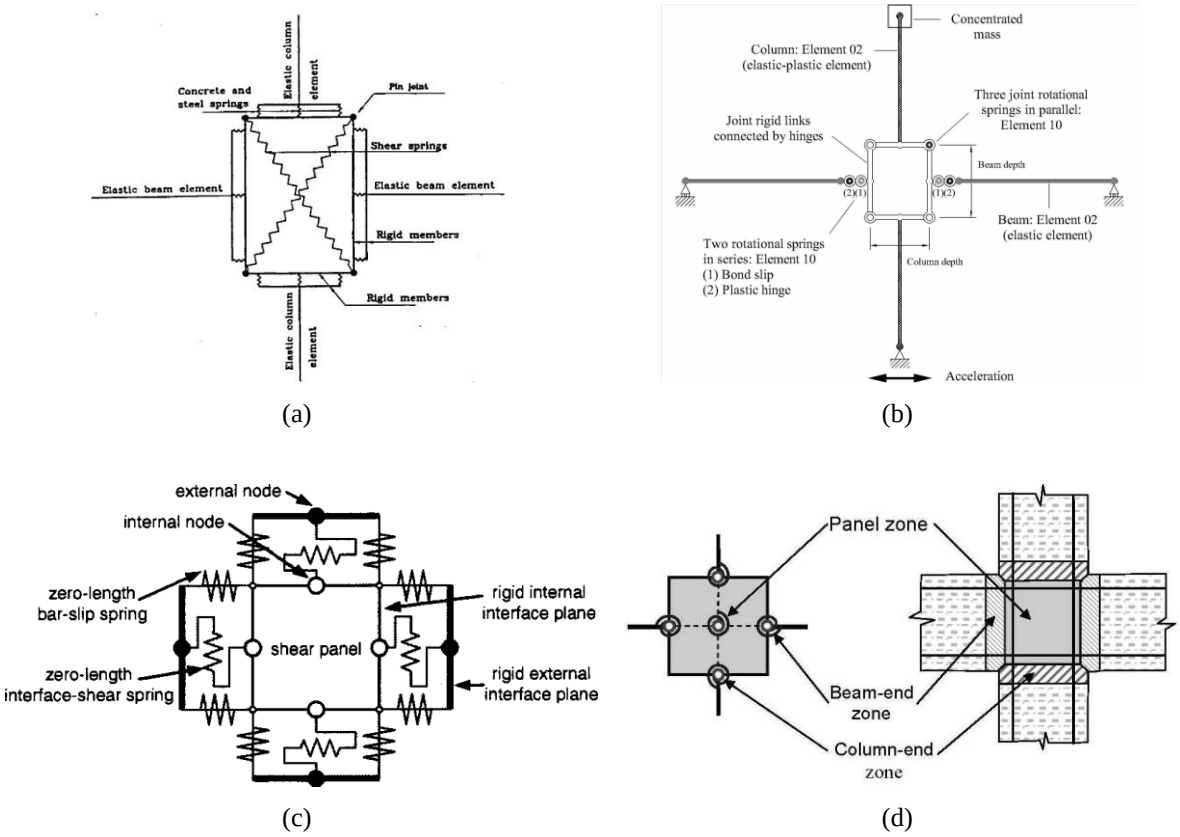

Figure 2.10 - Joint models proposed by: a) Youssef and Ghobarah [60]; b) Shin and LaFave [63]; c) Lowes and Altoontash [41]; d) Altoontash [62].

According to Favvata *et al.* [52], the type of models previously shown are difficult to implement in the seismic analysis of an entire RC frame structure. Studies that include the influence of joint damage and failure in the assessment of the seismic response of RC

structures typically adopt simple rotational spring elements, as in the joint model proposed by Calvi *et al.* [50] depicted in Figure 2.11 (see also [49]).

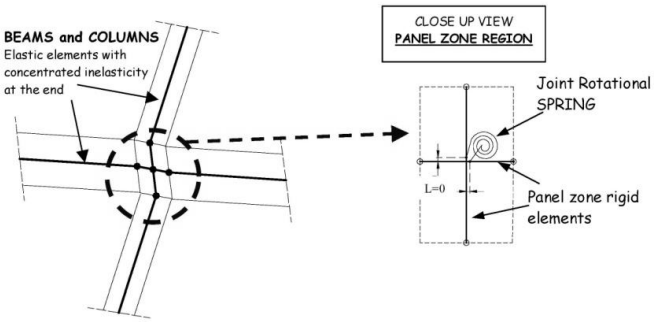

Figure 2.11 - Joint model proposed by Calvi *et al.* [50].

The effectiveness of nonlinear finite element procedures in capturing the nonlinear response of beam-column joints was recently investigated by Sagbas *et al.* [67]. A finite element program was used to simulate the behaviour of 12 beam-column joints, giving particular attention to the effects of shear deformation and bond-slip. The latter was simulated using "link" elements (two-node non dimensional elements consisting of two orthogonal springs, in which the two nodes can displace independently from each other, simulating the relative displacement between concrete and steel) placed at the interface between the concrete and the steel reinforcement elements. Based on the outcomes of the conducted analyses, Sagbas *et al.* [67]: conclude that nonlinear finite element analysis procedures can be an accurate and reliable tool in assessing the seismic performance of seismically designed and non-seismically designed beam-column joints; and, give general guidelines for the effective finite element modelling of beam-column joints regardless of the software being used. For the particular case of elements with plain reinforcing bars, the authors highlight the need for an improved model to describe the cyclic behaviour of plain bars towards a more accurate simulation of non-seismically designed joints containing this type of steel reinforcement.

2.3 - CONCRETE-STEEL BOND BEHAVIOUR OF PLAIN REINFORCING BARS

Data available about the concrete-steel bond behaviour (monotonic and cyclic) of plain reinforcing bars is significantly less rich and detailed than that available for deformed bars.

Consequently, the influence of the parameters that affect bond behaviour (like concrete strength, concrete cover, rib pattern of the reinforcing bar, casting direction with respect to bar orientation, rate and type of loading, confining effects, among others [2, 16, 68]) has not yet been comprehensively understood for elements with plain bars.

In terms of experimental studies, many 50 year old and even older experimental results on plain bars can be found in the published literature, but they are basically presented as reference data for deformed bars [22]. Moreover, most of the tests were principally aimed at the assessment of maximum bond strength, and information regarding the bond behaviour in the cyclic and pos-elastic fields is scarce [69, 70]. Recent reports of experimental studies on the bond behaviour of plain reinforcing bars can be found in [20, 21, 69, 71-74]. For example:

i) Fabbrocino *et al.* [21] performed a series of monotonic beam tests and pullout tests on plain reinforcing bars aimed at describing in detail the force-slip relationship of the bond mechanism for straight rebars and for anchoring end details, namely 180º hooks. The tests results revealed that slippage due to anchoring devices is relevant and cannot be neglected, especially in the larger post-yielding field.

ii) Feldman and Bartlett [20] performed an extensive experimental campaign consisting of 252 cylindrical pullout tests on specimens with plain reinforcing bars. The parameters investigated were: concrete compressive strength, bar size, bar shape, concrete cover and bar surface roughness. Empirical equations were presented for predicting maximum and residual average bond stresses.

iii) Cosenza and Prota [71] carried out an experimental campaign consisting of monotonic tensile and compressive tests on plain bar specimens with different values of the *L/D* ratio, where *L* stands for the stirrup spacing and *D* for the longitudinal bar diameter. The tests results confirm that the tensile behaviour of the bars slightly changes as *L/D* varies, and highlight the fact that the compressive behaviour depends on the *L/D* ratio and is not influenced by the bar diameter.

iv) Prota *et al.* [72] performed cyclic tests on plain bar specimens similar to those tested by Cosenza and Prota [71]. The tests results show that the cyclic behaviour of plain reinforcing bars was influenced by the loading history and the *L/D* ratio. Comparison was established with available results for deformed bars with the same

L/D ratio. The authors also tested the capability of existing hysteretic models, developed for deformed bars (Giuffrè-Pinto [75], Menegotto-Pinto [76], and Monti-Nuti [77, 78]), to predict the behaviour of plain bars under cyclic loading. The models were shown to reproduce with sufficiently good accuracy the cyclic behaviour of plain reinforcing bars for $L/D \leq 8$.

v) Verderame *et al.* [69] performed a series of monotonic and cyclic pullout tests aimed at the assessment of the bond performances of plain reinforcing bars. The results of the cyclic tests showed a significant degradation of bond capacities.

Bond behaviour is usually described in terms of the bond stress-slip relationship. The existing literature offers many constitutive relationships, monotonic and hysteretic, for describing the concrete-steel bond behaviour of elements with deformed bars (see [16]). Considering the different nature of the interaction mechanisms at the surface between concrete and steel in elements with deformed bars and elements with plain reinforcing bars, the models available for deformed bars are not considered suitable for plain bars, particularly with respect to cyclic loading [70]. For plain reinforcing bars, the only code instructions relative to the local constitutive bond-slip relationship can be found in CEB-FIP Model Code 90 [38].

Figure 2.12 depicts the CEB-FIP Model Code 90 [38] local constitutive bond-slip relationship for deformed bars, which is based on the bond stress-slip relationship proposed by Eligehausen *et al.* [79]. The code proposal for plain reinforcing bars is depicted in Figure 2.13. The model was calibrated using the results of the experimental work carried out by Rehm [80]. The model parameters (mean values) are presented in Table 2.1 and Table 2.2 for deformed bars and plain bars respectively. Parameter α is related to the shape of the ascending branch. Parameters τ_{max} and s_1 correspond to the peak resistance condition. Parameter τ_f is the frictional bond strength. As stated by Varum [2], the comparison between the model parameters for deformed bars (Table 2.1) and plain bars (Table 2.2) shows that, for equivalent conditions, the maximum bond stress for plain reinforcing bars is only 12% of that for deformed bars. Detailed information about the models can also be found in the CEB-217 report [68].

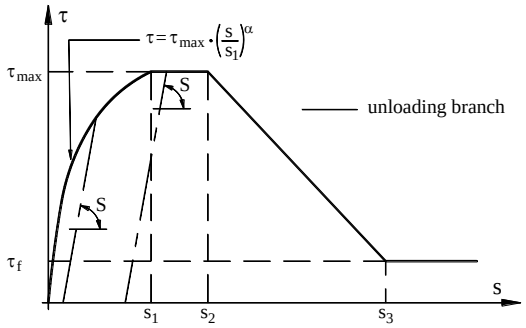

$$\tau = \begin{cases} \tau_{max} \cdot (s/s_1)^{\alpha} & 0 \le s \le s_1 \\ \tau_{max} & s_1 < s \le s_2 \\ \tau_{max} - (\tau_{max} - \tau_f) \cdot \left(\dfrac{s - s_2}{s_3 - s_2} \right) & s_2 < s \le s_3 \\ \tau_f & s_3 < s \end{cases}$$

Figure 2.12 - Bond stress-slip relationship given by CEB-FIP Model Code 90 for deformed bars [2, 68].

Table 2.1 - Parameters (mean values) of the bond stress-slip relationship of deformed bars [68]

Values	Unconfined concrete(1)		Confined concrete(2)	
	Bond conditions		Bond conditions	
	Good	All other cases	Good	All other cases
s_1	0.6 mm	0.6 mm	1.0 mm	
s_2	0.6 mm	0.6 mm	3.0 mm	
s_3	1.0 mm	2.5 mm	clear rib spacing	
α	0.4		0.4	
τ_{max}	$2.0\sqrt{f_{ck}}$	$1.0\sqrt{f_{ck}}$	$2.5\sqrt{f_{ck}}$	$1.25\sqrt{f_{ck}}$
τ_f	$0.15\,\tau_{max}$		$0.40\,\tau_{max}$	

(1) Failure by splitting of the concrete (2) Failure by shearing of the concrete between the ribs

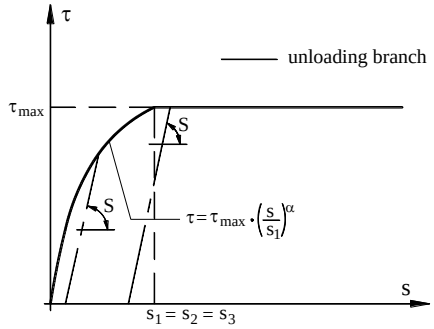

$$\tau = \begin{cases} \tau_{max} \cdot (s/s_1)^{\alpha} & 0 \le s \le s_1 = s_2 = s_3 \\ \tau_f & s_3 < s \end{cases}$$

Figure 2.13 - Bond stress-slip relationship given by CEB-FIP Model Code 90 for plain bars [2, 68].

Table 2.2 - Parameters (mean values) of the bond stress-slip relationship of plain bars [2, 68]

Values	Cold drawn wire		Hot rolled bars	
	Bond conditions		Bond conditions	
	Good	All other cases	Good	All other cases
$s_1=s_2=s_3$	0.01 mm		0.1 mm	
α	0.5		0.5	
$\tau_{max} = \tau_f$ (N/mm^2)	$0.1\sqrt{f_{ck}}$	$0.05\sqrt{f_{ck}}$	$0.3\sqrt{f_{ck}}$	$0.15\sqrt{f_{ck}}$

Verderame *et al.* [70] and Feldman and Bartlett [81] state that the bond model given by CEB-FIP Model Code 90 for plain bars is inconsistent with experimental observations, namely because it indicates no reduction in bond strength with increasing slip. Based on experimental results, the bond-slip relationship for plain reinforcing bars can be described as follows [70]: first, an ascending branch up to a peak strength value corresponding to very low values of slippage; second, and in contrast to the CEB-FIP Model Code 90 model, a softening branch (transition curve) related to the progressive degradation of friction mechanism. According to Verderame *et al.* [70], the model that best fits the experimental bond stress-slip behaviour for plain bars is the model proposed by Eligehausen *et al.* [79] modified by removing the plateau branch according to [82]. The model is depicted in Figure 2.14-a.

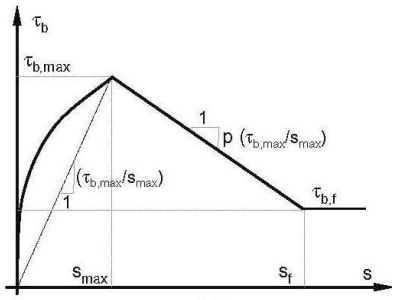

$$\tau = \begin{cases} \tau_{max} \cdot (s/s_1)^{\alpha} & 0 \le s \le s_1 = s_2 \\ \tau_{max} - p\dfrac{\tau_{max}}{s_1} \cdot (s - s_1) & s_1 \le s \le s_3 \\ \tau_f & s_3 < s \end{cases}$$

(a)

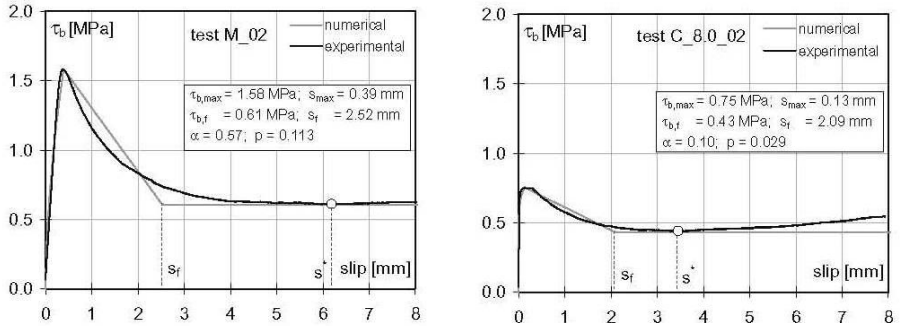

(b)

Figure 2.14 - Bond stress-slip relationship according to Eligehausen *et al.* [79] and modified by Cozenza *et al.* [82] (a), and comparison with test results from Verderame *et al.* [70] (b).

Several models are proposed in the literature for describing the bond behaviour of deformed bars under cyclic loading (Figure 2.15). Details on some of the available models can be found in [16]. Nowadays, the analytical bond-slip model proposed by Eligehausen *et al.* [79] (Figure 2.15-e), and subsequently modified by Filippou *et al.* [83], is considered

to be the most reliable model for describing the cyclic bond performance of deformed bars in the absence of splitting failure [70].

Conversely, for plain reinforcing bars a cyclic bond-slip model has not yet been established. A model proposal was recently presented by Verderame *et al.* [70] based on the results of the cyclic pullout tests carried out by the authors (described in [69]). The model is depicted in Figure 2.16. According to Verderame *et al.* [70], the proposed model represents well the degradation phenomena regarding the interaction mechanisms at the interface between concrete and steel due to cyclic excitations.

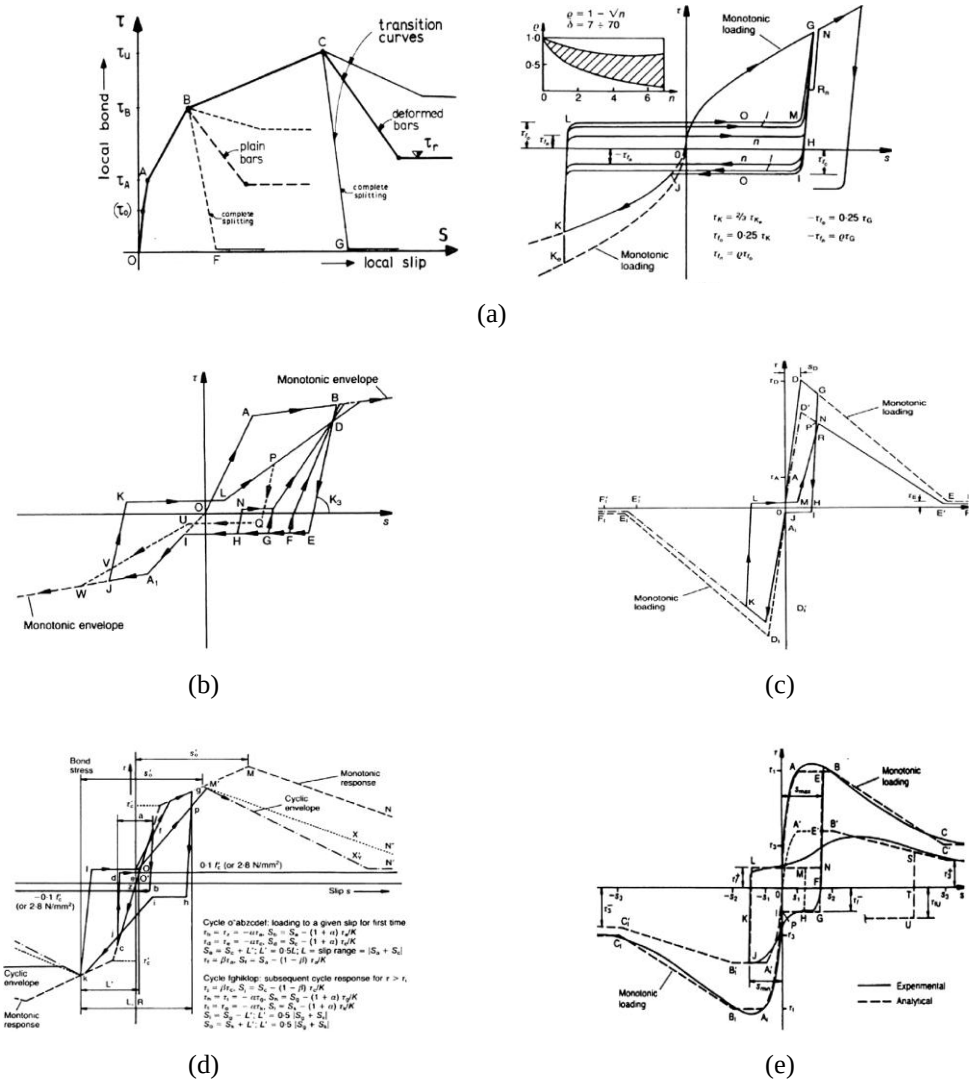

(a)

(b)

(c)

(d)

(e)

Figure 2.15 - Bond-slip models for cyclic loading (deformed bars) proposed by: a) Tassios [84] (monotonic envelope and cyclic rules); b) Morita and Kaku [85]; c) Viwathanatepa *et al.* [86]; d) Hawkins *et al.* [87]; e) Eligehausen *et al.* [79].

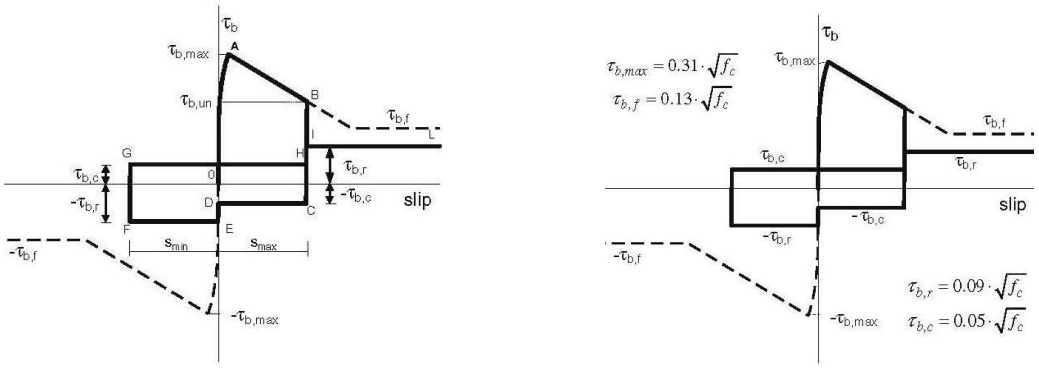

(a) (b)

Figure 2.16 - Cyclic bond-slip model for plain reinforcing bars proposed by Verderame *et al.* [70]: a) hysteretic bond-slip relationship; b) summary of the model parameters.

2.4 - PAST EXPERIMENTAL STUDIES ON THE CYCLIC BEHAVIOUR OF RC STRUCTURAL ELEMENTS WITH PLAIN REINFORCING BARS

The available data about the cyclic behaviour of RC structural elements results mainly from experimental tests carried out on elements with deformed bars. Experimental data referring to elements with plain reinforcing bars without specific detailing for seismic demands is scarce. As a consequence, the influence of the bond properties of plain bars on the elements' response has not yet been comprehensively understood. In this section are briefly described examples of recent relevant experimental work aimed at the investigation of the cyclic behaviour of substandard RC elements with plain bars (beams, columns, beam-column joints, and frame structures).

2.4.1 - Beams

If reports of experimental studies on RC elements with plain reinforcing bars are limited, this is particularly evident with respect to RC beams. Recently, Marefat *et al.* [88] carried out an experimental campaign consisting on monotonic and cyclic tests on RC beam specimens built half-scale. Three types of beam specimens were considered: i) specimens with deficient seismic detailing and plain reinforcing bars (substandard specimens); ii) specimens designed according to the American code for structural concrete ACI-318-99 (standard specimens) and built with plain reinforcing bars; and, iii) standard specimens with deformed bars. The tests results show that [88]: i) in comparison to the specimens with deformed bars, the specimens with plain reinforcing bars displayed a more evident

pinching effect and fewer and wider cracks (that were spread over a smaller length, Figure 2.17-a), and sustained larger slip and smaller yield strength; ii) regarding the specimens with plain reinforcing bars, only the standard specimens were able to develop the full flexural strength of the element; iii) slippage of the longitudinal reinforcing bars at the base had an important contribution to the overall deformation of the specimens with plain reinforcing bars (more than 50% of the total deformation of the substandard specimens, Figure 2.17-b).

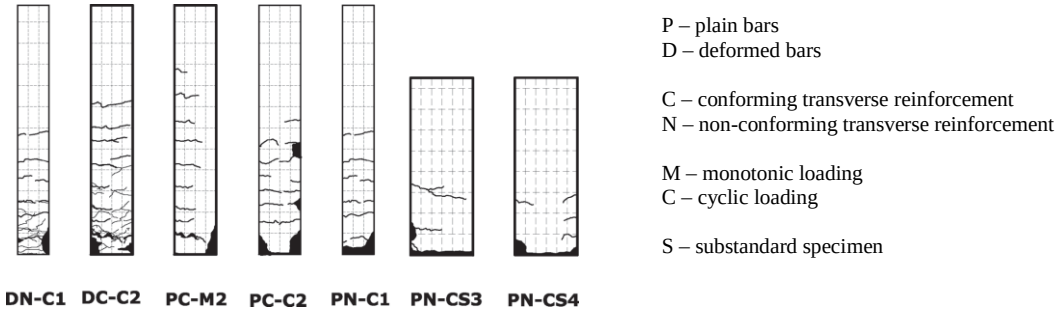

(a)

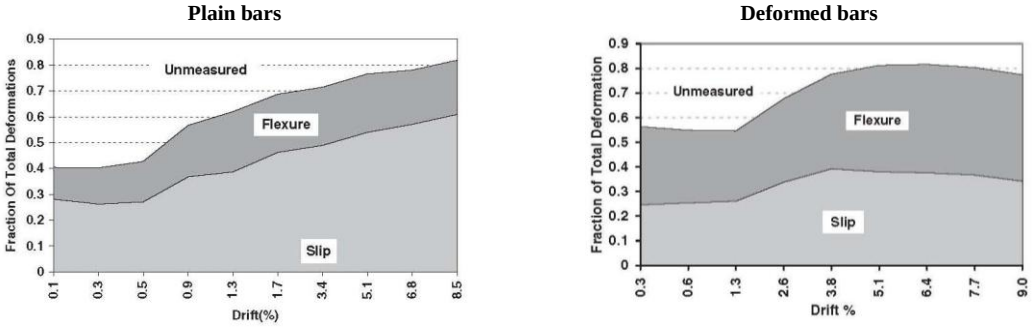

(b)

Figure 2.17 - Results of the experimental tests on RC beams carried out by Marefat *et al.* [88]: a) crack pattern at ultimate state; b) deformation components in specimens PC-C2 (plain bars) and DC-C2 (deformed bars).

2.4.2 - Columns

Verderame *et al.* [24, 25] carried out monotonic and cyclic tests on substandard RC column specimens with plain reinforcing bars (Figure 2.18), paying particular attention to the rotation capacity of the columns. The parameters under analysis were the lapping of the longitudinal reinforcing bars, the level of axial load and the displacement history. The tests results show that [24, 25]: i) the hysteretic response of the columns was affected by a pronounced pinching effect, which was less evident in the specimens with higher axial

load; ii) the crack pattern was characterised by a reduced number of cracks with large opening; iii) the rotational capacity of the specimens was strongly influenced by the column base rotation, in particular that of the columns with lap-splices; iv) when plain reinforcing bars are used, chord rotation results from a combined action of the fixed end rotation at the base and yielding spreading over the column length; v) the rules given by Eurocode 8 – Part 3 (EC8-3 [89]) for estimating the ultimate rotation capacity of RC elements with plain reinforcing bars underestimated the ultimate rotation capacity of the column specimens.

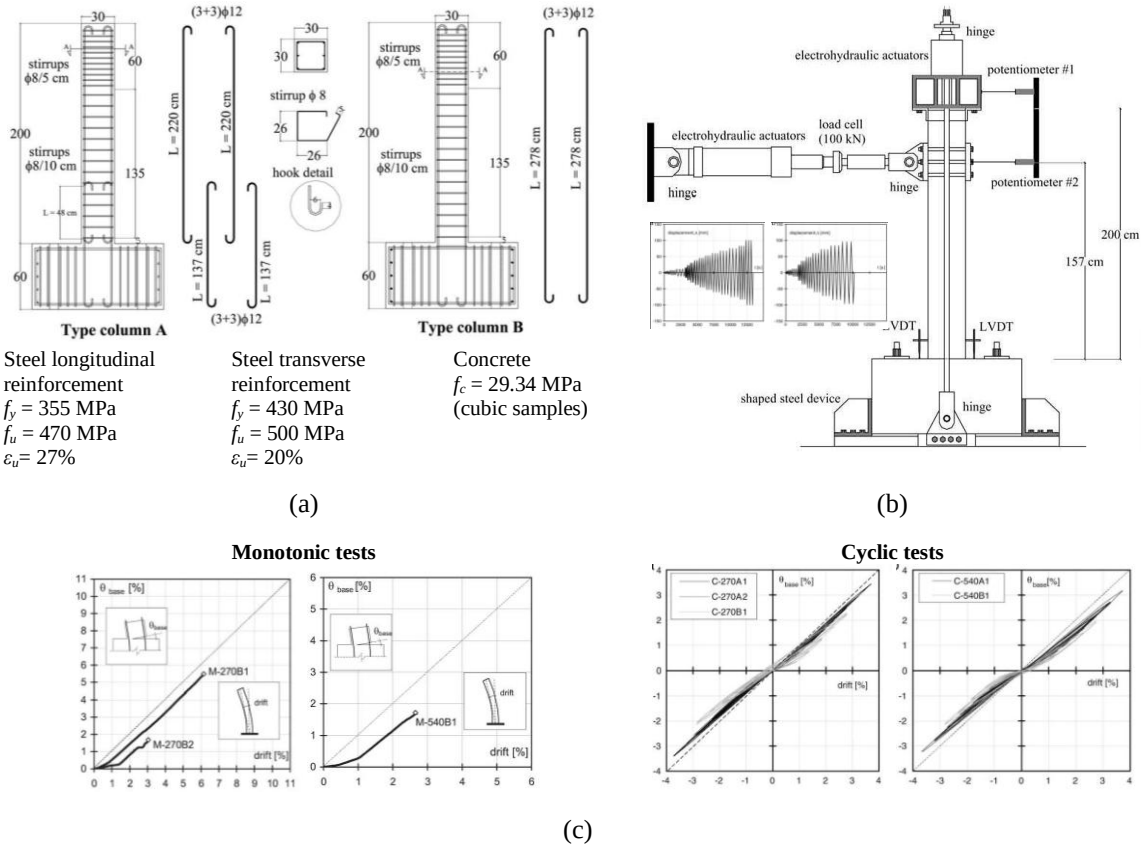

Figure 2.18 - Experimental campaign on RC columns carried out by Verderame *et al.* [24, 25]: a) column specimens and materials properties; b) test setup and displacement histories; c) column base rotation versus drift relationships.

The ultimate rotation capacity of columns was also investigated by Di Ludovico *et al.* [90]. Monotonic and cyclic tests were conducted on RC column specimens with plain and deformed reinforcing bars. The tests results show that: i) damage in the specimens with plain reinforcing bars was concentrated in a smaller number of wider cracks in comparison to the specimens with deformed bars; ii) the ultimate rotation capacity of the specimens

with plain reinforcing bars was higher than that of the specimens with deformed bars; iii) the contribution of column base rotation (fixed-end rotation) to the overall column deformation was particularly relevant for the specimens with plain reinforcing bars (66% and 75% of the total drift in the monotonic and cyclic tests, respectively).

A critical review of some of the formulations available to estimate the ultimate rotation capacity of RC elements with plain reinforcing bars was conducted by Verderame *et al.* [11]. Focus was put on the EC8-3 [89] approach. EC8-3 evaluates the ultimate rotation capacity of RC elements with plain reinforcing bars by applying an empirically calibrated correction coefficient to the capacity formulations calibrated on elements with deformed bars and seismically detailed. The correction coefficient, always inferior to 1, implies a reduction in the deformation capacity, which increases if lapping of longitudinal bars is present. However, recent experimental results ([11, 90]) indicate that the rotational capacity of RC elements with plain reinforcing bars is higher than that of elements with deformed bars, given equal the structural characteristics and details. As stated by Verderame *et al.* [11], considering the small number of experimental data for elements with plain reinforcing bars, a higher reliability of the correction coefficients can only be obtained by extending the experimental database so that a wider range of loading conditions, and geometrical and mechanical characteristics can be covered. Based on the experimental data available in the literature ([24, 25, 91-95]), Verderame *et al.* [11] also proposed a new correction coefficient to be applied to the EC8-3 expressions.

Bousias *et al.* [96] investigated the effectiveness of RC jacketing and of FRP wrapping for the seismic retrofitting of RC columns built with plain reinforcing bars. In addition to the type of retrofitting technique, the parameters studied were the lapping of longitudinal reinforcing bars, the number of FRP layers and the length of application of FRP wrapping. The impact of previous unrepaired damage on the effectiveness of concrete jackets was also investigated. The tests results indicate that lapping of the reinforcing bars did not have a significant effect on the behaviour of the unretrofitted specimens. Overall, FRP wrapping of just the plastic hinge and any splice region was shown to be more effective than concrete jacketing in enhancing the deformation and energy dissipation capacities of old-type columns with plain reinforcing bars, with or without lap-splicing.

2.4.3 - Beam-column joints

Experimental results of simulated seismic load tests on interior and exterior beam-column joints with substandard details, typical of RC buildings constructed in New Zealand before the 1970s, are reported by Park [97] (Figure 2.19). Comparison is established between the tests results obtained for specimens with plain bars [48, 98] and specimens with deformed bars [46, 99]. Concerning the exterior joints, two anchorage solutions for the longitudinal bars in the beams were investigated: i) beam bar hooks bent away from the joint core (typical in RC buildings built before the 1970s); ii) beam bar hooks bent into the joint core (as in current practice). The tests results indicate that [97]: i) the seismic performance of typical interior beam-column joints of pre-1970s RC moment resisting frames without joint transverse reinforcement would be poor in a severe earthquake, due to diagonal tension cracking in the joint core and bond-slip; ii) the cyclic behaviour of the exterior joints was significantly improved when the ends of the hooks were bent into the joint core; and, iii) the exterior joint specimens with plain reinforcing bars displayed poor performance when compared to the analogous specimens with deformed bars, displaying larger flexibility and lower strength.

The influence of the type of anchorage solution adopted for the beam bars in exterior joints with plain reinforcing bars (bent away from or bent into to the joint) was also studied by Liu and Park [48]. The dimensions and detailing of the joint specimens were similar to those depicted in Figure 2.19-b. The influence of column axial load (with or without) was also investigated. The tests results show that [48]: i) the flexural strength of the elements was lower than that predicted assuming perfect bond conditions; ii) the presence of axial load led to a large increase in the initial stiffness and global strength of the specimens, and also delayed premature concrete tension cracking initiated by the beam bar hooks; iii) the influence of the type of arrangement of the beam bar hooks was particularly evident in the performance of the specimens tested without column axial load; and, iv) bending the beam bar hooks into the joint core (as in current practice) resulted in higher flexural strength than bending the beam bar hooks away from the joint core.

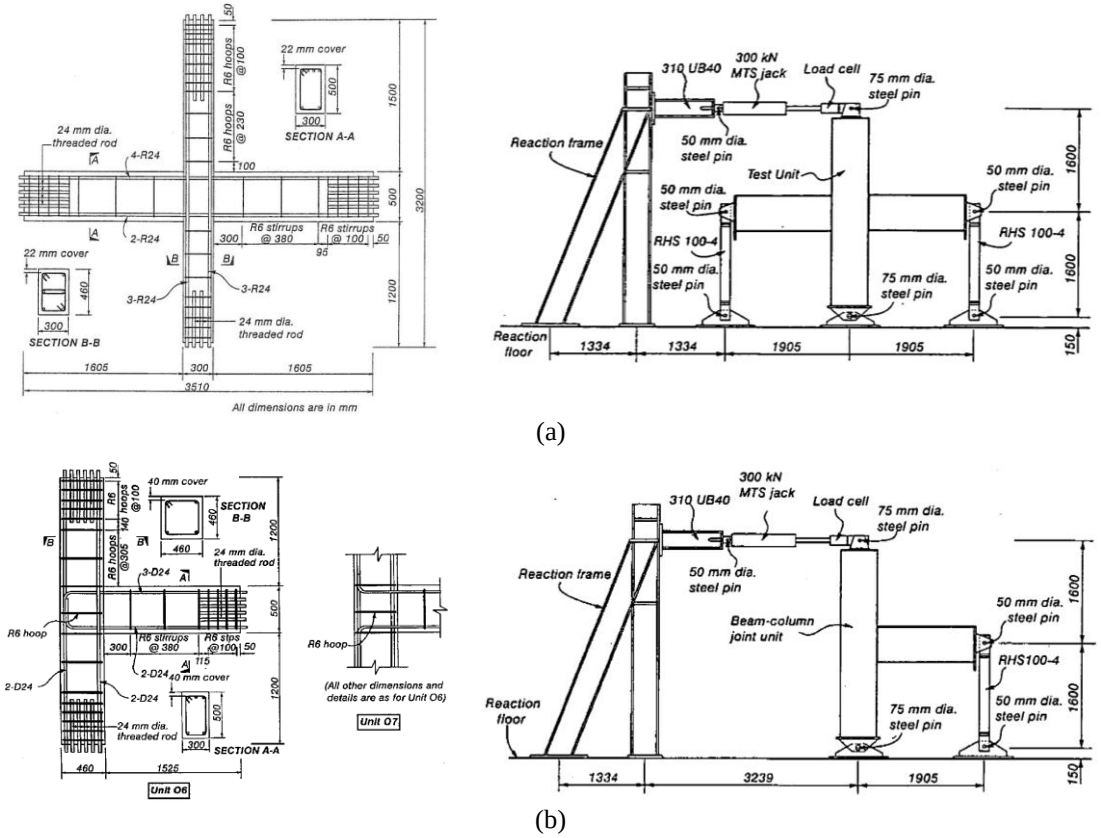

Figure 2.19 - Test specimens and test setup of the experimental tests on beam-column joints with plain and deformed reinforcing bars reported in [97]: a) interior beam-column joints; b) exterior beam-column joints.

Pampanin *et al.* [8] tested the cyclic behaviour of 2/3-scaled interior and exterior beam-column joints (Figure 2.20) with structural deficiencies typical of the Italian construction practice between the 50s and 70s (namely, gravity load design, absence of transverse reinforcement in the joint, and poor anchorage detailing). In the interior joint specimens, two different types of anchorage solutions for the beam longitudinal reinforcement through the joint region were considered: continuous reinforcement or lapped splices with end-hook anchorage outside the joint. The tests results show that [8]: i) the global response of the specimens was characterised by a marked pinching effect due to bar slippage of the longitudinal reinforcement; ii) the exterior tee-joint specimens displayed a hybrid brittle failure mechanism associated with the combination of joint shear damage with slippage of the longitudinal beam bar within the joint region with concentrated compressive force at the end-hook anchorage, resulting in severe damage within the joint core with spall off of a "concrete wedge"; and, iii) the presence of lapped splices and hook-end anchorage improved the global performance of the interior joint specimens, the behaviour of which was dominated by the column flexural damage, without damage in the joint region.

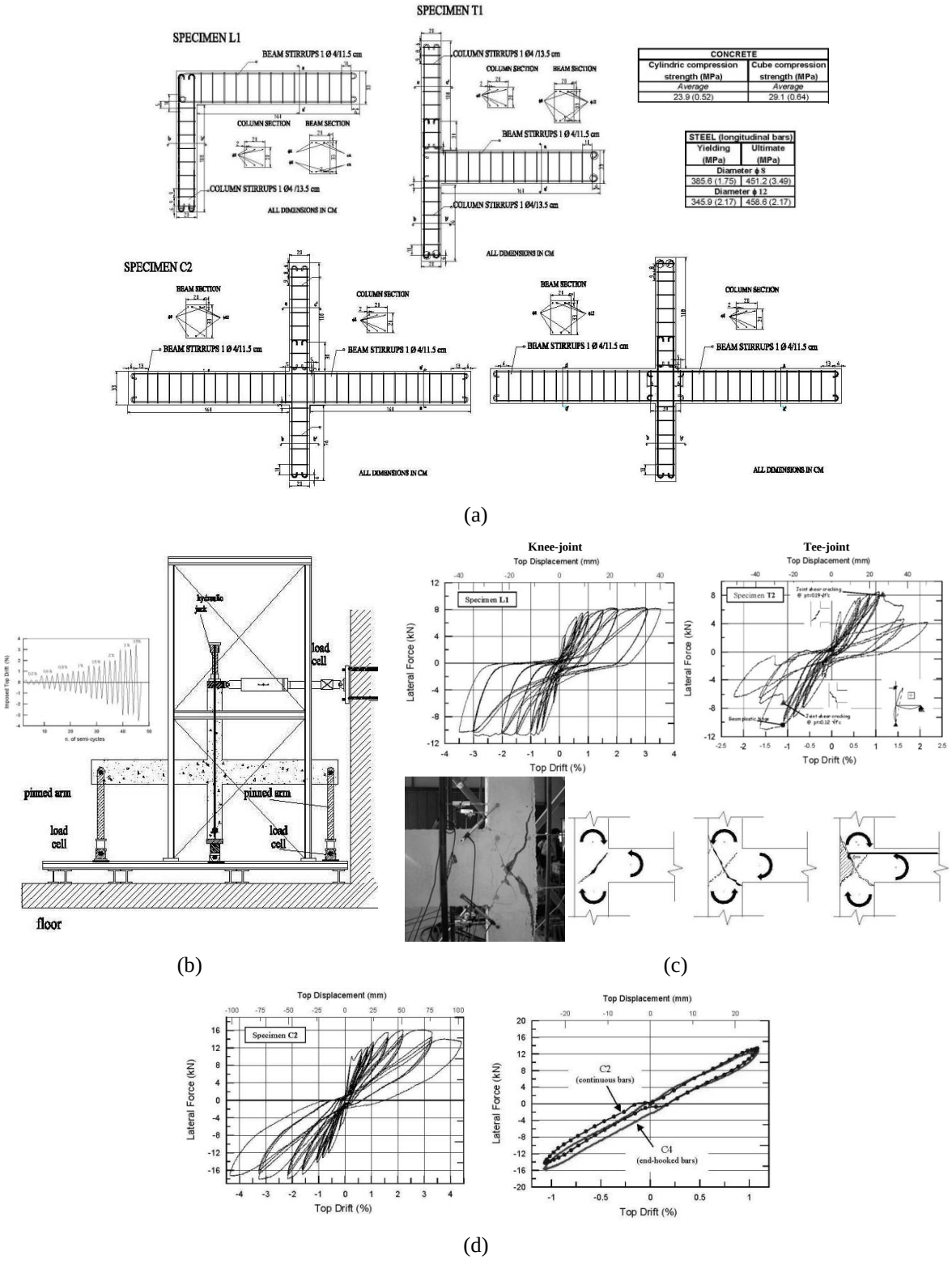

Figure 2.20 - Experimental campaign on RC joints carried out by Pampanin *et al.* [8]: a) joint specimens and materials properties; b) test setup and displacement history; c) test results for the exterior joint specimens (force-drift diagrams, damage and development of the "concrete wedge" mechanism); d) test results for the interior joint specimens (force-drift diagrams and comparison between anchorage solutions).

Hertanto [12] carried out cyclic tests on 2/3-scaled plane frame and space frame exterior beam-column joints with plain and deformed reinforcing bars. The specimens were subjected to a lateral reversed cyclic loading applied to the top of the column and column axial load, which was varied during the test in proportion to the lateral load. The space frame specimens were subjected to bi-directional cyclic loading. The tests results show that [12]: i) bond properties (plain bars versus deformed bars) had a major role in determining the type of failure (Figure 2.21); namely, the use of plain reinforcing bars can lead to joint shear failure, and beam flexural failure (as desired in seismic design) is more likely to occur when using deformed bars; ii) joint transverse reinforcement has an important beneficial effect on confinement and can alter the failure mechanism of the elements; iii) the variation in column axial load can have a positive or negative effect on the joint strength depending on the loading direction under analysis; and, iv) a certain amount of strength reduction has to be considered due to the effect of bi-directional loading (25% reduction is proposed for the global strength, and 40% reduction is indicated for the joint principle stress).

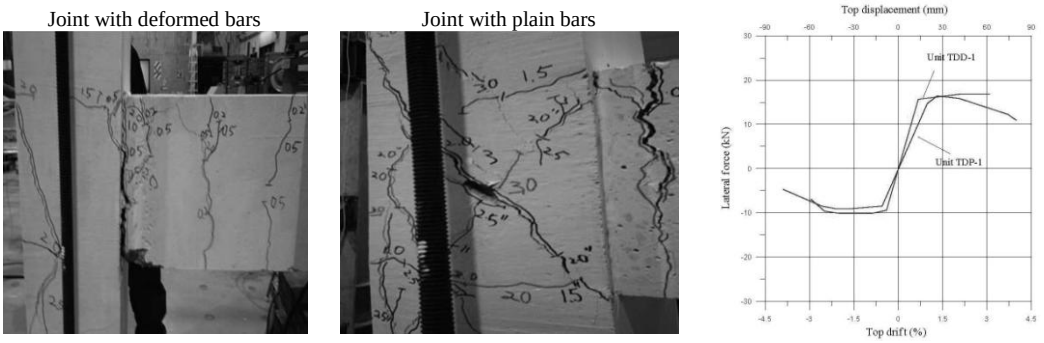

(b)

Figure 2.21 - Differences recorded between the deep beam joint specimens with plain and deformed reinforcing bars (final damage state and hysteretic envelopes) tested by Hertanto [12].

Bedirhanoglu *et al.* [100] investigated the cyclic behaviour of full-scale exterior beam-column joints with plain reinforcing bars and low-strength concrete (Figure 2.22). The parameters investigated were the column axial load (with or without, and different levels of axial load), displacement history (different number of target drifts), presence and amount of joint transverse reinforcement, presence of transverse beam and transverse slab, and anchorage solution within the joint region. The tests results show that [100]: i) the increase in column axial load led to a small increase in strength, lower pinching effect and larger

energy dissipation; ii) the influence of displacement history was negligible; iii) the presence of joint transverse reinforcement resulted in thinner inclined cracks in the joint region, larger maximum lateral load and energy dissipation capacity, and larger strains in the beam longitudinal reinforcement; and, iv) the presence of transverse beam and slab led to an increase in the lateral load capacity and to slight enhancement in the energy dissipation capacity.

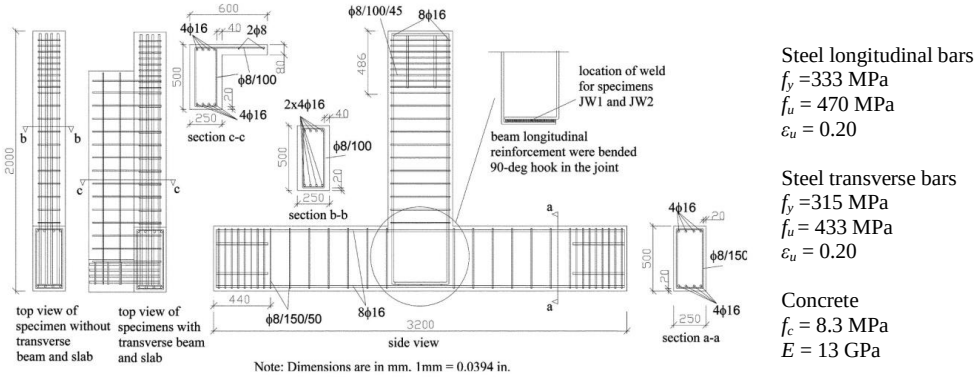

(a)

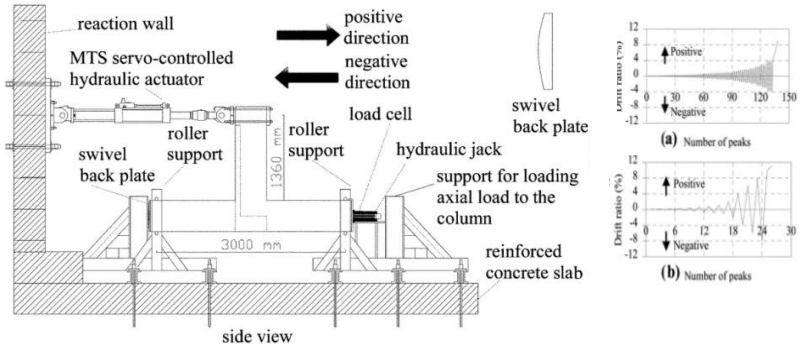

(b)

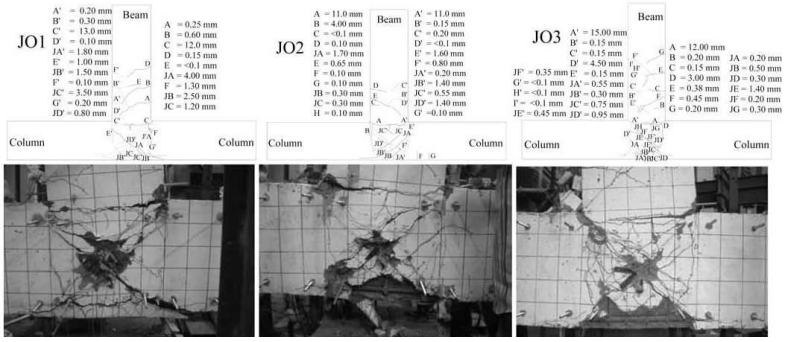

(c)

Figure 2.22 - Cyclic testing of exterior beam-column joints carried out by Bedirhanoglu *et al.* [100]: a) joint specimens and material properties; b) test setup and displacement histories; c) final damage state (examples).

Liu and Carr [101] tested the cyclic behaviour of RC beam-column joins, interior and exterior, representative of an existing RC frame building constructed in New Zealand in the late 1950s, the seismic performance of which was also investigated by the authors resorting to nonlinear static and dynamic analyses. Comparison was established with the test results of similar specimens with deformed bars [99, 102]. The main conclusions drawn from the tests results and comparative analysis, were [101]: i) the post elastic behaviour of the specimens with plain reinforcing bars was primarily governed by the flexural behaviour at the fixed-ends, where the majority of the post-elastic deformation was concentrated; conversely, the specimens with deformed bars displayed a more widely spread damage distribution (Figure 2.23-a); and, ii) column bar buckling and severe bond-slip along the longitudinal bars occurred adjacent to the joint region in the specimens with plain reinforcing bars, leading to lower flexural strength and stiffness in comparison to that registered for the specimens with deformed bars (Figure 2.23-b).

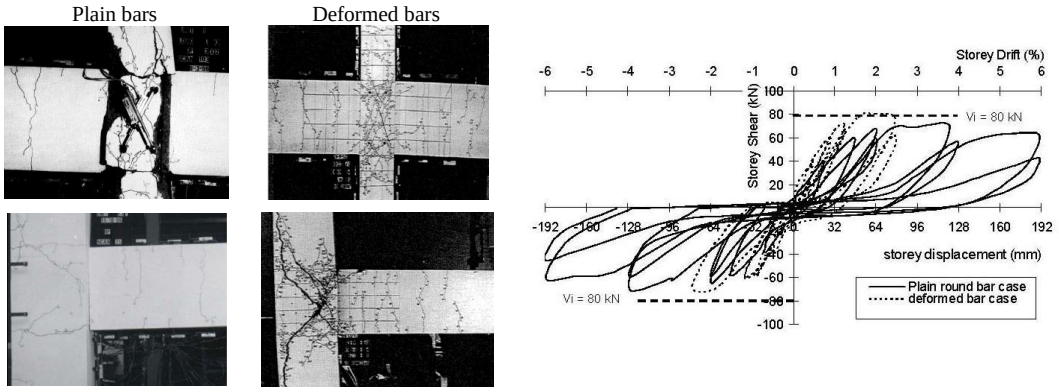

(a) (b)

Figure 2.23 - Comparison between beam-column joint specimens with plain and deformed reinforcing bars [101]: a) final damage state in beam-column joint specimens; b) storey shear versus storey displacement for the interior joints.

Reports of experimental work devoted to the investigation of different retrofitting techniques of substandard exterior beam-column joints with plain reinforcing bars can be found in [103-106]: i) Akguzel and Pampanin [103, 106] studied the feasibility and efficiency of a retrofitting technique based on Glass Fibre Reinforced Polymer (GFRP) composites, which was shown to provide satisfactory improvement of the behaviour of the as-built specimens (Figure 2.24-a); ii) Genesio *et al.* [104] proposed the retrofitting of RC beam-column joints using a fully fastened diagonal haunch element, which was shown to

improve the hysteretic behaviour of the as-built specimens thanks to the more ductile failure mode constituted by the beam flexural hinge instead of brittle shear failure (Figure 2.24-b); iii) Kam and Pampanin [105] presented selective-weakening and joint post-tensioning as feasible seismic retrofit strategies and techniques for non-ductile exterior beam-column joints.

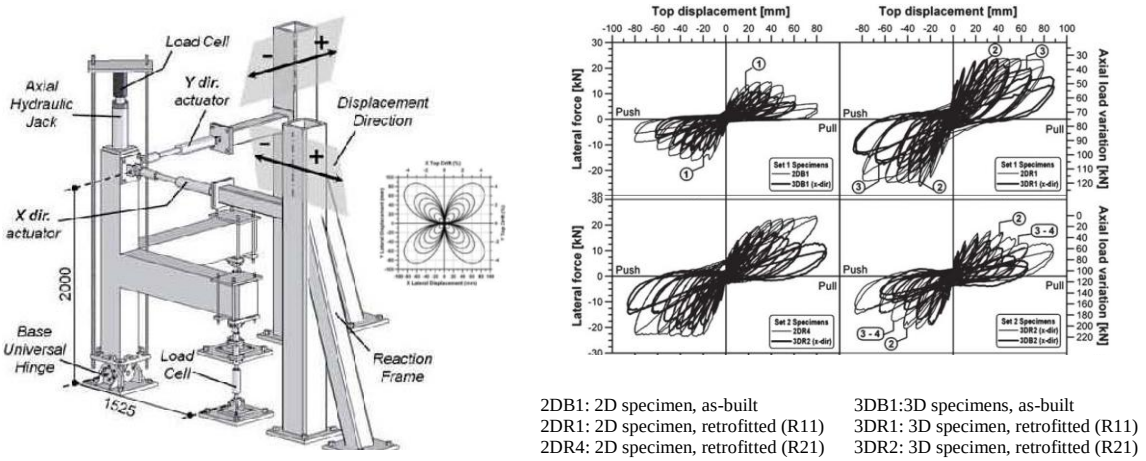

(a)

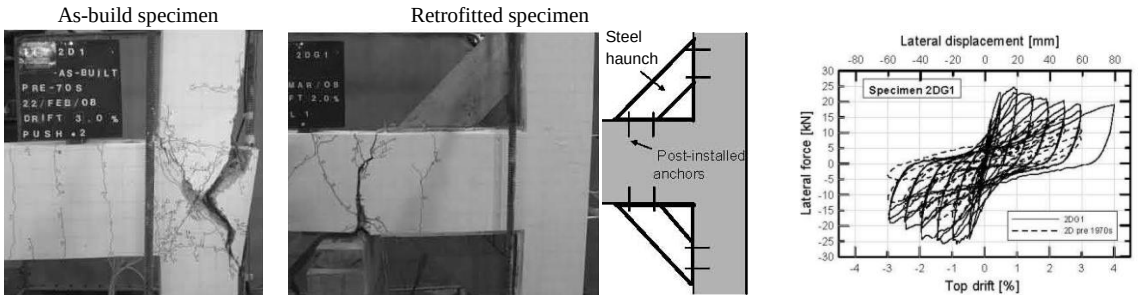

b)

Figure 2.24 - Experimental investigation on retrofitting techniques for exterior beam-column joints carried out by: a) Akguzel and Pampanin [106]; b) Genesio *et al.* [104].

2.4.4 - Framed structures

Calvi *et al.* [107] carried out a quasi-static cyclic test on a 3-storey RC frame structure, 2/3-scaled, built with plain reinforcing bars and without structural detailing adequate for seismic demands. The test results confirm the high vulnerability of the joint panel zone and also the tendency to develop undesirable global mechanisms due to the absence of an adequate strength hierarchy.

In the framework of the research programme ICONS, pseudo-dynamic tests on two full-scale models of existing non-seismic resisting RC frame structures (Figure 2.25-a), built with plain reinforcing bars, were carried out at the European Laboratory for Structural Assessment (ELSA) with the objective of assessing the seismic vulnerability of a bare frame, the effectiveness of different retrofitting techniques and the influence of masonry infill walls. Detailed information about the experimental investigation and tests results, which confirm the significant seismic vulnerability of existing structures constructed in the 1960s, can be found in [2, 108, 109]. In the numerical analyses performed by Varum [2], considering bond-slip effects in the numerical models was fundamental to achieve a more realistic description of the cyclic and ultimate behaviour of the frames (see Figure 2.8).

Pseudo-dynamic testing of a full-size 3-storey frame structure representative of old-type constructions in Southern European countries (without specific provisions for earthquake resistance and built with plain reinforcing bars) was performed as the core of the research project SPEAR (Seismic Performance Assessment and Rehabilitation of Existing Structures). The experimental investigation was also performed at the ELSA laboratory (Figure 2.25-b) and consisted of three rounds of pseudo-dynamic tests on the structure in three different configurations: as-built structure; retrofitted structure with FRP wraps; and, retrofitted structure with RC jacketing. Detailed information about the test campaign and tests results can be found in [110, 111].

(a) (b)

Figure 2.25 - Full-scale RC frame models pseudo-dynamically tested at the ELSA laboratory in the framework of the research programme: a) ICONS [2]; b) SPEAR [110].

CHAPTER 3

CYCLIC TESTING OF INTERIOR RC BEAM-COLUMN JOINTS

3.1 - INTRODUCTION

This section addresses the quasi-static cyclic tests carried out on six full-scale RC beam-column joint specimens designed and built to represent interior beam-column connections in existing pre-1970s RC building structures. Five specimens were built with plain reinforcing bars and one specimen was built with deformed bars. The behaviour of the specimens was analysed in terms of strength and stiffness, deformation, damage, energy dissipation, equivalent damping and ductility demands. The sensitivity of the specimens' response to displacement history, column axial load, concrete-steel bond properties, and amount of steel reinforcement was investigated.

The test results and comparative analysis concerning the two analogous joint specimens described in this chapter, one with plain bars and the other with deformed bars, were partially published in the IBRACON Structures and Materials Journal [1]. A comprehensive analysis of the test results for the six joint specimens will be published in the ACI Structural Journal [2].

3.2 - TEST SPECIMENS

3.2.1 - Geometrical characteristics and reinforcement detailing

The specimens were designed to represent an interior beam-column connection in a RC building frame structure. More specifically, in each specimen (Figure 3.1): each beam

element represents a half-span beam, with length equal to 2 m and 0.30x0.40 m^2 rectangular cross-section; and, each column element represents a half-storey column, with length equal to 1.5 m and 0.30x0.30 m^2 square cross-section. The six specimens were built full-scale.

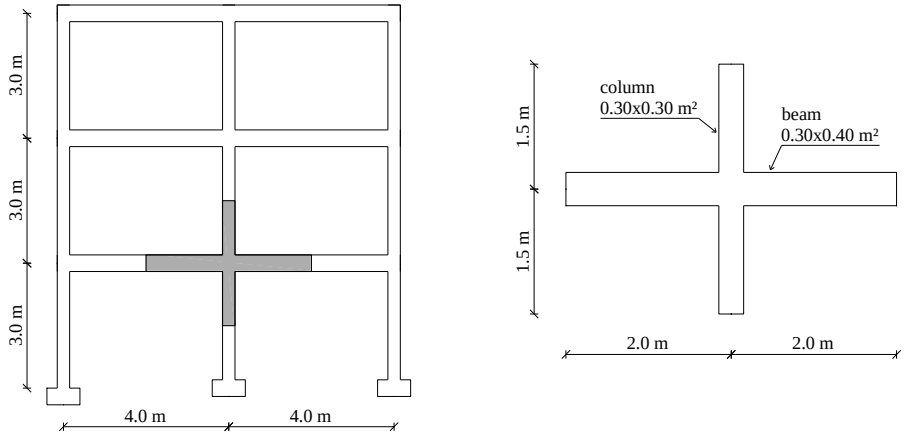

Figure 3.1 - Idealization of the beam-column joint elements under investigation.

Five specimens were built with plain bars as longitudinal and transverse steel reinforcement. These specimens are designated here as JPA-1, JPA-2, JPA-3, JPB and JPC. One additional specimen, JD, was built with deformed bars. All the other characteristics of JD were made equal to those of JPA-1 in order to allow a performance comparison between the two specimens. Figure 3.2 to Figure 3.4 depict the dimensions and reinforcement detailing of the joint specimens. It should be noted that the length of the beams and columns indicated in Figure 3.1 was modified in order to fulfill the geometrical conditions imposed by the adopted test setup.

The steel reinforcement details were specified in order to represent those typically adopted in existing pre-1970s RC building structures, designed and built without specific detailing for seismic demands. Inadequate transverse reinforcement in the elements framing to the joint, absence of joint transverse reinforcement, moment capacity of the columns lower than the moment capacity of the beams, inadequate anchorage solutions, and poor material properties (namely the use of plain reinforcing bars) are the main deficiencies associated with the detailing adopted for the steel reinforcement in the joint specimens under investigation. Comparison between the reinforcement detailing in the joint specimens and the specifications of the modern design codes is provided in Section 3.2.4.

In specimens JPA-1, JPA-2, JPA-3, and JD (Figure 3.2): i) the beams were reinforced with 6ϕ12 bars in the longitudinal direction and the transverse reinforcement consisted of ϕ8 closed stirrups at a spacing of 200 mm; ii) the columns were reinforced with 4ϕ12 bars in the longitudinal direction and the transverse reinforcement consisted of ϕ8 closed stirrups at a spacing of 250 mm. The amount of steel reinforcement adopted in specimens JPA-1, JPA-2, JPA-3, and JD is referred to herein as standard amount of steel reinforcement.

In comparison to the specimens mentioned above, JPB (Figure 3.3) and JPC (Figure 3.4) were built with twice the amount of column longitudinal reinforcement, composed by 8ϕ12 bars. JPC was also built with larger amount of transverse reinforcement in the beams and columns, consisting of ϕ8 closed stirrups at a spacing of 100 mm.

In all specimens the stirrups were bent with 90º bends, the longitudinal reinforcement of the elements was continuous ending with 90º bends, and there was no transverse reinforcement in the joint region. The concrete cover over transverse reinforcement was equal to 20 mm in the beams and columns.

Table 3.1 summarizes the values of longitudinal and transverse reinforcement ratios in the beams and columns, computed according to Eurocode 2 (EC2) [3]. In Table 3.1: d_{bl} is the diameter of the longitudinal reinforcing bars; d_{bw} is the diameter of the transverse reinforcing bars; ρ_l is the bottom longitudinal reinforcement ratio (in the beam); ρ_l' is the top longitudinal reinforcement ratio (in the beam); ρ_{tot} is the total longitudinal reinforcement ratio; ρ_w is the transverse reinforcement ratio; and, s is the distance between transverse reinforcing bars.

Table 3.1 - Steel reinforcement details

		Beam							Column				
		Longitudinal reinforcement				Transverse reinforcement			Longitudinal reinforcement		Transverse reinforcement		
Specimen	Steel	d_{bl} (mm)	ρ_l (%)	ρ_l' (%)	ρ_{tot} (%)	d_{bw} (mm)	s (mm)	ρ_w (%)	d_{bl} mm	ρ_{tot} (%)	d_{bw} (mm)	s (mm)	ρ_w (%)
JPA-1	Plain	12	0.38	0.19	0.57	8	200	0.17	12	0.50	8	250	0.13
JPA-2	Plain	12	0.38	0.19	0.57	8	200	0.17	12	0.50	8	250	0.13
JPA-3	Plain	12	0.38	0.19	0.57	8	200	0.17	12	0.50	8	250	0.13
JPB	Plain	12	0.38	0.19	0.57	8	200	0.17	12	1.01	8	250	0.13
JPC	Plain	12	0.38	0.19	0.57	8	100	0.34	12	1.01	8	100	0.34
JD	Deformed	12	0.38	0.19	0.57	8	200	0.17	12	0.50	8	250	0.13

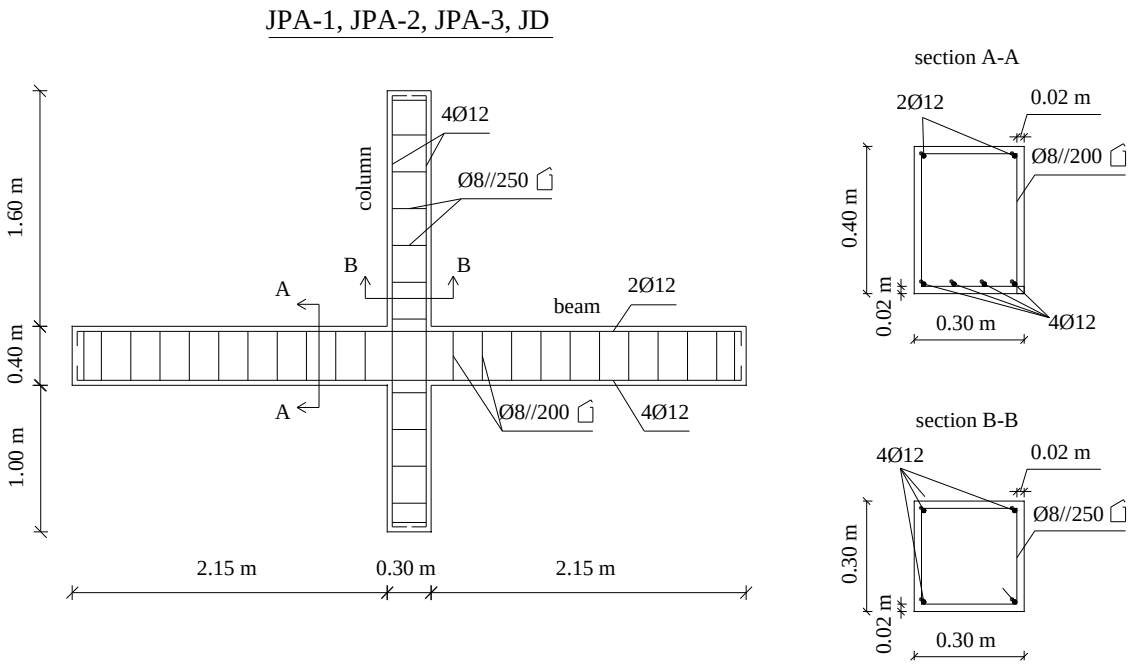

Figure 3.2 - Dimensions and reinforcement detailing of specimens JPA-1, JPA-2, JPA-3, and JD.

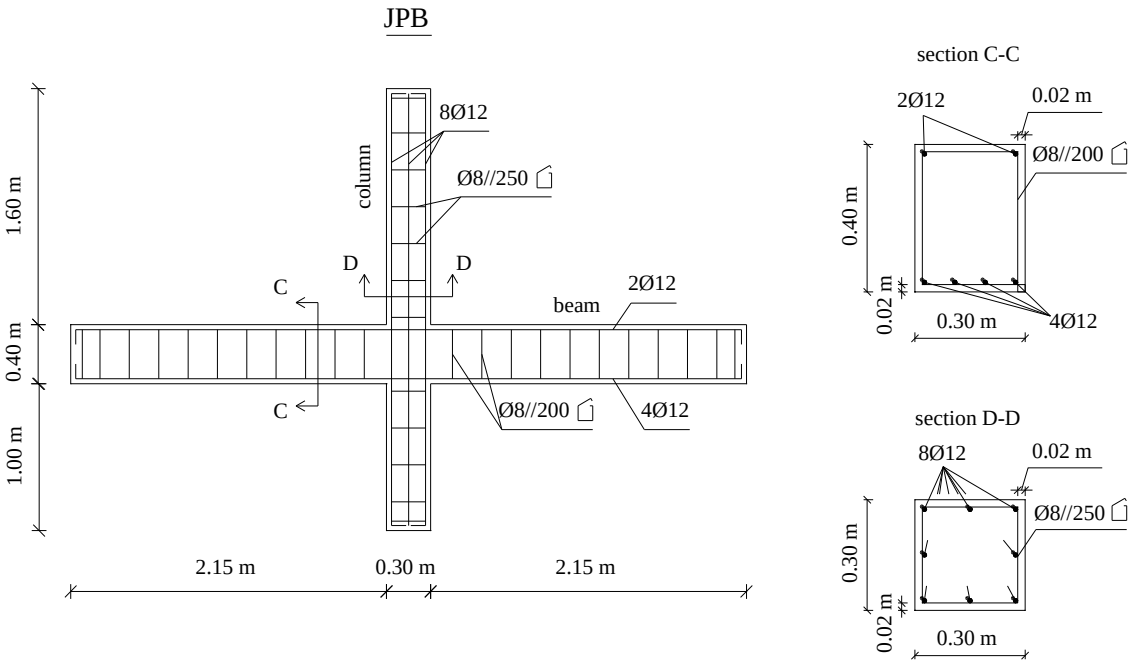

Figure 3.3 - Dimensions and reinforcement detailing of specimen JPB.

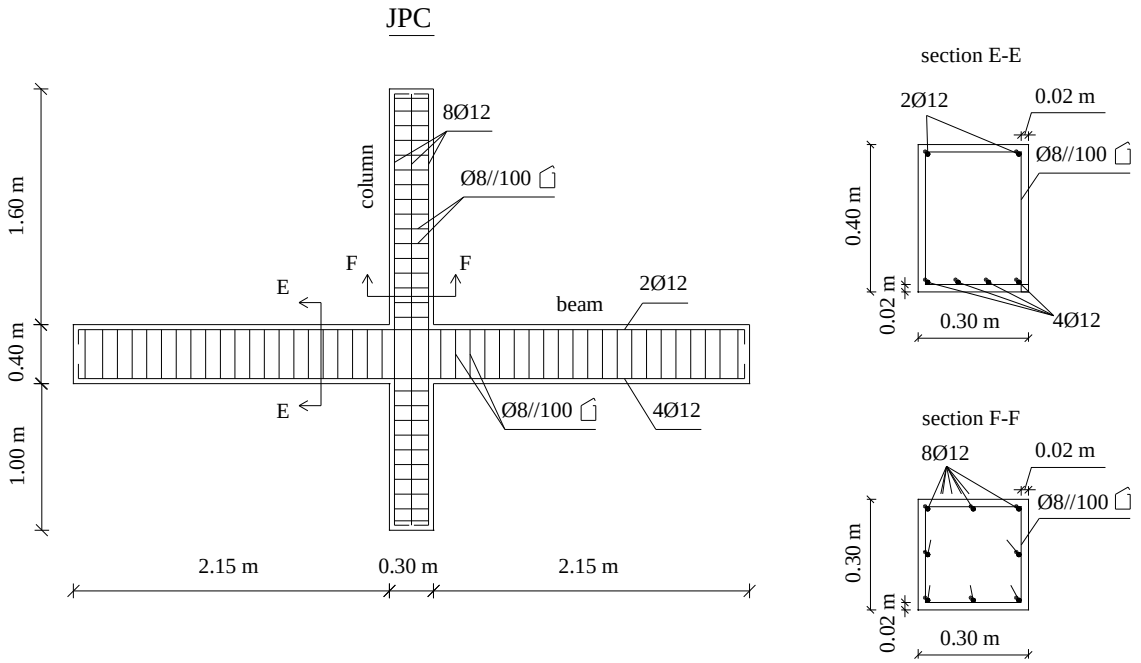

Figure 3.4 - Dimensions and reinforcement detailing of specimen JPC.

3.2.2 - Materials

Concrete

The six joint specimens were cast on the same day, with the same concrete mixture. Compressive tests on 0.15×0.15×0.15 m^3 cubic concrete samples, cast together with the specimens, were conducted according to the NP EN 12390-3 standard [4] to determine the concrete compressive strength. The mean value of concrete strength obtained in the compression tests is equal to 23.8 MPa, with a coefficient of variation equal to 4%. The characteristic compressive strength was estimated according to the NP EN 206-1 standard [5] and is equal to 19.8 MPa. Therefore, the concrete used in the construction of the joint specimens can be included in the concrete grade C16/C20 (EC2 classification).

Steel reinforcement

The mechanical properties of the plain reinforcing bars used in the construction of the joint specimens were determined resorting to tensile strength tests, carried out according to the EN ISO 6892-1 standard [6]. The tests were performed at the Faculty of Engineering of the University of Porto. Table 3.2 shows the mean values obtained for the mechanical properties of the plain reinforcing bars. The values of yield strength and ultimate strength

are substantially higher than those presented in the literature as typical values of steel strength of plain bars used in old-type RC structures. Nowadays, plain bars with mechanical properties similar to those used up to the 1970s are generally out of market. Based on the investigation conducted by Verderame *et al.* [7] on mechanical properties of steel reinforcement used in Italy and other countries until the early 1970s, 330 MPa and 470 MPa can be considered appropriate reference values for the yield strength and ultimate strength, respectively, of plain bars used in that period. However, considering that the cyclic behaviour of RC structures is strongly influenced by the concrete-steel bond properties and that premature bond degradation is expected to occur in the presence of plain reinforcing bars hence preventing the steel from mobilising its capacity, the abnormally high values of strength determined for the steel reinforcement were not expected to have a significant influence on the specimens' response. This assumption was confirmed in the analysis of the tests results of specimens JPA-1 and JD (Section 3.5), as well as in the numerical analysis described in Chapter 4.

The steel grade A400NR (REBAP [8] classification) was specified for the construction of specimen JD. The mean values of the mechanical properties are also indicated in Table 3.2.

Table 3.2 - Mechanical properties of the steel reinforcement (mean values)

Characteristics	Plain bars	Deformed bars
Yielding strength, f_y (MPa)	590	480
Ultimate strength, f_u (MPa)	640	601
Elastic modulus, E (GPa)	198	199

3.2.3 - Strength capacity prediction for the beam and column sections

Table 3.3 indicates the flexural and shear capacities ($M_{i,EC2}$ and $V_{i,EC2}$ respectively) predicted for the beams and columns according to the EC2 specifications**.** It should be noted that the formulation included in EC2 considers the plane section assumption and perfect bond conditions between concrete and steel. Therefore, the empirical procedure included in EC2 may not estimate accurately the strength capacity of RC elements with plain reinforcing bars.

Table 3.3 - Flexural and shear capacities of the beams and columns computed according to EC2

Specimen	Flexural capacity			Shear capacity	
	Beam		Column	Beam	Column
	positive direction	negative direction			
	$M_{b,EC2}^{+}$ (kN.m)	$M_{b,EC2}^{-}$ (kN.m)	$M_{c,EC2}$ (kN.m)	$V_{b,EC2}$ (kN)	$V_{c,EC2}$ (kN)
JPA-1	89	46	52	244	142
JPA-2	89	46	52	244	142
JPA-3	89	46	81	244	142
JPB	89	46	120	244	142
JPC	89	46	120	488	354
JD	67	35	52	178	103

3.2.4 - Comparison with modern code requirements for earthquake resisting structures

As previously stated, the beam-column joint specimens under investigation do not meet the modern code seismic design requirements. Inadequate detailing of transverse and longitudinal reinforcing bars, poor anchorage of longitudinal bars, absence of joint transverse reinforcement, and the use of plain bars as steel reinforcement are the main deficiencies in the joint specimens.

This section presents a comparison between the main detailing characteristics of the joint specimens and the rules established by Eurocode 8 - Part 1 (EC8-1) [9]. In general, differences can be found between the EC8-1 provisions for medium ductility class (DCM) and those for high ductility class (DCH). Whenever necessary, comparison with the EC2 [3] provisions is also presented. Again, it should be noted that the codes provisions consider perfect bond between concrete and steel.

The EC8-1 and EC2 provisions referring to the beam longitudinal reinforcement are mainly satisfied by the six joint specimens. The amounts of longitudinal reinforcement comply with the code specifications. However, for DCH, EC8-1 states that at least two high bond bars with 14 mm diameter should be provided both at the top and the bottom of the beam that run along the entire length of the beam.

To satisfy the necessary ductility conditions, among other requirements, EC8-1 states that the hoops diameter (d_{bw}) within the critical regions of primary seismic beams should not be less than 6 mm and the spacing between hoops should not exceed the minimum value

indicated in Equations (3.1) and (3.2) (for DCM and DCH respectively), where d_{bL} is the minimum longitudinal bar diameter and h_w is the beam depth.

$$s = min\{h_w/4; 24d_{bw}; 225; 8d_{bL}\} \quad (3.1)$$

$$s = min\{h_w/4; 24d_{bw}; 175; 6d_{bL}\} \quad (3.2)$$

According to EC2, the maximum spacing between transverse reinforcing bars (s_{max}) is given by Equation (3.3), where d is the effective depth of the cross-section and α is the inclination of the transverse bars to the longitudinal axis of the beam.

$$s_{max} = 0.75d \cdot (1 + \cot g\alpha) \quad (3.3)$$

The joint specimens under investigation satisfy the provisions regarding the diameter of transverse reinforcing bars. Table 3.6 summarizes the codes provisions in terms of maximum distance between beam transverse reinforcing bars and comparison is established with the distances used in the specimens. As observed, neither of the specimens complies with the EC8-1 provisions. In opposition, the EC2 requirement is fulfilled in all cases.

Table 3.4 - EC2 and EC8-1 provisions about maximum distance between beam transverse reinforcing bars (in mm)

Specimen	EC8-1		EC2	Used in the specimens
	DCM	DCH		
JPA-1, -2, -3	96	72	279	200
JPB, JPC				100
JD				200

Regarding columns, EC2 states that the diameter of the longitudinal bars should not be less than 8 mm. This is met by the six joint specimens under investigation.

EC8-1 states that in symmetrical cross-sections symmetrical reinforcement should be provided. Also, at least one intermediate bar should be provided between corner bars along each column side, to ensure the integrity of the beam-column joints. EC8-1 also requires the distance between consecutive longitudinal bars engaged by hoops or cross-ties not to

exceed 200 mm for DCM and 150 mm for DCH. Symmetrical longitudinal reinforcement in the columns was provided in all the joint specimens. In relation to the other two provisions, these are only fulfilled by specimens JPB and JPC.

EC8-1 states that the total longitudinal reinforcement ratio in primary seismic columns should not be less than 0.01 and not more than 0.04. According to EC2, the minimum amount of longitudinal reinforcement ($A_{s,min}$) should be derived from Equation (3.4), where: N_{sd} is the design axial compression force; f_{yd} is the design yield strength of the reinforcement; and, A_c is the total cross-sectional area of the column. The six joint specimens comply with the minimum requirements of 0.2%, given by EC2, which prevails in Equation (3.4). However, only specimens JPB and JPC meet the EC8-1 minimum requirements.

$$A_{s,min} = max\{0.10 N_{sd} / f_{yd} ; 0.002 A_c\} \tag{3.4}$$

According to EC8-1, the mechanical volumetric ratio of confining hoops, ω_{wd} (Equation (3.5)) within the critical regions at the base of the primary seismic columns should be at least equal to 0.08 for DCM, and 0.12 for DCH or 0.08 in all column critical region above the base. The mechanical volumetric ratio of column transverse reinforcement was computed for each specimen and is presented in Table 3.5. As observed, the six joint specimens comply with the EC8-1 requirements.

$$\omega_{wd} = \frac{\text{volume of confining hoops}}{\text{volume of concrete core}} \cdot \frac{f_{yd}}{f_{cd}} \tag{3.5}$$

Table 3.5 - EC8-1 provisions for minimum mechanical volumetric ratio of column transverse reinforcement

Specimen	EC8-1	Used in the specimens
JPA-1, -2, -3, JPB		0.11
JPC	0.08	0.23
JD		0.08

Within the critical regions of the primary seismic columns, hoops and cross-ties of at least 6 mm for DCM and the minimum value expressed by Equation (3.6) for DCH, should be provided at a spacing such that a minimum ductility is ensured and local buckling of longitudinal bars is prevented. With this purpose, the spacing *s* of the hoops should not exceed the minimum value given in Equation (3.7) for DCM, and in Equation (3.8) for DCH, where b_o is the minimum dimension of the concrete core (to the centreline of the hoops).

$$d_{bw} \geq 0.4 d_{bL,max} \cdot \sqrt{f_{ydL} / f_{y\,dw}} \tag{3.6}$$

$$s = min\{b_o/2; 175; 8d_{bL}\} \tag{3.7}$$

$$s = min\{b_o/3; 125; 6d_{bL}\} \tag{3.8}$$

According to EC2, in the vicinity of the joints the distance between hoops should not exceed the value expressed by Equation (3.9), where b_{min} stands for the minimum dimension of the column cross-section.

$$s = 0.6 \cdot min\{20d_{bL}; b_{min}; 400\} \tag{3.9}$$

The provisions regarding the diameter of transverse steel reinforcement are fulfilled by the six joint specimens under investigation. Table 3.6 summarizes the codes provisions in terms of maximum distance between column transverse reinforcing bars, and comparison is established with the distances used in the specimens. As observed, neither of the specimens meets the EC8-1 provisions. The EC2 requirement is only fulfilled by specimens JPB and JPC.

Table 3.6 - EC2 and EC8-1 provisions about maximum distance between column transverse reinforcing bars (in mm)

Specimen	EC8-1		EC2	Used in the specimens
	DCM	DCH		
JPA-1, -2, -3				250
JPB, JPC	96	72	144	100
JD				250

In beams and columns, for hoops used as transverse reinforcement, EC8-1 states that closed stirrups with 135º hooks and extensions of length $10d_{bw}$ should be provided. Contrarily to the code provisions, transverse bars with 90º bends were used in the joint specimens under investigation.

EC2 requires the reinforcing bars to be anchored in a way that the bond forces are safely transmitted to the concrete avoiding longitudinal cracking or spalling. The code considers that bends and hooks (illustrated in Figure 3.5) do not to contribute to compression anchorages. In the joint specimens under investigation, the longitudinal reinforcement was continuous ending with 90º bends. The poor anchorage, especially when combined with the use of plain reinforcing bars, may not be effective in preventing the bars from slipping.

The beam-column joint specimens were built without joint transverse reinforcement. However, EC8-1 states that: i) the horizontal confinement reinforcement in the joint should be not less than that provided along the column critical regions; and, ii) at least one intermediate vertical bar (between column corner bars) should be provided at each side of the joint.

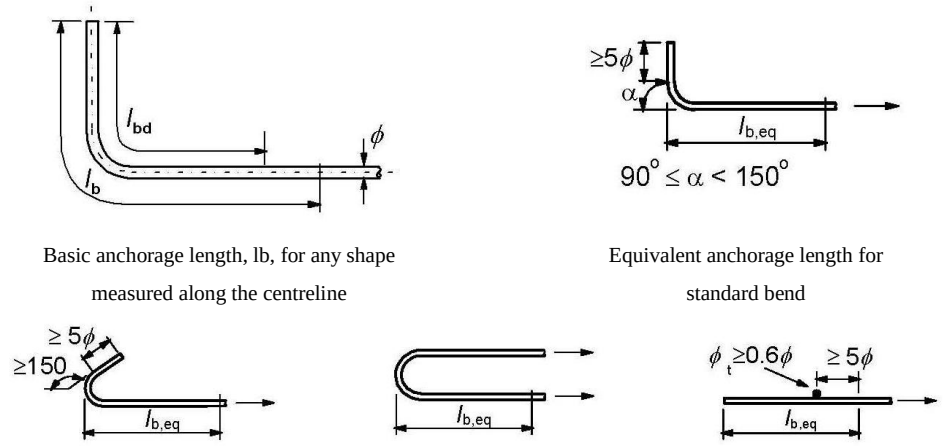

Figure 3.5 - Methods of anchorage other than by straight bars according to EC2 [3].

In terms of material properties, EC8-1 stipulates that concrete grade lower than C16/20 for DCM and C20/25 for DCH should not be used in primary seismic elements. In addition, only ribbed bars should be used as reinforcing steel in critical regions of primary seismic elements (with the exception of closed stirrups and cross-ties). The specification regarding

the concrete grade is met by the six joint specimens, but only for DCH. Regarding the steel reinforcement, with exception of specimen JD all specimens were built with plain bars hence against the code provisions.

3.3 - TEST SETUP AND TESTING PROGRAMME

The quasi-static cyclic tests were carried out under displacement controlled conditions. The joint specimens were tested under a lateral displacement history imposed on the free end of the columns, and constant column axial load. This section describes the test setup adopted to simulate the idealized support and loading conditions, as well as the adopted test procedure and loading patterns.

3.3.1 - Test setup

Figure 3.6 illustrates the test setup that was designed and built for the cyclic tests, with indication of the idealized support and loading conditions, and the nomenclature adopted for the elements (left and right beams, superior and inferior columns). The space restrictions in the laboratory, the maximum loads and displacements to be imposed in the cyclic tests, the stiffness and strength capacity of the specimens, and the capacity of the hydraulic actuators were the main parameters taken into account in the design of the test setup. The cyclic tests were conducted at the Civil Engineering Department of the University of Aveiro. Figure 3.7 depicts the test setup assembled in the laboratory.

The available literature about experimental tests on RC structural elements shows that beam-column joint specimens are usually tested in the vertical position. In the present work, the joint specimens were tested in the horizontal position. The adopted reaction elements (strong floor and steel reaction frames), with the joints placed horizontally, conduct to a stiffer support system. To minimize the frictional forces associated with this configuration, four high load-carrying capacity devices with reduced friction were placed below the specimens to carry their self-weight (Figure 3.8).

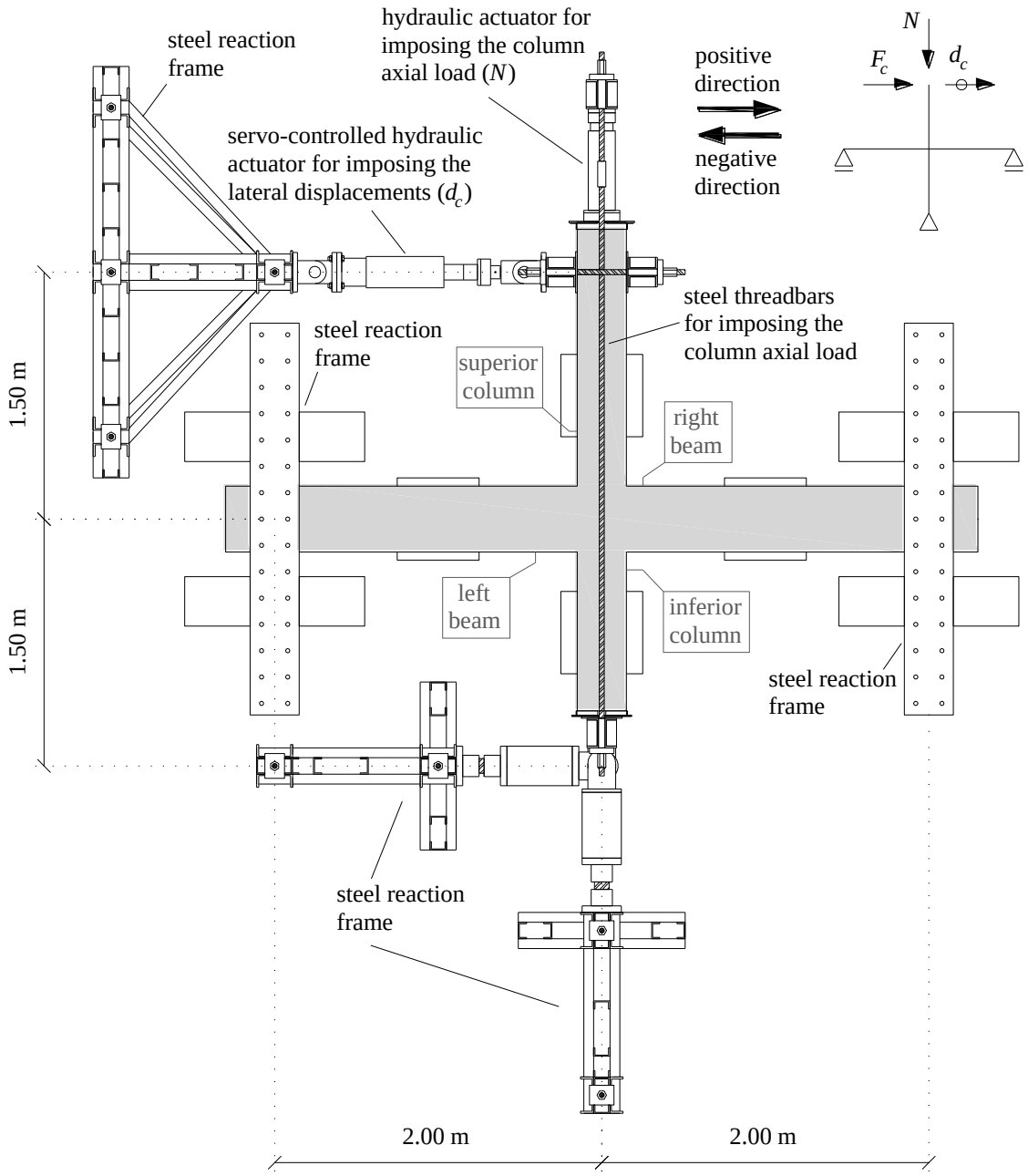

Figure 3.6 - Schematics of the test setup.

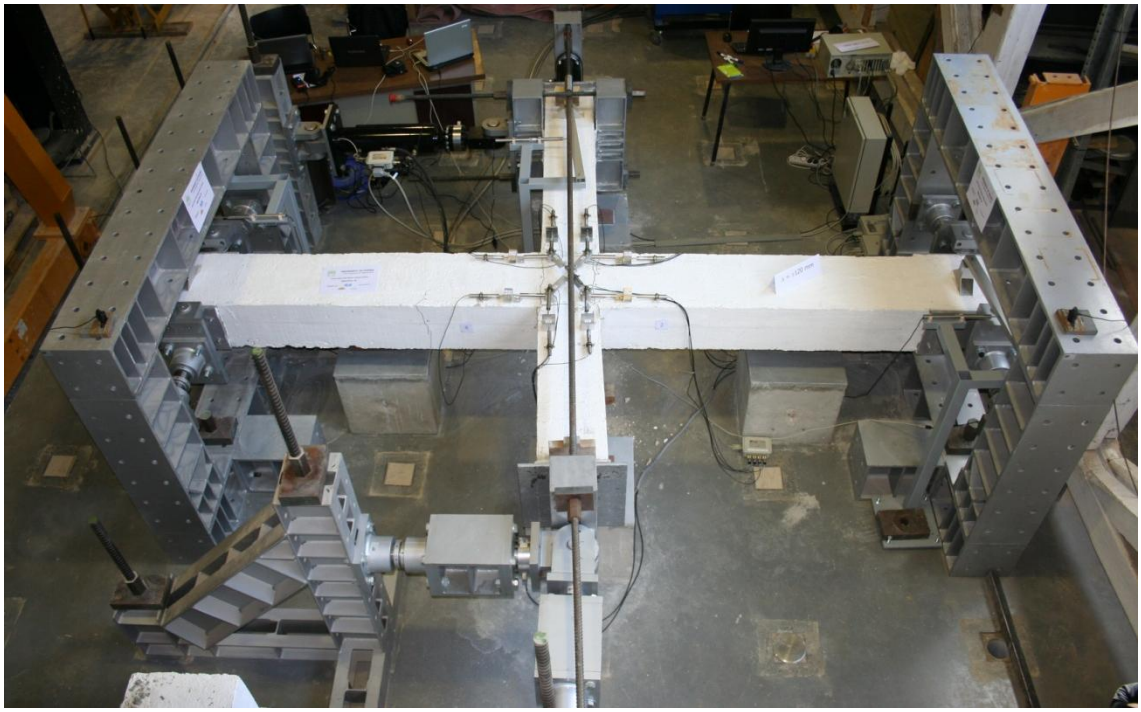

Figure 3.7 - General view of the test setup.

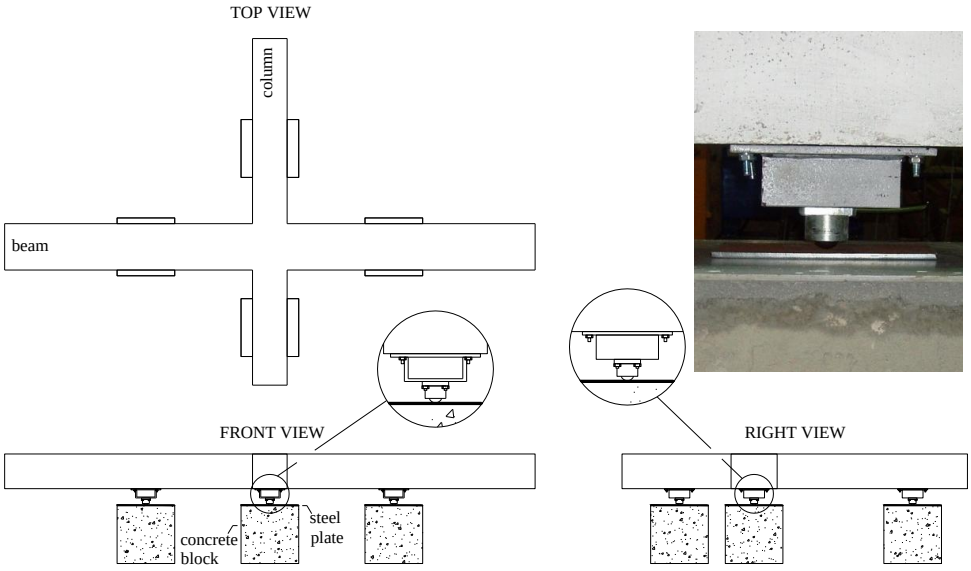

Figure 3.8 - Location and details of the high-load carrying capacity devices used to support the self-weight of the joint specimens.

Two steel reaction frames associated with sliding devices (one frame placed at each free end of beams) were used to simulate the support conditions of the left and right beams, only allowing displacements in the longitudinal direction of the beams and on-plane rotations (Figure 3.9). Two steel reaction frames (Figure 3.10) associated with a pinned connection at the base of the inferior column were used to simulate the column pinned

support only allowing on-plane rotations. A fifth reaction frame was designed to support the hydraulic servo-actuator used to impose the lateral displacements on the superior column (Figure 3.11). The five reaction frames were connected to the strong floor resorting to prestressing steel threadbars.

The frictional forces in the devices used to carry the self-weight of the specimens and to simulate the support conditions of the beams were estimated to be less than 2% of the maximum lateral load imposed by the servo-actuator.

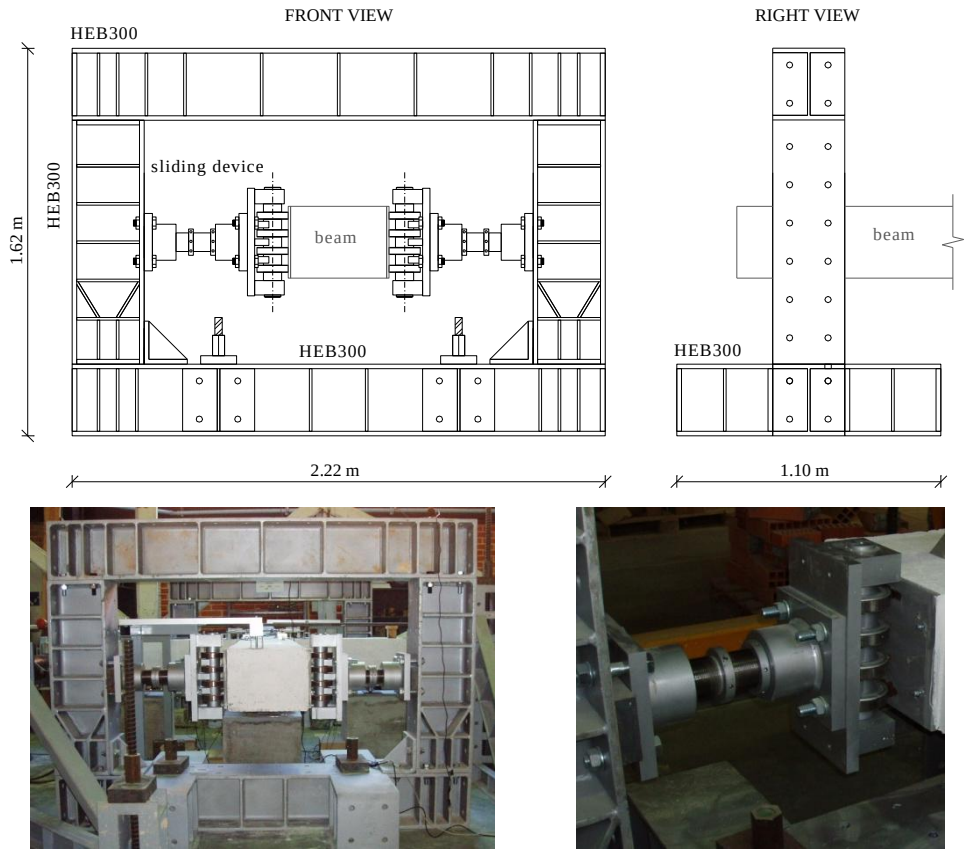

Figure 3.9 - Reaction frames and sliding devices designed to simulate the support conditions of the beams.

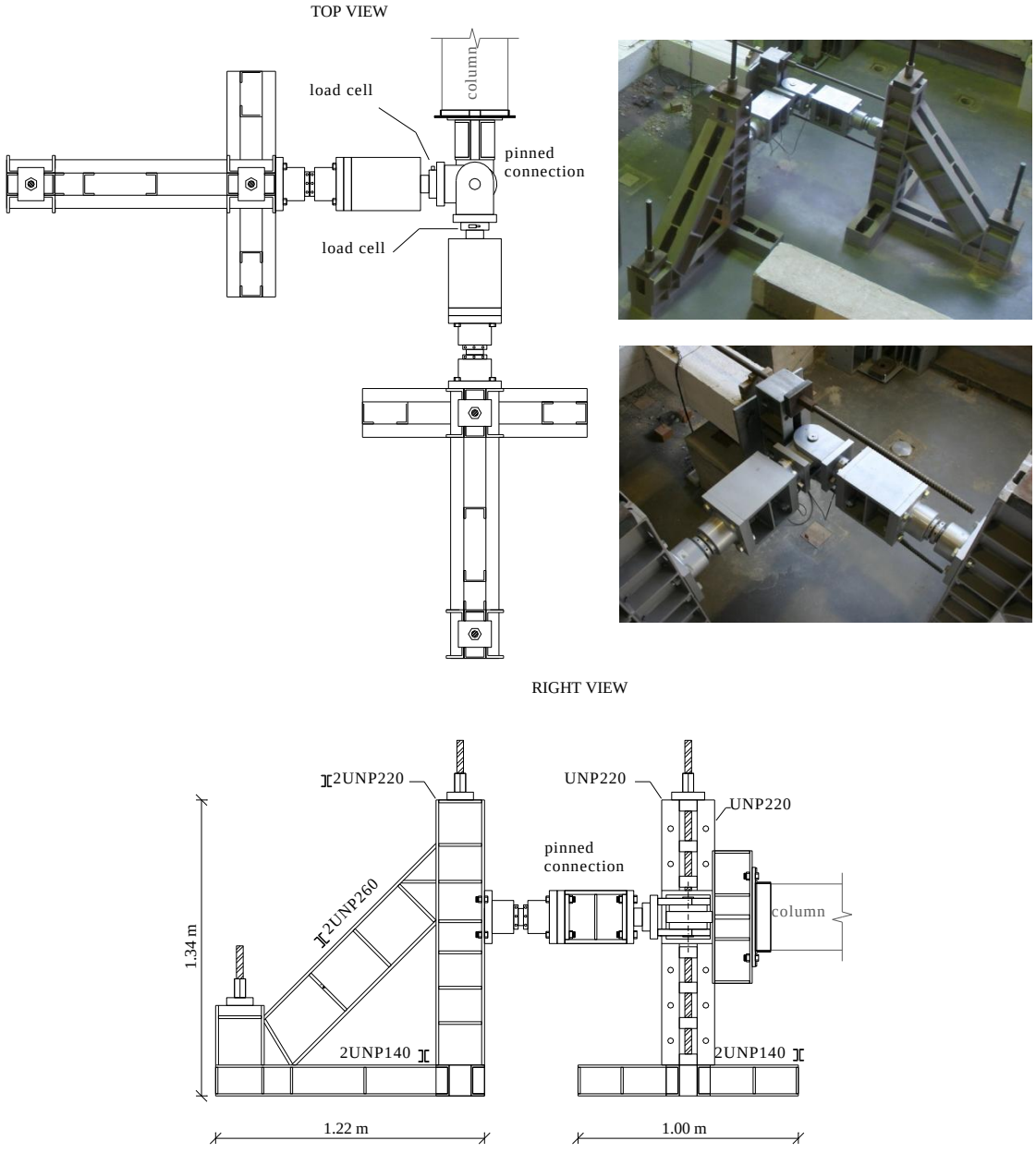

Figure 3.10 - Reaction frames and pinned connection designed to simulate the support conditions of the columns.

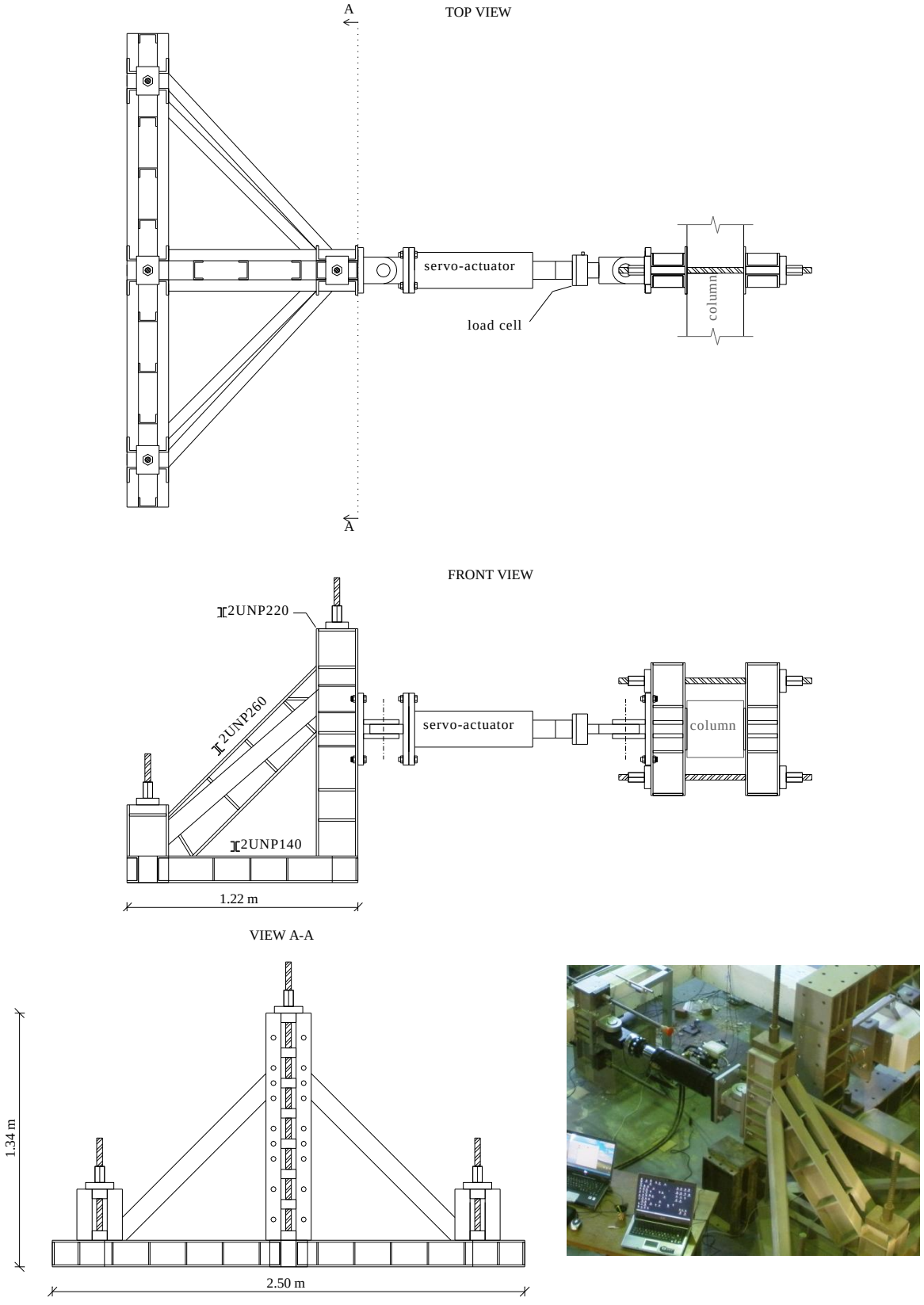

Figure 3.11 - Reaction frame and hydraulic servo-actuator used to impose the lateral displacements.

3.3.2 - Instrumentation

Hydraulic actuators

One hydraulic servo-actuator and one hydraulic actuator (manual control) were arranged at the top of the superior column to impose the lateral displacements (d_c) and the axial load (N) respectively. Figure 3.12 depicts the way the axial load was imposed on the columns. Two prestressing steel threadbars were placed along the columns, one above and the other below, and tensioned resorting to the hydraulic actuator, thus compressing the columns. This method allowed imposing the axial load without the need for an additional reaction frame, and minimizing the second order effects at the column-joint interfaces.

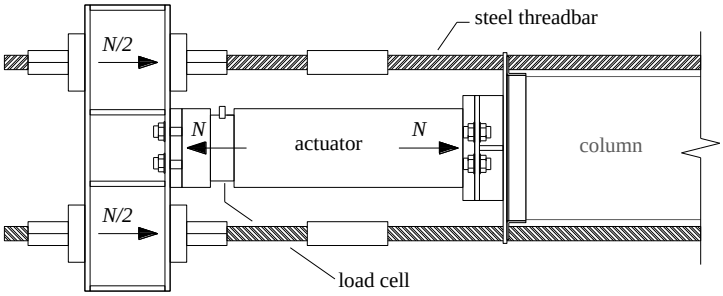

Figure 3.12- Method used to impose the column axial load.

Load cells

Two loads cells were connected to the column pinned support to monitor the horizontal and vertical reaction forces (see Figure 3.10). One load cell was attached to the hydraulic servo-actuator to monitor the lateral loads associated with the lateral displacements imposed on the superior column (see Figure 3.11). One load cell was attached to the hydraulic actuator to control the axial load imposed on the columns (see Figure 3.12).

LVDTs

A total of 21 Linear Variable Displacement Transducers (LVDTs) in each joint specimen were used to monitor the lateral displacements of the free end of the superior column and beams, as well as the local deformation and evolution of crack opening in the joint region and vicinities. Figure 3.13 depicts the instrumentation setup adopted.

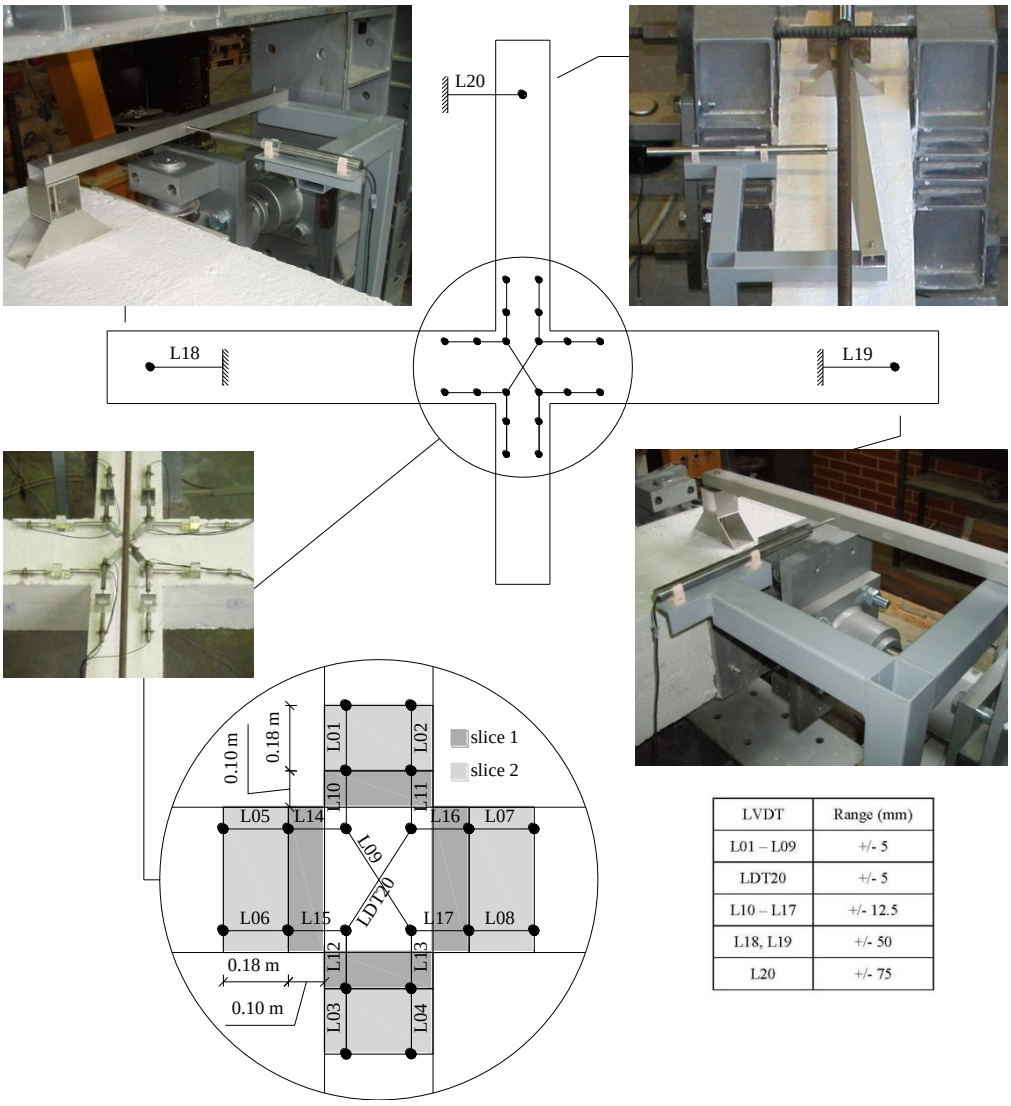

LVDT	Range (mm)
L01 – L09	+/- 5
LDT20	+/- 5
L10 – L17	+/- 12.5
L18, L19	+/- 50
L20	+/- 75

Figure 3.13 - LVDTs setup.

3.3.3 - Testing programme

Each joint specimen was subjected to a reversed cyclic lateral displacement history imposed on the free end of the superior column, and to constant axial load applied on the column top.

Two types of displacement histories were considered (Table 3.7 and Figure 3.14) in order to assess the influence of magnitude of drift interval and of number of cycles on the joints' response, namely on the degradation of stiffness and strength. Displacement history type 1 was imposed on all specimens except JPA-2, and is constituted by a series of push-and-pull cycles, three cycles at each level of displacement, with a total of 18 levels up to 120 mm

corresponding to a total drift (Δ) equal to 4%. In the displacement history type 2 (imposed on specimen JPA-2) only one push-and-pull cycle is performed at each level of displacement, with a total of seven levels, also up to 4% drift.

Table 3.7 - Lateral displacement histories

	d_c (mm)	1	2	4	6	10	15	20	25	30	40	50	60	70	80	90	100	110	120
	Δ (%)	0.03	0.07	0.1	0.2	0.3	0.5	0.7	0.8	1.0	1.3	1.7	2.0	2.3	2.7	3.0	3.3	3.7	4.0
		Number of cycles																	
Displ. history	Type 1	1	1	1	3	3	3	3	3	3	3	3	3	3	3	3	3	3	3
	Type 2	-	-	1	-	1	1	-	-	1	-	-	1	-	-	1	-	-	1

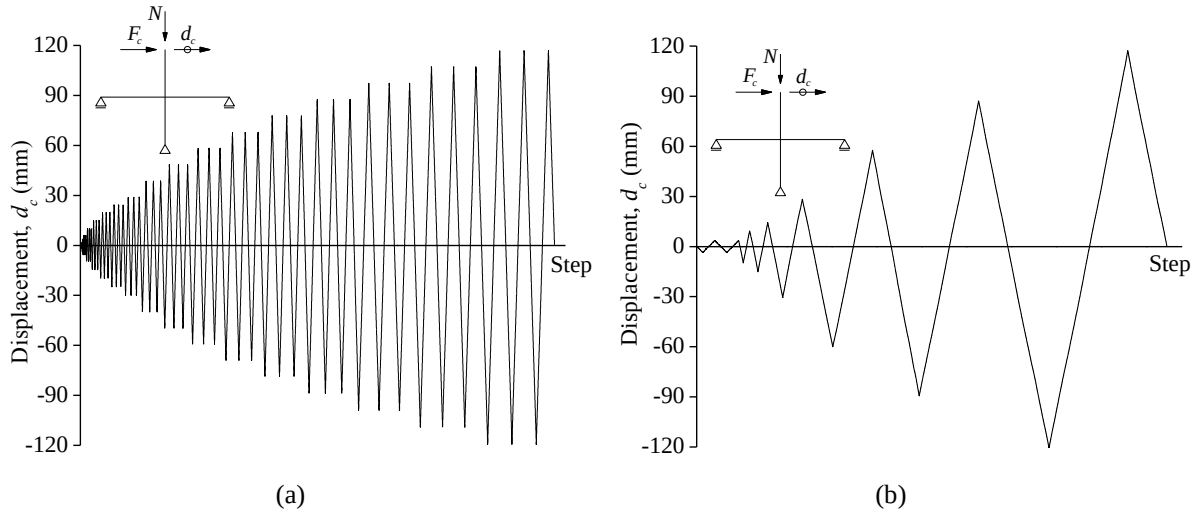

Figure 3.14 - Lateral displacement history: a) type 1; b) type 2.

Two levels of axial load were considered: 200 kN, representative of 2-3 storey buildings (corresponding to a normalized axial load equal to 9.4%); and, 450 kN, representative of 4-5 storey buildings (corresponding to a normalized axial load equal to 21.3%). Small variations in the axial load, resulting from the stiffness degradation associated with the damage evolution, were registered for the six joint specimens. The maximum variation in column axial load ranged from 2.8% (for JPB) to 10.3% (for JPA-3).

Table 3.8 indicates the type of displacement history and level of column axial load imposed on the joint specimens.

Table 3.8 - Column axial load and type of lateral displacement history imposed on the joint specimens

Specimen	JPA-1	JPA-2	JPA-3	JPB	JPC	JD
Axial load (kN)	200	200	450	450	450	200
Lateral displacement history	1	2	1	1	1	1

3.4 - ANALYSIS OF TESTS RESULTS

3.4.1 - Lateral load versus drift diagrams

Figure 3.15 depicts the lateral load versus imposed drift diagrams of the beam-column joint specimens. The corresponding peak envelopes are plotted together in Figure 3.16. For each specimen, the corresponding lateral load-drift diagram shows that the global response of the specimen was approximately symmetric both in terms of lateral load and stiffness. Table 3.9 indicates for each specimen: the maximum lateral load ($F_{c,max}$); the drift level ($\Delta_{Fc,max}$) at which $F_{c,max}$ was registered; and, the maximum strength degradation ($\Delta F_{4\%}$), computed as the ratio between the lateral load at maximum drift and $F_{c,max}$. The maximum difference between the maximum lateral loads in the positive and negative loading directions is: less than 1% for JPA-1, JPA-2 and JD; and, equal to 3% for JPA-3, 10% for JPB, and 4% for JPC. The relatively larger difference registered for JPB is mainly related to the asymmetric damage distribution in the specimen (see Section 3.4.3).

Within the drift range imposed on the specimens, JPA-1 was the specimen for which was registered the lowest strength and lowest maximum strength degradation. Specimen JPA-3 exhibited the greatest strength (1.3 times the strength of JPA-1 in the positive loading direction) and also the largest maximum strength degradation. In fact, only for JPA-3 was registered the conventional failure condition corresponding to a 20% reduction in strength with respect to the maximum lateral load. The pinching effect is observed for all specimens, being less important for the joint specimen with deformed bars and more evident in the responses of specimens JPB and JPC. The differences registered between the joint specimens in terms of maximum lateral load and strength degradation are well depicted by the lateral load-drift peak envelopes in Figure 3.16.

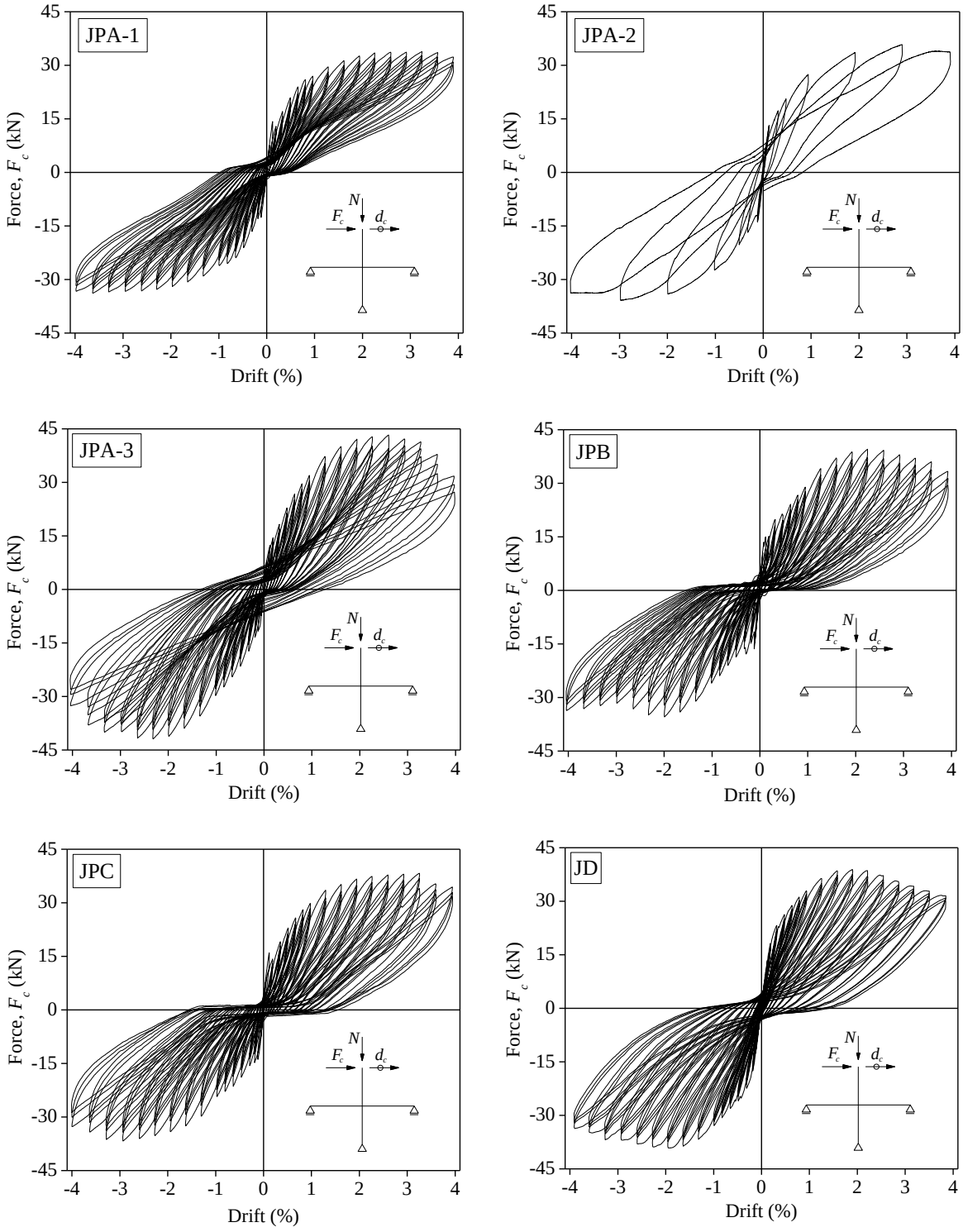

Figure 3.15 - Lateral load versus drift diagrams of the beam-column joint specimens.

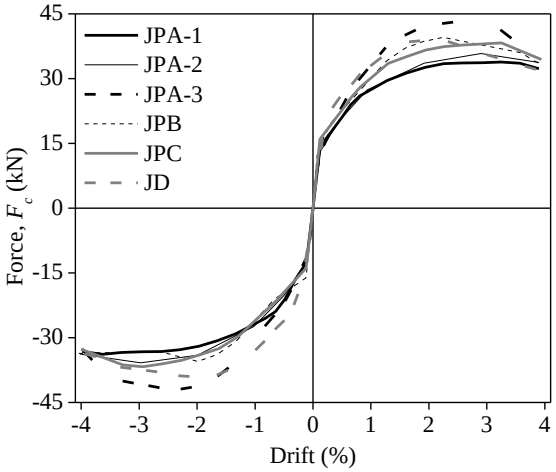

Figure 3.16 - Peak envelopes of the lateral load-drift diagrams.

Table 3.9 - Maximum lateral load and maximum strength degradation

Specimen	Positive loading direction			Negative loading direction		
	$F_{c,max}$ (kN)	$\Delta_{Fc,max}$ (%)	$\Delta F_{4\%}$ (%)	$F_{c,max}$ (kN)	$\Delta_{Fc,max}$ (%)	$\Delta F_{4\%}$ (%)
JPA-1	34.0	3.3	4.5	34.0	3.7	1.7
JPA-2	35.8	3.0	5.8	35.8	3.0	5.7
JPA-3	43.3	2.7	26.6	41.9	2.3	22.1
JPB	39.5	2.3	15.8	35.4	2.0	5.1
JPC	38.3	3.3	10.0	36.7	3.0	11.1
JD	39.0	2.0	19.0	39.1	2.0	13.9

Figure 3.17 represents for each specimen the values of the peak lateral load registered at each level of imposed drift, measured in the first cycle, in the positive loading direction. The values are represented from the drift level at which the specimens reached the maximum lateral load $F_{c,max}$. In Figure 3.17-b, for each specimen, the values of lateral load are normalized to $F_{c,max}$. The observed strength degradation is directly related to the damage. Specimens JPA-3 and JD display a more pronounced strength degradation due to the damage developed in the joint region (see Section 3.4.3). Even if not depicted in Figure 3.17, the strength degradation that occurred within the same level of imposed drift, from the first to the third cycle, is equal to about: 5% to 10% in JPA-1, 7% to 14% in JPA-3, 8% to 12% in JPB, 7% to 12% in JPC, and 4% to 6% in JD.

Figure 3.18 represents for each specimen the evolution of the secant stiffness ($k_{sec} = F_c/d_c$), calculated for the first cycle of each level of imposed drift in the positive loading direction. The values are represented from 0.3% drift, for which the cracking had onset in all the joint

specimens. In Figure 3.18-b, for each specimen, the values of secant stiffness are normalized to the secant stiffness calculated for the cycle corresponding to 0.3% drift ($k_{sec,0.3\%}$). In general, the six joint specimens display similar evolutions of the secant stiffness. Until reaching the maximum lateral load, the specimen with deformed bars have slightly larger secant stiffness than the specimens with plain reinforcing bars. At the maximum drift, the secant stiffness is similar for all the tested specimens.

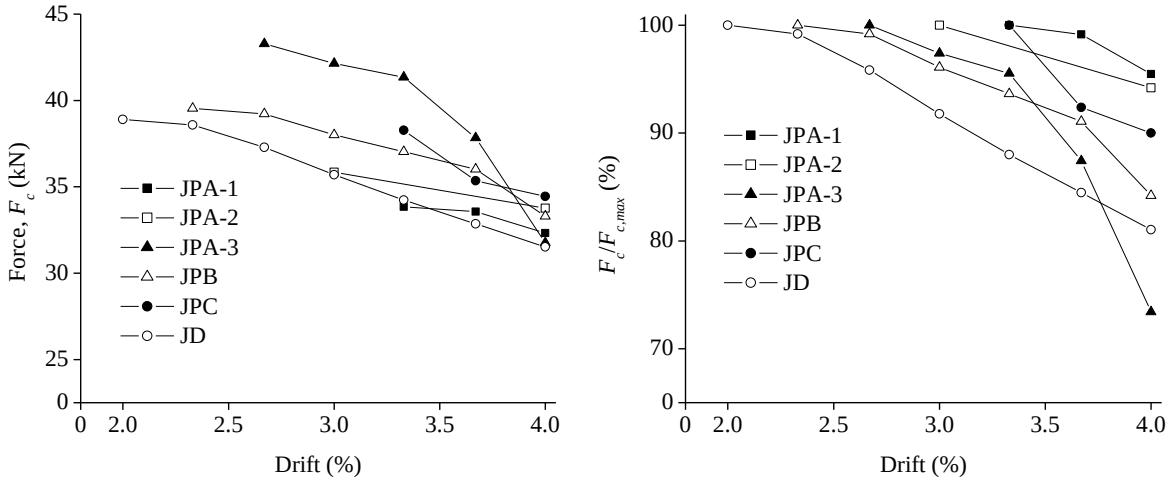

Figure 3.17 - Strength degradation: a) absolute values; b) values normalized to the maximum lateral load.

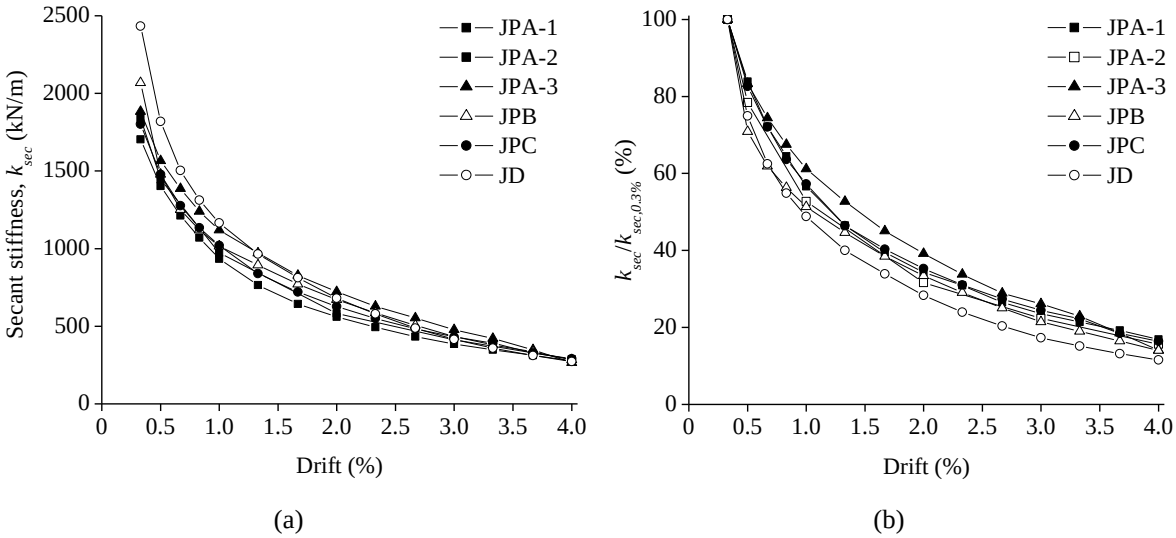

Figure 3.18 - Secant stiffness degradation: a) absolute values; b) values normalized to the secant stiffness at 0.3% drift.

3.4.2 - Moment versus curvature diagrams and curvature demands

Figure 3.19 and Figure 3.20 depict the moment-curvature diagrams of the joint specimens plotted for the middle section of slice 1 in the beams and columns. The moments were computed assuming a linear moment distribution along the elements' length. The curvature corresponds to the mean curvature estimated for slice 1. For each element and at each step, the mean curvature was computed as the $\theta_{1,2}/L_1$ ratio, in which $\theta_{1,2}$ stands for the relative rotation between the slice 1-slice 2 interface section and the slice 1-joint interface section, and L_1 is the length of slice 1. The relative rotation $\theta_{1,2}$ was computed as the ratio $\Delta l_1/b_1$, in which Δl_1 stands for the difference between the values of displacement recorded by the two LVDTs located in slice 1, and b_1 is the distance between the LVDTs. Regarding specimen JPA-3, the moment-curvature relationships of the beams and columns do not include the results corresponding to the last two drift levels due to problems with the LVDTs involved in the computation.

Figure 3.19 and Figure 3.20 also indicate the flexural capacity of the elements estimated according to EC2 (Table 3.3).

Table 3.10 indicates the ratio of maximum moment in the elements ($M_{b,max}$ and $M_{c,max}$, computed at the beam-joint and column-joint interfaces respectively) to the corresponding moment capacity predicted by EC2 (Table 3.3).

The response of the joint specimens was not perfectly symmetrical. Small differences in terms of both moment and curvature were registered between the right and left beams, and between the superior and inferior columns. In the comparative analyses presented next, the results are discussed only for one beam and one column.

Table 3.10 - Ratio between the maximum moment and the moment capacity according to EC2

	Beams		Columns
Specimen	$M_{b,max}^{+}/M_{b,EC2}^{+}$	$M_{b,max}^{-}/M_{b,EC2}^{-}$	$M_{c,max}^{+}/M_{c,EC2}^{+}$
JPA-1	0.67	0.67	0.84
JPA-2	0.69	0.87	0.89
JPA-3	0.85	0.87	0.68
JPB	0.81	0.68	0.40
JPC	0.83	0.69	0.40
JD	1.09	1.05	0.97

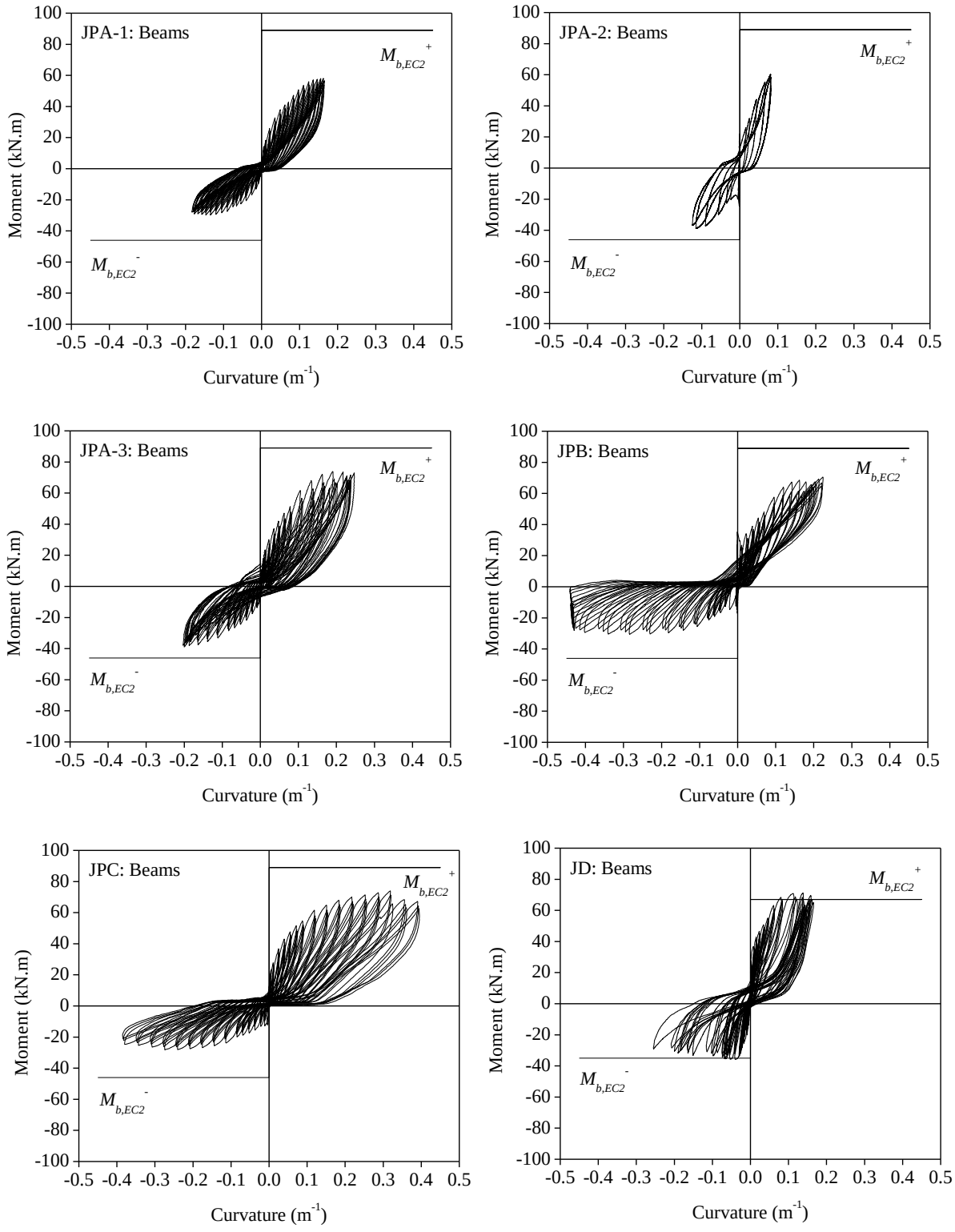

Figure 3.19 - Moment-curvature diagrams of slice 1 in the beams.

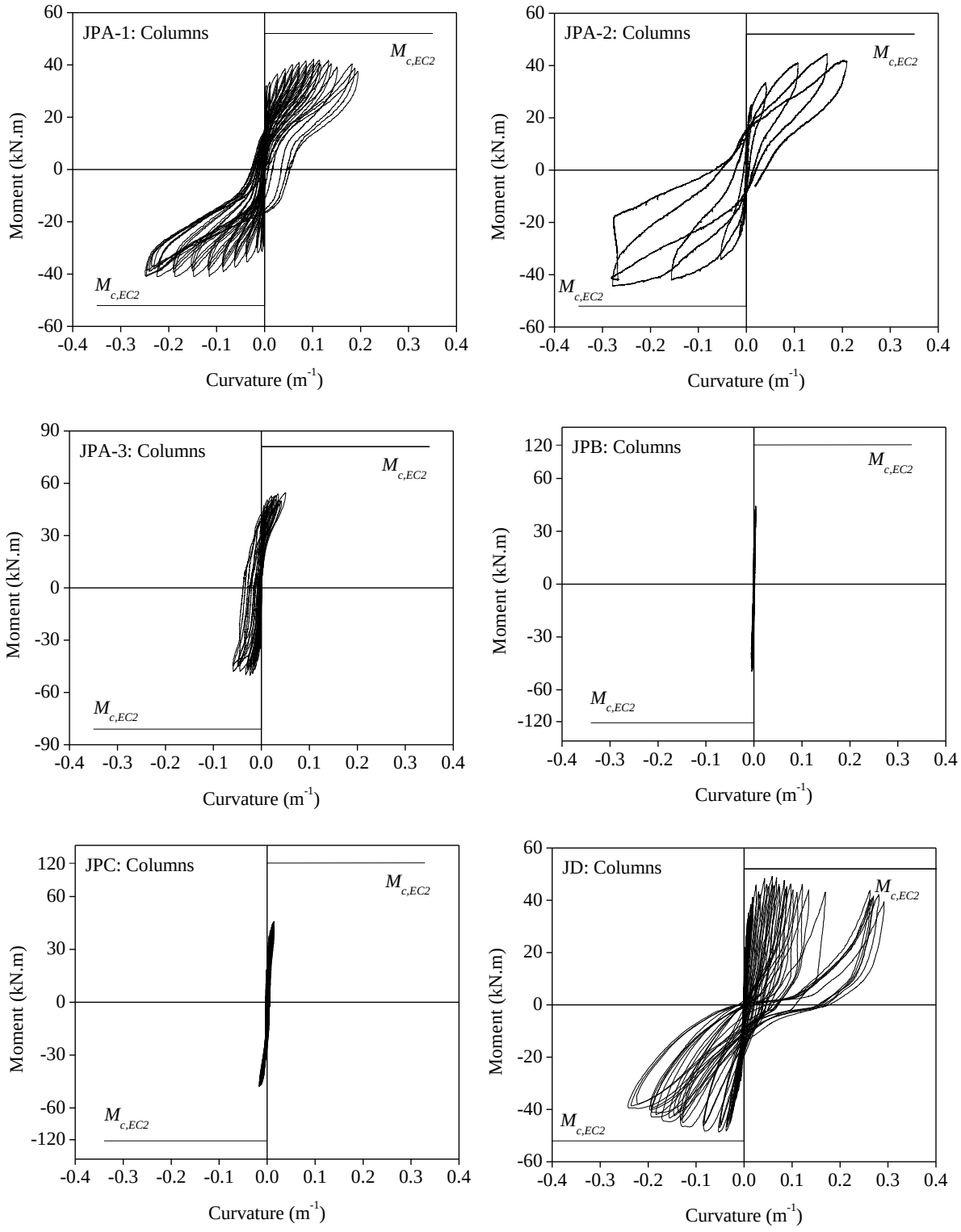

Figure 3.20 - Moment-curvature diagrams of slice 1 in the columns.

The analysis of the moment-curvature diagrams and Table 3.10 shows that:

- In the specimens with plain reinforcing bars, the maximum flexural demands imposed on the beams and columns are lower than the corresponding flexural capacities computed according to the EC2 expressions.
- In the specimens with plain reinforcing bars, the flexural capacity of the beams was reached in both the positive and negative loading directions and is equal to, respectively: $0.67M_{b,EC2}^{+}$ and $0.67M_{b,EC2}^{-}$ for JPA-1; $0.69M_{b,EC2}^{+}$ and $0.87M_{b,EC2}^{-}$ for JPA-2; $0.85M_{b,EC2}^{+}$ and $0.87M_{b,EC2}^{-}$ for JPA-3; $0.81M_{b,EC2}^{+}$ and $0.68M_{b,EC2}^{-}$ for JPB; and, $0.83M_{b,EC2}^{+}$ and $0.69M_{b,EC2}^{-}$ for JPC.
- In the specimens with plain reinforcing bars, the flexural capacity of the columns was reached in all the tested specimens except in JPB and JPC, and is equal to $0.84M_{c,EC2}$ for JPA-1, $0.89M_{c,EC2}$ for JPA-2, and $0.68M_{c,EC2}$ for JPA-3. Figure 3.20 shows that for JPB and JPC the column response at the maximum imposed drift is mainly elastic. The maximum flexural demands imposed on the columns of JPB and JPC are equal to $0.40M_{c,EC2}$.
- In the specimen with deformed bars, the flexural capacity of the beams was reached in both the positive and negative loading directions and is equal to $1.09M_{b,EC2}^{+}$ and $1.05M_{b,EC2}^{-}$ respectively. The flexural capacity of the columns was also reached and is equal to $0.97M_{c,EC2}$.

Therefore, it can be concluded that EC2 provided a good estimate of the elements' strength for the specimen with deformed bars, overestimating the beams' strength in 9% and underestimating the columns' strength in 3%. Conversely, for the specimens with plain reinforcing bars the EC2 expressions overestimated the elements' strength in about 13% to 33%. In these specimens, the elements' maximum strength was conditioned by the poor bond conditions between the concrete and the plain reinforcing bars.

Figure 3.21 depicts the estimated values of maximum mean curvature of slice 1, in the beams and columns, at each level of imposed drift. Again, it should be noted that the maximum mean curvature in the elements of specimen JPA-3 is not represented for the last two drift levels due to problems with the LVDTs involved in the computation. The curvature envelope determined for each specimen is consistent with the damage evolution in the elements (beams and columns) described in Section 3.4.3.

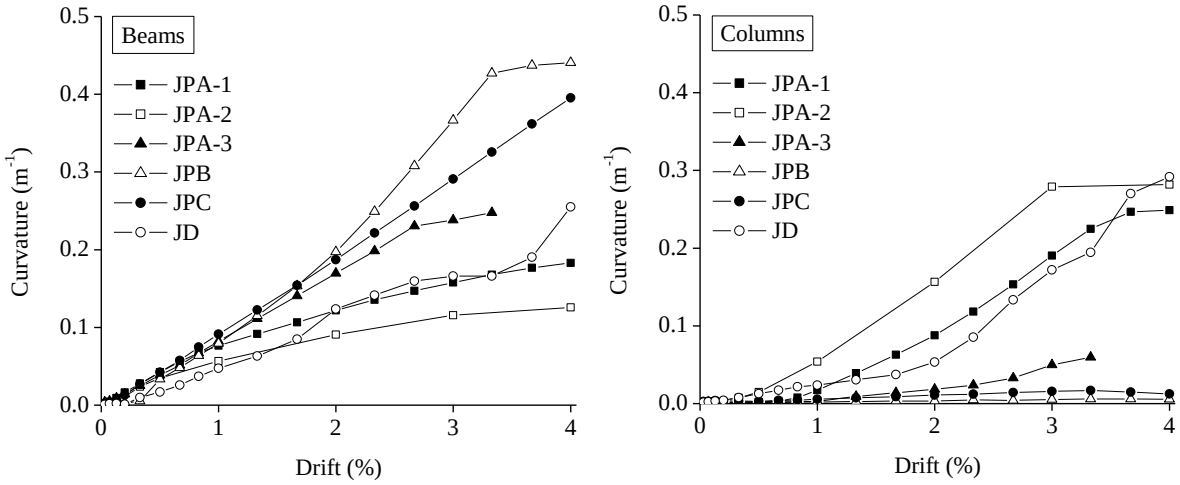

Figure 3.21 - Maximum mean curvatures of slice 1.

3.4.3 - Damage observed

The specimens with plain reinforcing bars displayed, in general, a similar damage distribution (Figure 3.22-a). Damage was heavily concentrated at the beam-joint and column-joint interfaces (within slice 1), in one main crack at each interface section. Damage within slice 2 was in most cases negligible, and damage was not observed from slice 2 to the end of the elements' length. Cracking in the right beam of specimens JPA-3 and JPB was initiated within slice 2, at a position coincident with the location of a stirrup, and not at the beam-joint interface. In specimens JPB and JPC, cracking was mostly concentrated at the beam-joint interfaces, while cracking at the column-joint interfaces was minor. Specimen JPA-3 also displayed severe cracking in the joint region, with concrete cover spalling. In this specimen, despite a few inclined cracks with relatively small opening, the damage in the joint region was mainly defined by two diagonal cracks.

Conversely to what was observed in the joint specimens with plain bars, the joint specimen with deformed bars displayed a more widely spread damage distribution (Figure 3.22-b). Cracking was spread along the length of the beams and columns, and cracking and concrete cover spalling was observed within the joint region. Contrarily to what was observed in JPA-3, several inclined cracks with relatively small opening were developed in the joint region. Similar differences in cracking pattern between joint specimens with plain and deformed reinforcing bars were observed, for example, in the experimental tests carried out by Genesio *et al.* [10]. In the joint specimens with deformed bars several

diagonal cracks covered the whole joint core, whereas in the case of the joint specimen with plain bars two large cracks determined the joint behaviour.

(a) (b)

Figure 3.22 - General damage distribution observed in the specimens with plain reinforcing bars (a) and damage distribution in the specimen with deformed bars (b).

Table 3.11 indicates the drift levels corresponding to the onset of cracking at the beam-joint and column-joint interfaces, and onset of diagonal cracking in the joint region. In all specimens, cracking was first registered in the beams at drift levels ranging from 0.07% to 0.20%. Cracking in the columns was registered at drift levels ranging from 0.33% to 2%. The onset of cracking in the columns tested with larger axial load (in specimens JPA-3, JPB, and JPC) occurred at drift levels superior to those registered for the columns with lower axial load. Table 3.11 also indicates the values determined for the maximum crack opening.

Figure 3.23 depicts the damage state in the specimens at the maximum imposed drift (4%). Figure 3.24 illustrates the crack pattern corresponding to the final damage state.

Table 3.11 - Drift corresponding to the onset of cracking and maximum crack opening

Specimen	Cracking at the beam-joint and column-joint interfaces				Drift at first diagonal crack within the joint region (%)
	Beam		Column		
	Drift at first crack (%)	Maximum crack opening (mm)	Drift at first crack (%)	Maximum crack opening (mm)	
JPA-1	0.07	5.9	0.8	5.9	-
JPA-2	0.1	4.3	0.1	8.2	-
JPA-3	0.1	6.9	1.3	3.1	2.7
JPB	0.2	12.4	2.0	0.1	-
JPC	0.1	12.2	1.7	0.3	-
JD	0.1	5.4	0.3	10.4	1.7

JPA-1

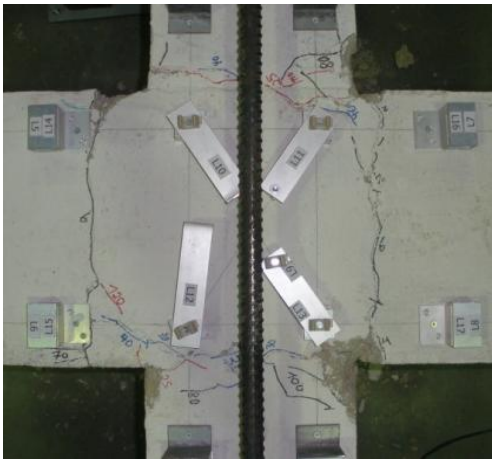

JPA-2

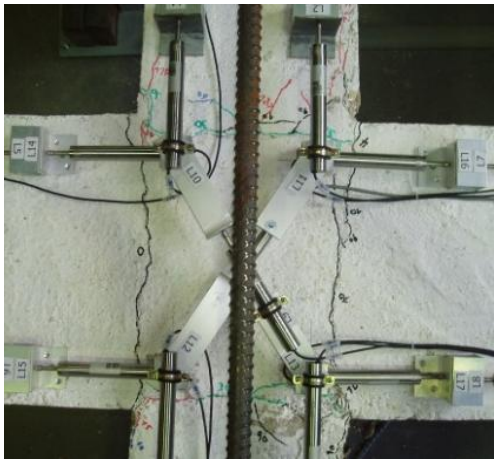

JPA-3

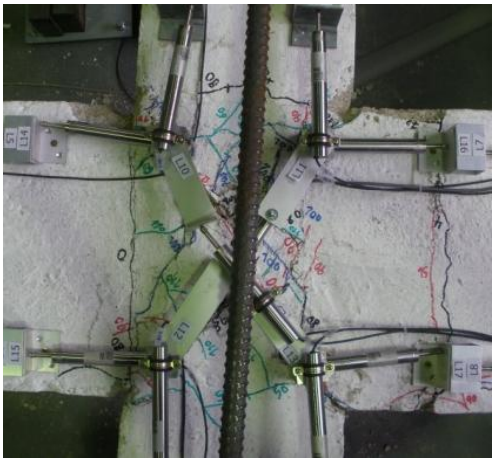

JPB

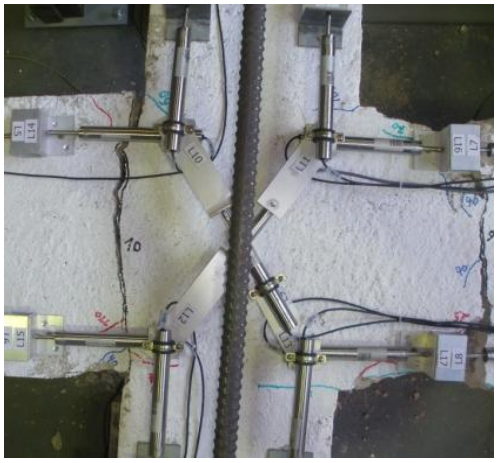

JPC

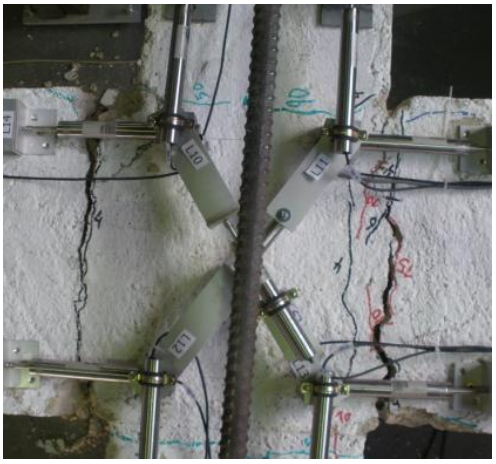

JD

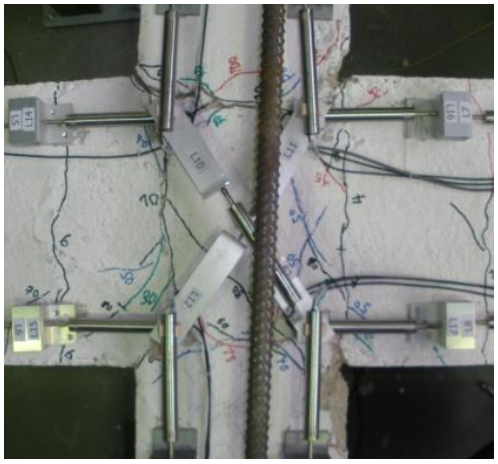

Figure 3.23 - Damage state at maximum drift.

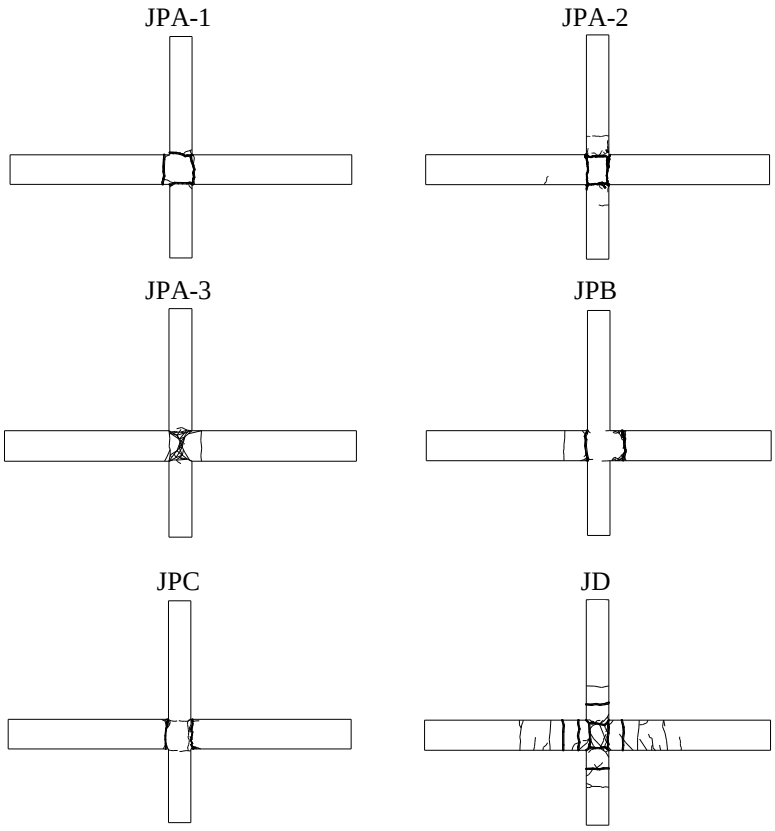

Figure 3.24 - Crack pattern corresponding to the final damage state.

3.4.4 - Shear forces and stresses in the joint

The joint shear stress is usually expressed in terms of the nominal shear stress, or in terms of the principal compression or tensile stresses.

The nominal shear stress (v_{jh}) in the joint concrete, if computed from the horizontal shear force, is given by Equation (3.10), where: V_{jh} is the horizontal shear force in the joint, given by Equation (3.11) according to Hakuto *et al.* [11]; b_j is the joint effective width, given by Equation (3.12) [9, 11, 12]; and, h_{jc} is the horizontal distance between the outermost layers of column reinforcement in the direction of the horizontal joint shear force. In Equation (3.11) (see also Figure 2.9 in Chapter 2): M_{b1} and M_{b2} are the beam moments at the face of the joint core; jd_1 and jd_2 are the lever arms between the tensile forces and the centroids of the compressive forces, at the right and left-hand sides of the joint respectively; and, V_C is the shear force in the column above the joint. In Equation (3.12), b_c and b_w denote the width of the column and width of the beam respectively.

$$\nu_{jh} = \frac{V_{jh}}{b_j \cdot h_{jc}} \tag{3.10}$$

$$V_{jh} = \frac{M_{b1}}{jd_1} + \frac{M_{b2}}{jd_2} - V_C \tag{3.11}$$

$$\begin{aligned} b_c > b_w \Rightarrow \quad & b_j = min\{b_c ; (b_w + 0.5 \cdot h_c)\} \\ b_c \le b_w \Rightarrow \quad & b_j = min\{b_w ; (b_c + 0.5 \cdot h_c)\} \end{aligned} \tag{3.12}$$

A measure of the principal stresses (p_t) at the mid-depth of the joint core, as found from the Mohr's circle, is given by Equation (3.13) [11], where: f_a stands for the nominal axial compressive stress on the column, computed from the column axial load N (Equation (3.14)); and compressive stresses are taken as negative. According to Hakuto *et al.* [11], Equation (3.13) is not adequate for determining the principal compression stresses after the onset of diagonal tension cracking.

$$p_t = -\frac{f_a}{2} \pm \sqrt{\left(\frac{f_a}{2}\right)^2 + \nu_{jh}^2} \tag{3.13}$$

$$f_a = \frac{N}{b_j \cdot h_c} \tag{3.14}$$

According to Hakuto *et al.* [11], one approach for the assessment of the shear strength of interior beam-column joints without shear reinforcement is to assume that the shear strength is reached at the stage of initial diagonal tension cracking of the joint core, that is, when the principle tensile stress exceeds the tensile strength of the joint concrete. However, Hakuto *et al.* [11] also state that this joint core failure criterion may be too conservative since the joint core may be able of transferring significantly higher shear forces after diagonal tension cracking occurs by means of the diagonal compression strut mechanism. In this case, the joint failure occurs as a result of diagonal compression failure. Therefore, limiting the nominal shear stress to a specific value expressed as function of the concrete compressive strength could be a more adequate criterion.

EC8 [9, 13] evaluates the shear capacity of the joints by limiting the diagonal compression induced in the joint by the diagonal strut mechanism to the concrete compressive strength (f_c) in the presence of transverse tensile strains. For interior joints, in the absence of a more precise model, this requirement may be fulfilled if Equation (3.15) is satisfied. In Equation (3.15), v is the normalized axial load in the column above the joint and η is computed using Equation (3.16).

$$V_{jh} \le \eta \cdot f_c \cdot \sqrt{1-\frac{\nu}{\eta}} \cdot b_j \cdot h_{jc} \tag{3.15}$$

$$\eta = 0.6 \cdot (1 - f_{ck} / 250) \tag{3.16}$$

Table 3.12 indicates for each joint specimen the estimated values of maximum horizontal shear force ($V_{jh,max}$), maximum principal tensile stress ($p_{t,max}$) expressed in terms of the square root of the concrete compressive strength, and the corresponding drift level ($\Delta_{(pt/\sqrt{fc})max}$). Figure 3.25 depicts the ratio of principal tensile stress to square root of the concrete compressive strength versus drift diagrams.

Assuming that the maximum shear strength of the joint is reached when diagonal tension cracking occurs, only specimens JPA-3 and JD developed the full strength capacity of the joint. The principal tensile stress was increased up to $0.30\sqrt{f_c}$ in JPA-3 and $0.39\sqrt{f_c}$ in JD, corresponding to the occurrence of diagonal cracking in the joint. As shown in Table 3.12, for JPA-3 and JD were determined the maximum demands in terms of shear force and principal tensile stress respectively.

In comparison to JPA-3, lower shear force demands were computed for the other joint specimens with plain reinforcing bars (JPA-1, JPA-2, JPB and JPC). The corresponding maximum principal tensile stresses are, however, similar to those computed for JPA-3, particularly for JPA-1 and JPA-2. However, as previously stated, diagonal cracking in the joint region did not occur in these specimens. It should be noted that, in Equation (3.13), used to estimate the principal tensile stresses in the joint, the stresses v_{jh} and f_a are both nominal values since they are not uniform over the horizontal plane at the mid-depth of the joint core [11]. In addition, the stress distribution inside the joint core is rather complex and strongly dependent on the concrete-steel bond properties.

Figure 3.25 shows for the six joint specimens a reduction in the principal tensile stresses in the joint. For JPA-3 and JD, the stresses in the joint are significantly reduced after diagonal tension cracking occurs. For the other specimens, the principal tensile stresses reduction after the maximum value is relatively smoother due to the evolution of damage in the beam and column extremities, reducing the force and deformation demands imposed on the joint.

Table 3.12 - Maximum values of horizontal shear force and maximum principal tensile stress in the joint

	Positive loading direction			Negative loading direction		
Specimen	$V_{jh,max}$ (kN)	$p_{t,max}$ (MPa)	$\Delta_{(pt/\sqrt{fc})max}$ (%)	$V_{jh,max}$ (kN)	$p_{t,max}$ (MPa)	$\Delta_{(pt/\sqrt{fc})max}$ (%)
JPA-1	247	$0.32\sqrt{f_c}$	3.3	249	$0.32\sqrt{f_c}$	3.7
JPA-2	264	$0.34\sqrt{f_c}$	3.0	264	$0.34\sqrt{f_c}$	3.0
JPA-3	318	$0.30\sqrt{f_c}$	2.7	308	$0.28\sqrt{f_c}$	2.7
JPB	291	$0.26\sqrt{f_c}$	2.3	261	$0.22\sqrt{f_c}$	2.0
JPC	282	$0.25\sqrt{f_c}$	3.3	270	$0.23\sqrt{f_c}$	3.0
JD	286	$0.39\sqrt{f_c}$	2.0	288	$0.39\sqrt{f_c}$	2.0

The upper limit given by EC8 for the horizontal shear force in the joints was computed using Equation (3.15) and is equal to: 1213 kN for JPA-1, JPA-2 and JD; and, 1044 kN for JPA-3, JPB and JPC. The maximum horizontal shear forces estimated for the specimens (Table 3.12) are therefore inferior to 35% of the EC8 limit.

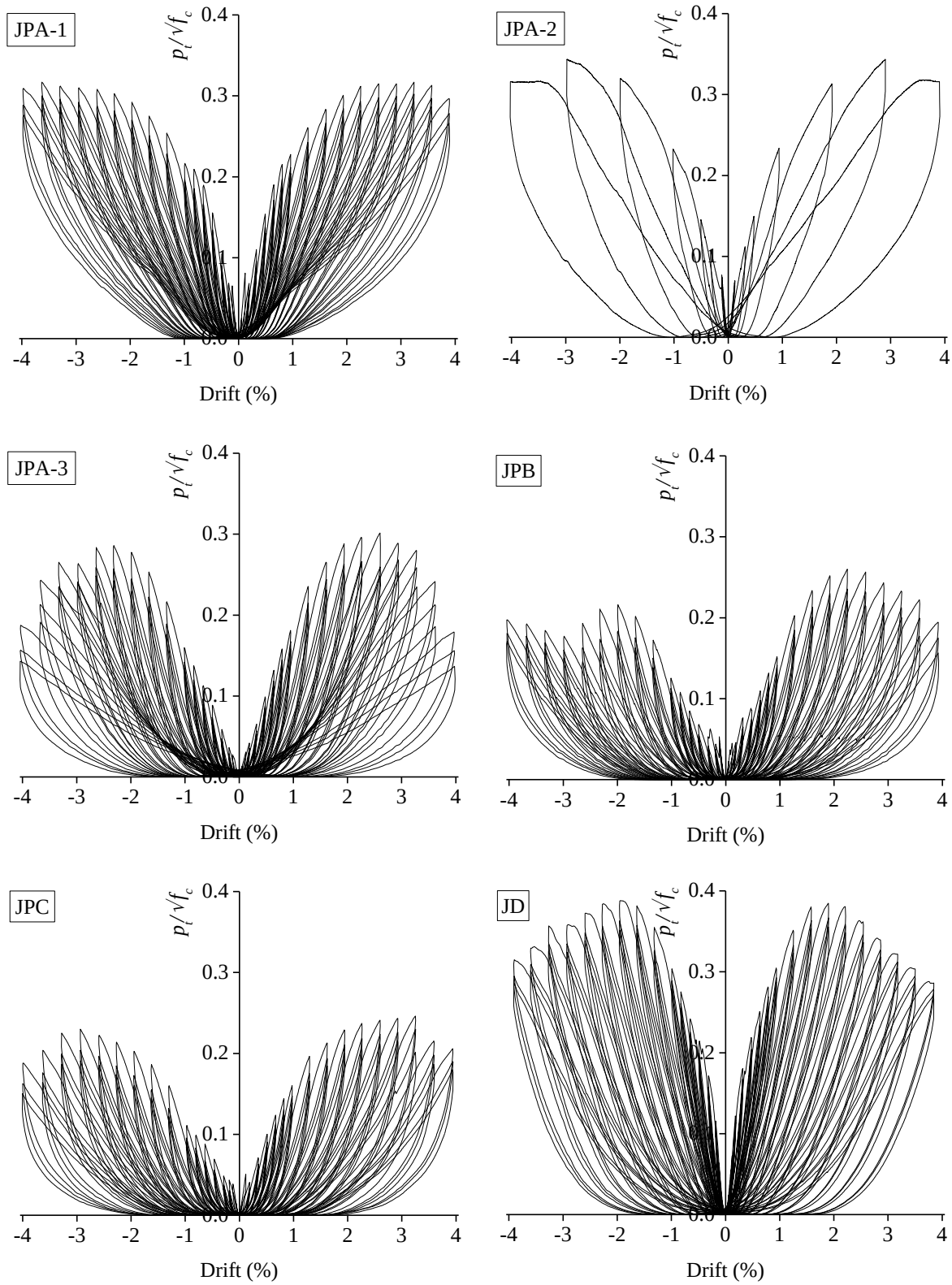

Figure 3.25 - Principal tensile stress versus drift diagrams.

3.4.5 - Drift components

This section studies, firstly, the relative contribution of the beam and column deformations to the overall deformation of the joint specimens with plain reinforcing bars and, secondly, the relative contribution of the linear and nonlinear deformation components. For each joint specimen, the direct integration method was used to estimate the total drift and the relative contribution of each component. Considering the type of damage in the specimens with plain reinforcing bars (concentrated at the beam-joint and column-joint interfaces), neglecting the shear deformation in the elements, and assuming a linear distribution of moment along the beam and column lengths, the curvature distribution in each element was analytically established. Thus, in the analytical formulation the following assumptions were made for the curvatures of each element (Figure 3.26): a linear variation from the element extremity (where the curvature is zero) to the interface between slices 1 and 2, that is, from point A to point B; and a parabolic variation between this section and the interface between slice 1 and the joint (where the maximum curvature occurs), that is, from point B to point D. In the calculations, the mean values of curvature measured in slices 1 and 2 ($curv_{slice1}$ and $curve_{slice2}$ respectively) were used as input in the analytical expressions derived. Considering the assumptions previously presented, the direct integration method was used to determine the deflection (d) and rotation (φ) along the length of the elements. Based on the analytical equations established for each element, and considering the compatibility conditions in terms of displacements and rotation at the joint, as well as the displacement restraints at the supports, the deformation equations of the specimens were obtained. With the expressions derived, the lateral displacement at the free end of the superior column ($d_{top,CS}$) was determined at each time step and compared to the corresponding value imposed in the cyclic test.

In general terms, a good match was found between the experimental and analytical results. Within the drift range for which was observed a better agreement between the experimental and analytical results (in general, from 0.3% to 4% drift), the maximum difference registered between the experimental and analytical displacements was: 8% for JPA-1, 7% for JPA-2, 15% for JPA-3, 19% for JPB, and 9% for JPC. Therefore, the analytical equations were used for determining the relative contribution of each element to the total lateral displacement (which is proportional to the lateral drift). The estimated

relative contribution of the beams and columns to the total drift is depicted in Figure 3.27 for the joint specimens with plain reinforcing bars.

Specimen JD was excluded from the drift components analysis. The curvature distribution adopted for the specimens with plain bars does not represent that in the specimen with deformed bars, and the experimental values of curvature (only measured in slices 1 and 2) are not sufficient for a precise definition of the curvature distribution in specimen JD.

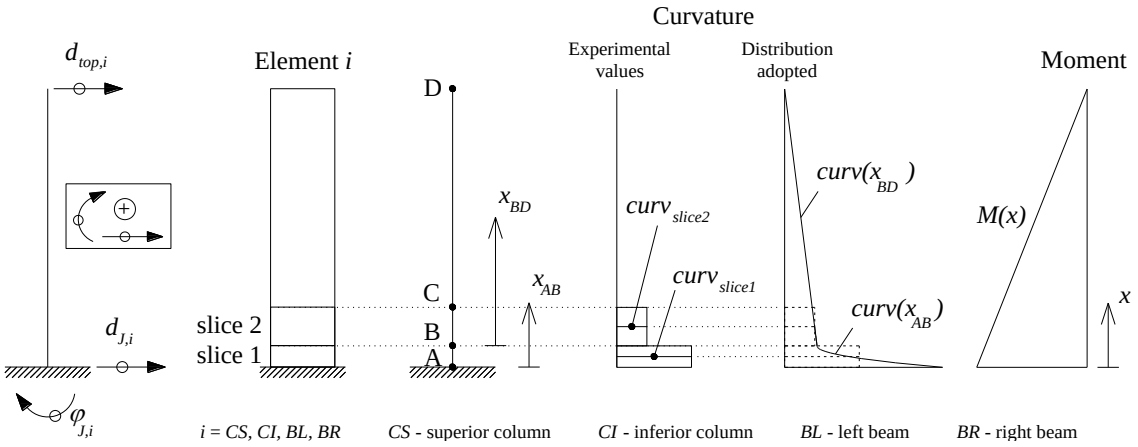

$$\varphi(x) = \int \frac{M(x)}{EI(x)} \cdot dx + \varphi_0$$

$$d(x) = \int\int \frac{M(x)}{EI(x)} \cdot dx + \varphi_0 \cdot x + d_0$$

$$\frac{M(x)}{EI(x)} = curv(x) \Leftrightarrow EI(x) = \frac{curv(x)}{M(x)}$$

$$\varphi_{AB}(x_{AB}) = \int curv(x_{AB}) \cdot dx_{AB} + \varphi_{J,i}$$
$$d_{AB}(x_{AB}) = \int\int curv(x_{AB}) \cdot dx_{AB} + \varphi_{J,i} \cdot x_{AB} + d_{J,i}$$

$$\varphi_{BD}(x_{BD}) = \int curv(x_{BD}) \cdot dx_{BD} + \varphi_{AB}\left(x_{AB} = \overline{AB}\right)$$
$$d_{BD}(x_{BD}) = \int\int curv(x_{BD}) \cdot dx_{BD} + \varphi_{AB}\left(x_{AB} = \overline{AB}\right) \cdot x_{BD} + d_{AB}\left(x_{AB} = \overline{AB}\right)$$

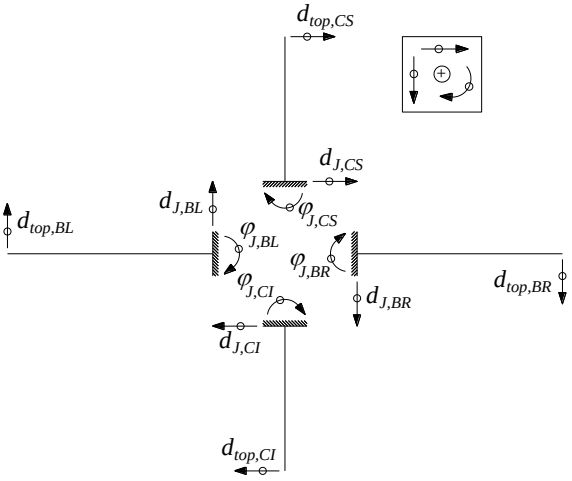

$$\varphi_{J,CS} = \varphi_{J,BL}$$
$$\varphi_{J,BL} = \varphi_{J,CI}$$
$$\varphi_{J,CI} = \varphi_{J,BR}$$
$$d_{top,BL} = 0$$
$$d_{top,BR} = 0$$
$$d_{top,CI} = 0$$
$$d_{J,BR} = -d_{J,BL}$$
$$d_{J,CS} = -d_{J,CI}$$

Figure 3.26 - Analytical formulation adopted for determining the deformation equations.

As previously stated, the main crack in the right beam of specimens JPA-3 and JPB was developed within slice 2 and not at the interface with the joint region. For this analysis, the experimental values of curvature determined for the left beam were used as reference values of curvature for the right beam.

For specimen JPA-3, the analytical results in Figure 3.27 are presented only up to 2.7% drift, for which was registered the onset of cracking in the joint region. From that point, the contribution of the joint shear deformation to the overall deformation of specimen JPA-3 becomes relevant hence against the assumptions considered in the analytical method.

The analytical results depicted in Figure 3.27 show that for lower imposed drift levels the beams deformation controls the total drift associated with the deformation of the joint specimens. For specimens JPA-1, JPA-2 and JPA-3, the relative contribution of the columns deformation to the total drift increases with the imposed lateral drift. However, this increase is less pronounced for JPA-3. Conversely, in specimens JPB and JPC, the relative contribution of the columns deformation decreases as the imposed drift increases. In all cases, the analytical results are in coherence with the observed damage evolutions. At the maximum imposed drift, the estimated relative contribution of the columns deformation to the total drift is equal to 60% for JPA-1, 73% for JPA-2, above 26% for JPA-3, 4% for JPB, and 6% for JPC.

A different curvature distribution was assumed for the analysis of the relative contribution of the elements' linear and nonlinear deformation components to the total drift imposed on the joint specimens. The linear curvature variation from the free end of the elements to the interface between slices 1 and 2 (depicted in Figure 3.26) was extended to the entire span of each element. The displacement at the free end of the superior column was again calculated, now corresponding to the contribution of the linear elastic deformation. The difference between the drifts obtained considering the first and the second approaches (with different curvature distributions) gives the contribution of the nonlinear deformation of the elements, which is associated with the damage and deformation mechanisms concentrated at the beam-joint and column-joint interfaces. Figure 3.28 represents the relative contribution of the linear elastic deformation and nonlinear deformation components for each joint specimen, showing the significant contribution of the latter from early drift levels (from 0.2% drift).

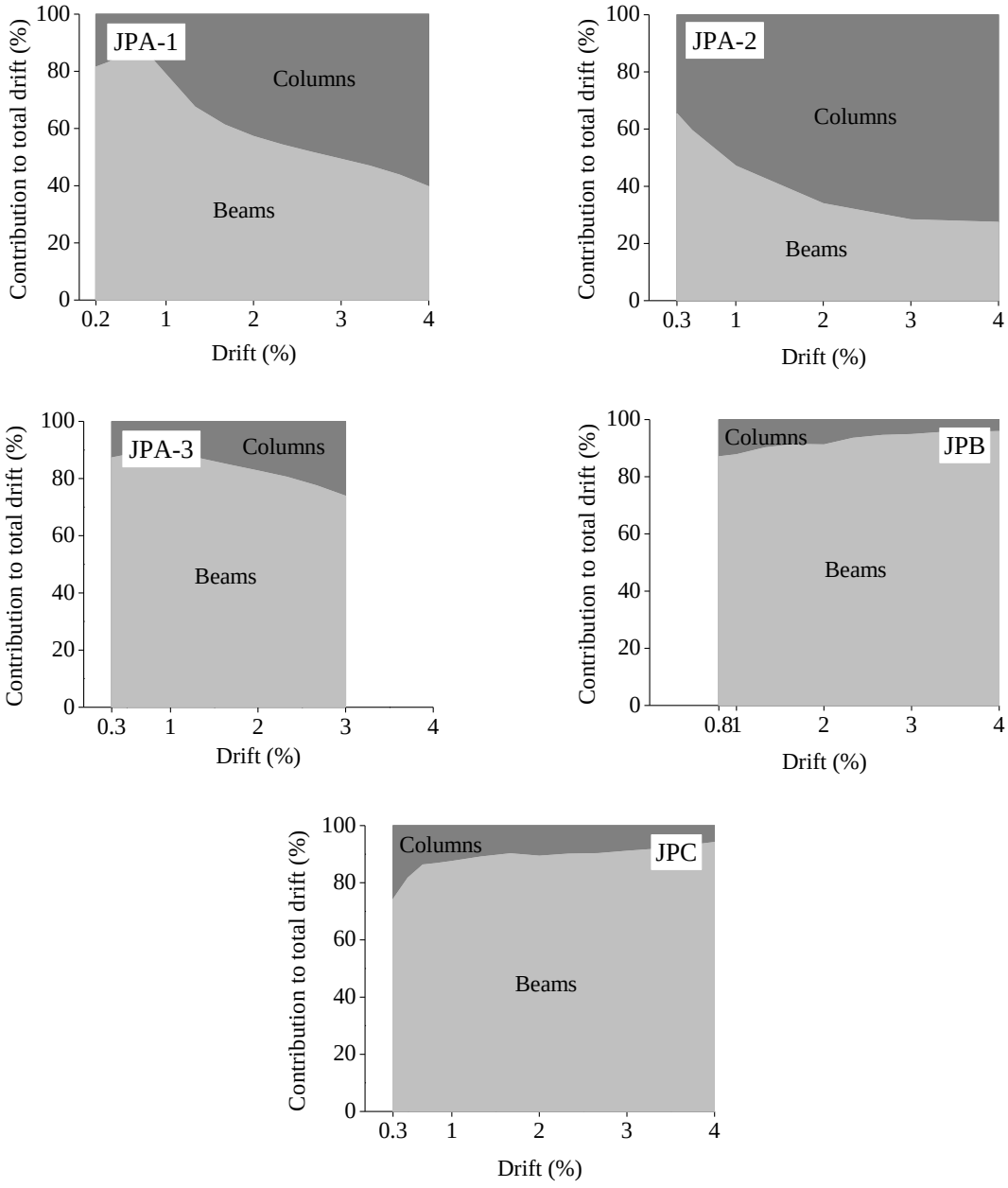

Figure 3.27 - Relative contribution of beams and columns to the total drift.

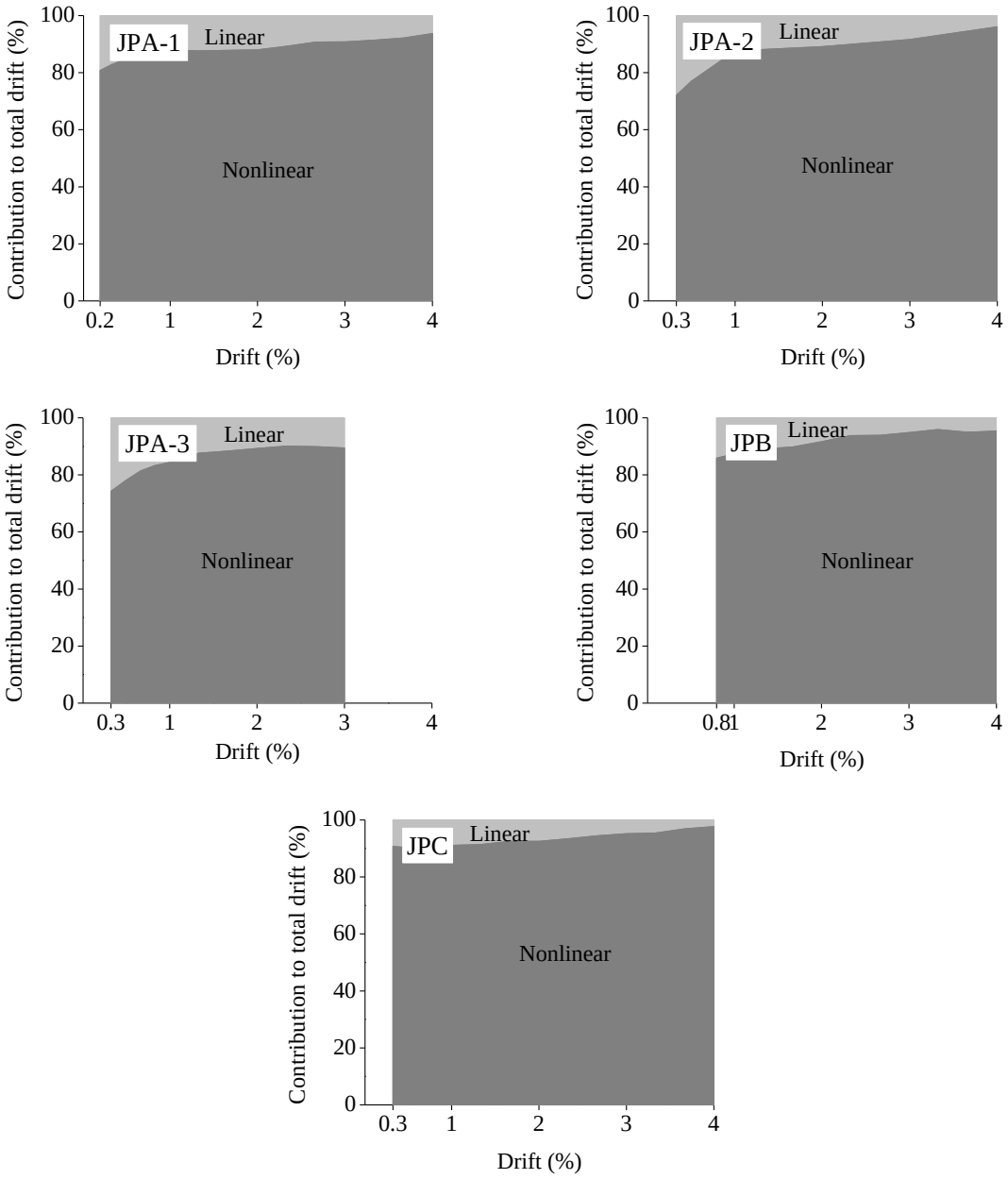

Figure 3.28 - Relative contribution of linear elastic deformation and nonlinear deformation to the total drift.

3.4.6 - Ultimate rotation capacity

The ultimate rotation capacity of the beam-column joint specimens was computed according to Eurocode 8 – Part 3 (EC8-3 [13]). EC8-3 evaluates the deformation capacity of RC elements (beams, columns and walls) in terms of the chord rotation, defined by the code as the angle between the tangent to the axis at the yielding end and the chord connecting that end with the end of the shear span, that is, the point of contraflexure. The

chord rotation is also equal to the element drift ratio. For elements with deformed bars and with seismic detailing, the ultimate rotation capacity is computed using Equation (3.17), where: γ_{el} is equal to 1.5 for primary seismic elements and to 1.0 for secondary seismic elements; L_v/h is the shear span ratio (L_v stands for the moment/shear ratio at the end section); v is the normalized axial load (positive for compression); ω and ω' are the mechanical reinforcement ratio of the tension and compression longitudinal bars respectively; f_c and f_{yw} are the concrete compressive strength and the stirrup yield strength respectively; ρ_{sx} is the ratio of transverse steel parallel to the direction x of loading; ρ_d is the steel ratio of diagonal reinforcement (if any) in each diagonal direction; and, α is the confinement effectiveness factor. Details about each parameter can be found in EC8-3.

For elements with plain reinforcing bars the ultimate rotation capacity is given by Equation (3.17) multiplied by a correction coefficient, which is always inferior to 1. For elements without lapping of the longitudinal bars (as the joint specimens under investigation) the correction coefficient is equal 0.575. This correction coefficient already takes into account the lack of seismic detailing.

$$\theta_{um} = \frac{1}{\gamma_{el}} \cdot 0.016 \cdot \left(0.3^{\upsilon}\right) \cdot \left[\frac{max\left(0.01,\omega'\right)}{max\left(0.01,\omega\right)} \cdot f_c\right]^{0.225} \cdot \left(\frac{L_V}{h}\right)^{0.35} \cdot 25^{\left(\alpha \cdot \rho_{sx} \cdot \frac{f_{yw}}{f_c}\right)} \cdot \left(1.25^{100\rho_d}\right) \qquad (3.17)$$

According to Verderame *et al.* [14] a "corrigenda" document to EC8-3 [15] was presented changing some of the code provisions, including those regarding the ultimate deformation capacity of RC elements with plain reinforcing bars. In particular, the correction coefficient aforementioned was increased to 0.80. In either case, the ultimate rotation capacity predicted by the code for elements with plain reinforcing bars is lower than that for elements with deformed bars, given equal the structural characteristics and details. However, recent experimental results [14, 16] indicate the contrary, showing the significant contribution of fixed-end rotations resulting from bar slippage to the rotation capacity of elements with plain reinforcing bars. As stated in Chapter 2, a critical review of some of the available formulations for estimating the ultimate rotation capacity of RC elements with plain reinforcing bars, with particular focus on the EC8-3 approach, was conducted by Verderame *et al.* [14]. Based on the comparison established between

available experimental values and the corresponding theoretical values resulting from the code expressions, the authors conclude that both the approaches presented in the literature and in EC8-3 are characterized by high values of the coefficient of variation of the experimental-to-predicted capacity ratio. A new correction coefficient was proposed by Verderame *et al.* [14] based on the test results of several test campaigns on RC columns with plain reinforcing bars. For elements without lapping of longitudinal bars the correction coefficient is equal to 1.0.

Table 3.14 presents the values of ultimate rotation capacity of the joint specimens computed using Equation (4.8) multiplied by the correction coefficient. The values adopted/estimated for the parameters involved in the computation are indicated in Table 3.13. The elements were considered as primary seismic elements according to the EC8-3 classification hence parameter γ_{el} was made equal to 1.5. Three correction coefficients were considered: i) the correction coefficient prescribed by EC8-3 [13], equal to 0.575; ii) the new EC8-3 correction coefficient, equal to 0.80 [14]; and, iii) the correction coefficient proposed by Verderame *et al.* [14], equal to 1.0. Accordingly and respectively, three values of ultimate rotation capacity for each joint specimen are presented in Table 3.13: $\theta_{u,EC8}$, $\theta'_{u,EC8}$ and $\theta_{u,Verd}$.

Table 3.13 - Values adopted for the parameters involved in the computation of the ultimate rotation capacity according to EC8-3

Specimen	Parameters								
	γ_{el}	ν	$\omega = \omega'$	f_c (MPa)	L_v/h	α	ρ_{sx}	f_{yw}	ρ_d
JPA-1	1.5	0.095	0.0631	23.8	5	0.11	0.001	590	0
JPA-2	1.5	0.095	0.0631	23.8	5	0.11	0.001	590	0
JPA-3	1.5	0.21	0.0631	23.8	5	0.11	0.001	590	0
JPB	1.5	0.21	0.1262	23.8	5	0.11	0.001	590	0
JPC	1.5	0.21	0.1262	23.8	5	0.279	0.003	590	0

Table 3.14 - Theoretical values of ultimate rotation capacity

Specimen	Ultimate rotation capacity, %		
	$\theta_{u,EC8}$	$\theta'_{u,EC8}$	$\theta_{u,Verd.}$
JPA-1	1.98	2.75	3.44
JPA-2	1.98	2.75	3.44
JPA-3	1.72	2.39	2.99
JPB	1.72	2.39	2.99
JPC	1.83	2.55	3.18

To make a comparison between the ultimate rotation capacity predicted by EC8-3 and ultimate rotation capacity estimated from the experimental results, joint rotation had to be subtracted from the total drift imposed on the specimens so that the columns' chord rotation could be obtained. Joint rotation was estimated resorting to the integration method used to determine the drift components in Section 3.4.5. For the reasons previously stated, specimen JD was excluded from the ultimate rotation capacity analysis. JPA-3 was also excluded from this analysis since for drift levels superior to 3% the direct integration method did not provide a good match between the experimental and analytical results. Therefore, the maximum column chord rotation could not be determined for this specimen.

Figure 3.29 shows the lateral load versus column chord rotation diagrams obtained for the joint specimens with indication of the failure condition for which the rotational capacity is usually evaluated (corresponding to a 20% reduction in strength) and the theoretical values of ultimate rotation capacity. A reduction in strength equal to or larger than 20%, measured in the lateral load versus chord rotation diagrams, was not registered for either of the joint specimens under investigation. In fact, the maximum reduction recorded is only equal to 6% (for specimen JPA-2). Therefore, it was not possible to determine the experimental values of ultimate rotation capacity of the joint specimens. Figure 3.29 shows that: i) JPA-1 achieves the ultimate rotation capacity $\theta_{u,EC8}$ for a reduction in strength equal to 4%; ii) JPA-2 reaches $\theta_{u,EC8}$ for its peak strength, and $\theta'_{u,EC8}$ for a reduction in strength equal to 6%; and, iii) JPB and JPC reach neither of the three theoretical values of ultimate rotation capacity. For JPA-2, and considering the tendency displayed by the lateral load versus column chord rotation diagram in the last cycles, the approach proposed by Verderame *et al.* [14] seems to give better results.

Table 3.15 presents the experimental values of maximum chord rotation ($\theta_{exp,max}$) estimated for each joint specimen, as well as the ratio of the latter to the theoretical values of ultimate rotation capacity ($\theta_{u,exp}/\theta_{u,EC8}$, $\theta_{u,exp}/\theta'_{u,EC8}$ and $\theta_{u,exp}/\theta_{u,Verd}$). The maximum values of column chord rotation determined for specimens JPB and JPC are very small (20% and 10% respectively, of the ultimate rotation capacity predicted by EC8-3). This is consistent with the damage distribution in the specimens and the results of the drift components analysis depicted in Figure 3.27, which shows the relatively minor contribution of the columns to the total drift imposed on the specimens.

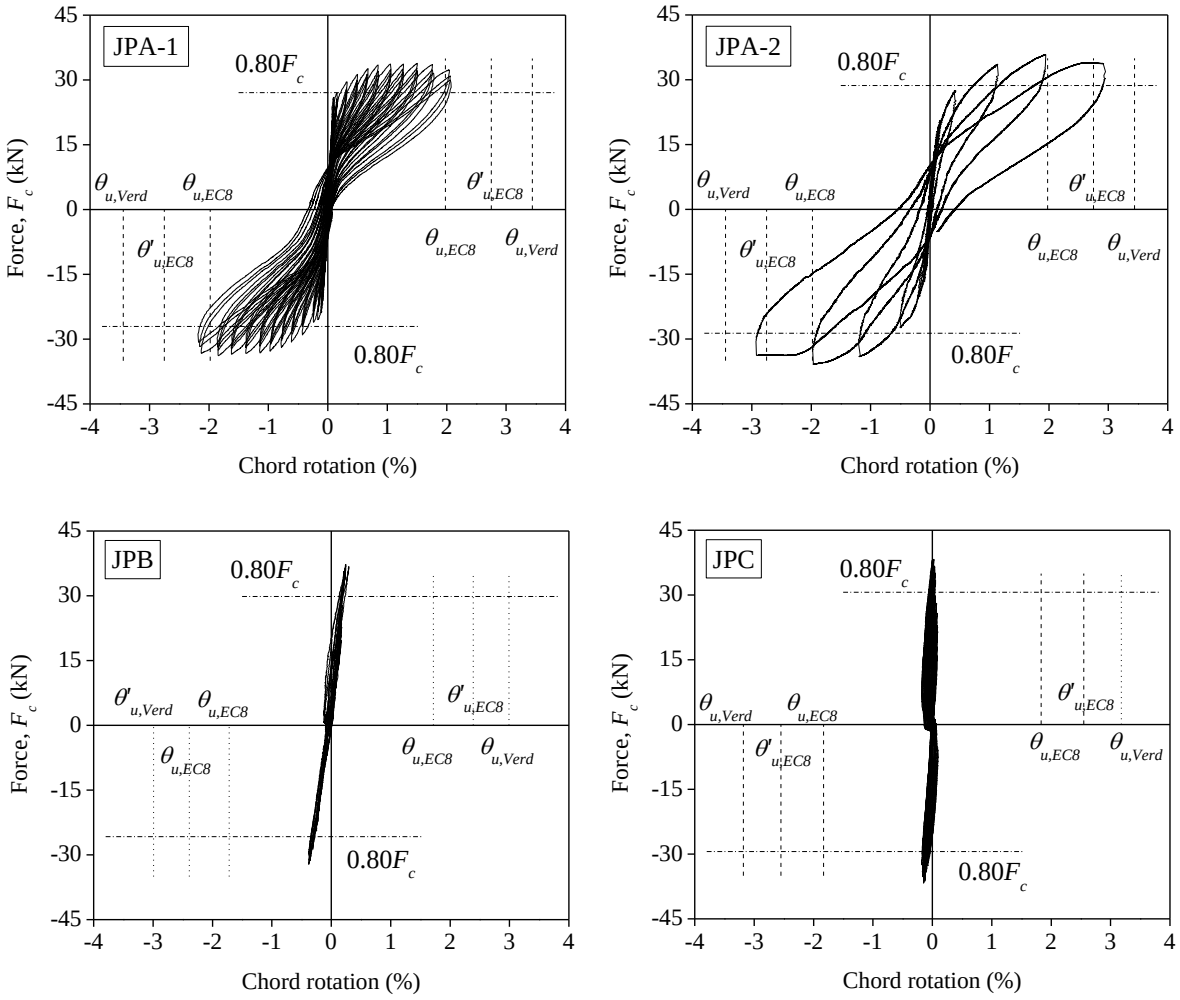

Figure 3.29 - Lateral load versus column chord rotation diagrams.

Table 3.15 - Maximum chord rotation and ratio to theoretical values of ultimate rotation capacity

Specimen	$\theta_{exp,max}$	$\theta_{exp,max}$ /$\theta_{u,EC8}$	$\theta_{exp,max}$ /$\theta'_{u,EC8}$	$\theta_{exp,max}$ /$\theta_{u,Verd}$
JPA-1	2.18	1.1	0.8	0.6
JPA-2	2.95	1.5	1.1	0.9
JPB	0.37	0.2	0.2	0.1
JPC	0.18	0.1	0.1	0.1

3.4.7 - Energy dissipation

In Figure 3.30 the evolution of dissipated energy, computed as the area under the lateral load-drift diagrams, is plotted for all specimens except JPA-2. Specimen JPA-2 was excluded from this analysis since it was subjected to a displacement history different from the one imposed on the other specimens.

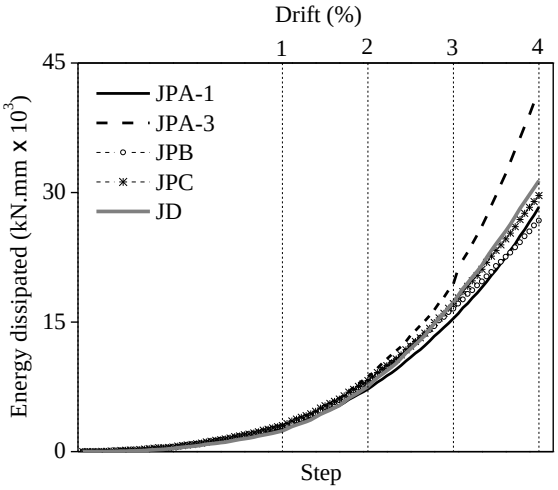

Figure 3.30 - Evolution of dissipated energy.

Figure 3.30 shows that up to 2% drift the evolutions of dissipated energy are similar. Afterwards, the energy dissipation increases with higher rate for specimen JPA-3 than for the other joint specimens, for which the evolution of dissipated energy remained relatively similar. The total energy dissipated by JPA-3 was about 1.5 times the total energy dissipated by each of the other joint specimens with plain reinforcing bars, and 1.4 times the total energy dissipated by the joint specimen with deformed bars.

Table 3.16 indicates for each specimen the values of energy corresponding to: i) dissipated energy up to 1%, 2%, 3% and 4% drift, that is, cumulative energy E_{cum}; ii) dissipated energy between these levels of drift, $E_{drift,i\text{-}i+1}$ (for example, $E_{drift,1\text{-}2}$ is the energy dissipated between 1% and 2% drift); and, iii) total dissipated energy E_{total}. The energy values E_{cum} and $E_{drift,i\text{-}i+1}$ are normalized to the maximum energy dissipated at or up to a given drift level among the specimens under analysis, allowing for a comparison between the energy dissipation rates.

Table 3.16 - Energy dissipation

Specimen	Normalized values of dissipated energy at different drift levels								E_{total} (kN.mm)
	1% drift		2% drift		3% drift		4% drift		
	E_{cum}	$E_{drift,1}$	E_{cum}	$E_{drift,1\text{-}2}$	E_{cum}	$E_{drift,2\text{-}3}$	E_{cum}	$E_{drift,3\text{-}4}$	
JPA-1	0.86	0.86	0.78	0.74	0.74	0.71	0.66	0.58	28003
JPA-3	1.00	1.00	1.00	1.00	1.00	1.00	1.00	1.00	42431
JPB	1.00	1.00	0.91	0.86	0.83	0.76	0.65	0.47	27379
JPC	0.97	0.97	0.87	0.82	0.82	0.78	0.69	0.58	29431
JD	0.78	0.78	0.81	0.82	0.83	0.84	0.72	0.63	30741

The relative contribution of the beams and columns to the total energy dissipated by the joint specimens was estimated at each level of imposed drift and is depicted Figure 3.31. The parcel of dissipated energy associated with each element was estimated from the corresponding moment-rotation diagrams plotted for the middle section of slices 1 and 2. It should be noted that in each case the rotation corresponds to the relative rotation measured between the start and end sections of the slice.

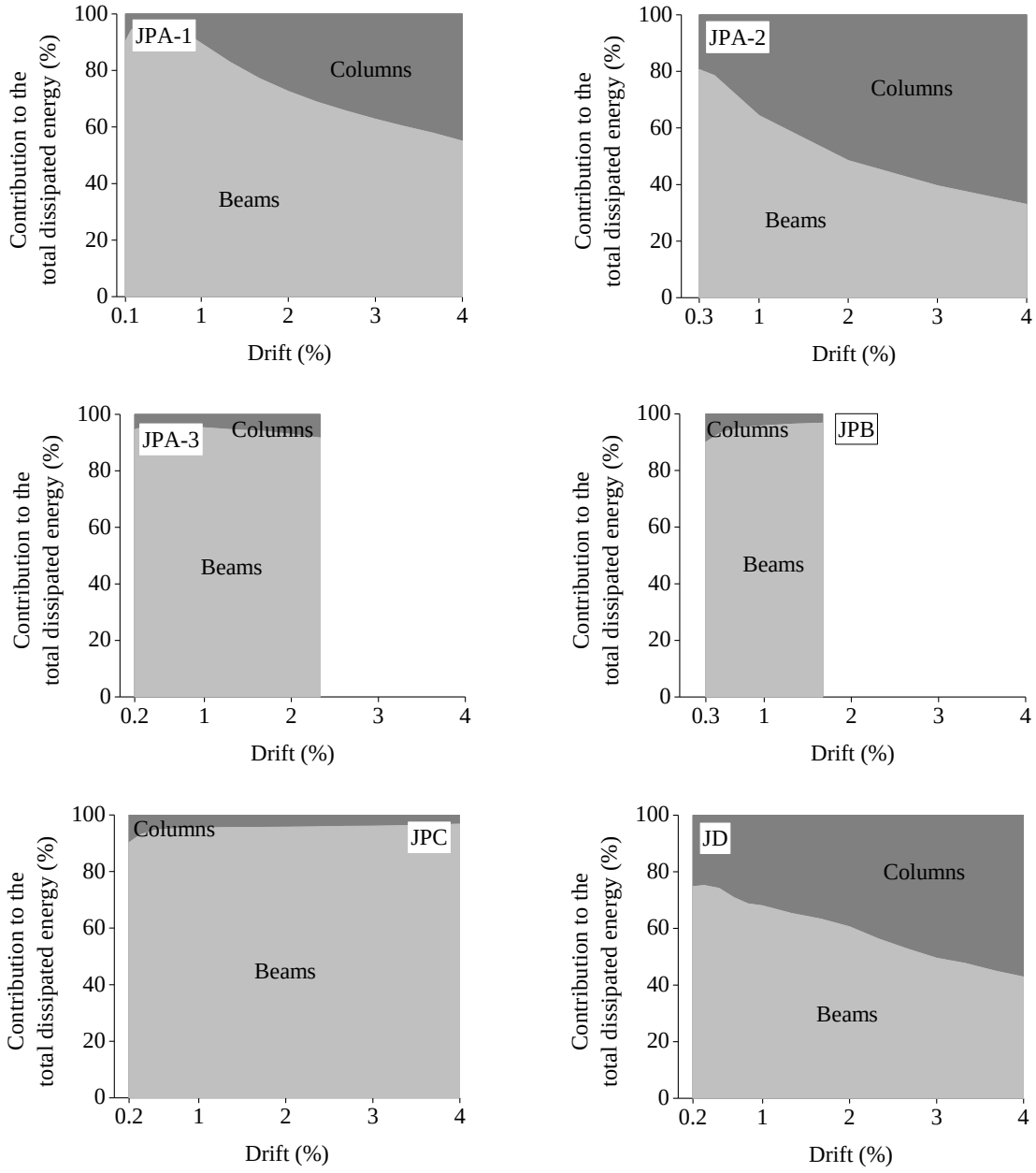

Figure 3.31 - Relative contribution of beams and columns to the total dissipated energy.

The maximum difference between the dissipated energy computed from the lateral load-drift diagrams and that computed as the sum of the parcels of energy estimated from the moment-rotation diagrams, registered for the maximum imposed drift, is equal to: 7% for JPA-1, 12% for JPA-2, 13% for JPA-3, 34% for JPB, 5% for JPC, and 11% for JD. These differences are related to the damage in the joint region (namely in specimens JPA-3 and JD), to bar slippage, and to the frictional forces in the testing devices (high-load carrying capacity devices used to support the self-weight of the specimens, and sliding devices in the beams).

In Figure 3.31 the relative contribution of the elements is represented from the drift level corresponding to the onset of cracking. For specimens JPA-3 and JPB the values are only represented up to 2.3% drift and 1.7% drift respectively due to problems with the LVDTs.

For all specimens, the results in Figure 3.31 show that for lower levels of imposed drift the energy dissipation is mainly associated with the beams deformation. For specimens JPA-1, JPA-2, JPA-3, and JD the relative contribution of the columns to the total dissipated energy increases as the imposed lateral drift increases. At the maximum drift, the estimated relative contribution of the columns is equal to 45% for JPA-1, 67% for JPA-2, superior to 8% for JPA-3, and 57% for JD. Conversely, in specimens JPB and JPC the relative contribution of the beams to the total dissipated energy is above 90% from the beginning to the end of the corresponding cyclic tests. The evolution of the relative contribution of the elements to the total dissipated energy is in agreement with the observed damage evolutions.

3.4.8 - Equivalent damping and ductility demands

Figure 3.32-a shows the response of the specimens in terms of equivalent damping versus displacement ductility. For specimens JPA-1, JPA-3, and JD Figure 3.32-a also shows the curves that best fit the experimental results. JPA-2 was also excluded from this analysis.

The total equivalent viscous damping equations proposed in the literature are divided into two parts [17]: ξ_0, the initial damping in the elastic range; and, ξ_{hyst}, the equivalent damping ratio that represents the dissipation due to the nonlinear (hysteretic) behaviour. For the quasi-static cyclic tests reported in this work, the equivalent damping is equal to the hysteretic damping. The latter was computed according to Varum [18], using Equation

(3.18), where $A_{half\text{-}loop}$ stands for the area under each half force-displacement cycle (hence, dissipated energy), and F_{max} and D_{max} are the maximum force and the corresponding displacement in that cycle respectively.

$$\xi_{hyst} = \frac{1}{\pi} \cdot \frac{A_{half-loop}}{F_{max} \cdot D_{max}} \tag{3.18}$$

The displacement ductility (μ_{Δ}) was computed as the ratio of lateral displacement to yielding displacement. The yielding displacement was determined according to Annex B.3 of EC8-1, and was estimated equal to: 28.2 mm for JPA-1 and JPA-2; 31.1 mm for JPA-3; 26.0 for JPB; 27.0 for JPC; and, 23.8 mm for JD.

Table 3.17 shows the values of equivalent damping and displacement ductility estimated for the maximum imposed drift. Within the drift range under analysis, the largest and lowest ductility demands were imposed on JD (μ_{Δ}=5.0) and JPA-3 (μ_{Δ}=3.8) respectively. However, even if the lowest demand in terms of ductility was imposed on JPA-3, it is recalled that this was the only joint specimen that reached the conventional failure condition.

Table 3.17 - Equivalent damping and displacement ductility at the maximum drift

Specimen	ξ_{eq} (%)	μ_{Δ} (%)
JPA-1	7.1	4.3
JPA-3	12.3	3.9
JPB	5.3	4.6
JPC	6.1	4.4
JD	7.1	5.0

Figure 3.32-b shows a comparison between the experimental results and the equivalent damping versus displacement ductility relationships computed using some of the existing equivalent damping equations [17], namely: Equation (3.19), proposed by Priestley [19] for concrete frames; and, Equation (3.20), associated with the Takeda model [20]. This comparative analysis was made considering that many of the existing RC building structures that were built without specific detailing for seismic demands tend to develop a soft-storey mechanism and, therefore, the response of the beam-column joints of a weak

storey can be correlated with the response of the overall structure. In Figure 3.32-b a comparison is also made with the equivalent damping versus displacement ductility relationship computed using Equation (3.21), proposed by Varum [18] based on the results of a series of pseudo-dynamic tests of a RC frame structure built with plain reinforcing bars. In Equation (3.20) the elastic damping (ξ_0) was made equal to 5%, as common practice [21]. In Equation (3.21), Δ stands for the inter-storey drift.

$$\xi_{eq} = 5 + \frac{120}{\pi} \cdot \left(1 - \frac{1}{\sqrt{\mu_\Delta}}\right) \tag{3.19}$$

$$\xi_{eq} = \xi_0 + 0.2 \cdot \left(1 - \frac{1}{\sqrt{\mu_\Delta}}\right) \tag{3.20}$$

$$\xi_{eq} = 11.041 \cdot ln(\Delta) + 9.9286 \tag{3.21}$$

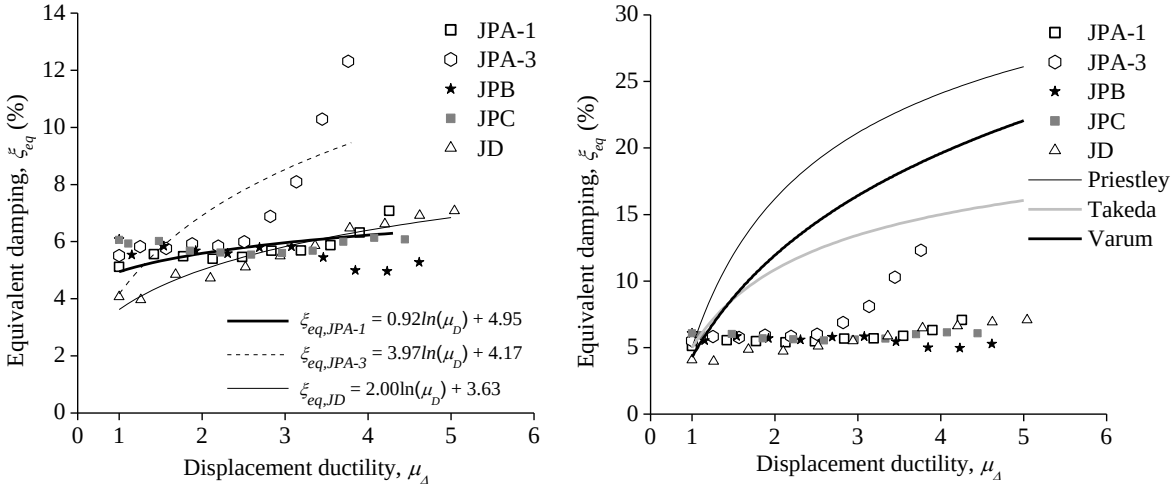

Figure 3.32 - Equivalent damping versus displacement ductility: a) experimental results; b) comparison with the results from existing equivalent damping equations.

The equivalent damping-displacement ductility relationships determined from Equations (3.19) to (3.21) significantly overestimate the experimental results. Equations (3.19) and (3.20) are more adequate for structures with larger energy dissipation capacities. This highlights the need for the development of simplified expressions, based on experimental

data, for the assessment of existing RC building structures built without specific detailing for seismic demands and, in particular, with plain reinforcing bars. Regarding Equation (3.21), the experimental results used by Varum [18] for determining the equivalent damping-displacement ductility relationship refer to a particular storey. In these tests, the storey response was mainly governed by the behaviour of a strong column. Conversely to what was observed in the joint specimens under investigation, damage in that strong column was not concentrated at the interface with the joint. Instead, it was spread along a relatively larger plastic hinge region. Therefore, the associated energy dissipation is expected to be larger than that displayed by the beam-column joint specimens under investigation.

3.4.9 - Damage index

Among the various damage indices available in the literature, the most widely used is the Park and Ang (PA) damage index [22], which expresses the seismic structural damage as a linear combination of the damages caused by the maximum deformation and by repeated cyclic loading effect (that is, energy dissipation) [18]. The PA damage index is calculated using Equation (3.22). It can be applied at different levels, namely at mechanism, storey and global levels, and as a combination of the local damage indices. In Equation (3.22) [18]: PA_i is the Park and Ang damage index for the storey i; $u_{max,i}$ is the maximum inter-storey displacement of storey i; $u_{u,i}$ is the ultimate inter-storey deformation (under monotonic loading); β is the strength deterioration parameter (non-negative); $P_{y,i}$ is the yielding strength; and, $\int dE_i$ is the incremental hysteretic dissipated energy. A value of the PA damage index larger than 1.0 indicates complete collapse or total damage.

$$PA_i = \frac{u_{\max,i}}{u_{u,i}} + \frac{\beta}{P_{y,i} \cdot u_{u,i}} \cdot \int dE_i \tag{3.22}$$

Many empirical expressions for the strength deterioration parameter (β) are available in the literature. According to Varum [18], one of the most used expressions is the one proposed by Kunnath *et al.* [23] and adapted by Arêde [24], expressed in the form of Equation (3.23), where: ρ_w is the volumetric confinement ratio (volume of closed stirrups divided by

the volume of confined concrete core); v the normalized axial load (taken positive if compressive); and, ω_t, the mechanical ratio of tension reinforcement.

$$\beta = 0.9^{100\rho_w}\left(0.37 \cdot \max\{v;0.05\} + 0.5 \cdot (\omega_t - 0.17)^2\right) \tag{3.23}$$

Park *et al.* [25] suggest an expression to estimate the ultimate displacement. This expression adapted to the SI units system (kN, m) can be written in the form of Equation (3.24) and considering Equations (3.25) to (3.27), where: $R_u(\%)$ is the ultimate rotational capacity (in percent); δ_u the ultimate horizontal displacement capacity; l/d the shear span ratio; ρ the normalized steel ratio; p_t the volumetric ratio of longitudinal steel; ρ_w the confinement ratio (in percent; replaced by 0.4%, if ρ_w < 0.4%); n_o the normalized axial stress (replaced by 0.05 if n_o < 0.05); P the axial load (in kN); b the width of the cross-section; d the effective depth of the cross-section; f_c the concrete strength (in kPa); and, f_y the yield strength of the steel reinforcement (in kPa).

$$R_u(\%) = 1.958 \cdot (l/d)^{0.93} \cdot \rho^{-0.27} \cdot \rho_w^{0.48} \cdot n_0^{-0.48} \cdot f_c^{-0.15} \tag{3.24}$$

$$R_u = \delta_u / l \tag{3.25}$$

$$\rho = p_t \cdot f_y / f_c \tag{3.26}$$

$$n_0 = P/(b \cdot d \cdot f_c) \tag{3.27}$$

The PA damage index was computed for each of the joint specimens under investigation. The PA damage index corresponding to each level of imposed drift was computed using Equation (3.22). The parameters involved in the computation were determined considering the columns properties. Table 3.18 indicates the values of the strength degradation parameter (Equation (3.23)) and ultimate displacement (Equation (3.24)) determined for the joint specimens.

Table 3.18 - Values estimated for the strength degradation parameter (β) and ultimate displacement (u_u)

	JPA-1	JPA-2	JPA-3	JPB	JPC	JD
β	0.039	0.039	0.082	0.077	0.073	0.041
u_u (m)	0.11	0.11	0.08	0.06	0.09	0.12

Figure 3.33 to Figure 3.38 depict the time evolution of the PA damage index estimated for the joint specimens, together with the contribution of the maximum deformation (u_{max}/u_u) to the damage index. The results show the relatively minor contribution of the energy dissipation to the PA damage index, what was also observed in the analyses carried out by Varum [18]. For the first levels of imposed drift, up to 0.2%, the average contribution of the maximum deformation to the PA damage index is equal to about 98% for the six joint specimens. For the last three levels of drift the average contribution of the maximum deformation is: 79% for JPA-1; 93% for JPA-2; 62% for JPA-3; 68% for JPB and JPC; and, 79% for JPA-1.

Figure 3.33 to Figure 3.38 also show the damage state categories suggested by Park *et al.* [25] based on damage observations in past earthquakes, and the corresponding global damage indices boundaries (Table 3.19). For each joint specimen Figure 3.33 to Figure 3.38 also indicate the drift corresponding to the onset of the main damage states observed in the cyclic tests, namely: cracking at the beam/column-joint interfaces, diagonal cracking in the joint region, and spalling of the concrete cover in the beams, columns and joint region. In general, the onset of cracking occurred within the ranges indicated in Table 3.19, while spalling of the concrete cover was registered for damage indices larger than the suggested. When established the comparison between the two analogous specimens, JPA-1 and JD, the drift at which the specimens reach each damage state is in general lower for the specimen with plain reinforcing bars. For example, damage index equal to 1 is registered at 3% drift for JPA-1, and 3.3% drift for JD.

Table 3.19 - Calculated damage index versus observed damage [18]

Damage inspection		Calculated damage index	
Degree of damage	Physical appearance	Local	Global
Collapse	Total or partial collapse of building	>1.0	>1.0
Severe	Extensive crushing of concrete. Disclosure of buckled reinforcements	0.75-1.0	0.50-1.0
Moderate	Extensive large cracks. Spalling of concrete in weaker elements	0.35-0.75	0.30-0.50
Minor	Minor cracks throughout building. Partial crushing of concrete columns	0.10-0.35	0.10-0.30
Slight	Sporadic occurrence of cracking	0.0-0.10	0.0-0.10

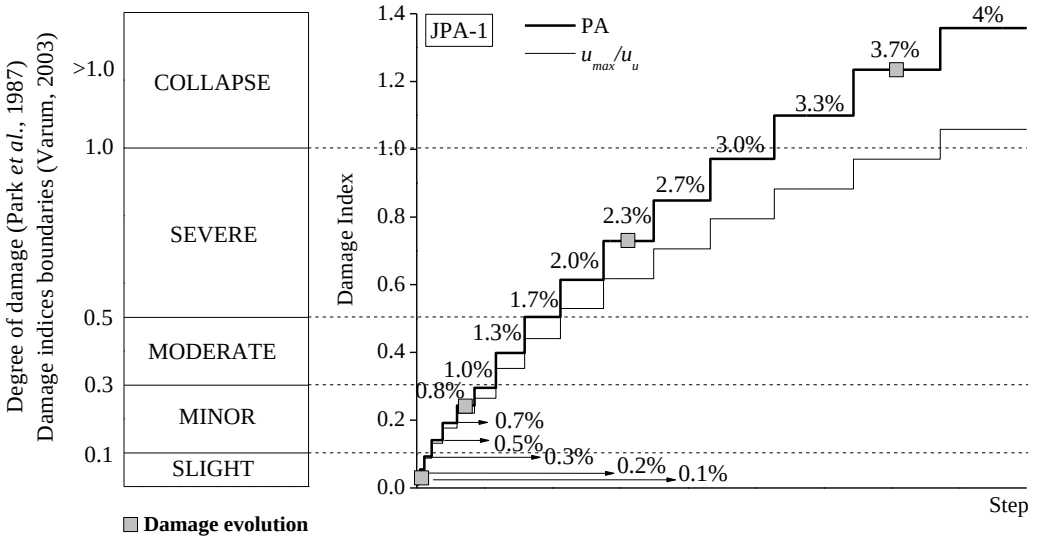

Damage evolution

0.07% drift: onset of cracking in the right beam **0.13% drift**: onset of cracking in the left beam

0.83% drift: onset of cracking in the columns **2.33% drift**: onset of concrete cover spalling in the beams

3.67% drift: onset of concrete cover spalling in the columns

Figure 3.33 - Time evolution of the PA damage index for specimen JPA-1.

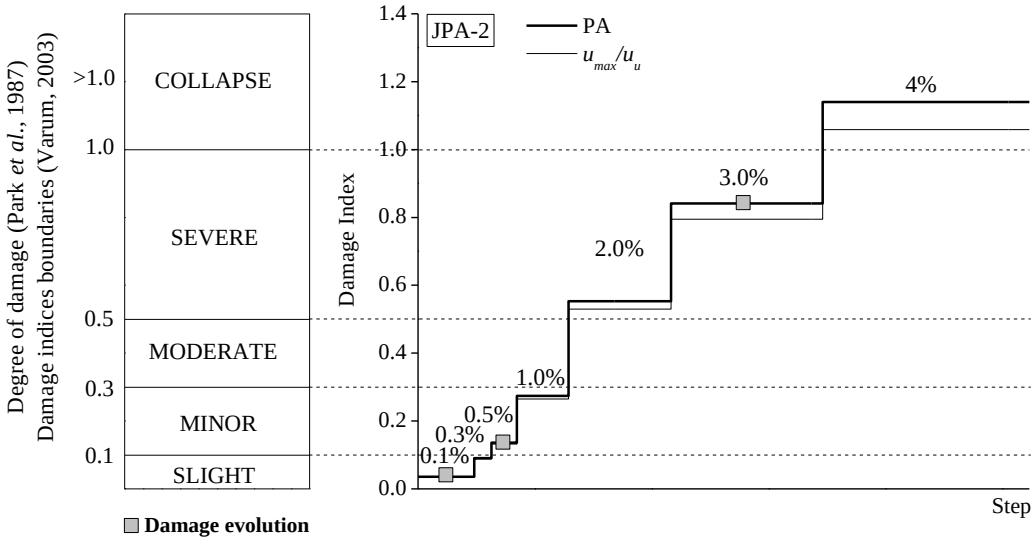

Damage evolution

0.13% drift: onset of cracking in the beams and inferior column

0.50% drift: onset of cracking in the superior column

3.00% drift: onset of concrete cover spalling in the columns

Figure 3.34 - Time evolution of the PA damage index for specimen JPA-2.

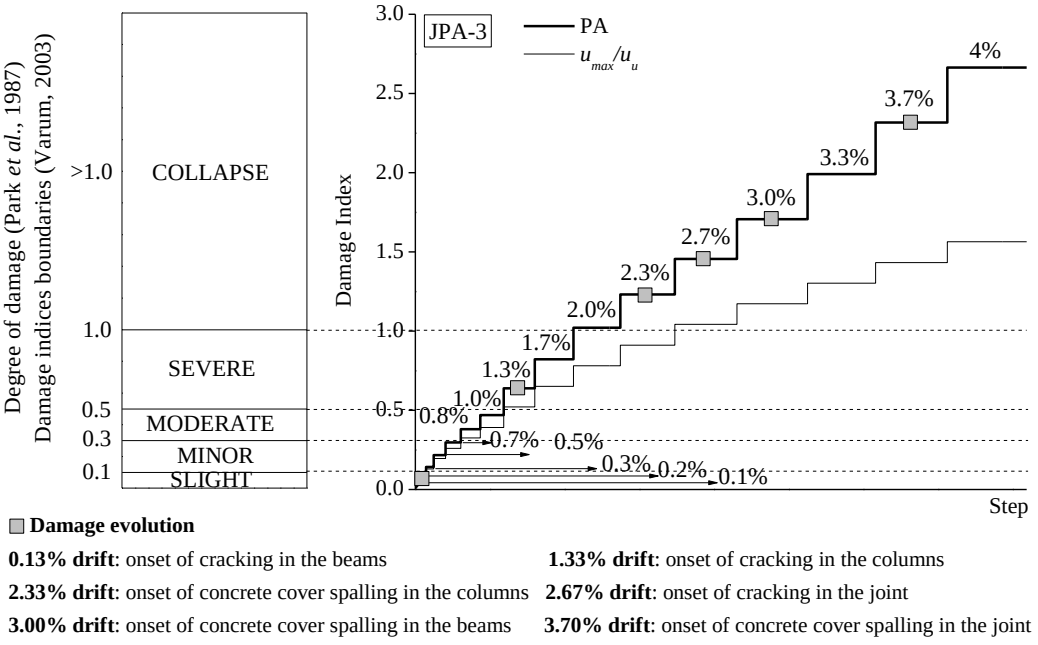

Figure 3.35 - Time evolution of the PA damage index for specimen JPA-3.

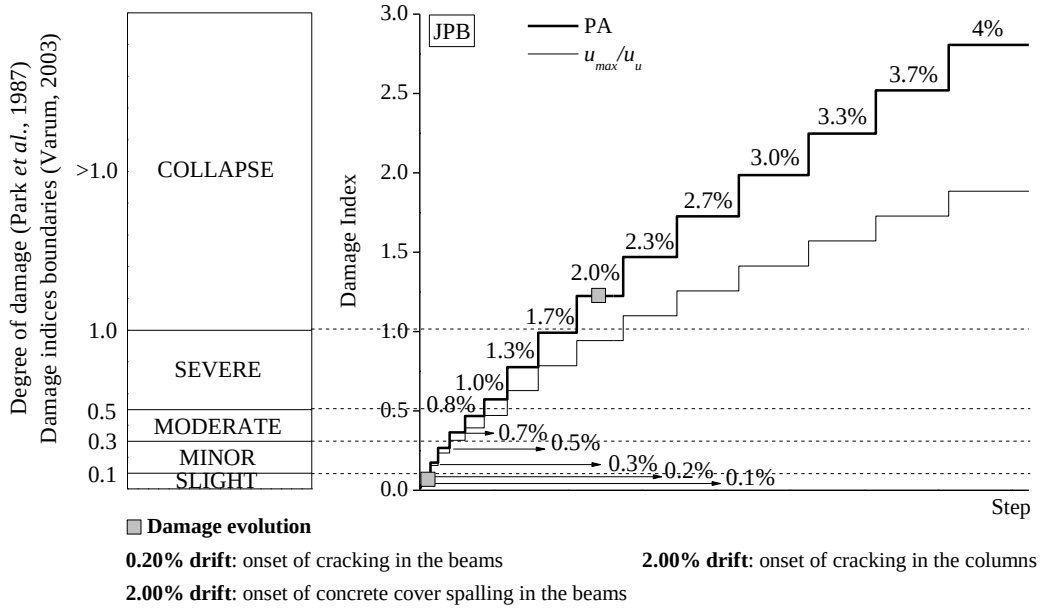

Figure 3.36 - Time evolution of the PA damage index for specimen JPB.

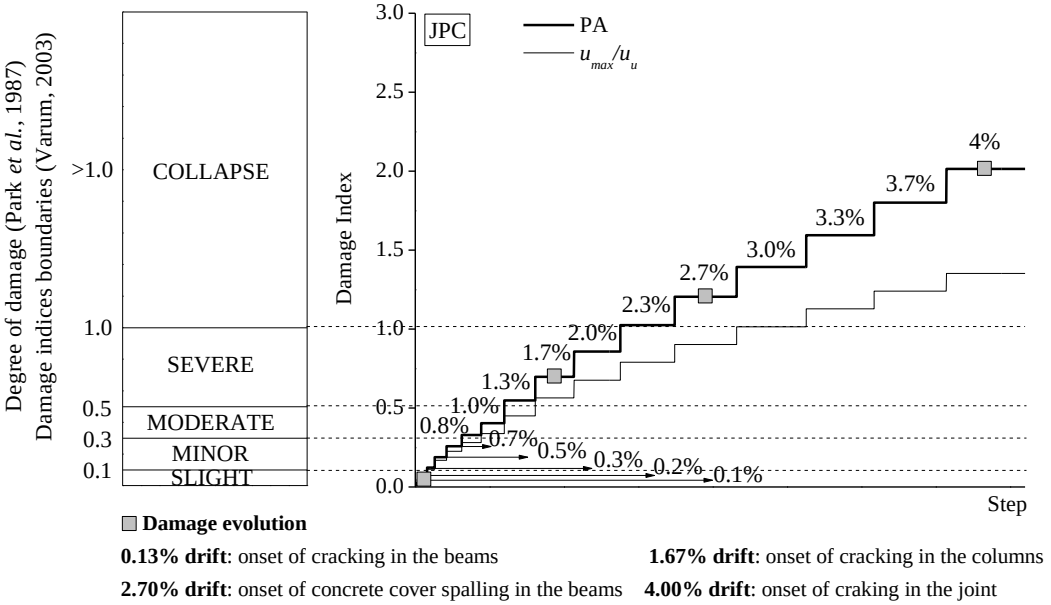

Figure 3.37 - Time evolution of the PA damage index for specimen JPC.

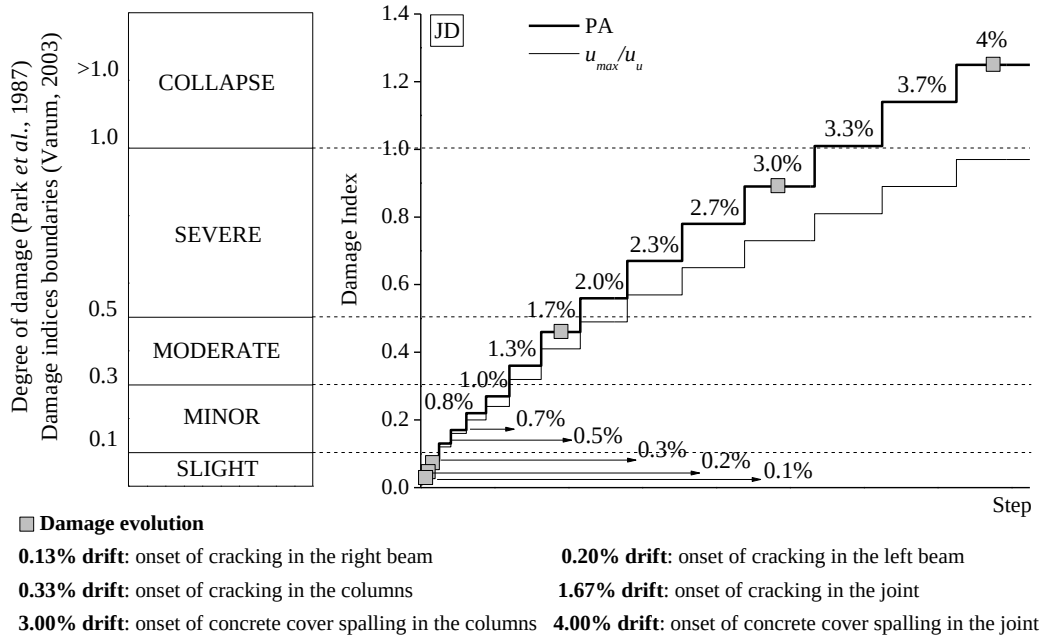

Figure 3.38 - Time evolution of the PA damage index for specimen JD.

3.5 - INFLUENCE OF DISPLACEMENT HISTORY, AXIAL LOAD, BOND, AND STEEL REINFORCEMENT

This section provides a more detailed analysis of the sensitivity of the beam-column joint specimens' response to displacement history, column axial load, bond properties, and amount of steel reinforcement. Thus, and respectively, comparison is established between the experimental results of: a) JPA-1 and JPA-2; b) JPA-1 and JPA-3; c) JPA-3 and JPB, and JPB and JPC.

3.5.1 - Displacement history

Specimens JPA-1 and JPA-2 were built with the same geometrical characteristics, reinforcement detailing and material properties, and subjected to the same level of column axial load. However, JPA-2 was tested under a displacement history with a number of cycles lower than that in the displacement history imposed on JPA-1.

The influence of displacement history on the specimens' response was minor. The comparison between the lateral load-drift diagrams of specimens JPA-1 and JPA-2 in Figure 3.39 shows that the two specimens reached similar values of maximum lateral load (5% difference) at approximately the same drift (3.3% for JPA-1 and 3% for JPA-2). The lateral load at the maximum imposed drift was also alike (5% difference), as well as the secant stiffness measured for the peak load in the cycles with the same drift level (see close-up in Figure 3.39).

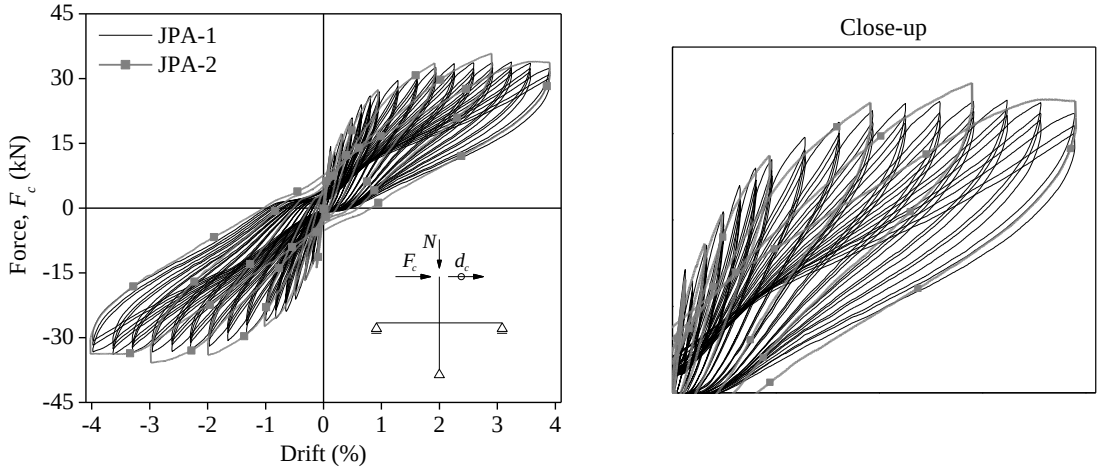

Figure 3.39 - Lateral load-drift diagrams of specimens JPA-1 and JPA-2.

The two specimens exhibited the same type of damage distribution, concentrated at the beam-joint and column-joint interfaces. The onset of cracking in the beams and columns occurred at similar drift levels in the two specimens. At the maximum drift, the crack opening in the beams of JPA-2 was about 73% of that in the beams of JPA-1, and the crack opening in the columns of JPA-2 was about 1.4 times that in the columns of JPA-1. The differences in terms of moment-curvature diagrams are depicted in Figure 3.40. As stated in Section 3.4.2, the moments are computed for the middle section of slice 1 in each element (beams and columns) assuming a linear moment distribution along the elements' length, and the curvatures correspond to the mean curvature estimated for slice 1. As a consequence of the relatively wider crack opening in the columns of JPA-2, the relative contribution of the columns deformation to the total drift is larger for JPA-2 than for JPA-1 (equal to 73% and 60% respectively, at maximum drift).

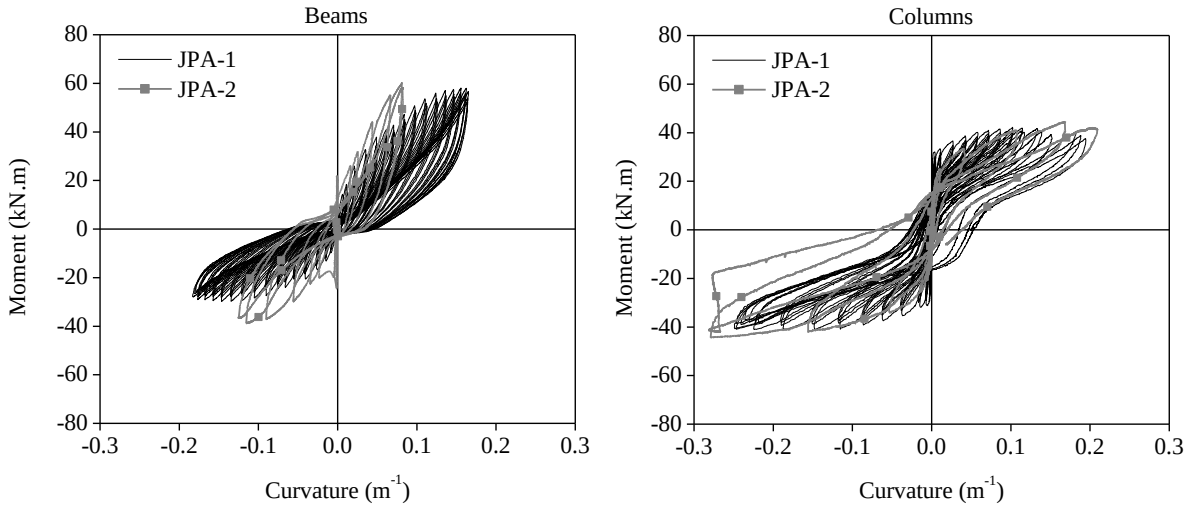

Figure 3.40 - Moment-curvature diagrams of specimens JPA-1 and JPA-2.

In the cyclic tests carried out by Bedirhanoglu *et al.* [26] on exterior beam-column joint specimens with plain reinforcing bars, the influence of displacement history was also concluded to be minor.

3.5.2 - Column axial load

Specimens JPA-1 and JPA-3 were built with the same geometrical characteristics, reinforcement detailing, and materials properties. The two specimens were tested under the

same lateral displacement history and the column axial load imposed on JPA-3 was 2.3 times that imposed on JPA-1.

Figure 3.41 depicts the comparison between the lateral load-drift diagrams of specimens JPA-1 and JPA-3. The increase in column axial load in JPA-3 led to an increase of 27% in the maximum lateral load, which was registered at a drift level (2.7%) lower than that for JPA-1 (at 3.3% drift). The strength degradation after the maximum lateral load was relatively more pronounced for JPA-3. As previously stated, only for JPA-3 was registered the conventional failure condition corresponding to 20% reduction in strength. The two specimens exhibited similar stiffness up to the onset of cracking. Afterwards, JPA-3 exhibited a relatively larger stiffness (see close-up in Figure 3.41). The pinching effect was similar, but it practically ceased in JPA-3 after the maximum lateral load was reached.

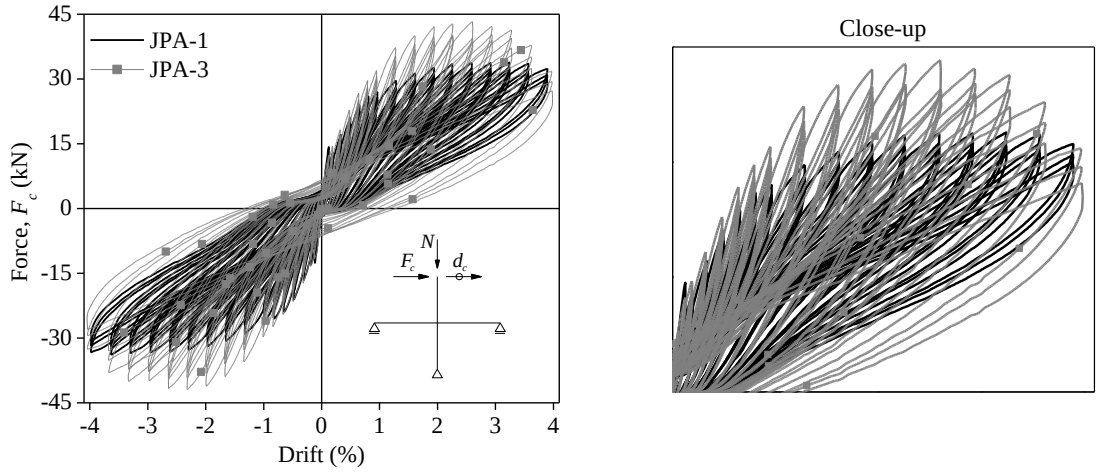

Figure 3.41 - Lateral load-drift diagrams of specimens JPA-1 and JPA-3.

Important differences were registered between the two specimens in terms of damage distribution. In addition to the damage developed at the beam-joint and column joint interfaces, for specimen JPA-3 was also observed severe diagonal cracking in the joint region with spalling of the concrete cover, contributing to the strength degradation of the specimen. The onset of cracking in the beams was registered at similar drift levels. The increase in column axial postponed the onset of cracking in the columns, which occurred at 0.8% drift for JPA-1 and 1.3% drift for JPA-3. As a consequence, for JPA-3 the ratio between the maximum crack opening in the columns and the maximum crack opening in the beams is less than half of that corresponding to JPA-1. The moment-curvature

diagrams are depicted in Figure 3.42. As a consequence of the differences in crack opening, the relative contribution of the columns deformation to the total drift is lower for JPA-3 than for JPA-1 (equal to 26% and 51% respectively, at 3% drift).

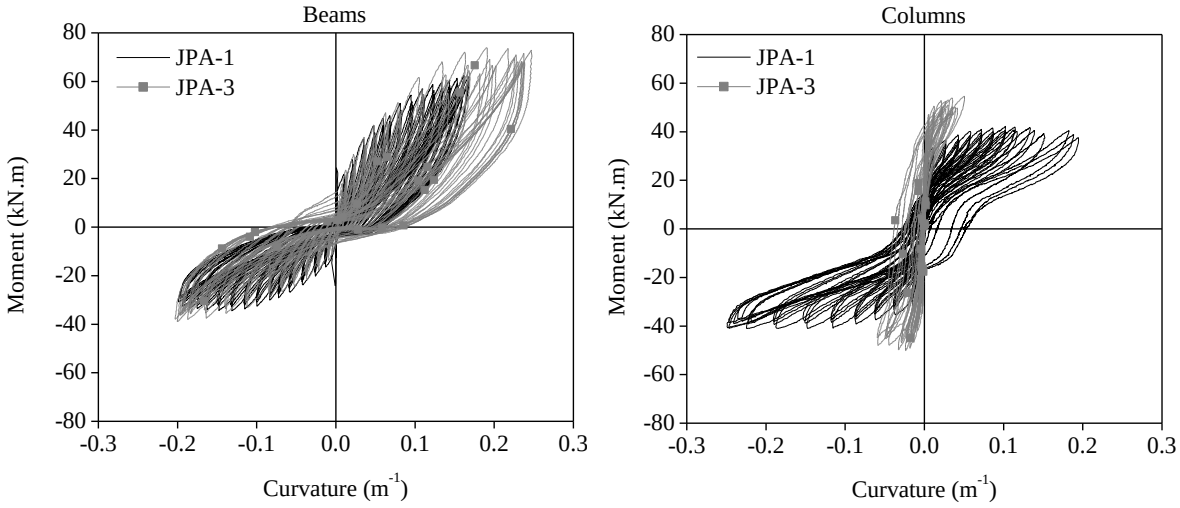

Figure 3.42 - Moment-curvature diagrams plotted of specimens JPA-1 and JPA-3.

Figure 3.43 compares the evolutions of the tensile stresses in the joint region of specimens JPA-1 and JPA-3, expressed in terms of the ratio of principal tensile stress to square root of the concrete compressive strength. The maximum principal tensile stress was estimated equal to $0.32\sqrt{f_c}$ for JPA-1 and $0.30\sqrt{f_c}$ for JPA-3 (at the drift level corresponding to the onset of diagonal cracking in the joint). The maximum joint shear force estimated for specimen JPA-3 is 1.3 times the maximum shear force determined for JPA-1.

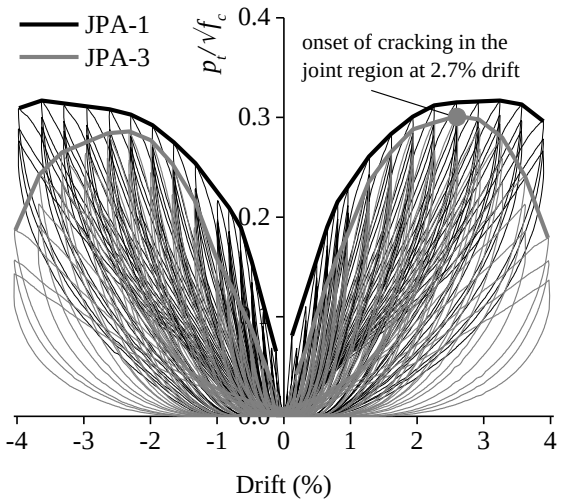

Figure 3.43 - Tensile stress-drift diagrams of specimens JPA-1 and JPA-3.

Within the drift range under analysis, increasing the level of column axial load resulted in larger energy dissipation. At the maximum drift, the total energy dissipated by JPA-3 was 1.5 times the total energy dissipated by JPA-1. Lower ductility demands were imposed on specimen JPA-3.

An increase in strength and energy dissipation, and a reduction of the pinching effect, as a consequence of larger axial load in the columns, was also observed in the cyclic tests carried out by Bedirhanoglu *et al.* [26] on exterior joint specimens with plain bars.

3.5.3 - Bond properties

Specimens JPA-1 and JD were built with the same geometrical characteristics, reinforcement detailing and concrete mechanical properties, but JPA-1 was built with plain reinforcing bars and JD with deformed bars. The two specimens were tested under the same lateral displacement history and with the same level of column axial load.

Figure 3.44 depicts the comparison between the lateral load-drift diagrams of specimens JPA-1 and JD. The maximum lateral load registered for the specimen with deformed bars (at 2% drift) is 15% higher than that registered for the specimen with plain reinforcing bars (at 3.3% drift). The strength degradation after the maximum lateral load was relatively larger for JD. The two specimens exhibited similar stiffness until cracking onset. Afterwards, for larger displacement demands, JPA-1 displayed lower unloading stiffness than JD (see close-up in Figure 3.44). The pinching effect was more evident for JPA-1.

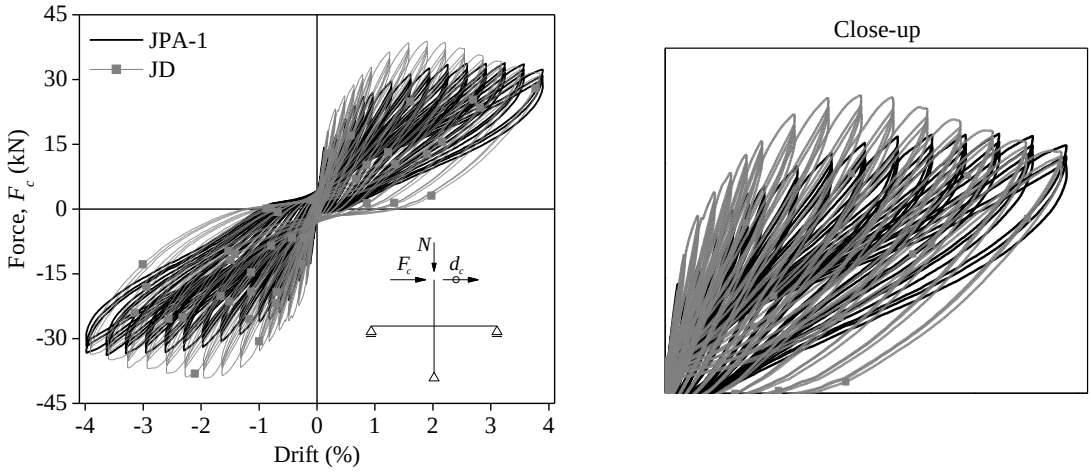

Figure 3.44 - Lateral load-drift diagrams of specimens JPA-1 and JD.

The effects of bond properties were particularly shown by the differences in the observed damage distribution. The specimen with plain reinforcing bars displayed damage concentrated at the beam-joint and column-joint interfaces. The specimen with deformed bars displayed a more spread damage distribution, with cracking along the elements' length. Diagonal cracking in the joint region was also observed in specimen JD, which contributed to the relatively larger strength degradation. The onset of cracking in the beams was registered at similar drift levels. The onset of cracking in the columns of JD was registered at lower drift (0.33%) than for JPA-1 (0.83%). The two specimens exhibited similar values of maximum crack opening at the beam-joint interfaces. The maximum crack opening at the column-joint interfaces of specimen JD was 76% higher than that in JPA-1. The moment-curvature diagrams are depicted in Figure 3.45. Figure 3.46 compares the maximum values of mean curvature estimated for slices 1 and 2 in the elements of specimens JPA-1 and JD at each level of imposed drift. The deformation demands in slice 1 are similar for the two specimens. Due to a more spread damage distribution in JD, the deformation demands in slice 2 of JD are larger than those in slice 2 of JPA-1, increasing up to the onset of cracking in the joint region (at 1.7% drift).

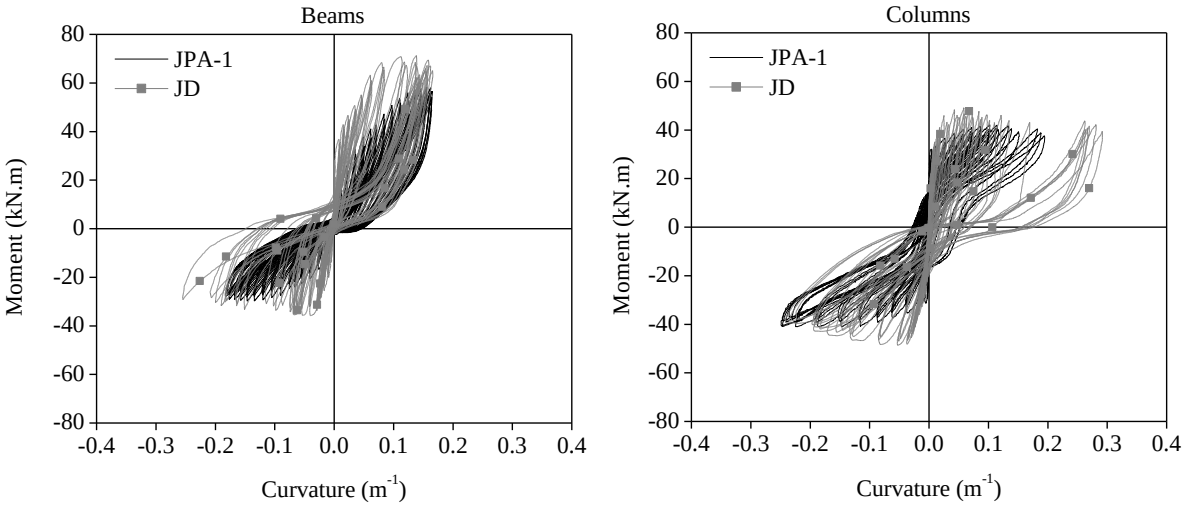

Figure 3.45 - Moment-curvature diagrams of specimens JPA-1 and JD.

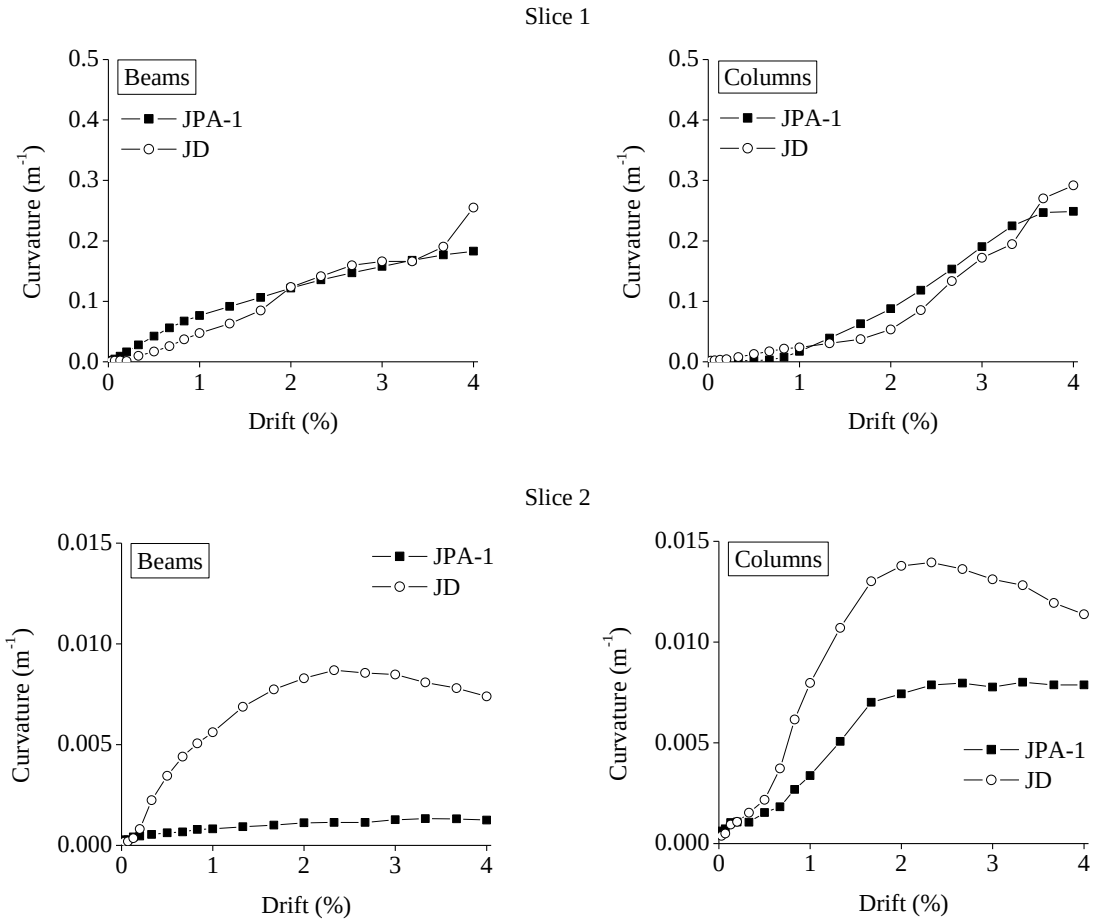

Figure 3.46 - Maximum curvature for JPA-1 and JD.

The observed damage evolutions indicate that concrete crushing did not occur in either of the specimens. Therefore, and considering: i) that the yielding point of the global response for specimen JD is associated with the yielding of the steel reinforcement in the elements; ii) that the yield strength of the plain bars is 1.4 times the yield strength of the deformed bars; iii) the lower lateral strength of JPA-1 in comparison to JD; and, iv) the moment-curvature diagrams in Figure 3.45 (showing similar moment demands for JPA-1 and JD, and the elements' maximum strength); it can be concluded that the poor bond properties, instead of the steel yield strength, limited the maximum strength of the elements with plain reinforcing bars.

Figure 3.47 compares the evolutions of the tensile stresses in the joint region of specimens JPA-1 and JD, expressed in terms of the ratio of principal tensile stress to square root of the concrete compressive strength. The maximum principal tensile stress was estimated

equal to $0.32\sqrt{f_c}$ for JPA-1 and $0.39\sqrt{f_c}$ for JD (at the drift level corresponding to the onset of diagonal cracking in the joint). In terms of shear force demands in the joint region, the maximum shear force estimated for JD is 16% higher than the maximum shear force determined for JPA-1, occurring at a drift level lower than in JPA-1.

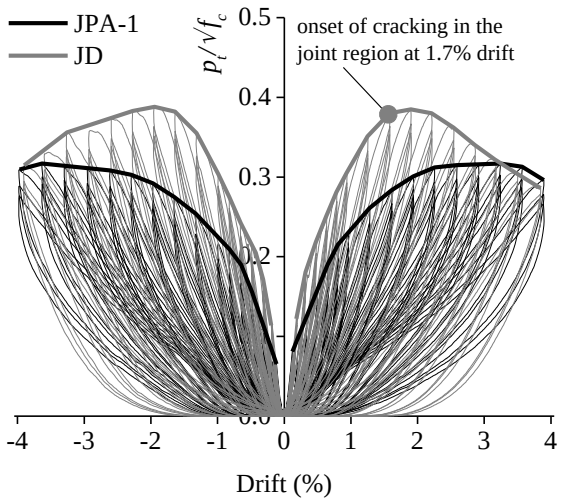

Figure 3.47 - Tensile stress-drift diagrams of specimens JPA-1 and JD.

Better bond properties led to larger energy dissipation. At the maximum imposed drift, the total energy dissipated by JD was 10% higher than that dissipated by JPA-1. Within the drift range under analysis, larger ductility demands were imposed on the specimen with deformed bars.

Similar differences between the damage distribution in RC elements with plain and deformed reinforcing bars were also observed in the cyclic tests carried out by Marefat *et al.* [27], Hertanto [28] and Genesio *et al.* [10].

3.5.4 - Amount of steel reinforcement

Specimens JPA-3, JPB and JPC were built with the same geometrical characteristics and material properties, and tested under the same lateral displacement history and with the same level of column axial load. When compared to JPA-3, specimens JPB and JPC were built with twice the amount of column longitudinal reinforcement. JPC was also built with twice the amount of beam transverse reinforcement and 2.5 times the amount of column transverse reinforcement.

Figure 3.48 shows the comparison between the lateral load-drift diagrams of specimens JPA-3 and JPB. The maximum lateral load registered for JPB was 91% (at 2.3% drift) of that registered for JPA-3 (at 2.7% drift). Specimen JPA-3 exhibited relatively larger strength degradation after the maximum lateral load. The stiffness of JPA-3 and JPB were similar up to cracking onset. Afterwards, JPA-3 exhibited larger stiffness than JPB (see close-up in Figure 3.48). The influence of increasing the amount of transverse reinforcement in specimen JPC in relation to JPB was minor, both in terms of lateral load and stiffness (see Figure 3.49). The pinching effect was particularly evident for specimens JPB and JPC.

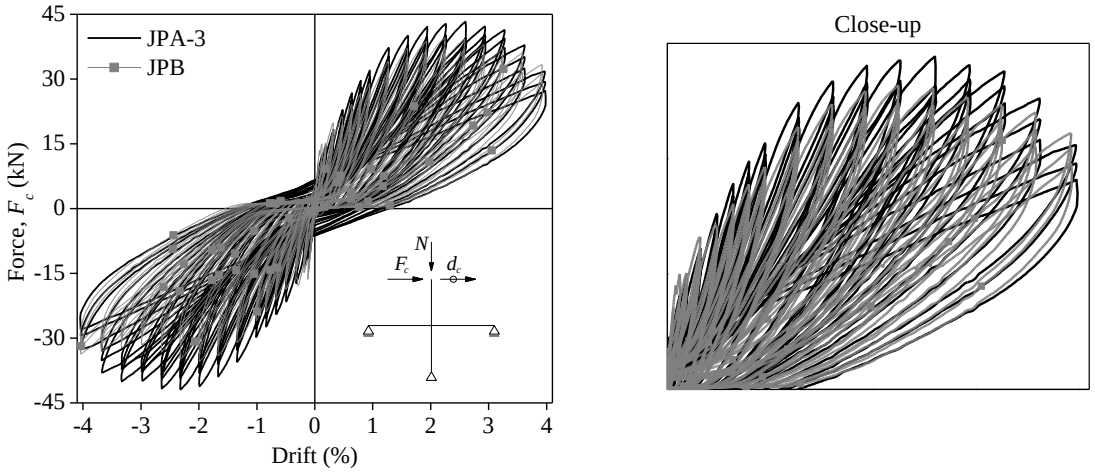

Figure 3.48 - Lateral load-drift diagrams of specimens JPA-3 and JPB.

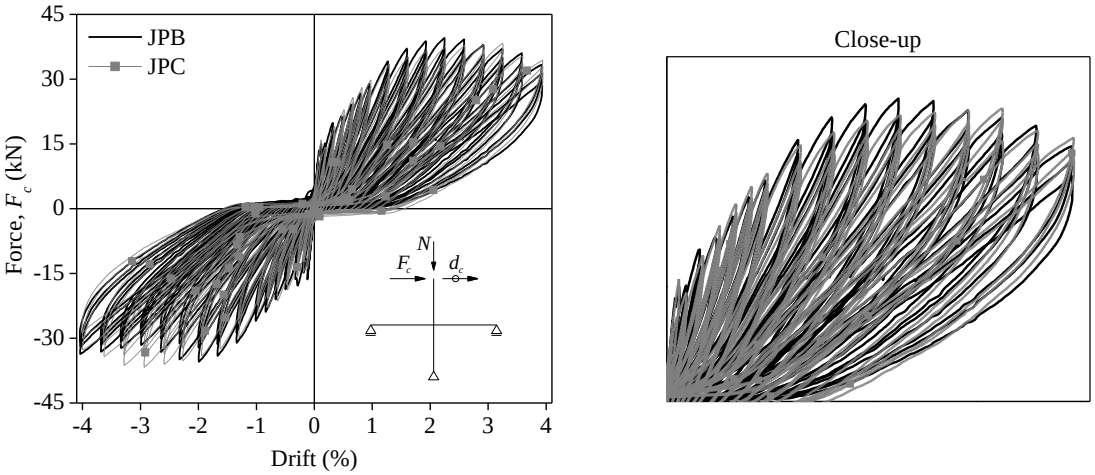

Figure 3.49 - Lateral load-drift diagrams of specimens JPB and JPC.

The smaller reduction in the lateral strength of specimens JPB and JPC, in comparison to that exhibited by JPA-3, is due to the differences observed in the damage distribution. In specimens JPB and JPC damage was observed to be mainly concentrated at the beam-joint interfaces and damage in the columns was minor. The larger flexural capacity of the columns resulting from the larger amount of column longitudinal reinforcement in specimens JPB and JPC delayed the onset of cracking in the columns. This fact, together with the poor bond properties, led to a significant increase in the crack opening at the beam-joint interfaces. Figure 3.50 and Figure 3.51 depict the moment-curvature diagrams, showing that for specimens JPB and JPC the columns response at the maximum imposed drift is mainly elastic.

As a consequence of the differences in damage distribution and crack opening, the drift imposed on specimens JPB and JPC was mainly contributed by the beams deformation. For JPB and JPC, lower lateral load demands than for JPA-3 were necessary to impose the same drift level. At 3% drift, the relative contribution of the columns deformation to the total drift was estimated equal to 26% for JPA-3, 5% for JPB, and 10% for JPC.

Figure 3.52 compares the evolutions of the tensile stresses in the joint region of specimens JPA-3, JPB, and JPC, expressed in terms of the ratio of principal tensile stress to square root of the concrete compressive strength. The maximum principal tensile stress was estimated equal to $0.30\sqrt{f_c}$ for JPA-3, $0.26\sqrt{f_c}$ for JPB, and $0.25\sqrt{f_c}$ for JPC.

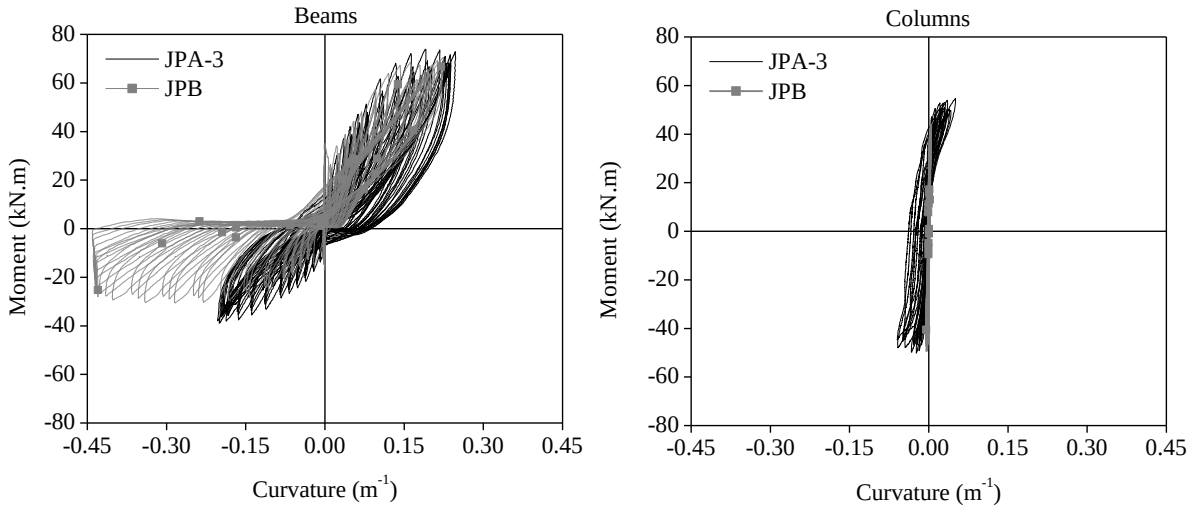

Figure 3.50 - Moment-curvature diagrams of specimens JPA-3 and JPB.

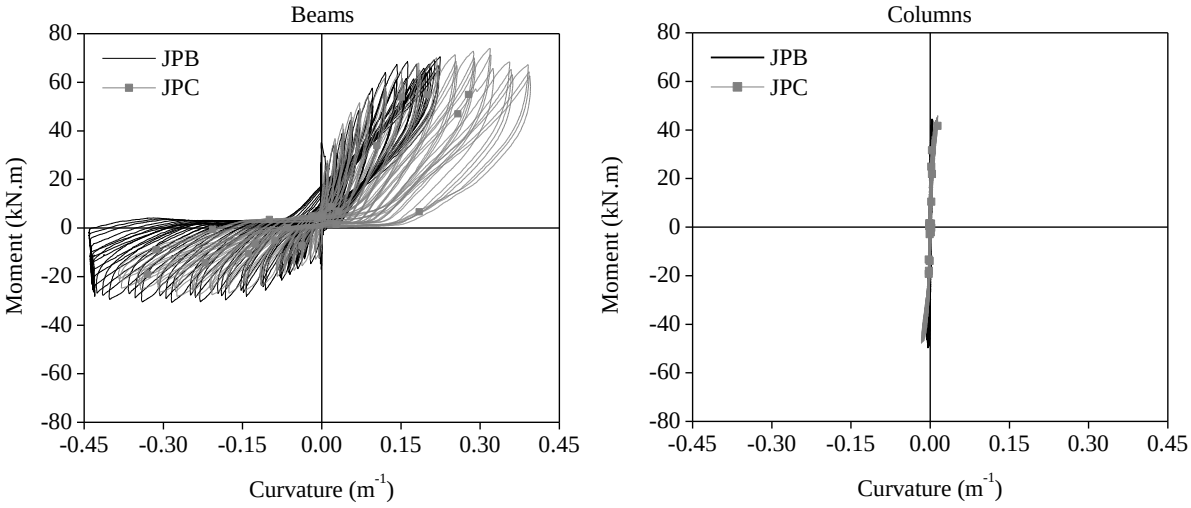

Figure 3.51 - Moment-curvature diagrams of specimens JPB and JPC.

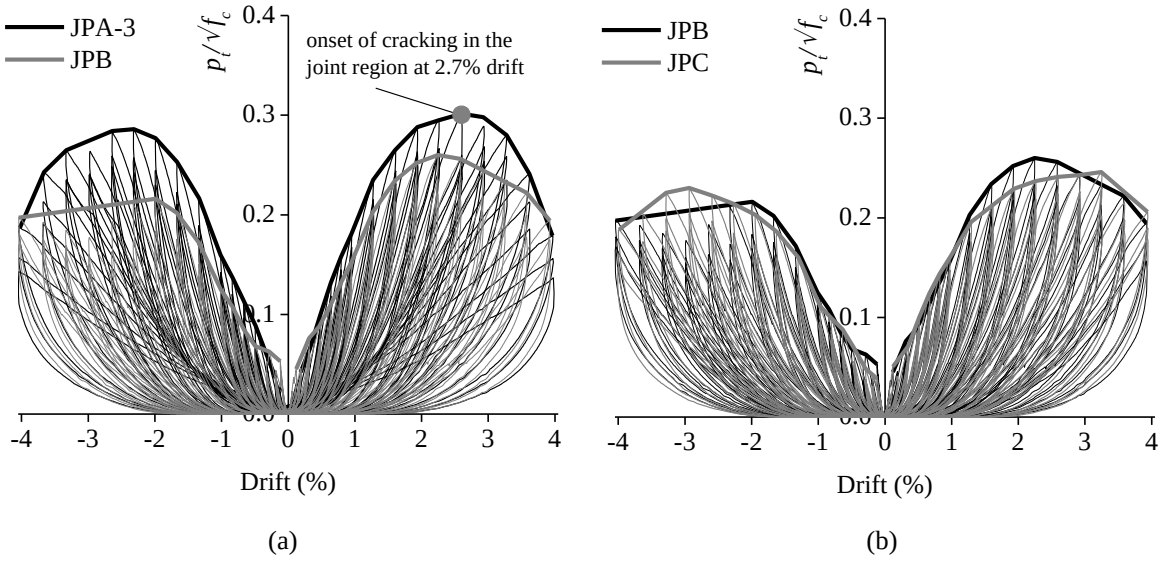

Figure 3.52 - Tensile stress-drift diagrams of specimens: a) JPA-3 and JPB; b) JPB and JPC.

The total energy dissipated by JPB and JPC was significantly lower than that dissipated by JPA-3. Increasing the amount of column longitudinal reinforcement in JPB led to a 35% reduction in the total dissipated energy. Increasing the amount of transverse reinforcement in JPC led to an increase of about 7% in the total dissipated energy in comparison to JPB, hence a 31% reduction in comparison to JPA-3. Within the drift range under analysis, larger ductility demands were imposed on specimens JPB and JPC in comparison to JPA-3.

The comparisons established between JPA-3 and JPB, and JPB and JPC, show that the global response of the specimens was more sensitive to the increase in amount of column

longitudinal reinforcement than to the increase in amount of transverse reinforcement (in the beams and columns).

3.6 - SUMMARY

This chapter described the experimental investigation performed to analyse the cyclic behaviour of substandard full-scale RC interior beam-column joints built with plain reinforcing bars. Five joint specimens with plain bars, and one additional joint specimen with deformed bars, were tested under reversed cyclic loading imposed on the specimens under displacement controlled conditions. The influence of displacement history, column axial load, bond properties, and amount of steel reinforcement was investigated. From the comparisons established between the tests results, the following conclusions can be drawn:

- The joint specimen with plain reinforcing bars and standard amount of steel reinforcement, and subjected to the higher level of column axial load displayed the largest lateral strength and also the greatest strength degradation after the maximum lateral load. Within the drift range under analysis, only for this specimen was registered the conventional failure condition corresponding to 20% reduction in strength. Small differences in stiffness were registered between the joint specimens with plain reinforcing bars. The pinching effect was evident for all the tested specimens, being less important for the joint specimen with deformed bars and particularly evident in the response of the two joint specimens with plain bars and larger amount of steel reinforcement.
- For the joint specimen with deformed bars, EC2 provided a good estimate of the elements' flexural strength, overestimating the beams' strength in about 9% and underestimating the columns' strength in 3%. Conversely, for the joint specimens with plain reinforcing bars the EC2 expressions overestimated the elements' strength in about 13% to 33%.
- Damage in the joint specimens with plain reinforcing bars was mainly concentrated at the beam-joint and column-joint interfaces, and only for the specimen with standard amount of steel reinforcement and higher level of column axial load was developed diagonal tension cracking in the joint region. Conversely, a more spread

damage distribution was observed for the joint specimen with deformed bars, with cracking along the elements length and significant damage in the joint region. The differences in damage distribution between the joint specimens with plain and deformed reinforcing bars are directly related to the concrete-steel bond properties.

- Within the drift range under analysis, the largest energy dissipation was determined for the joint specimen with plain reinforcing bars and standard amount of steel reinforcement, and with higher level of column axial load. For all the tested specimens, the total energy dissipation was mainly associated with the beams deformation. The evolution of the relative contribution of the beams and columns to the total energy dissipation is in agreement with the damage evolution in the specimens.
- The ultimate rotation capacity predicted by EC8-3 together with the failure condition corresponding to 20% reduction in strength did not provide a good estimate of the ultimate rotation capacity of the joint specimens subjected to the drift range and loading conditions imposed in the cyclic tests.
- The equivalent damping-ductility analysis shows that the highest ductility demands were imposed on the joint specimen with deformed bars, and the lowest ductility demands were imposed on the joint specimen with plain reinforcing bars and standard amount of steel reinforcement, and with higher level of column axial load.
- The influence of displacement history was concluded to be minor.
- The influence of column axial load was mainly observed in terms of lateral strength, damage distribution and energy dissipation. The lateral strength was significantly increased, as well as the total energy dissipated by the specimen. The relatively higher shear demands in the joint region led to diagonal tension cracking in the joint, which contributed to the relatively larger strength degradation after the maximum lateral load.
- The influence of bond properties was particularly shown by the differences observed in the damage distribution of the two analogous joint specimens, one with plain bars and the other with deformed bars. Conversely to the more widely spread damage distribution in the joint specimen with deformed bars, the joint specimen with plain bars displayed damage concentrated at the beam-joint and column-joint

interfaces. Accordingly, larger energy dissipation was displayed by the specimen with deformed bars. Better bond properties also led to an increase in the global lateral strength.

- The influence of the amount of steel reinforcement, in particular of the longitudinal reinforcement in the columns, was mainly shown by the differences observed in terms of damage distribution. In the two joint specimens with larger amount of steel reinforcement, damage was mainly concentrated at the beam-joint interfaces. Damage in the columns was minor. Therefore, the drift imposed on the specimens with larger amount of steel reinforcement was mainly contributed by the beams deformation. As a result of the poor damage distribution, as well of the marked pinching effect, the energy dissipation associated with these two specimens was significantly lower than that associated with the specimen with standard amount of steel reinforcement. Increasing the amount of column longitudinal reinforcement had a more significant influence than increasing the amount of transverse reinforcement in the elements.

CHAPTER 4

NUMERICAL MODELLING OF THE BEAM-COLUMN JOINTS

4.1 - INTRODUCTION

This chapter addresses the numerical modelling of the cyclic behaviour of the two analogous RC beam-column joint specimens described in Chapter 3, one with plain bars (JPA-1) and the other with deformed bars (JD), both tested under the same lateral displacement history and with the same level of column axial load. Nonlinear fibre-based models of the joint specimens were built using the SeismoStruct software [1], and calibrated with the experimental results. A simple strategy was adopted to incorporate the bond-slip effects in the numerical modelling.

Firstly, a model was calibrated for the joint specimen with deformed bars without taking into account the bond-slip mechanism. Then, the calibrated model was adopted to simulate the response of the joint specimen with plain bars and only the yield strength of the steel reinforcement was changed. This analysis allowed checking how inadequate it was to model the response of the joint specimen with plain bars without taking into account the effects of bar slippage.

Secondly, and only for the joint specimen with plain bars, nonlinear rotational springs were incorporated in the model to include the bond-slip effects.

The comparisons established between the numerical and experimental results allowed to conclude about the importance of considering bond-slip, and also check the adequacy of the strategy adopted to incorporate its effects in the numerical modelling of the joint specimen with plain bars.

4.2 - NUMERICAL MODEL WITHOUT BOND-SLIP EFFECTS

4.2.1 - Modelling strategy

The numerical modelling was conducted with the Seismostruct software. SeismoStruct is an internet downloadable finite element package, capable of predicting the large displacement behaviour of space frames under static or dynamic loading, taking into account both geometric nonlinearities and material inelasticity.

Seismostruct provides two main types of inelastic beam/column elements: displacement-based (DB) and force-based (FB) frame elements, both with distributed inelasticity; and, plastic hinge frame elements featuring a distributed inelasticity force-based formulation similar to that associated with the FB elements, but concentrating such inelasticity within a fixed length of the element (plastic hinges). The elements' cross-section is idealized through fibre modelling. Each fibre is associated with a uniaxial stress-strain relationship. The sectional stress-strain state of the elements is then obtained through the integration of the nonlinear uniaxial stress-strain response of the individual fibres in which the section has been subdivided. There is no need to introduce the rules of hysteretic behaviour since they are implicitly defined by the material constitutive model.

Figure 4.1 depicts the model adopted to simulate the response of the joint specimens. In the model, each structural element is represented by five DB inelastic frame elements. The two DB elements immediately after each interface with the joint region are representative of the regions defined as slice 1 and slice 2 in the cyclic tests (length of slice 1 equal to 0.10 m and length of slice 2 equal to 0.18 m). The cross-section of the DB elements was divided into 250 longitudinal fibres. The cross-sectional dimensions and steel reinforcement detailing were made equal to those described in Chapter 3 for specimens JPA-1 and JD. The support conditions in the numerical model are also representative of those adopted in the cyclic tests (simple supports in the beams and pinned support in the inferior column).

The joint region was modelled as rigid. This assumption can be considered adequate in the case of the joint specimen with plain reinforcing bars since the damage was concentrated at the beam-joint and column-joint interfaces. Regarding the joint specimen with deformed bars, the experimental results (namely the observed damage) indicate that joint shear

deformation should not be neglected. However, for comparison with specimen JPA-1, and considering that the numerical analyses herein presented intended to focus on the effects of the bond-slip mechanism, the rigid joint assumption was also adopted for specimen JD.

As previously stated, first, the model was calibrated for the joint specimen with deformed bars. Afterwards, the calibrated model was adopted to simulate the response of the joint specimen with plain reinforcing bars and only the yield strength of the steel reinforcement was changed.

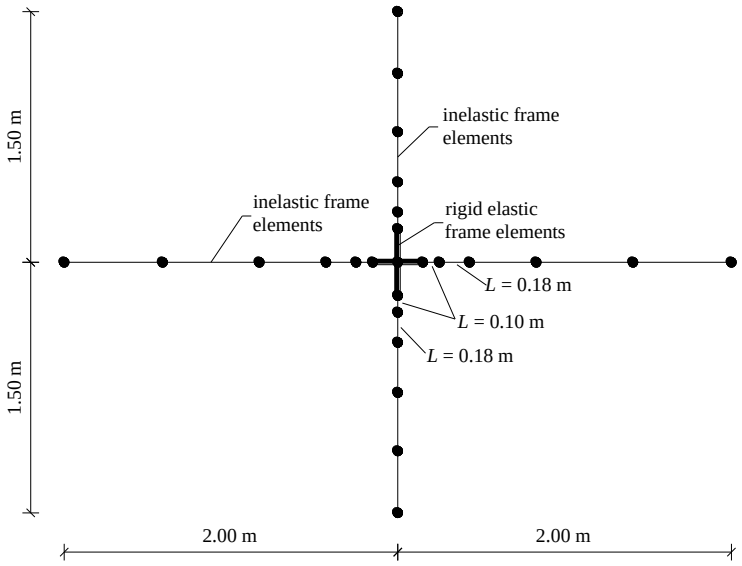

Figure 4.1 - Model adopted to simulate the response of the beam-column joint specimens.

4.2.2 - Material models

Concrete

Figure 4.2 depicts the material model adopted for the concrete. The model follows the constitutive relationship proposed by Mander *et al.* [2] and the cyclic rules proposed by Martinez-Rueda and Elnashai [3]. The confinement effects provided by the lateral transverse reinforcement are incorporated through the rules proposed by Mander *et al.* [2] whereby constant confining pressure is assumed throughout the entire stress-strain range. In SeismoStruct, the concrete model parameters are: compressive strength (f_c); tensile strength (f_t); strain at peak stress (ε_c); confinement factor (k_c); and, specific weight (γ). The confinement factor was automatically computed by SeimoStruct based on the input values

of the cross-sectional dimensions and properties of longitudinal and transverse reinforcing bars.

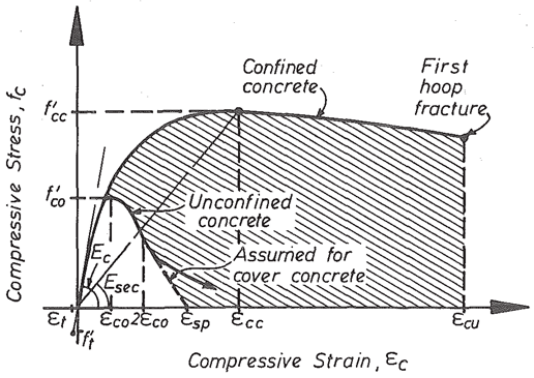

Figure 4.2 - Stress-strain model for monotonic loading of confined and unconfined concrete proposed by Mander *et al.* [2].

Table 4.1 gives the values adopted for the concrete model parameters. As stated in Chapter 3, the mean value of concrete compressive strength was determined from compression tests on concrete cubic samples. The concrete strength in SeismoStruct refers to the cylinder compressive stress capacity. The value adopted for the concrete compressive strength is equal to 19 MPa (80% of the mean value of strength registered in the compression tests). According to the software instructions, the concrete tensile stress can be usually estimated as $f_t=k_t\sqrt{f_c}$, where k_t varies from 0.5 (concrete in direct tension) to 0.75 (concrete in flexural tension), as suggested by Priestley *et al.* [4]. The concrete tensile stress was made equal to 2.9 MPa, which corresponds to $0.67\sqrt{f_c}$.

Table 4.1 - Values adopted for the concrete model parameters

Concrete	f_c (MPa)	f_t (MPa)	ε_c (mm/mm)	k_t	γ (kN/m^3)
Unconfined	19.0	2.9	0.0022	1	24
Confined				1.04	

Steel reinforcement

Figure 4.3 depicts the material model adopted for the steel reinforcement. The model is based on the Menegotto-Pinto model [5] coupled with the isotropic hardening rules proposed by Filippou *et al.* [6]. In SeismoStruct, the model parameters are: modulus of elasticity (E_s); yield strength (f_y); strain hardening parameter (μ); transition curve initial shape parameter (*R0*); transition curve shape calibrating coefficients (*a1* and *a2*); isotropic

hardening calibrating coefficients (*a3* and *a4*); fracture/buckling strain (ε_{ult}); and, specific weight (γ).

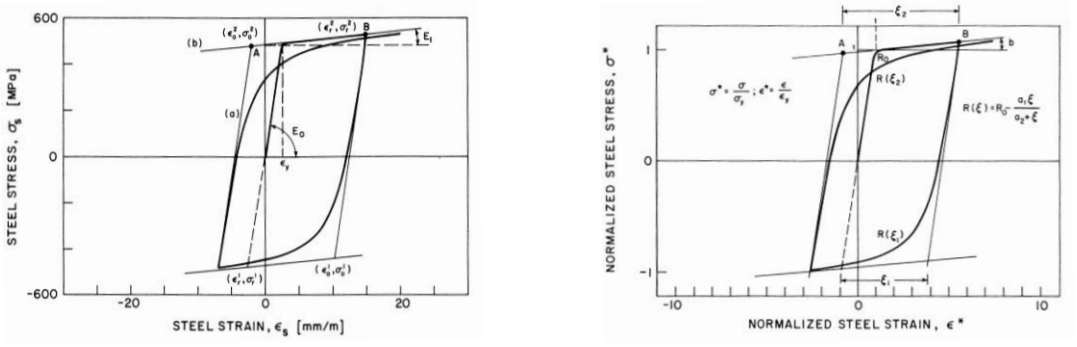

(a) (b)

Figure 4.3 - Menegotto-Pinto steel model (a) and definition of curvature parameter *R* [6] (b).

Table 4.2 gives the values adopted for the steel model parameters, as well as the corresponding value or range of values recommended in SeismoStruct. As previously stated, the values adopted for the steel model parameters in the numerical model of the joint specimen with plain bars (JPA-1) were made equal to those adopted in the numerical model of the joint specimen with deformed bars (JD), with exception of the yield strength. For specimen JD, the yield strength was made equal to 455 MPa (5% lower than that indicated in Chapter 3). For specimen JPA-1, the yield strength was made equal to 590 MPa (mean value indicated in Chapter 3). Following the recommendations of SeismoStruct, isotropic hardening was disabled, that is, parameters *a3* and *a4* were made equal to 0 and equal to 1 respectively.

Table 4.2 - Values adopted for the steel model parameters

Model parameter	Recommended value/range	Adopted value	
		Deformed bars (JD)	Plain bars (JPA-1)
E (GPa)	-	200	
f_y (MPa)	-	455	590
μ	0.005 - 0.015	0.008	
R0	-	19.5	
a1	18.5	18.8	
a2	0.05 - 0.15	0.15	
a3	0.01 - 0.025	0	
a4	2 - 7	1	
ε_{ult}	-	0.1	
γ (kN/m^3)	-	78	

4.2.3 - Loading pattern

Figure 4.4 depicts the loading conditions imposed on the joint specimens in the numerical models. The numerical loading conditions simulate those imposed in the cyclic tests. Thus, they consisted of: constant column axial load, equal to 197 MPa (mean value registered in the cyclic tests); and, lateral displacement history (d_{top}) equal to that adopted in the cyclic tests, imposed on the end node of the superior column. In addition, a lateral displacement history equal to $d_{top}/2$ was imposed on the central node to guarantee that both the superior and inferior columns were subjected to the same lateral displacement demands.

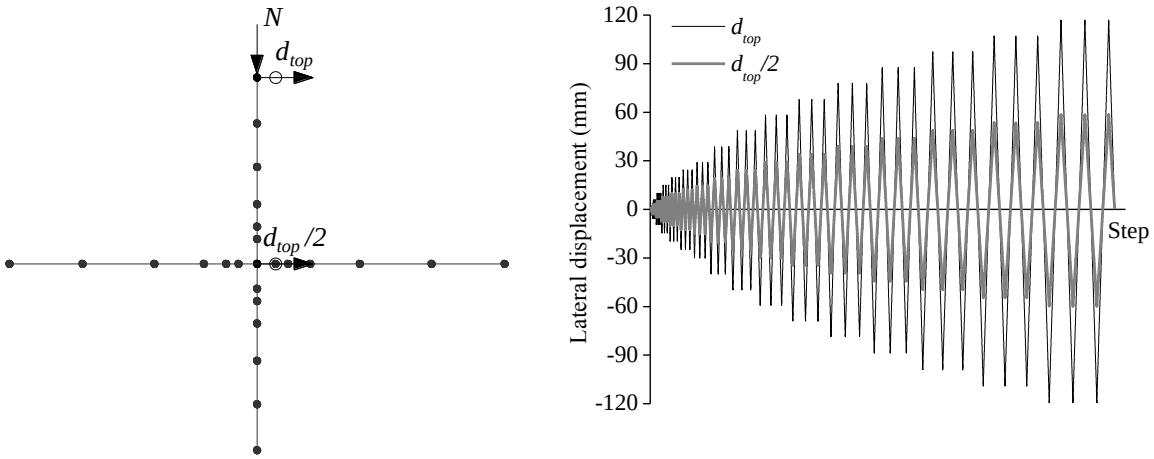

Figure 4.4 - Loading conditions in the numerical models.

4.2.4 - Comparison between the numerical and experimental results of the joint specimen with deformed bars

Figure 4.5 depicts the comparison between the numerical and experimental lateral load-drift diagrams of specimen JD, showing that:

i) In general terms, the numerical model provides a good simulation of the experimental lateral load-drift envelope, namely in terms of tangent stiffness and maximum lateral load. However, the model does not represent the strength degradation. The pinching effect is also not well simulated, being relatively less severe in the numerical response.

ii) The numerical and experimental values of maximum lateral load are similar. However, the numerical maximum lateral load is reached at 1.3% drift while in the cyclic test it was registered at 2.0% drift.

iii) The numerical initial stiffness is 1.6 times the experimental initial stiffness.

iv) The stiffness of the reloading branches is significantly overestimated.

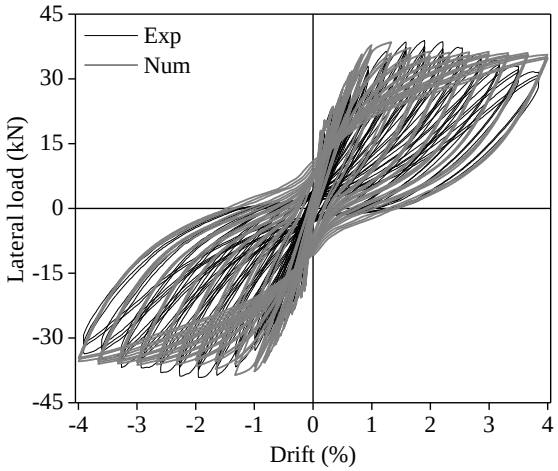

Figure 4.5 - Lateral load-drift diagrams of specimen JD (experimental and numerical).

Figure 4.6 compares the numerical and experimental evolutions of dissipated energy. The significant overestimation of the reloading stiffness and the relatively poor representation of the pinching effect led to a poor simulation of the dissipated energy evolution, particularly after 1.5% drift. At the maximum imposed drift, the numerical dissipated energy is 2.4 times the experimental energy.

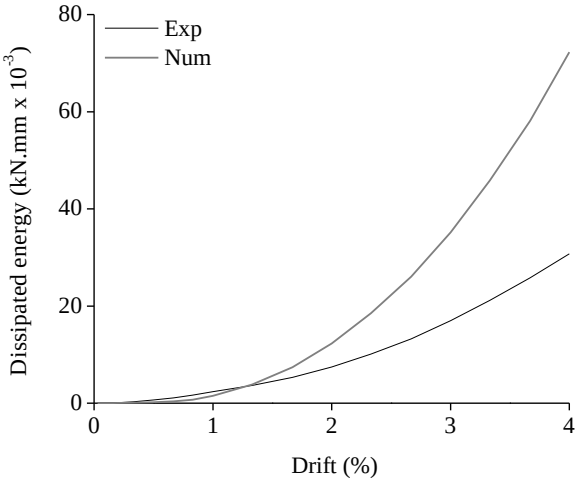

Figure 4.6 - Evolution of dissipated energy for specimen JD (experimental and numerical).

In the numerical model, the onset of cracking in the beams occurs at 0.1% drift, as in the cyclic test. The onset of cracking in the columns occurs at 0.2% drift, while in the cyclic test it occurred at 0.3% drift.

In the numerical model, cracking of the unconfined concrete occurs along 68% of the beams' length and 72% of the columns' length. In the cyclic test, cracking in the beams also occurred approximately along 68% of the beams' length, and cracking in the columns occurred approximately along 38% of the columns' length. Therefore, a better agreement between the numerical and experimental cracking distributions was determined for the beams.

Figure 4.7 and Figure 4.8 compare the numerical moment-curvature diagrams plotted for the middle section of slices 1 and 2 in the beams and columns respectively, with the corresponding moment-curvature diagrams determined from the experimental results (Chapter 3). As stated in Chapter 3, the curvatures correspond to the mean curvatures estimated for the slice under analysis.

Regarding the beams, the numerical model does not reproduce well the moment-curvature relationship of slice 1. Despite the similarity between the numerical and experimental values of maximum moments, the curvature demands are significantly lower in the numerical response. At the maximum drift, the numerical curvature of slice 1 is 22% and 29% of the experimental curvature in the positive moment direction and negative moment direction respectively. For slice 2, the numerical and experimental moment-curvature relationships are similar.

Regarding the columns, the moment-curvature relationship in slice 1 is relatively better reproduced. The numerical and experimental values of maximum moment are similar. At the maximum drift, the numerical curvature of slice 1 is 20% higher in one direction, and 42% higher in the other direction, than the corresponding experimental curvature. For slice 2, the numerical and experimental moment-curvature relationships are in good agreement.

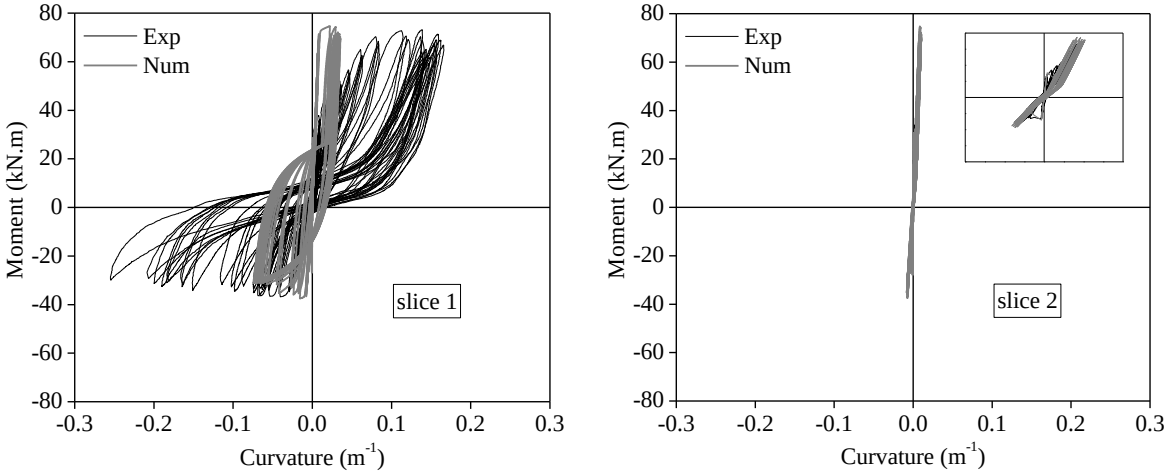

Figure 4.7 - Moment-curvature diagrams of the beams for specimen JD (experimental and numerical).

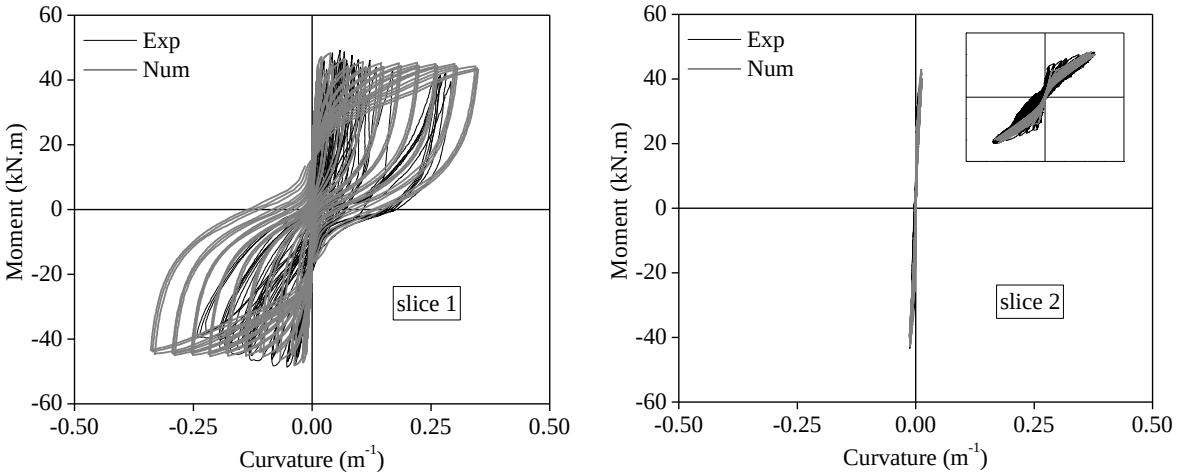

Figure 4.8 - Moment-curvature diagrams of the columns for specimen JD (experimental and numerical).

4.2.5 - Comparison between the numerical and experimental results of the joint specimen with plain reinforcing bars

Figure 4.9 depicts the comparison between the numerical and experimental lateral load-drift diagrams of specimen JPA-1, showing that:

i) The numerical model provides a poor simulation of the experimental lateral load-drift envelope, considerably overestimating the maximum lateral load and the tangent stiffness. The strength degradation is not represented. The pinching effect

in the numerical response is significantly less severe than that in the experimental response.

ii) The numerical maximum lateral load (reached at 1.3% drift) is 32% higher than the experimental maximum lateral load (at 3.3% drift).

iii) The numerical initial stiffness is 10% higher than the experimental initial stiffness.

iv) The numerical model does not represent well the stiffness of the reloading and unloading branches. In both cases, the numerical stiffness is significantly larger than the experimental stiffness.

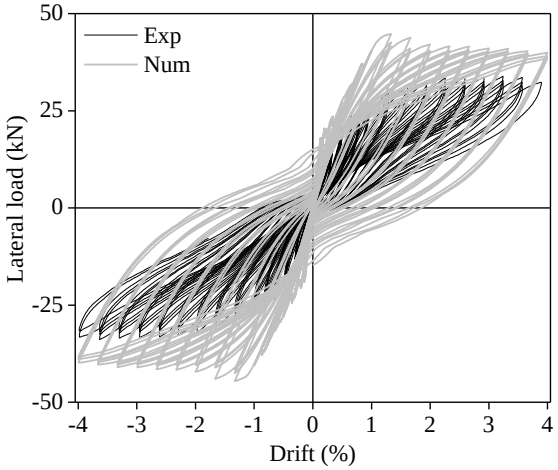

Figure 4.9 - Lateral load-drift diagrams of specimen JPA-1 (experimental and numerical).

Figure 4.10 compares the numerical and experimental evolutions of dissipated energy. The significant overestimation of stiffness and strength, and the poor representation of the pinching effect, led to a poor simulation of the dissipated energy evolution. At the maximum imposed drift, the numerical dissipated energy is 2.7 times the experimental energy.

In the numerical model, the onset of cracking in the beams (at 0.1% drift) occurs at a drift level close to that registered in the cyclic test (0.07% drift). Conversely, the onset of cracking in the columns (at 0.1% drift) occurs at a drift level significantly inferior to the experimental (0.8% drift).

In the numerical model, cracking of the unconfined concrete occurs along approximately the entire length of the beams and columns. In the cyclic test, cracking in the beams and

columns of specimen JPA-1 was heavily concentrated at the beam-joint and column-joint interfaces respectively. Therefore, the numerical and experimental cracking distributions are not in agreement.

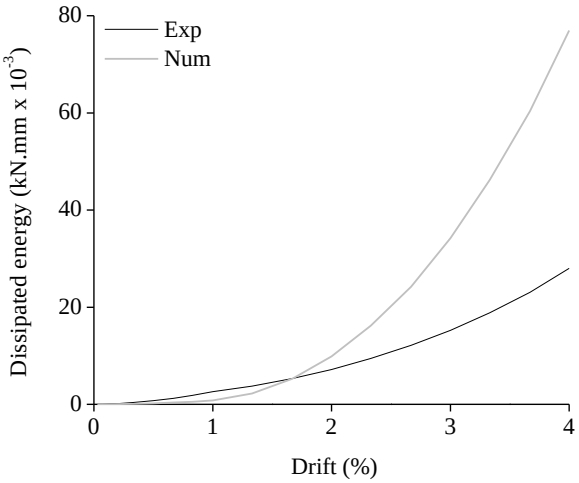

Figure 4.10 - Evolution of dissipated energy for specimen JPA-1 (experimental and numerical).

Figure 4.11 and Figure 4.12 compare the numerical moment-curvature diagrams plotted for the middle section of slices 1 and 2 in the beams and columns respectively, with the corresponding moment-curvature diagrams determined from the experimental results. Regarding the beams, and similarly to what was previously concluded for specimen JD, the numerical model does not reproduce well the moment-curvature relationship of slice 1. The maximum moment is overestimated in 23% in the positive moment direction, and in 36% in the negative moment direction. The curvature demands are significantly lower in the numerical response. At the maximum drift, the numerical curvature of slice 1 in the beams is only 5% and 13% of the experimental curvature in the positive and negative moment directions respectively.

Regarding the columns, the numerical maximum moment of slice 1 is 32% higher than the experimental. At the maximum drift, the experimental curvature of slice 1 is overestimated in 90% in one direction and in 47% in the other direction.

The moment-curvature relationships of slice 2 are also not reproduced well, for both the beams and columns.

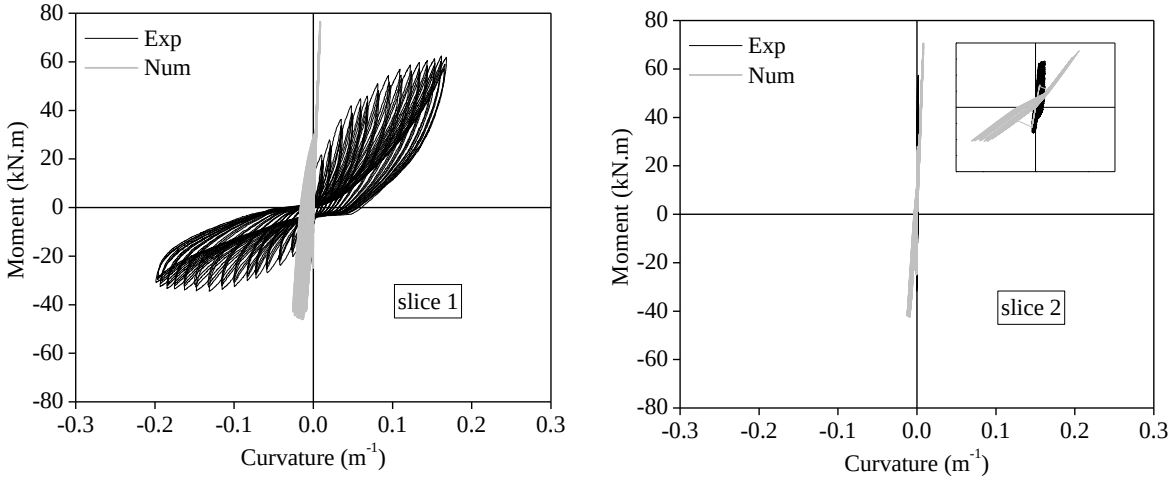

Figure 4.11 - Moment-curvature diagrams of the beams for specimen JPA-1 (experimental and numerical).

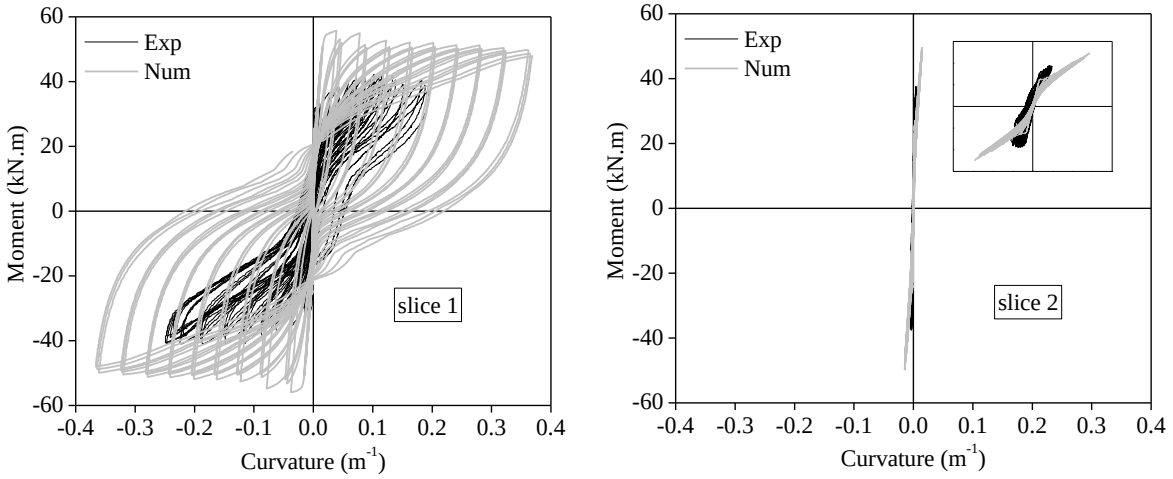

Figure 4.12 - Moment-curvature diagrams of the columns for specimen JPA-1 (experimental and numerical).

Despite the shortcomings of the adopted model to simulate the response of the joint specimen with deformed bars (Section 4.2.4), the differences between the numerical and experimental results (in terms of maximum lateral load, stiffness, pinching effect, moment-curvature relationships, cracking distribution and even dissipated energy) are considerably increased when the same model is used to simulate the response of the analogous joint specimen with plain reinforcing bars.

4.3 - NUMERICAL MODEL WITH BOND-SLIP EFFECTS

4.3.1 - Modelling strategy

As stated in Chapter 2, among the various models proposed in the literature to simulate the cyclic response of beam-column joints, one of the most commonly adopted, and simple, strategies for incorporating the effects of bar slippage (namely, fixed-end rotations) consists in placing nonlinear springs at the elements ends.

Based on the joint model proposed by Lowes and Altoontash [7] (Figure 4.13-a), Yu [8] proposed the simple joint model depicted in Figure 4.13-b for the simulation of the cyclic behaviour of interior beam-column joint specimens, the numerical analysis of which was also carried out with the SeismoStruct software. The model consists of nine components: four rotational springs fitted in the beam-joint and column-interfaces, to model the rotation of the cross-section due to bar slippage; four interface-shear springs, to model the shear-transfer failure at the beam-joint and column-joint interfaces; and, one rotational spring fitted in the centre of the shear panel zone, to model the relative rotation between beams and columns.

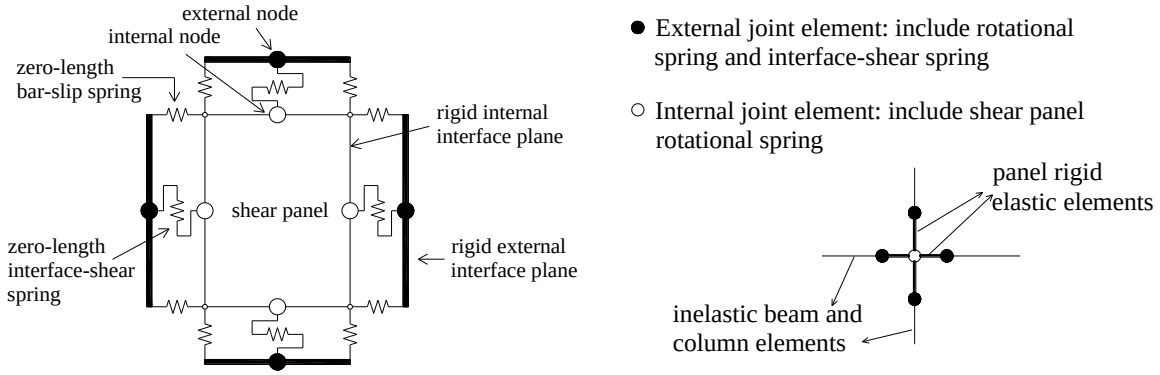

Figure 4.13 - Joint model by: a) Lowes and Altoontash (adapted from [7]); b) Yu (adapted from [8]).

Based on the modelling strategy proposed by Yu [8], rotational springs, fitted in the beam-joint and column-joint interfaces, were implemented in the model previously adopted to simulate the response of the joint specimen with plain reinforcing bars (JPA-1). The interface-shear springs and shear panel rotational spring that also constitute the model proposed by Yu [8] were not included in the model of specimen JPA-1 since the objective

of the analysis was to evaluate the influence of taking into account the effects of bar slippage. Moreover, as previously stated, damage in JPA-1 was concentrated at the beam-joint and column-joint interfaces, thus being appropriate to assume that joint shear deformation was minor. The model with the rotational springs is depicted in Figure 4.14.

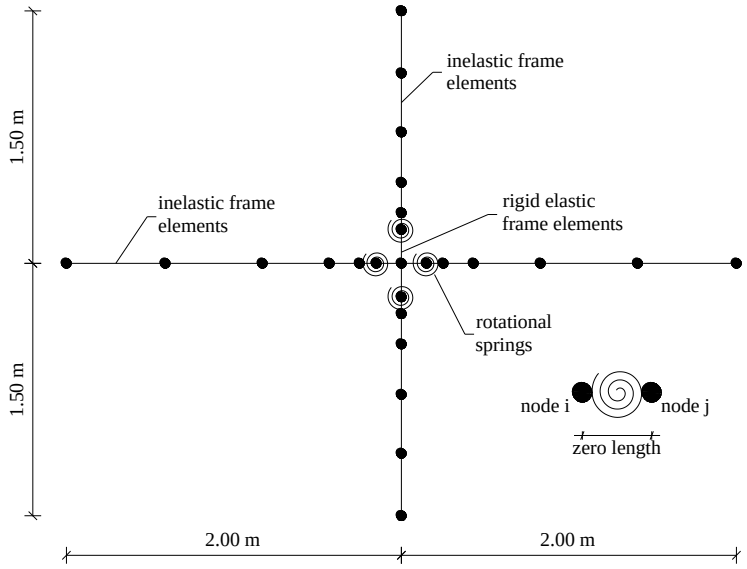

Figure 4.14 - Model with rotational springs.

In SeismoStruct, the springs are modelled by defining 3D link elements with uncoupled axial, shear and moment actions. The link elements connect two initially coincident structural nodes and require the definition of an independent force-displacement (or moment-rotation) response curve for each of its local six degrees of freedom. In the model of specimen JPA-1, the moment-rotation relationship of each spring (Section 4.3.3) was only assigned to the degree of freedom corresponding to the on-plane rotation of the elements.

4.3.2 - Material models

The values adopted for the parameters of the concrete and steel material models are those previously presented in Section 4.2.2 for specimen JPA-1.

4.3.3 - Calibration of the rotational springs

Model background

The joint model proposed by Lowes and Altoontash [7], which is currently implemented in the Open System for Earthquake Engineering Simulation software (OpenSees [9]), includes a general one-dimensional constitutive model (force-displacement response envelope, unload-reload paths and damage rules) for the springs. This model is not available in SeismoStruct. Therefore, in the numerical analyses carried out by Yu [8], the simplified bilinear Takeda response curve available in SeismoStruct was adopted to model the force-deformation response of the bar slip rotational springs. The corresponding moment-rotation relationships were derived from the bar stress versus bar slip relationship and bar stress versus spring force relationship proposed by Lowes and Altoontash [7], described in the next paragraphs. Figure 4.15 summarizes the methodology adopted by Yu [8].

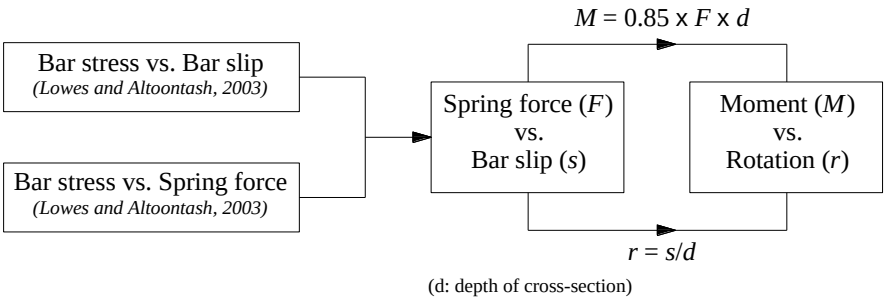

Figure 4.15 - Derivation procedures of the moment-rotation relationships of the bar slip rotational springs in the joint model proposed by Yu [8].

The constitutive model proposed by Lowes and Altoontash [7] was developed to simulate the load-deformation history of the bond-slip springs that simulate inelastic anchorage-zone response. The model was calibrated based on experimental data regarding the testing of anchorage-zone specimens with deformed bars, and considering the following assumptions about the bond stress distribution within the joint region [7]: i) bond stress along the anchored length of a reinforcing bar is uniform for reinforcement that remains elastic or piecewise uniform for reinforcement loaded beyond yield; ii) slip defines the relative movement of the reinforcing bar with respect to the perimeter of the joint and is function of the strain distribution along the bar; and, iii) the bar exhibits zero slip at the point of zero bar stress. Based on these assumptions, Lowes and Altoontash [7] proposed

Equations (4.1) and (4.2) to define the bar stress versus slip relationship, where: f_s is the bar stress at the joint perimeter; f_y is the steel yield strength; E is the steel elastic modulus; E_h is the strain hardening modulus assuming a bilinear stress-strain response; τ_E is the bond strength for elastic steel; τ_Y is the bond strength for yielded steel; A_b is the nominal bar area; and, d_b is the nominal bar diameter. In Equations (4.3), l_e and l_y stand for, respectively, the lengths along the reinforcing bar for which steel stress is less than and greater than the yield stress.

$$f_s < f_y : slip = 2 \cdot \frac{\tau_E}{E} \cdot \frac{l_{fs}^{\,2}}{d_b} \tag{4.1}$$

$$f_s \geq f_y : slip = 2 \cdot \frac{\tau_E}{E} \cdot \frac{l_e^{\,2}}{d_b} + \frac{f_y}{E} \cdot l_y + 2 \cdot \frac{\tau_Y}{E_h} \cdot \frac{l_y^{\,2}}{d_b} \tag{4.2}$$

with

$$l_{fs} = \frac{f_s}{\tau_{ET}} \cdot \frac{A_b}{\pi \cdot d_b} \qquad l_e = \frac{f_y}{\tau_{ET}} \cdot \frac{A_b}{\pi \cdot d_b} \qquad l_y = \frac{f_s - f_y}{\tau_{YT}} \cdot \frac{A_b}{\pi \cdot d_b} \tag{4.3}$$

The bond strength values involved in the bar slip computation are calculated according to Table 4.3, where the concrete compressive strength (f_c) is expressed in MPa.

Table 4.3 - Average bond strengths as function of steel stress state [7]

Bar stress	Average bond strength (MPa)
Tension, $f_s < f_y$	$\tau_{ET} = 1.8\sqrt{f_c}$
Tension, $f_s > f_y$	$\tau_{YT} = 0.4\sqrt{f_c}$ to $0.05\sqrt{f_c}$
Compression, $-f_s < f_y$	$\tau_{EC} = 2.2\sqrt{f_c}$
Compression, $-f_s > f_y$	$\tau_{YC} = 3.6\sqrt{f_c}$

In the joint model proposed by Lowes and Altoontash [7] the tensile and compressive spring forces equilibrate the axial and flexural loads carried by the beams and columns framing into the joint. The bar stress defines the load carried by the longitudinal reinforcing bars that is transferred into the joint core through bond. For the case of a tensile spring force, Lowes and Altoontash [7] assume that the total spring force is carried by the

steel reinforcement. For a compressive spring force, the load is distributed between concrete and steel hence only a fraction of the total spring force is transferred into the joint through bond. Lowes and Altoontash [7] use Equation (4.4) to compute the compressive spring force ($F_{spring,C}$), where: C_s' is the steel compression resultant; C_c is the concrete compression resultant; f_s is bar stress; f_c is the nominal concrete compressive strength; w is the width of the cross-section; d is the depth to the tension reinforcement; d' is the depth to centroid of the compression reinforcement; E_s is the steel reinforcement elastic modulus; A_s' is the area of steel reinforcement carrying compression; β is a scale factor to account for the use of a uniform concrete compressive stress distribution in place of the true stress distribution; and, $j*d$ is the distance between tension and compression resultants acting on the cross-section (j can be assumed equal to 0.85 for beams and 0.75 for columns [7]).

In the Yu [8] model, the moments associated with the spring forces are computed as stated in Figure 4.15.

$$F_{spring,C} = C_s' + C_c = f_s' \cdot A_s' \cdot \left(1 + \frac{0.85 \cdot f_c \cdot dw}{E_s \cdot A_s'} \cdot \frac{2 \cdot (1 - j)}{0.003 \cdot \beta \cdot \left(1 - \frac{d}{d'} \cdot \frac{\beta}{2 \cdot (1 - j)} \right)} \right) \tag{4.4}$$

The results of the numerical-experimental comparative analysis conducted by Yu [8] concerning the cyclic response of beam-column joint specimens with deformed bars show that the adopted modelling strategy provided a satisfactory simulation of the joint specimens' response. However, two main shortcomings were identified, underlining the need for further improvements in the proposed model [8]: first, the pinching effect was not modelled well; second, there was no descending branch. According to Yu [8], these drawbacks are mainly due to the fact that the constitutive curve adopted for the springs does not display a descending branch.

Modelling strategy adopted

Figure 4.16-a depicts the asymmetric bilinear model adopted for the rotational springs in the beams. This simple model allows taking into account the asymmetric beam behaviour related to the differences in total area of steel reinforcement between the top bars and the

bottom bars. However, it does not feature degradation of either strength or stiffness. The model parameters are: initial stiffness in the positive region (K_0+); yield force (or moment) in the positive region (F_y+); post-yield hardening ratio in positive region (r+); initial stiffness in the negative region (K_0-); yield force (or moment) in the negative region (F_y-); and, post-yield hardening ratio in the negative region (r-).

Figure 4.16-b depicts the model adopted for the rotational springs in the columns. The model consists of a bilinear simplification of the original trilinear model proposed by Takeda *et al.* [10], featuring the unloading rules proposed by Emori and Schonobrich [11], as described in [12]. The model parameters are: yield strength or moment (F_y); initial stiffness (K_y); post yielding to initial stiffness ratio (α); outer loop stiffness degradation factor (β_0); and, inner loop stiffness degradation factor (β_1). The model does not feature strength degradation.

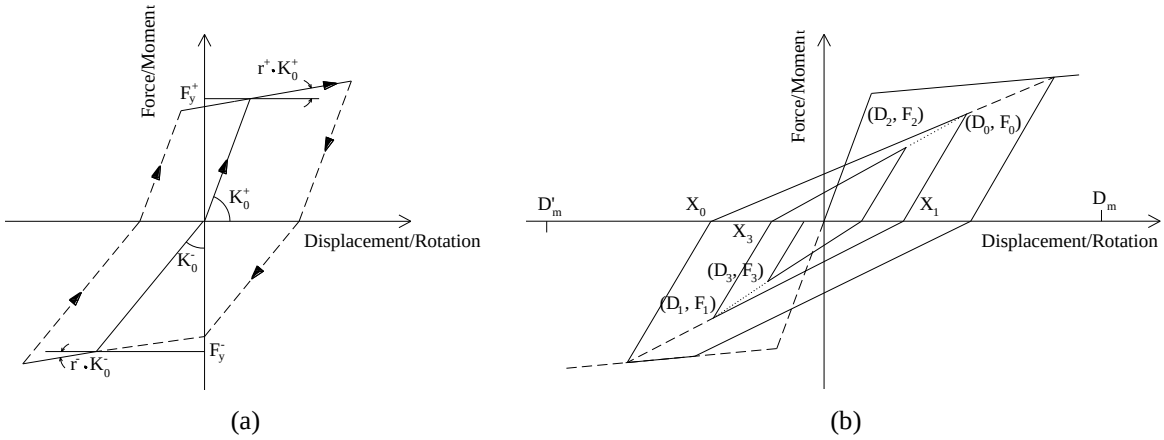

Figure 4.16 - Response curves assigned to the spring elements: a) in the beams (bilinear asymmetric curve); b) in the columns (simplified bilinear Takeda curve).

The model parameters, namely the yielding moment associated with the spring force at yielding (Equation (4.4)) and the initial stiffness (estimated based on the rotation corresponding to bar slip at yielding, given by Equation (4.1)), were computed based on the methodology proposed by Yu [8] (Figure 4.15). However, this methodology applied to the joint specimen under investigation led to a poor simulation of the specimen's response. In comparison to the numerical results obtained from the model without the rotational springs (Section 4.2.5), the effects on the lateral load-drift diagrams were minor both in

terms of stiffness and strength. Alterations in the moment-curvature relationships for both the beams and columns were also insignificant.

As previously stated, the assumptions associated with the method adopted by Yu [8] to calibrate the bar slip rotational springs were established based on experimental data concerning elements with deformed bars, and also assuming the longitudinal reinforcing bars anchored in the joint region. The joint specimen under investigation in this work was built with plain reinforcing bars, for which the nature of the interaction mechanisms between concrete and steel is very different from that in elements with deformed bars. In addition, in JPA-1 the longitudinal reinforcing bars were continuous along the elements length, passing through the joint region. Bar slippage in specimen JPA-1 is expected to have occurred along a larger extension of the steel bars in comparison to that assumed in the Yu [8] model. Therefore, the proposed model was inadequate to simulate the response of specimen JPA-1.

The parameters of the response curves were then calibrated to fit the experimental results. The corresponding values are presented in Table 4.4 and Table 4.5, for the springs in the beams and for the springs in the columns respectively.

Table 4.4 - Values adopted for the model parameters of the rotational springs in the beams

Model parameter	Adopted value
K_0+	4000 kN.m
F_y+	60 kN.m
r+	0.07
K_0-	4000
F_y-	-22 kN.m
r-	0.07

Table 4.5 - Values adopted for the model parameters of the rotational springs in the columns

Model parameter	Adopted value
F_y	41 kN.m
K_y	17000 kN.m
α	0.001
β_0	0.9
β_1	0.9

4.3.4 - Loading pattern

The loading conditions imposed on the joint specimen in the model with the rotational springs are the same that were imposed in the previous model (Section 4.2.3).

4.3.5 - Comparison between the numerical and experimental results

Figure 4.17 depicts the comparison between the numerical and experimental lateral load-drift diagrams of specimen JPA-1, and the comparison between the numerical results obtained with and without considering the bond-slip effects. The comparative analyses show that the numerical model with the rotational springs, thus including bond-slip, provides a satisfactory simulation of the experimental lateral load-drift envelope. The maximum lateral load and the tangent stiffness are considerably better represented when bond-slip effects are taken into account. In particular, the difference in terms of maximum lateral load between the numerical and experimental results is reduced from 32% to 6%. However, strength degradation is not represented.

The stiffness of the reloading branches and stiffness of the unloading branches are also relatively better reproduced when the effects of bar slippage are included in the model.

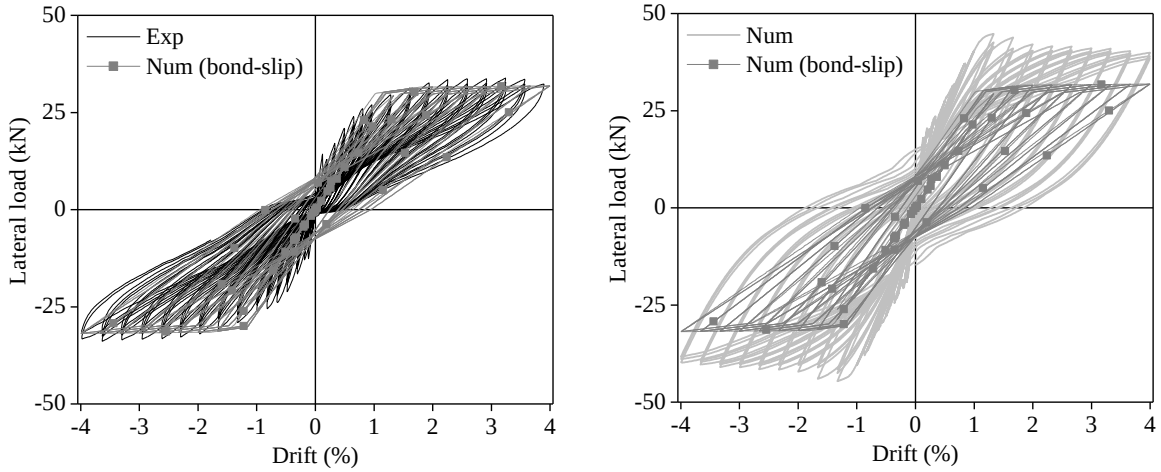

Figure 4.17 - Lateral load-drift diagrams of specimen JPA-1 (experimental and numerical with and without considering bond-slip).

Figure 4.18 compares the numerical (with and without considering bond-slip) and experimental evolutions of dissipated energy. Despite the considerable reduction in dissipated energy (of about 57% at the maximum drift) with respect to that computed from

the numerical results without bond-slip, the numerical model with the springs is also not capable of reproducing well the dissipated energy evolution. This is considered to be mainly related to the models adopted for the rotational springs, namely for the springs in the beams, which feature neither degrading strength nor degrading stiffness. At the maximum imposed drift, the dissipated energy associated with the numerical response with bond-slip effects is 1.6 times the dissipated energy computed from the experimental results.

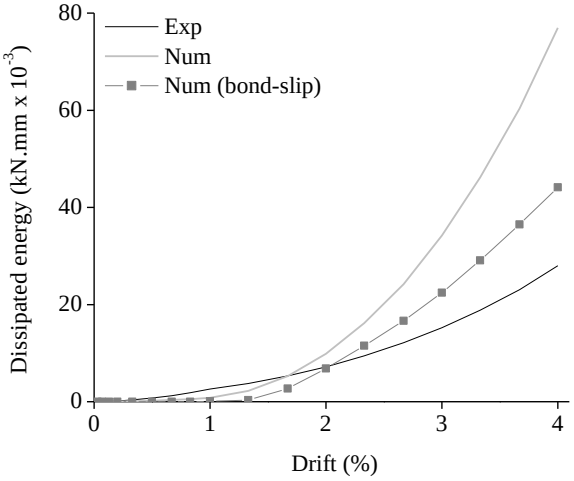

Figure 4.18 - Evolutions of dissipated energy for specimen JPA-1 (experimental and numerical with and without considering bond-slip).

In the numerical model with the rotational springs, cracking of the unconfined concrete is concentrated at the beam-joint and column-joint interfaces, where the rotational springs are located. This is consistent with the experimental observations. From the interface with the joint region to the other element end, the elements response is elastic (which is also confirmed by the moment-curvature diagrams of slice 2, depicted in Figure 4.20 and Figure 4.22).

Figure 4.19 to Figure 4.22 depict the comparison between the numerical and experimental moment-curvature diagrams plotted for the middle section of slice 1 and slice 2 in the beams and columns of specimen JPA-1. Figure 4.19 to Figure 4.22 also depict the comparison between the numerical results with and without considering bond-slip. The comparative analyses show that, by including the bond-slip effects in the numerical model:

i) The differences in maximum moment between the numerical and experimental results are reduced from 23% to 2% for the beams (from 36% to 10% in the negative moment direction), and from 32% to 6% for the columns.

ii) For slice 1 in the beams, the differences in maximum curvature between the numerical and experimental results are reduced from 95% to 2% in the positive moment direction, and from 87% to 10% in the negative moment direction. For slice 1 in the columns, the differences in maximum curvature are reduced from 90% to 37% in one moment direction, and from 47% to 6% in the other moment direction.

iii) The agreement between the numerical and experimental moment-curvature relationships of slice 2 is significantly improved for the beams and columns, both in terms of moment and curvature.

It should be noted that, despite the better approximation to the experimental results attained by including bond-slip in the model of specimen JPA-1, the numerical results (namely the moment-curvature relationships determined for the beams) show the inadequacy of the models adopted for the rotational springs. More adequate models should be hence implemented in SeismoStruct, featuring a more refined envelope curve, as well as appropriate parameters to control the stiffness and strength degradations.

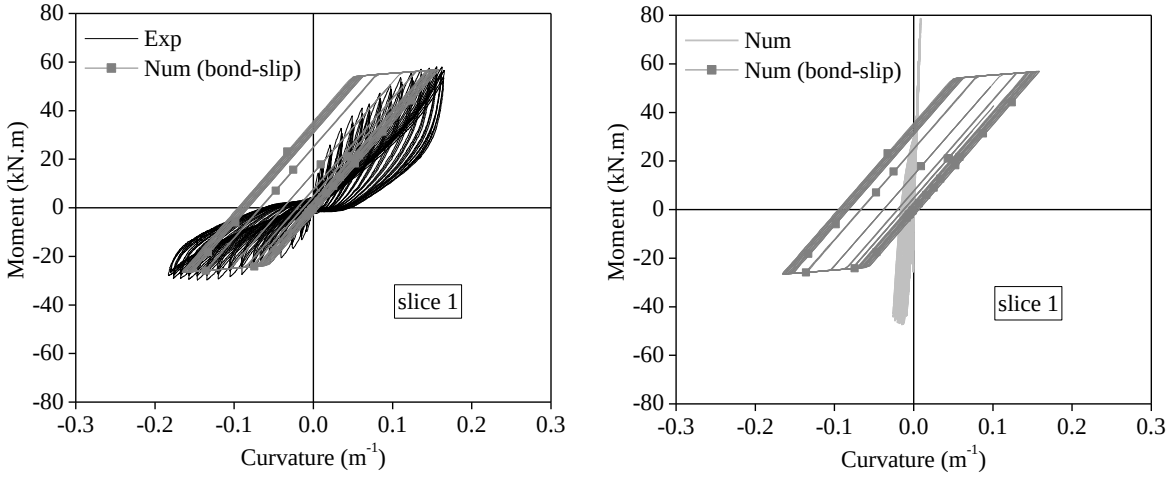

Figure 4.19 - Moment-curvature diagrams of slice 1 in the beams of specimen JPA-1 (experimental and numerical with and without considering bond-slip).

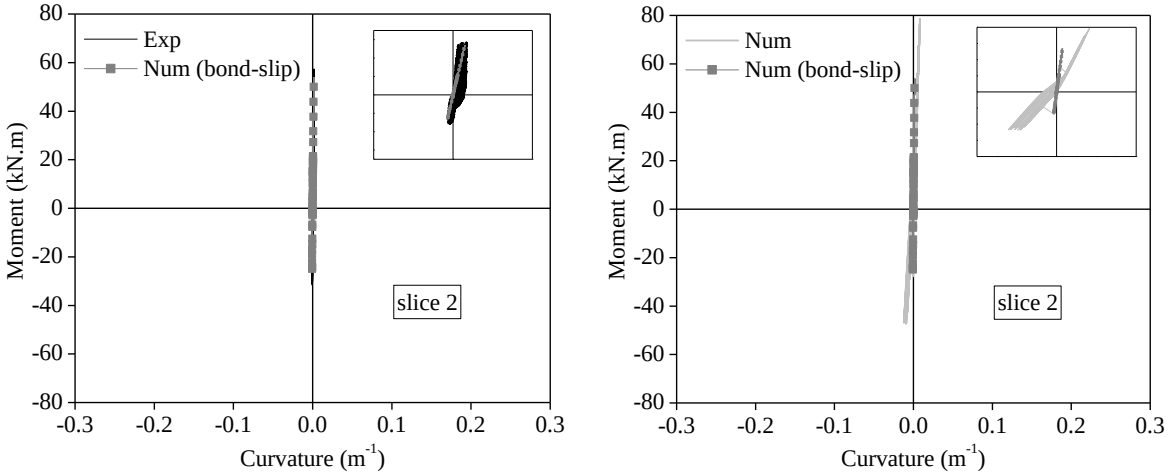

Figure 4.20 - Moment-curvature diagrams of slice 2 in the beams of specimen JPA-1 (experimental and numerical with and without considering bond-slip).

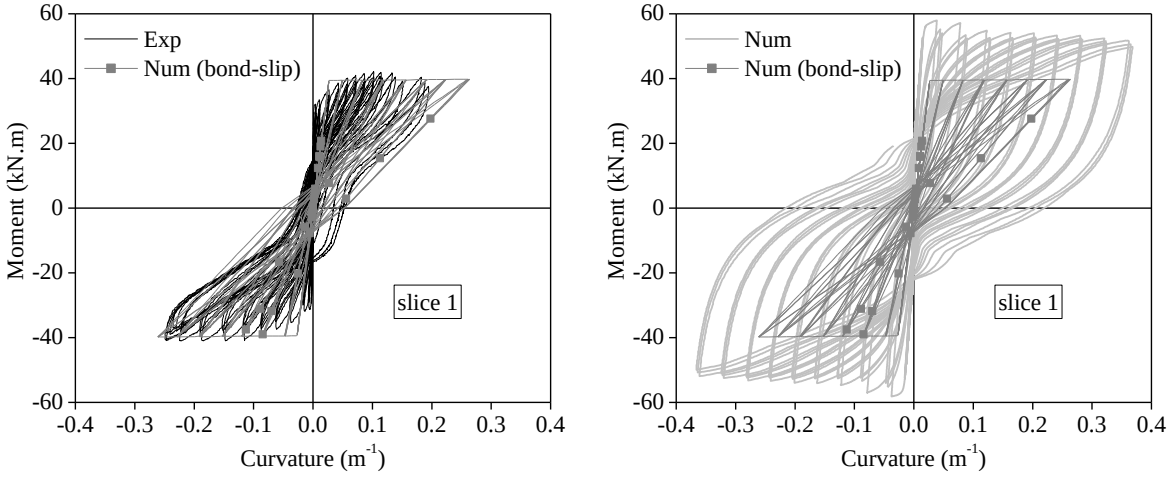

Figure 4.21 - Moment-curvature diagrams of slice 1 in the columns of specimen JPA-1 (experimental and numerical with and without considering bond-slip).

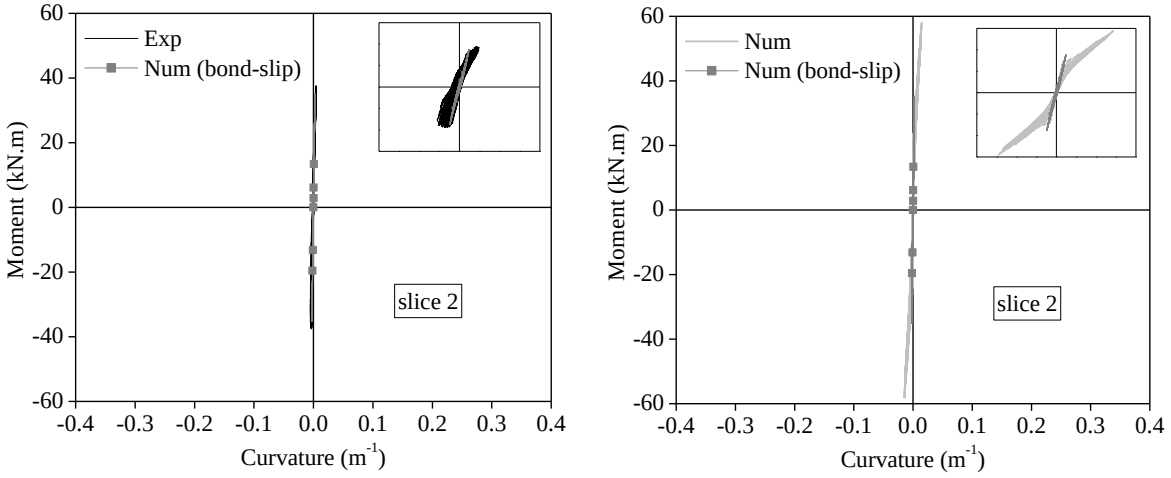

Figure 4.22 - Moment-curvature diagrams of slice 2 in the columns of specimen JPA-1 (experimental and numerical with and without considering bond-slip).

4.4 - SUMMARY

This chapter addressed the numerical modelling of the cyclic behaviour of the two analogous beam-column joint specimens described in Chapter 3, one with plain reinforcing bars and the other with deformed bars. The analyses were carried out with the SeismoStruct software. A simple modelling strategy was adopted to incorporate the effects of bar slippage in the numerical model of the joint specimen with plain bars.

The results of the comparative analyses underline the importance of accounting for the bond-slip mechanism in the numerical modelling of RC elements with plain reinforcing bars towards a more accurate simulation of the elements response. Moreover, it was highlighted the inadequacy of the current modelling strategies developed under assumptions established for elements with deformed bars to incorporate the effects of bar slippage in the analysis of elements with plain bars. This is particularly relevant for beam-column joints, in which the bond-slip behaviour is complex and its influence on the joint response is not yet comprehensively understood.

CHAPTER 5

CYCLIC TESTING OF A RC BEAM COLLECTED FROM AN EXISTING BUILDING STRUCTURE

5.1 - INTRODUCTION

This chapter addresses the cyclic test of a two-span RC beam with plain reinforcing bars that was collected from the Santa Joana Museum (an aggregate of ancient constructions, part of the cultural and historical heritage of the city of Aveiro, Portugal), in 2007, during the partial demolition of one of the museum's buildings. The beam was located at the roof, had three supports symmetrically distributed (two spans with equal length) and was loaded by two vertical elements, one at each middle-span section of the beam, which gave support to the roof structure. In this chapter, the beam properties and the adopted test setup and procedure are described, and the main experimental results are presented and discussed.

The test results and analyses presented in this chapter were partially published in the journal Periodica Polytechnica Civil Engineering [1].

5.2 - BEAM SPECIMEN

5.2.1 - Geometrical characteristics and reinforcement detailing

The beam was characterized by a 0.18x0.22 m^2 rectangular cross-section and the total span was approximately equal to 8 m. The cross-section of the beam is depicted in Figure 5.1. Information about the steel reinforcement detailing and materials mechanical properties were not available. The number, diameter and position of the reinforcing bars, and the

concrete cover were estimated resorting to a rebar detector. The measurements were confirmed by the demolition of the beam after the cyclic test. The longitudinal steel reinforcement was continuous with 180º hooks, and consisted of 2ϕ12 plus 2ϕ10 reinforcing bars at the bottom and 2ϕ12 reinforcing bars at the top. The transverse reinforcement consisted of ϕ8 stirrups at a spacing of about 180 mm. The stirrups were not closed, describing a U shape. The longitudinal and transverse reinforcement ratios, computed according to Eurocode 2 (EC2 [2]), are summarized in Table 5.1, where: d_{bl} is the diameter of the longitudinal reinforcing bars; d_{bw} is the diameter of the transverse reinforcing bars; ρ_l is the bottom longitudinal reinforcement ratio; ρ_l' is the top longitudinal reinforcement ratio; ρ_{tot} is the total longitudinal reinforcement ratio; ρ_w is the transverse reinforcement ratio; and, s is the distance between transverse reinforcing bars. The mean value of concrete cover over transverse reinforcement was estimated equal to 22 mm.

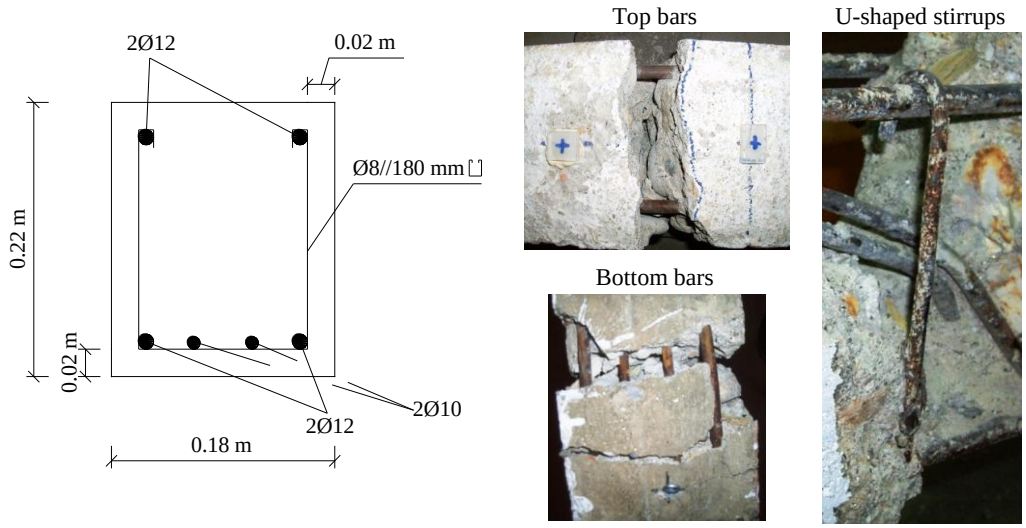

Figure 5.1 - Steel reinforcement detailing.

Table 5.1 - Steel reinforcement detailing

Longitudinal reinforcement				Transverse reinforcement		
d_{bl} (mm)	ρ_l (%)	ρ_l' (%)	ρ_{tot} (%)	d_{bw} (mm)	s (mm)	ρ_w (%)
10, 12	1.16	0.68	1.84	8	180	0.31

5.2.2 - Materials

Concrete

Four cylindrical concrete samples were extracted from the beam after the cyclic test and subjected to compression tests conducted according to the NP EN 12504-1 standard [3]. The tests results are presented in Table 5.2, where *L/D* is the length-to-diameter ratio of the sample and f_c is the concrete strength corresponding to the maximum load at failure. According to the "Standard Test Method for Obtaining and Testing Drilled Cores and Sawed Beams of Concrete" (ASTM C42/C42M [4]), for *L/D* values between 1.00 and 1.75 the concrete strength must be multiplied by a correction factor (see Table 5.3). The correction factor estimated for each concrete sample and the corresponding corrected value of concrete strength ($f_{c,cor}$) are also presented in Table 5.2.

The mean value of concrete strength obtained in the compression tests is approximately equal to 19 MPa, with a coefficient of variation equal to 11%. The corresponding characteristic compressive strength was estimated in line with the NP EN 206-1 standard [5] and is equal to 16.8 MPa. Thus, the concrete can be included in the concrete grade C16/20 according to the EC2 classification.

Table 5.2 - Results of the compression tests and correction of the concrete strength according to ASTM C42/C42M [4]

Sample	*L/D*	f_c (MPa)	Correction factor	$f_{c,cor}$ (MPa)
C1	0.85	20.9	0.83	17.5
C2	1.36	19.4	0.94	18.4
C3	0.80	26.6	0.82	21.9
C4	1.71	17.6	0.98	17.2

Table 5.3 - Strength correction factors for *L/D* values between 1.00 and 1.75 [4]

L/D	Correction Factor
1.75	0.98
1.50	0.96
1.25	0.93
1.00	0.87

Steel reinforcement

Plain bars were used in the construction of the beam, as both longitudinal and transverse steel reinforcement. The steel mechanical properties were unknown. Bars samples were not available to perform tensile strength tests.

5.2.3 - Comparison with modern codes requirements for earthquake resisting structures

In this section a comparison is established between the reinforcement detailing of the RC beam under investigation and the rules given by Eurocode 8 - Part 1 (EC8-1 [6]). As stated in Chapter 3, some differences can be found between the EC8-1 provisions for medium ductility class (DCM) and those for high ductility class (DCH). Whenever necessary, comparison with the EC2 [2] provisions is also presented. It should be noted that for this analysis the beam was considered a primary seismic element according to the EC8-1 classification.

Regarding the longitudinal reinforcement, the EC2 and EC8-1 provisions are mainly satisfied. The amount of longitudinal reinforcement complies with the specifications of the two codes. However, for DCH, EC8-1 states that at least two high bond bars with 14 mm diameter should be provided both at the top and bottom of the beam that run along the entire length of the beam.

To satisfy the necessary ductility conditions, among other requirements, EC8-1 states that the hoops diameter (d_{bw}) within the critical regions of primary seismic beams should not be less than 6 mm and the spacing between hoops should not exceed the minimum value given by Equations (3.1) and (3.2) (for DCM and DCH respectively) in Chapter 3. The maximum spacing between beam transverse reinforcing bars is given by Equation (3.3) in Chapter 3. For the beam under investigation, the maximum allowable distance between transverse bars is equal to 55 mm and 138 mm according to EC8-1 and EC2 respectively. Therefore, in the beam, the distance between the transverse bars does not comply with the two codes' specifications.

The anchorage of the transverse bars is not in accordance with EC8-1. The code specifies that for hoops used as transverse reinforcement, closed stirrups with 135º hooks and extensions of length $10d_{bw}$ should be provided.

In terms of material properties, EC8-1 stipulates that concrete grades lower than C16/20 for medium ductility class (DCM) and C20/25 for high ductility class (DCH) should not be used in primary seismic elements. In addition, only ribbed bars should be used as reinforcing steel in critical regions of primary seismic elements (with the exception of closed stirrups and cross-ties). The concrete grade requirement is satisfied only for DCH. Plain bars were used as both longitudinal and transverse steel reinforcement hence against the code provisions.

5.3 - TEST SETUP, LOADING PATTERN AND INSTRUMENTATION

Figure 5.3 illustrates the test setup adopted for the cyclic test, which was carried out at the Civil Engineering Department of the University of Aveiro. Two spans and symmetrical support conditions were considered (Figure 5.2), simulating the support conditions of the beam observed at the museum. The loading conditions to which the beam was subjected at the museum were also taken into account. Accordingly, two vertical forces (F) with the same value and symmetrically positioned at the mid-span sections (left mid-span and right mid-span) were imposed on the beam resorting to two hydraulic servo-actuators. The servo-actuators were placed bellow the strong floor and the force transmission from the servo-actuators to the beam was made resorting to four X-shaped steel elements, two placed above the beam and the other two placed below the strong floor. Threaded steel bars were used to connect the top steel elements to the bottom steel elements.

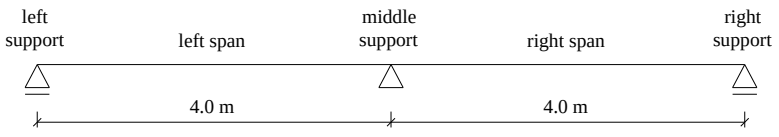

Figure 5.2 - Support conditions adopted in the cyclic test and identification of spans and supports.

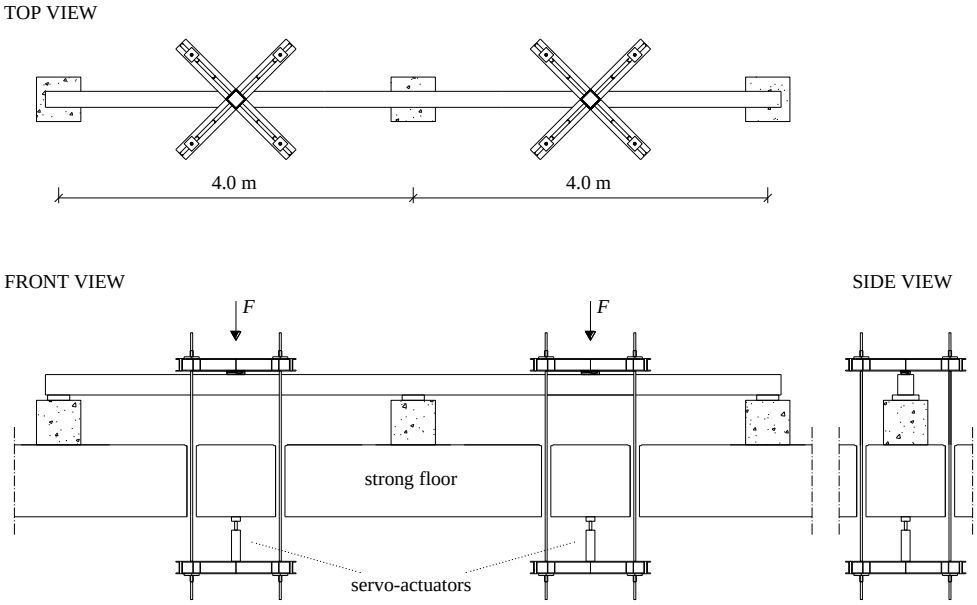

(a)

(b)

Figure 5.3 - Test setup: a) schematics; b) general view.

The quasi-static cyclic test was conducted under force controlled conditions. The adopted loading history is depicted in Figure 5.4. The forces were always descending, describing series of three loading-unloading cycles of increasing amplitude until a maximum force approximately equal to 25 kN, corresponding to the maximum capacity of the beam. The self-weight of the beam (approximately equal to 1/4-1/3 of the maximum force) is not considered in Figure 5.4.

Small differences were registered between the vertical forces imposed on the left and right spans. The maximum difference was equal to 3%. Larger force values were registered for the right span. The loading history represented in Figure 5.4 corresponds to the average between the forces imposed on the left and right spans.

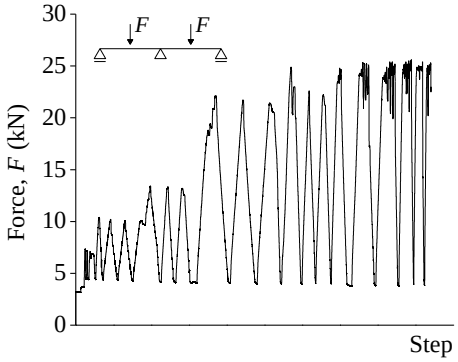

Figure 5.4 - Vertical loading history.

Fourteen draw wire displacement transducers were placed along the beam to monitor the vertical displacements. Dial indicators placed at the support regions were used to estimate the rotation of the beam at the supports. The vertical displacements and rotations monitored in the cyclic test are indicated in Figure 5.5, where: d_l and d_r are the left span deflection and right span deflection respectively; θ_l and θ_r are the beam rotations measured at the left and right supports respectively; and, $\theta_{m,l}$ and $\theta_{m,r}$ are the beam rotations measured at the left and right sides of the middle support respectively.

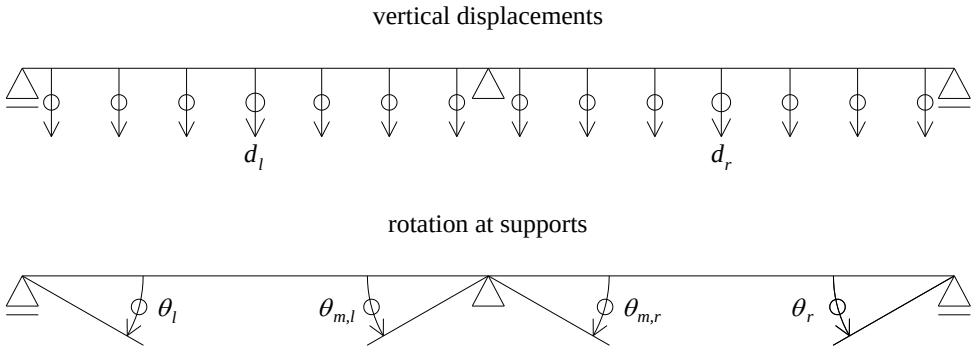

Figure 5.5 - Vertical displacements and rotations monitored in the cyclic test.

5.4 - TEST RESULTS

5.4.1 - Force-deflection diagrams

Figure 5.6 shows the force-deflection diagrams plotted for the left and right mid-span sections of the beam. Despite the symmetrical conditions in terms of the geometry of the beam, support conditions and imposed loading, the beam response was not symmetric. In comparison to the left span, the right span displayed slightly larger force values and stiffness, and significantly lower mid-span displacements. This can be related to differences in the geometrical characteristics (namely spans length), support conditions, material properties, reinforcement detailing, and eventual pre-existing minor damage, implying not perfectly symmetrical distribution of stiffness and strength.

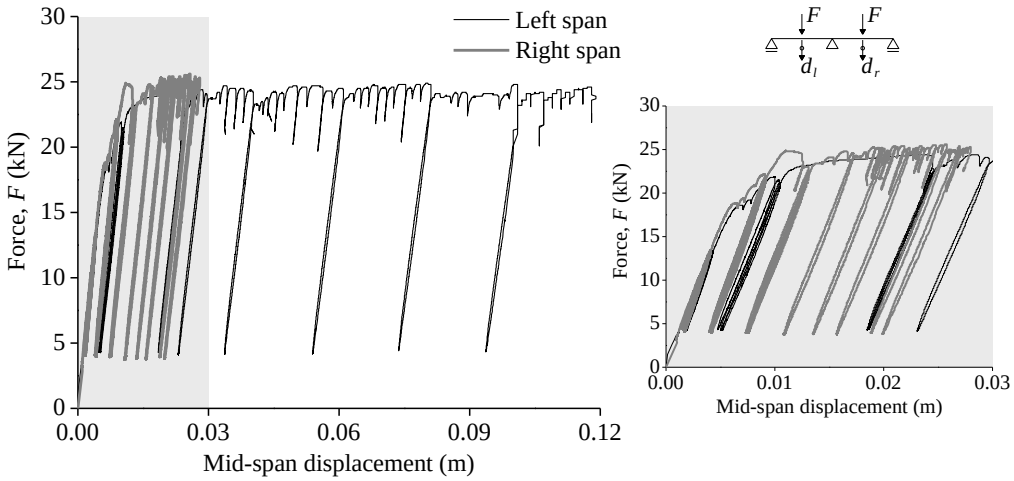

Figure 5.6 - Force-deflection diagrams.

5.4.2 - Beam deflection and deformed shape, and rotation at supports

Figure 5.7 shows the evolution of the left span deflection and right span deflection recorded by the displacement transducers. The two spans exhibited a similar deflection approximately up to the onset of cracking at the mid-span sections. Afterwards, the left span deflection began to increase significantly in comparison to the right span deflection. At the end of the test the left span deflection and right span deflection were equal to 0.12 m and 0.03 m respectively. Figure 5.8 illustrates the general evolution of the beam's deformed shape.

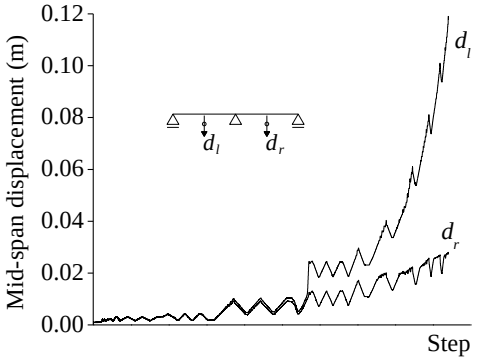

Figure 5.7 - Evolution of the spans deflection.

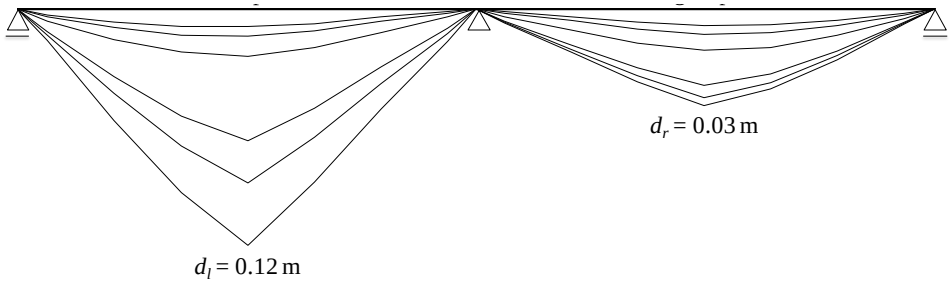

Figure 5.8 - Evolution of the beam's deformed shape.

The readings of the dial indicators that were placed at the support regions were used to estimate the rotation of the beam at the two external supports. The rotation of the beam at the middle support could not be properly estimated. The damage developed in the middle support region affected the readings of the corresponding dial indicators.

Since the beam deformation in the vicinities of the external supports was minor, the rotation of the beam at these points was computed considering rigid the beam slice between the external support and the first displacement transducer. The corresponding force-rotation (absolute values) diagrams are depicted in Figure 5.9. The rotations are similar up to the point at which significant differences between the left span deflection and right span deflection began to be observed. The maximum rotation of the beam at the left support and right support was estimated equal to 0.018 rad and 0.011 rad respectively.

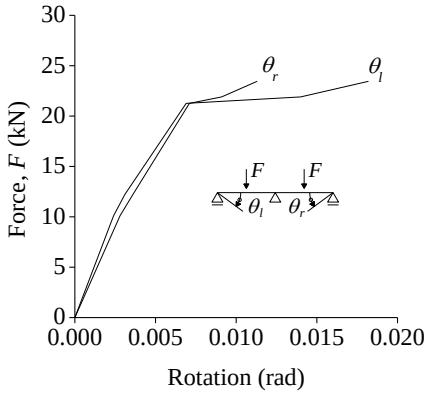

Figure 5.9 - Force-rotation (absolute values) diagrams for the left and right supports.

5.4.3 - Damage observed

Damage was concentrated in three short plastic hinge regions, being characterized by a low number of cracks with large opening. Cracking outside the plastic hinge regions was negligible. The onset of cracking was registered at the middle support region for a vertical displacement equal to 3.5 mm in the left and right mid-span sections. The onset of cracking at the left and right mid-spans occurred in the following loading-unloading cycle for a mid-span displacement equal to 4 mm.

Figure 5.10 illustrates the location of the plastic hinges with indication of the corresponding observed length. The first hinge was developed at the middle support, the second hinge at the left mid-span, and the third hinge at the right mid-span.

The reduced length of the plastic hinges and the limited crack spreading are consequence of the relative slippage between the longitudinal reinforcing bars and the surrounding concrete resulting from bond degradation.

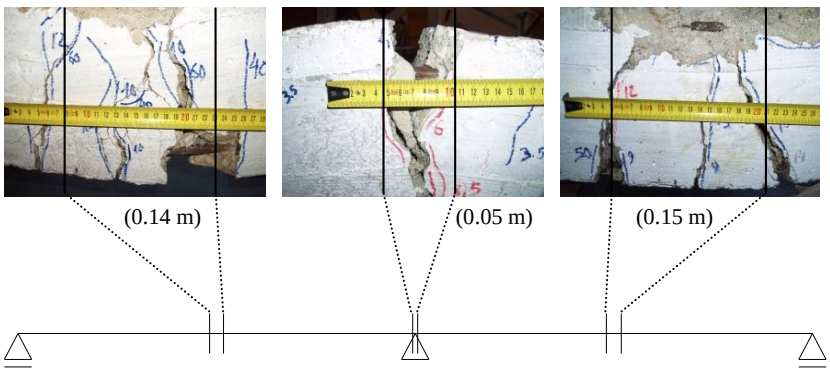

Figure 5.10 - Location and length of the plastic hinges.

The observed crack pattern suggests flexural failure. The shear strength of the beam, computed according to EC2, is equal to 61 kN hence 2.4 times the maximum load imposed on the beam (25 kN). Thus, it is concluded that shear failure did not occur.

5.4.4 - Energy dissipation

Figure 5.11 depicts the evolution of the total energy dissipated by the beam during the cyclic test, computed from the force-deflection diagrams plotted for the left and right mid-span sections, and equal to the cumulative sum of the energy dissipated in each cycle. Since the mid-span displacement demands imposed on the left span were larger than those imposed on the right span, the left span had a more significant contribution to the total energy dissipation than the right span.

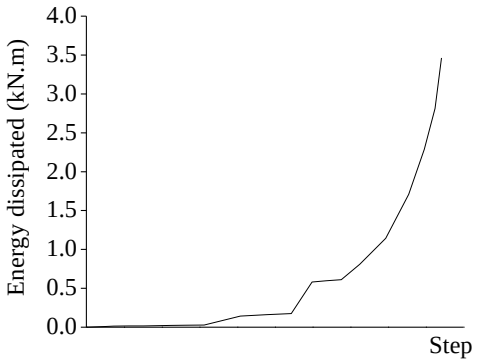

Figure 5.11 - Evolution of the total energy dissipated by the beam.

5.5 - SUMMARY

In this chapter was discussed the experimental investigation of the cyclic behaviour of a two-span RC beam with plain reinforcing bars that was collected from an ancient building structure. Symmetrical geometrical and support conditions were considered in the cyclic test. The beam was subjected to symmetrical unidirectional cyclic loads imposed at the two mid-span sections under force controlled conditions. The analysis of the test results shows that:

- The beam deformation was asymmetric. Differences in stiffness and strength were also observed between the left and right spans. The observed differences are possibly due to non-perfect symmetry of the beam in terms of spans' length,

support conditions, material properties and reinforcement detailing, and to eventual pre-existing minor damage.

- The beam displayed a flexural failure, characterized by wide cracks concentrated in three short plastic hinges developed in the regions of maximum bending moments.
- The limited damage distribution and reduced plastic hinge lengths confirm the occurrence of significant relative slippage between the longitudinal reinforcing bars and the surrounding concrete.

CHAPTER 6

NUMERICAL MODELLING OF THE BEAM

6.1 - INTRODUCTION

This chapter addresses the numerical modelling of the cyclic behaviour of the RC beam described in Chapter 5. A nonlinear fibre-based model of the beam was built using the Open System for Earthquake Engineering Simulation (OpenSees [1]) software. The support and loading conditions imposed in the cyclic test were reproduced in the model. Bond-slip effects were taken into account resorting to a method proposed in OpenSees for simulating bar slippage. The results of the cyclic test were used to calibrate the model.

The adopted modelling strategy is described. Comparison is established between the numerical and experimental results to analyse the capacity of the model to simulate the beam response. The contribution of the bond-slip mechanism to the beam deformation is analysed by comparing the numerical results, considering and not considering bond-slip, with the experimental results.

The numerical analyses described in this chapter were partially published in the journal Engineering Structures [2].

6.2 - NUMERICAL MODEL OF THE BEAM

6.2.1 - Modelling strategy

The numerical modelling was carried out using OpenSees, an object-oriented open-source software framework for simulation of the seismic response of structural and geotechnical

systems using finite element methods. A wide range of material models, elements and solution algorithms are available in OpenSees.

Figure 6.1 depicts the numerical model adopted to simulate the beam response. The model is constituted by *BeamWithHinges* elements and *Zero-length Section* elements, the cross-sections of which are idealized through fibre modelling. The elements are hence represented by unidirectional steel and concrete fibres to which are assigned the proper material stress-strain relationships describing the material's monotonic response and hysteretic rules. A general description of the *BeamWithHinges* and *Zero-length Section* elements is presented in the next two sub-sections.

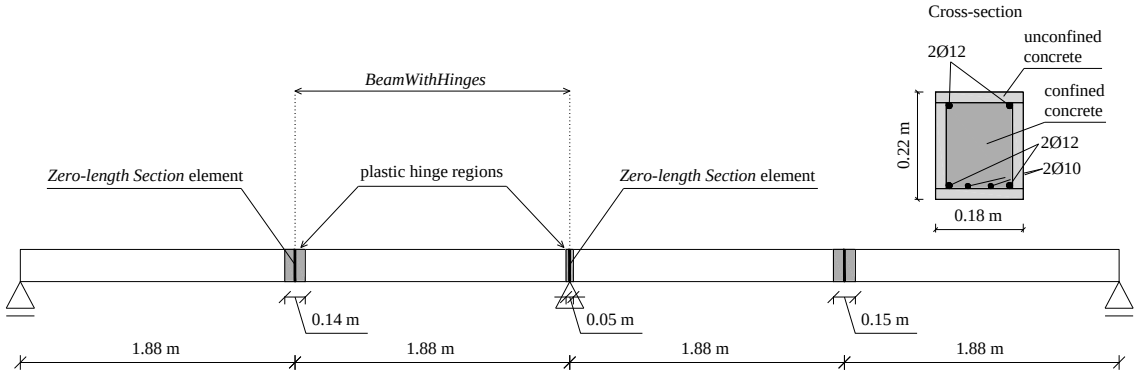

Figure 6.1 - Numerical model adopted for the RC beam (adapted from [3]): elements' location and dimensions, plastic hinge lengths, and cross-section of the beam.

Beam/column elements

Two main types of nonlinear beam/column elements are available in OpenSees: force-based elements, with distributed plasticity or concentrated plasticity with elastic interior; and, displacement based elements with distributed plasticity and linear curvature distribution. As stated in Chapter 5, the damage in the beam was concentrated in the plastic hinge regions. Therefore, *BeamWithHinges* force-based elements with plasticity concentrated over specified hinge lengths at the elements ends were adopted for representing the beam in the numerical model. Each *BeamWithHinges* element is divided in three parts (see Figure 6.2): two hinges at the ends, and a linear-elastic region in the middle. The hinges are defined by assigning to each a previously-defined section. The length of each hinge is specified by the user. The integration points are localized in the hinge regions (two integration points per hinge region).

In the numerical model of the beam, the total length of each *BeamWithHinges* element was made equal to the effective distance between the corresponding points of support in the cyclic test. The plastic hinge lengths were made equal to the values estimated in the cyclic test (see Figure 6.1): 0.14 m for the hinge at the left mid-span; 0.05 m for the hinge at the middle support region; and, 0.15 m for the hinge at the right mid-span.

Zero-length Section element

A zero-length section element is a fibre discretization of the cross-section of a structural element, and is generally used for section analyses to calculate the moment-curvature responses. The *Zero-length Section* element in OpenSees, placed at the end of a beam/column element, can be used to incorporate the fixed-end rotation caused by strain penetration to the beam/column element [4, 5]. The element is assumed to have a unit length such that the element deformation (for example, elongation and rotation) is equal to the section deformation (for example, axial strain and curvature). The unit length assumption also implies that the material model for the steel fibres in the *Zero-length Section* element represents the bar slip, instead of strain, for a given bar stress. Therefore, a specific material model, defined by a bar stress versus slip relationship (see Section 6.2.2), should be assigned to the steel fibres in the *Zero-length Section* element.

A duplicate node (that is, two nodes with the same coordinates as shown in Figure 6.2) is required between the beam-column element and the *Zero-length Section* element. The translational degree-of-freedom of one node to the other must be constrained to prevent sliding of the beam/column element under lateral loads, because the shear resistance is not included in the *Zero-length Section* element.

In the numerical model of the beam, *Zero-length Section* elements were placed between the *BeamWithHinges* elements hence concentrating the bond-slip effects in the plastic hinge regions.

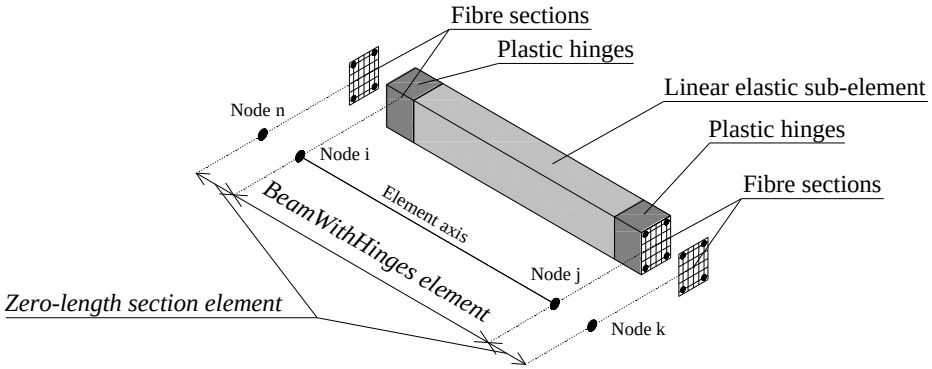

Figure 6.2 - Beam/column element *BeamWithHinges* linked to the *Zero-length Section* element.

6.2.2 - Material models

Concrete

Figure 6.3 depicts the concrete material models (*Concrete01* and *Concrete02*) that were assigned to the concrete fibres in the numerical model of the beam. The *Concrete01* model displays degraded linear unloading/reloading stiffness and no tensile strength. The *Concrete02* model displays tensile strength and linear tension softening. The models parameters are: compressive strength (f_c); strain at compressive strength (ε_0); crushing strength (f_u); and, strain at crushing strength (ε_u). In addition, *Concrete02* has also as model parameters: the ratio between unloading slope at (f_u , ε_u) and initial slope (λ); the tensile strength (f_t); and, the tension softening stiffness (E_t).

The *Concrete02* model was assigned to the *BeamWithHinges* elements. The *Concrete01* model was assigned to the *Zero-length Section* elements. The values adopted for the corresponding model parameters are presented in Table 6.1. The compressive strength of the unconfined concrete was made equal to the mean value of strength obtained in the compression tests, equal to 19 MPa. The crushing strength of the confined and unconfined concrete was made equal to 50% and 60% respectively of the maximum strength registered in the compression tests.

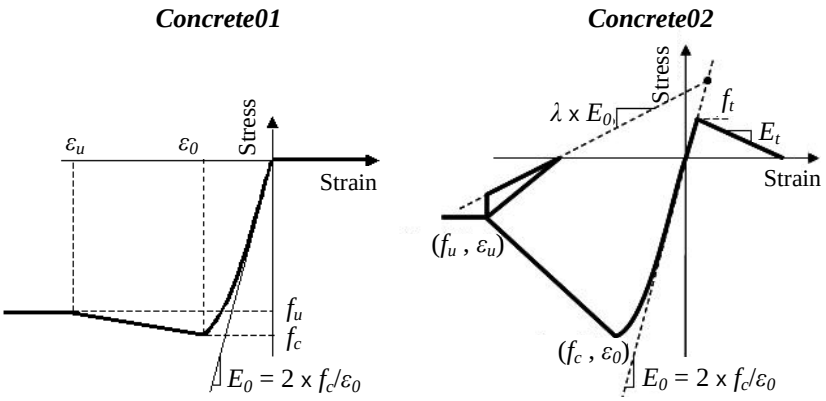

Figure 6.3 - *Concrete01* and *Concrete02* material models (adapted from [4]).

Table 6.1 - Values adopted for the *Concrete01* and *Concrete02* models parameters

Concrete	E (GPa)	f_c (MPa)	ε_0 (‰)	f_u (MPa)	ε_u (‰)	f_t (MPa)	ε_{0t} (‰)
Unconfined	18.5	19.0	2.0	9.5	7.0	1.2	0.12
Confined	17.9	19.2	2.1	11.5	33.0	1.2	0.12

The relationship between the mechanical properties of the unconfined and confined concrete was established based on the model proposed in Guedes [6], depicted in Figure 6.4. The corresponding behaviour rules are expressed by Equations (6.1) to (6.5), where: σ_{c0} and σ_{c0}* are the compressive strength of the confined and unconfined concrete respectively; ε_{c0} and ε_{c0}* are the strain at compressive strength of the confined and unconfined concrete respectively; Z and Z* are the slope of the softening branch of the confined and unconfined concrete respectively; and, β is the confinement factor. The confinement factor is computed using Equation (6.5), where α is a parameter that expresses the effect of the longitudinal bars and the density of the stirrups on the degree of confinement of the core concrete, and ω_w is the mechanical volumetric ratio of the stirrups. Parameter α is calculated using Equation (6.4), where: n is the number of longitudinal bars on the perimeter of the cross-section that are placed in an angle of a stirrup; b_c and h_c are the dimensions of the confined concrete measured from the centreline of the stirrups; and s is the distance between stirrups along the member axis. For the RC beam under investigation, Equation (6.5) gives a small value of confinement factor, equal to 1.01. Therefore, the confined and unconfined concrete are assumed to have similar behaviour in terms of maximum strength and corresponding strain, as well as similar post-peak behaviour. As stated in Chapter 5, the detailing of the transverse steel reinforcement in the beam is not in agreement with the specifications of the modern design codes. In the

National design code in force at the time of the beam erection (RBA [7]) the transverse reinforcement was normally designed only for shear resistance. The confinement effect provided by the closed stirrups was not a concern in those codes.

$$\sigma_{c0}{}^{*} = \beta \cdot \sigma_{c0} \tag{6.1}$$

$$\varepsilon_{c0}{}^{*} = \beta^{2} \cdot \varepsilon_{c0} \tag{6.2}$$

$$Z^{*} = \frac{\beta - 0.85}{\beta \cdot \left(0.1 \cdot \alpha \cdot \omega_{w} + 0.0035 + \varepsilon_{c0}{}^{*}\right)} \tag{6.3}$$

$$\alpha = \left(1 - \frac{8}{3 \cdot n}\right) \cdot \left(1 - \frac{s}{2 \cdot b_{c}}\right) \cdot \left(1 - \frac{s}{2 \cdot h_{c}}\right) \tag{6.4}$$

$$\beta = min\left(1 + 2.5 \cdot \alpha \cdot \omega_{w}; 1.125 + 1.25 \cdot \alpha \cdot \omega_{w}\right) \tag{6.5}$$

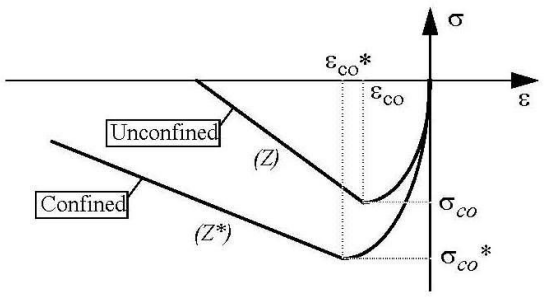

Figure 6.4 - Confinement effect in the concrete according to Guedes [6].

Steel reinforcement

The *Steel02* and *Bond_SP01* models were assigned to the steel fibres in the *BeamWithHinges* elements and *Zero-length Section* elements respectively. The *Bond_SP01* model is defined by the bar stress-slip relationship described in the following section.

The *Steel02* model is based on the model initially proposed by Giuffré and Pinto and implemented by Menegotto and Pinto [8], with isotropic strain hardening (see Figure 4.3 in Chapter 4). The *Steel02* model parameters are: steel yield strength (f_y); initial elastic tangent (E_0); strain-hardening ratio (b, equal to ratio between post-yield tangent E_1 and initial elastic tangent E_0); parameters to control the transition from elastic to plastic

branches (R_0, cR_1 and cR_2); isotropic hardening parameters (a_1, a_2, a_3 and a_4); and, initial stress (σ_0).

Table 6.2 gives the values adopted for the *Steel02* model parameters in the numerical model of the beam. As stated in Chapter 5, the mechanical properties of the plain reinforcing bars were unknown. The best agreement between the numerical and experimental results was obtained considering the steel yield strength equal to 260 MPa. The strain-hardening ratio was made equal to zero, which represents the typical yielding plateau with large deformation for hot rolled steel. For the parameter R_0, the Menegotto-Pinto model suggests a value of 20. In the beam calibrated model this parameter was made equal to 16.5. Isotropic hardening was not considered.

Table 6.2 - Values adopted for the *Steel02* model parameters

Model parameter	Recommend value/range	Adopted value
f_y	-	260 MPa
E	-	200 GPa
b	-	0
R0	10 - 20	16.5
cR1	0.925	0.925
cR2	0.15	0.15
σ_0	-	0

Bar stress-slip model

Focusing on column and wall longitudinal bars anchored in footings and bridge joints, the bar stress versus slip constitutive model (*Bond_SP01* in OpenSees) shown in Figure 6.5 was proposed by Zhao and Sritharan [5] for the steel fibres in the *Zero-length Section* element. The model was developed based on measured bar stress and loaded end slip from pullout tests of well-anchored deformed steel reinforcing bars. The corresponding hysteretic rules were established using the results of cyclic pullout tests and cyclic tests on RC columns. The proposed methodology was used by Zhao and Sritharan [5] to simulate the cyclic response of two concrete cantilever columns and a bridge tee-joint system. Based on the comparisons established between the numerical and experimental results, the authors state that the strain penetration effects should not be ignored in the analysis of concrete members, and that the *Zero-length Section* element incorporating the proposed constitutive model for the steel fibres can be used in nonlinear fibre-based analysis to

accurately capture the strain penetration effects (namely bar slippage) and thus the global and local responses of concrete flexural members.

The *Bond_SP01* model parameters are: steel yield strength (f_y); steel ultimate strength (f_u); slip at yield strength (s_y); slip at ultimate strength (s_u); initial hardening ratio (b); and, pinching factor for the cyclic bar stress-slip relationship (R). The slip values s_y and s_u are determined using Equations (6.6) and (6.7) respectively, where: d_b is the bar diameter; f_c is the concrete compressive strength; and, α is a tuning parameter used for adjusting the local bond stress-slip relationship. In the model proposal, α is made equal to 0.4 similarly to what is suggested in the bond-slip model for deformed bars proposed by the CEB-FIP Model Code 90 [9].

$$s_y(mm) = 2.54 \cdot \left(\frac{d_b(mm)}{8437} \cdot \frac{f_y(MPa)}{\sqrt{f_c(MPa)}} \cdot (2\alpha + 1) \right)^{1/\alpha} + 0.34 \tag{6.6}$$

$$s_u(mm) = 30 \sim 40 \cdot s_y \tag{6.7}$$

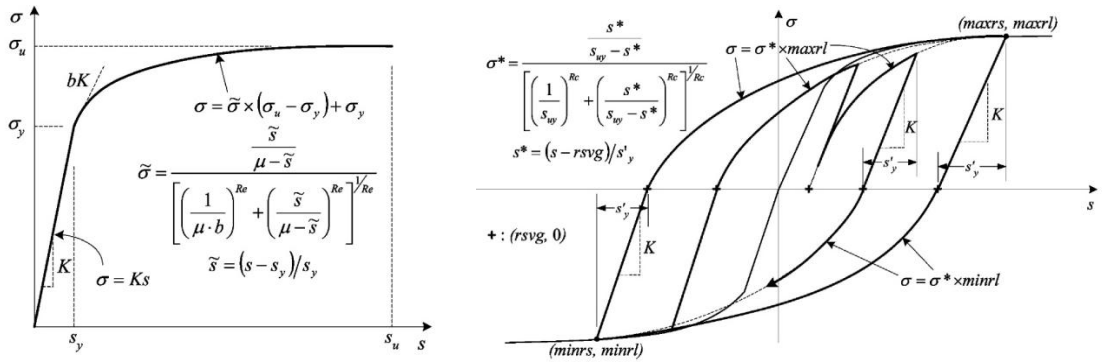

(a) (b)

Figure 6.5 - Bar stress-slip model proposed by Zhao and Sritharan [5]: a) envelope curve; b) hysteretic response.

The *Bond_SP01* model was assigned to the steel fibres in the *Zero-length Section* elements. Table 6.3 gives the values adopted for the model parameters in the numerical model of the beam. As previously stated, the model was developed for well-anchored deformed reinforcing bars. The beam under investigation was built with plain reinforcing bars and, considering the reinforcement detailing, good anchorage of the longitudinal bars can be

assumed. Taking into account the type of steel reinforcement (plain bars), parameter α was increased from 0.4 to 0.5 according to the specifications of CEB-FIP Model Code 90 [9]. Regarding the other model parameters, the best agreement between the numerical and experimental results was achieved considering the maximum value recommended for the ultimate slip ($s_u = 40s_y$) and the minimum value recommended for the initial hardening ratio ($b = 0.3$).

Table 6.3 - Values adopted for the *Bond_SP01* model parameters

Model parameter	Recommended value/range	Adopted value
f_y	-	260 MPa
f_u	-	360 MPa
s_y	-	0.4433
s_u	$30s_y$ - $40s_y$	$40s_y$ (mm)
b	0.3 – 0.5	0.3
R	0.5 – 1.0	0.80

6.2.3 - Loading pattern

In the cyclic test, the beam was tested under force-controlled symmetrical loading conditions. However, as stated in Chapter 5, the beam response was not symmetric, namely in terms of mid-span displacements. Therefore, in the numerical model of the beam, instead of imposing equal vertical forces as in the cyclic test (which would lead to a symmetrical numerical response), it were imposed the vertical displacement histories recorded at the mid-span sections (d_l and d_r in Figure 6.6).

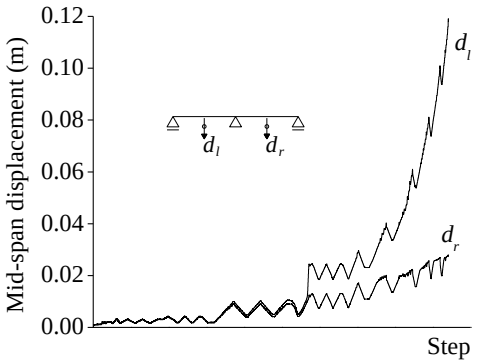

Figure 6.6 - Vertical mid-span displacements imposed in the numerical model.

6.3 - COMPARISON BETWEEN NUMERICAL AND EXPERIMENTAL RESULTS

6.3.1 - Force-displacement diagrams

Figure 6.7 establishes the comparison between the numerical and experimental force-displacement diagrams of the left mid-span and right mid-span sections of the beam. A good agreement between the numerical and experimental results is shown both in terms of maximum force and stiffness.

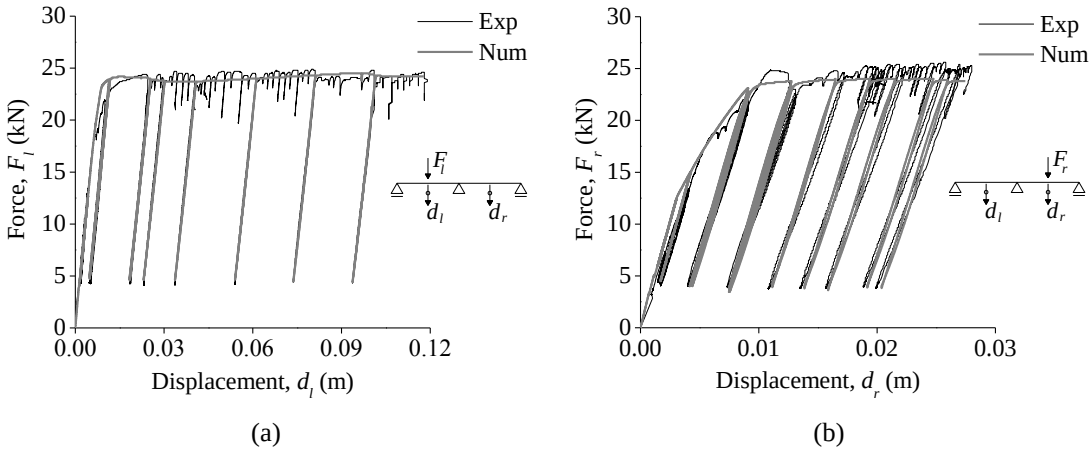

Figure 6.7 - Force-displacement diagrams (numerical and experimental): a) left mid-span section; b) right mid-span section.

Plotting together the numerical force-displacement diagrams of the left and right mid-span sections (Figure 6.8) it is observed that the two spans display similar maximum force equal to about 25 kN, as in the cyclic test. For a given level of imposed displacement the unloading stiffness of the right span is larger than that of the left span, which is also in agreement with the experimental results. It should be noted that the comparative analysis in Figure 6.8 is presented for displacement values up to the maximum displacement imposed on the right span (equal to 0.03 m).

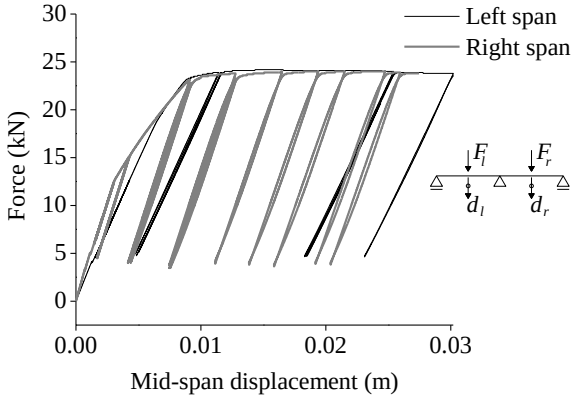

Figure 6.8 - Numerical force-displacement diagrams of the left mid-span and right mid-span sections.

6.3.2 - Damage evolution

For better understanding the damage evolution and its influence on the global response of the beam, the stress versus imposed displacement diagrams were computed for the concrete and steel and confronted with the numerical force-displacement diagrams previously shown in Figure 6.7. The results of this comparative analysis are illustrated in Figure 6.9 where the force-displacement diagrams of the left mid-span and right mid-span sections are plotted with indication of the points corresponding to the onset of cracking, yielding of the reinforcing bars and concrete crushing.

Similarly to what was observed in the cyclic test, in the numerical model the onset of cracking occurs first at the middle support region, second and almost simultaneously at the left mid-span, and third at the right mid-span. The early cracking stage does not show an important influence on the global force-displacement relationships. The numerical results suggest that yielding of the longitudinal reinforcing bars is the damage state that followed the onset of cracking: first, yielding of the top bars at the middle support section; second, yielding of the bottom bars at the left mid-span section; and third, yielding of the bottom bars at the right mid-span section. For larger displacement demands the model suggests that compressive crushing of concrete took place at the middle support section, left mid-span section, and right mid-span section in that order. Despite the large deformation demands imposed on the left span, rupture of steel did not occur, what is considered to be due to the occurrence of relative slippage between the longitudinal reinforcing bars and the surrounding concrete.

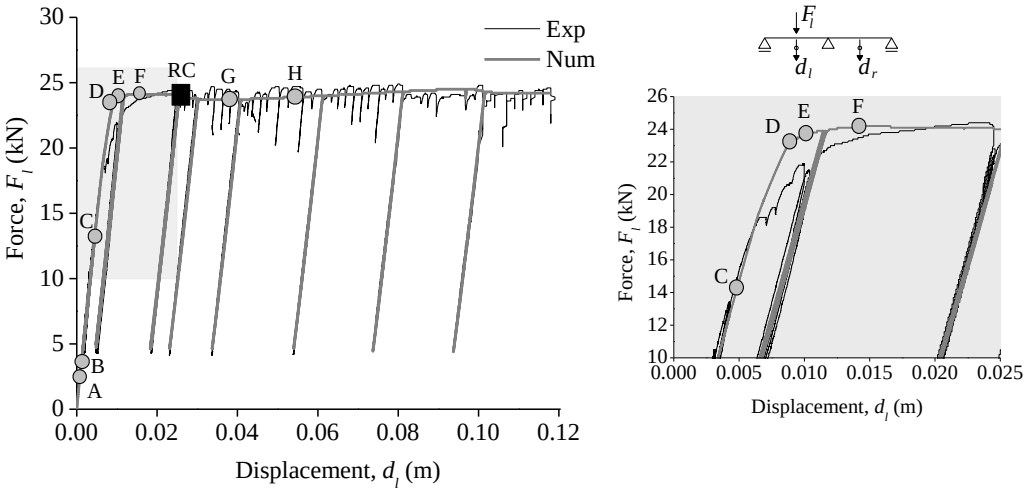

(a)

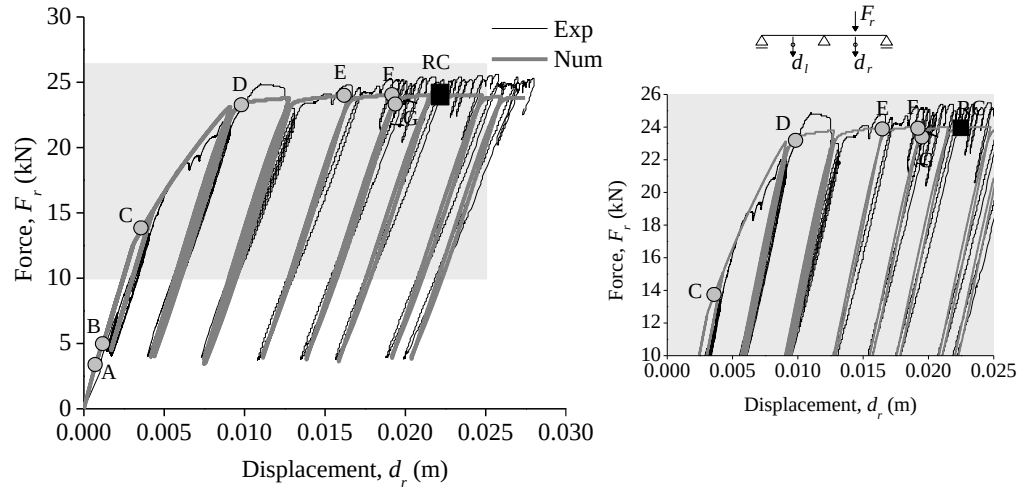

(b)

Legend:

A – Onset of concrete cracking at the middle support section

B – Onset of concrete cracking at the mid-span section

C – Yielding of the top steel bars at the middle support section

D – Yielding of the bottom steel bars at the mid-span section

E – Compressive crushing of the unconfined concrete at the middle support section

F – Compressive crushing of the unconfined concrete at the mid-span section

G – Compressive crushing of the confined concrete at the middle support section

H – Compressive crushing of the confined concrete at the mid-span section

RC – Ultimate Rotation Capacity

Figure 6.9 - Damage evolution at: a) left mid-span section; b) right mid-span section.

Figure 6.9 also indicates the theoretical value of ultimate rotation capacity of the beam computed according to Eurocode 8 - Part 3 (EC8-3 [10]) using Equation (3.17). Details about the method used by EC8-3 to compute the ultimate rotation capacity of RC elements

with plain reinforcing bars were provided in Chapter 3. Table 6.4 presents the values adopted/estimated for the parameters involved in the computation. The beam was considered a primary seismic element hence parameter γ_{el} in Equation (3.17) was made equal to 1.5. The correction coefficient was made equal to 0.575, as specified by EC8-3 for elements without lap-splices. The ultimate rotation capacity of the beam was estimated equal to 0.023 rad. Figure 6.9 shows that the theoretical value of ultimate rotation capacity occurs after yielding of the reinforcing bars and crushing of the unconfined concrete.

As stated in Chapter 3, the ultimate rotation capacity is generally evaluated referring to a fixed reduction in strength, usually equal to 20% [11]. Therefore, since strength degradation was not observed in the beam response, the experimental values of ultimate rotation capacity could not be determined. Only the maximum values of rotation were estimated, being equal to 4.8 times and 2.8 times the theoretical value of ultimate rotation capacity, for the left span and right span respectively.

Table 6.4 - Parameters involved in the computation of the ultimate rotation capacity of the beam according to EC8-3

γ_{el}	ν	ω	ω'	f_c (MPa)	L_v/h	α	ρ_{sx}	f_{yw}	ρ_d
1.5	0.21	0.132	0.078	23.8	9.09	0.071	0.003	260	0

6.3.3 - Energy dissipation

Figure 6.10 compares the numerical and experimental evolutions of total dissipated energy. The results show an excellent experimental-numerical agreement, featuring a maximum difference of about 1.7%.

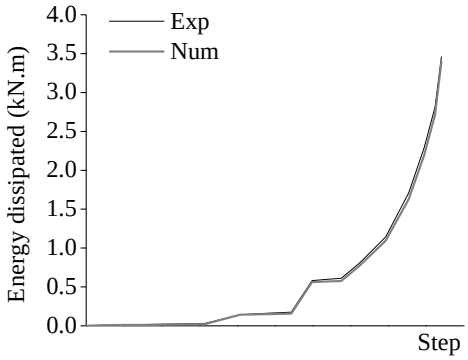

Figure 6.10 - Evolution of the total dissipated energy (numerical and experimental).

6.4 - ANALYSIS OF THE RESPONSE AT LOCAL LEVEL

The numerical model was used to analyse other features of the beam response, namely in terms of moment-curvature relationships, and stress and strain in the concrete and steel.

6.4.1 - Evolution of bending moments

Figure 6.11 represents the evolution of the bending moments computed at the middle support, left mid-span and right mid-span sections. Figure 6.11 also shows the theoretical values of flexural strength for sagging and hogging moments (M_{sag} and M_{hog} respectively) determined according to Eurocode 2 (EC2 [12]). Table 6.5 compares the theoretical values of strength with the numerical values of maximum moment. A good agreement was found between the numerical and theoretical values, underlining the adequacy of the numerical model. Figure 6.11 shows that when the flexural strength for hogging moments is reached at the middle support section, the bending moment at the left and right mid-span sections is about 68% of the flexural strength determined for sagging moments. Therefore, sagging bending moments of larger magnitude could still be developed at the left and right mid-span sections.

Figure 6.12 depicts the bending moment diagrams computed for the loading steps corresponding to the onset of cracking and yielding of the reinforcing bars at the middle support and mid-spans sections. Figure 6.12 also depicts the bending moment diagrams obtained with a linear elastic analysis to illustrate the redistribution of bending moments within the nonlinear response. The moment redistribution is not significant until yielding of the longitudinal bars occurs at the middle support section, that is, when the beam flexural strength for hogging moments is reached.

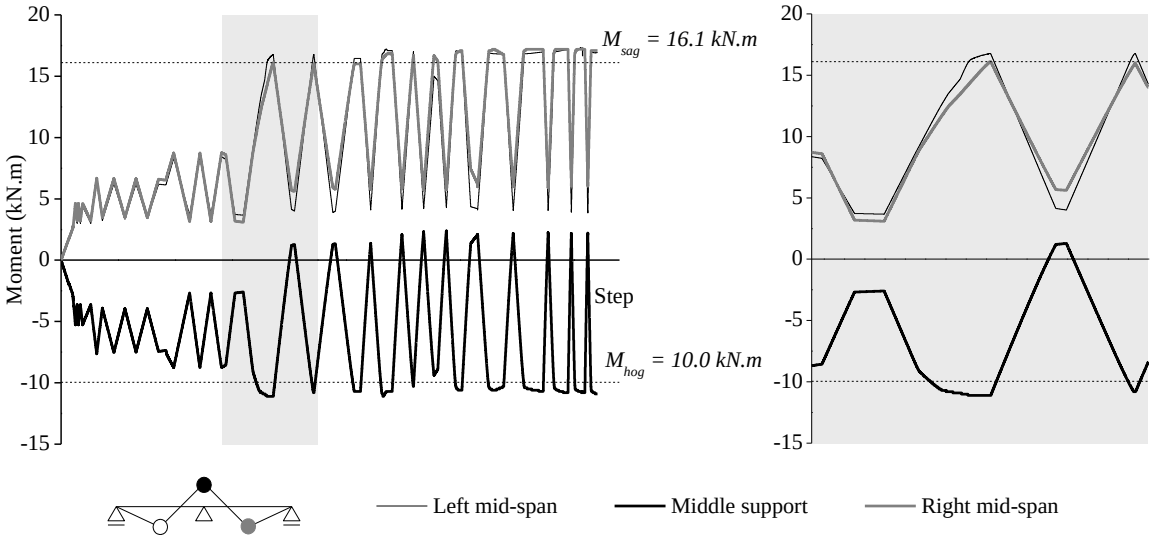

Figure 6.11 - Evolution of bending moments.

Table 6.5 - Comparison between the beam flexural strength computed according to EC2 and the numerical values of maximum moment

	Flexural strength for sagging moments (kN·m)	Flexural strength for hogging moments (kN·m)
EC2	16.1	10.0
Numerical	17.2	11.2
Difference (%)	6%	11%

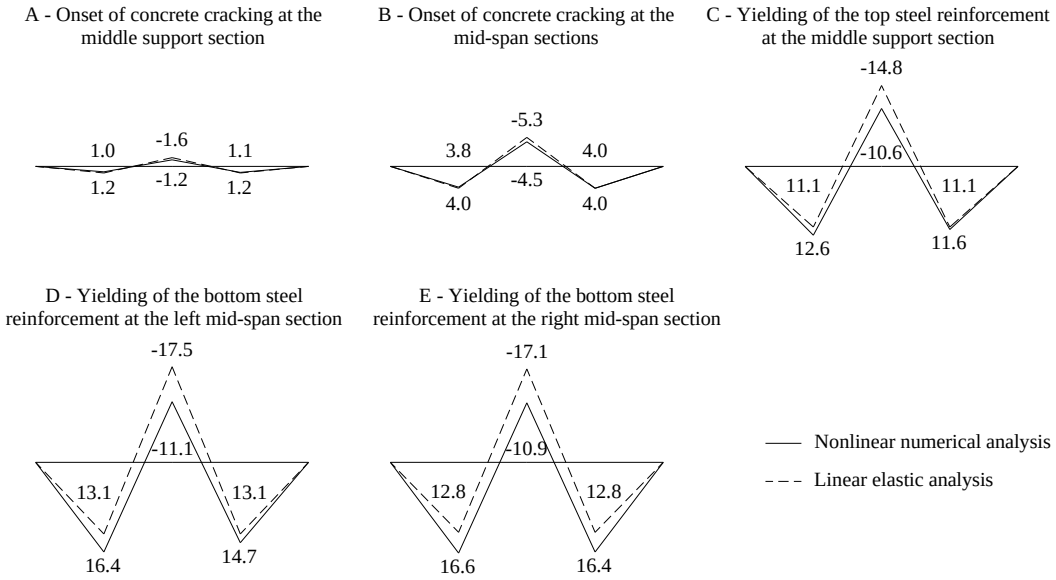

Figure 6.12 - Bending moment diagrams (in kN·m).

6.4.2 - Moment-curvature diagrams

Figure 6.13 depicts the moment-curvature diagrams plotted for the middle support section (left and right sides) and mid-span sections. Up to the occurrence of yielding of the steel reinforcement in the middle support section, the moment-curvature relationships are linear and similar. Regarding the unloading and reloading branches of the cyclic response, the moment-curvature relationships are linear and the stiffness is similar to the stiffness of the initial branch. The curvature of the left and right mid-span sections corresponding to the maximum flexural strength was estimated equal to 6.7×10^{-4} m^{-1} and 2.2×10^{-3} m^{-1} respectively.

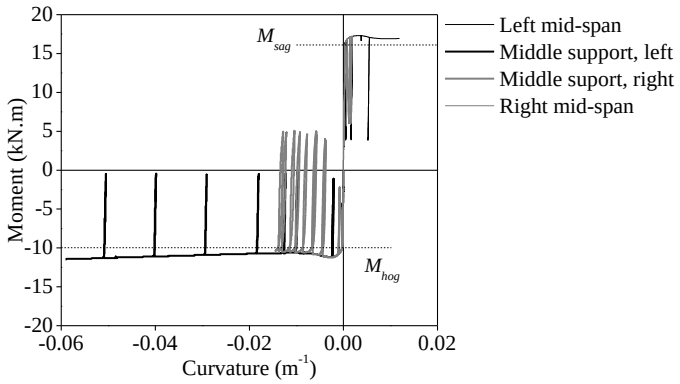

Figure 6.13 - Moment-curvature diagrams.

6.4.3 - Evolution of the neutral axis position

Figure 6.14 depicts for the middle support section and left and right mid-span sections the shifting of the neutral axis position in relation to the geometric gravity centre of the cross-section. This allows identifying at each time step which part of the concrete cross-section is compressed. The onset of cracking at the middle support and the yielding of the bottom steel reinforcement at the mid-spans (both marked in Figure 6.14) are shown to be the damage states to which are associated the most abrupt changes in the position of the neutral axis. Up to the onset of cracking the neutral axis is located below the geometric gravity centre of the cross-section due to the differences in total area of steel between the top and bottom longitudinal bars. Within the unloading and reloading branches, the maximum variation in the neutral axis position was estimated equal to about 6 mm. After concrete crushing occurs at the left and right mid-span sections, the neutral axis stabilizes

at a position close to the gravity centre of the longitudinal reinforcing bars under compression and confined-unconfined concrete interface.

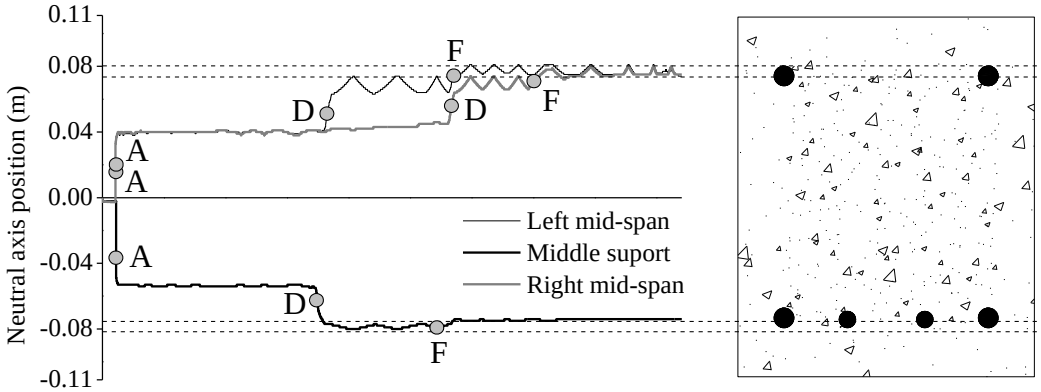

A - Onset of concrete cracking at the middle support section
D - Yielding of the bottom steel reinforcement at the mid-span section
F - Compressive crushing of the unconfined concrete at the mid-span section

Figure 6.14 - Evolution of the neutral axis position.

6.4.4 - Stress-strain diagrams

Table 6.6 shows the stress and strain distributions in the cross-section of the beam (concrete and steel) at the time steps corresponding to the main damage states referred in the previous sections. The diagrams are plotted for the left mid-span section.

The stress diagrams are roughly symmetrical until the onset of cracking. Afterwards, the stress in the bottom longitudinal bars is significantly increased, reaching the yielding state but not failure. The confined and unconfined concrete reach the concrete compressive strength.

At the confined-unconfined concrete interface, the unconfined concrete tends to display larger maximum strain demands than the confined concrete. This is related to the position of the neutral axis in the last cycles, which is close to the longitudinal reinforcing bars under compression and, therefore, to the confined-unconfined concrete interface.

The linearity of the stress diagrams is in agreement with the plane section assumption for the response in the elastic branch.

Table 6.6 - Stress and strain distributions in the cross-section of the beam (left mid-span section)

Damage	Strain distribution (‰)	Stress distribution (MPa)	
		Concrete	Steel
0 - Before cracking (no damage)	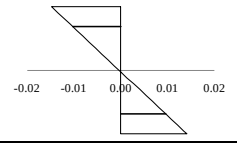	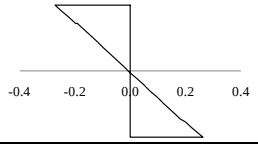	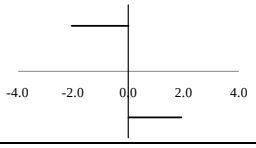
A – Onset of concrete cracking at the middle support	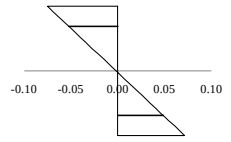	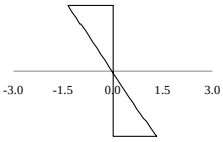	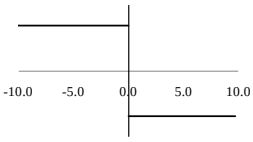
B – Onset of concrete cracking at the left mid-span section	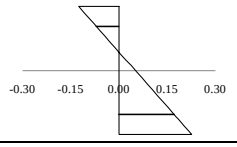	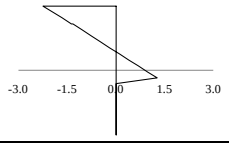	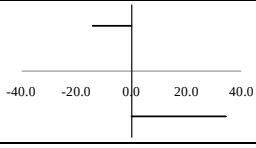
C - Yielding of the top steel bars at the middle support	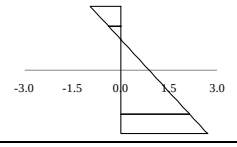	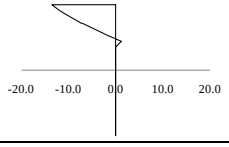	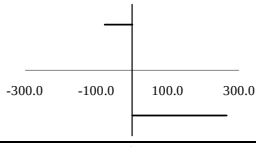
D - Yielding of the bottom steel bars at the left mid-span section	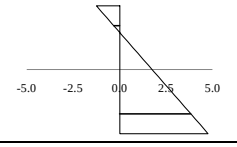	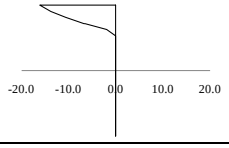	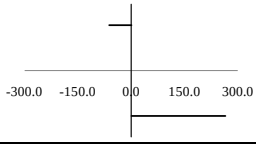
D - Yielding of the bottom steel bars at the right mid-span section	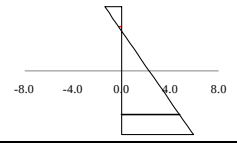	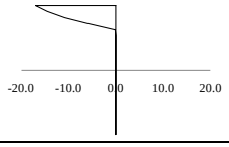	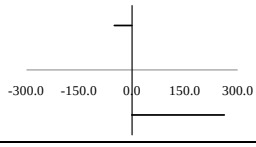
E - Compressive crushing of the unconfined concrete at the middle support section	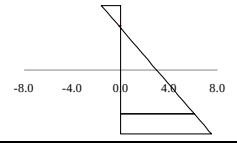		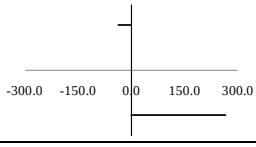
F - Compressive crushing of the unconfined concrete at the left mid-span section	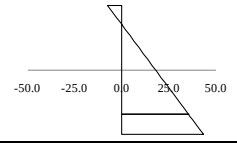	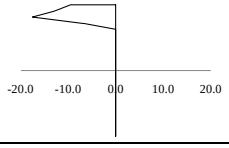	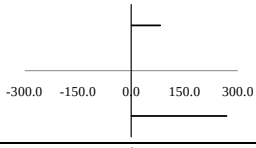
F - Compressive crushing of the unconfined concrete at the right mid-span section	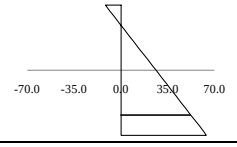	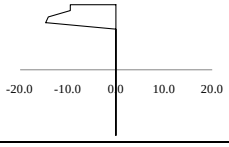	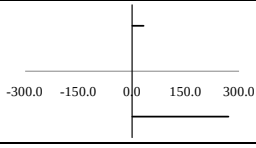
G - Compressive crushing of the confined concrete at the middle support	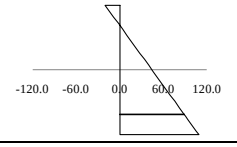		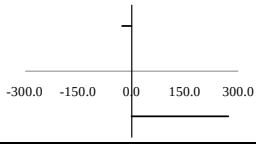

6.5 - BOND-SLIP INFLUENCE

Figure 6.15 depicts the relative contributions of the bond-slip mechanism and bending to the total mid-span displacements, determined from the numerical results. The shear influence is not significant and is included in the parcel corresponding to bending. The results show that the importance of bond-slip increases as the mid-span displacements increase. For the imposed loading conditions, the initial relative contribution of bond-slip is equal to about 10% for both the left and right spans. For the maximum mid-span displacement imposed on the beam, the relative contribution of bond-slip rises to 85% and 45% for the left span and right span respectively. Confronting the diagrams of Figure 6.15 with the force-displacement diagrams in Figure 6.7 it is observed that the bond-slip contribution is significantly increased within the displacement range corresponding to the yielding.

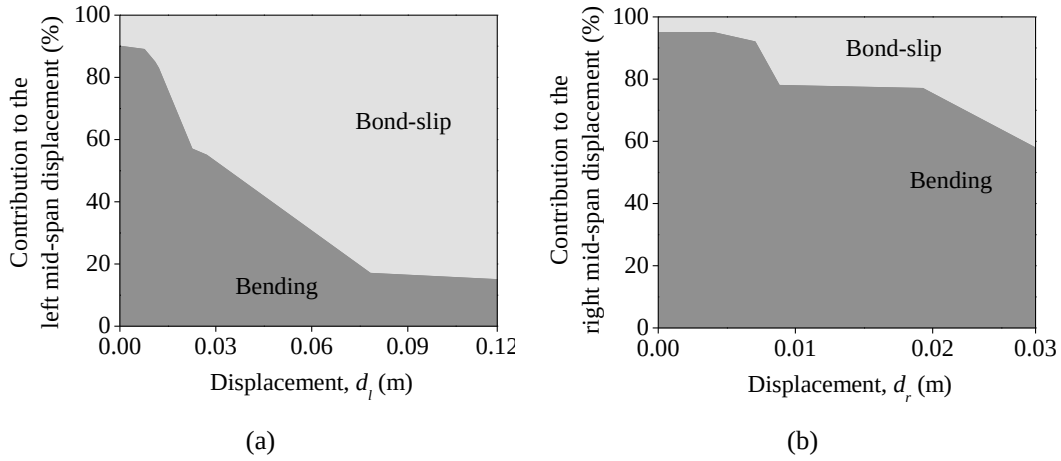

Figure 6.15 - Relative contributions of bond-slip and bending to the mid-span displacement of the: a) left span; b) right span.

For better understanding the importance of considering the bond-slip effects towards a more accurate simulation of the beam response, an additional numerical analysis was conducted without considering bond-slip, that is, without the *Zero-length Section* elements in the model. Figure 6.16 compares the experimental force-displacement diagrams with the numerical diagrams obtained with and without considering bond-slip. The corresponding diagrams of energy dissipation are depicted in Figure 6.17. The force-displacement diagrams show that, even if the maximum force is achieved whether considering or not

considering the bond-slip mechanism, the stiffness is overestimated when bond-slip is neglected. The total energy dissipated by the beam is also overestimated. The maximum difference in total dissipated energy between the numerical and experimental results rises from 1.7% to 10% when bond-slip is not taken into account.

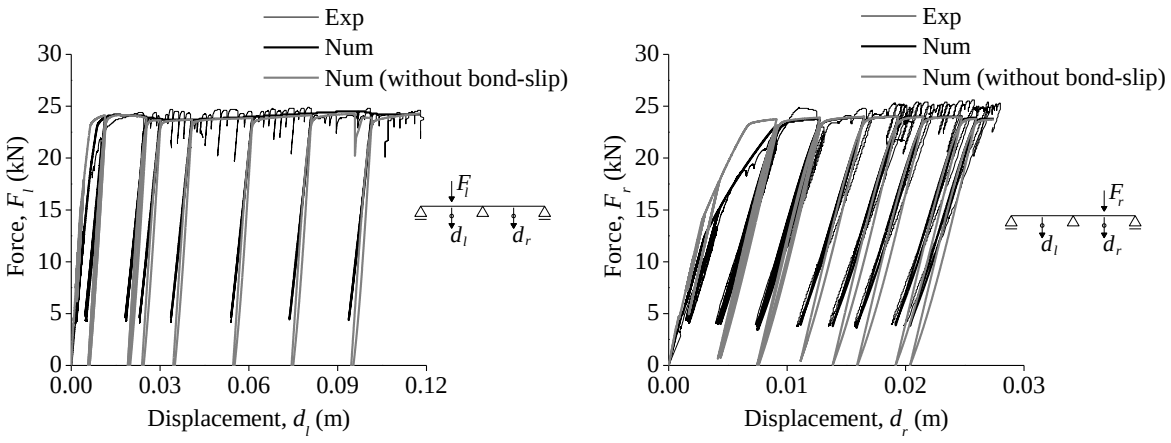

Figure 6.16 - Force-displacement diagrams (experimental and numerical with and without bond-slip): a) left mid-span section; b) right mid-span section.

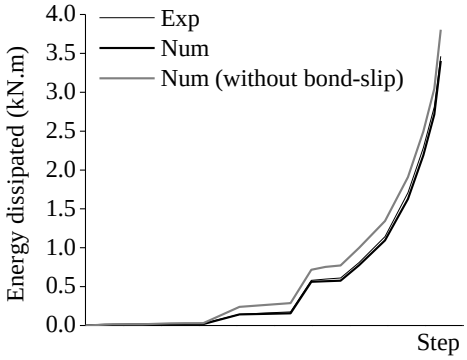

Figure 6.17 - Evolution of the total dissipated energy (experimental and numerical with and without bond-slip).

6.6 - SUMMARY

This chapter addressed the numerical modelling of the cyclic behaviour of the RC beam described in Chapter 5. The numerical analyses were carried out using OpenSees. The bar stress-slip model available in OpenSees was implemented in the model in order to account for the bond-slip effects. The adequacy of the model to simulate the beam response was

analysed by comparing the numerical and experimental results. An additional numerical analysis was conducted without taking into account the bond-slip effects, and new comparison was established between the numerical results (with and without considering bond-slip) and the experimental results. The main conclusions taken from the conducted analyses were:

- The good agreement registered between the numerical and experimental results, in terms of force-displacement diagrams (initial stiffness, maximum strength, unloading-reloading internal cycles), energy dissipation and damage evolution, shows that the global behaviour of the beam is well represented by the numerical model when bond-slip is considered.
- The relative contribution of the bond-slip mechanism to the overall deformation of the beam increases with the mid-span displacements. For the maximum mid-span displacements, approximately 85% of the left span deflection and 45% of the right span deflection are due to bar slippage.
- When bond-slip is not taken into account in the numerical model, the strength capacity of the beam is not affected, but both the stiffness and dissipated energy are overestimated.

CHAPTER 7

CONCLUSIONS AND FUTURE RESEARCH

7.1 - CONCLUSIONS

This thesis presented the experimental and numerical assessment of the cyclic behaviour of RC structural elements built with plain reinforcing bars and lacking specific detailing for seismic demands. Particular focus was put on the influence of the concrete-steel bond properties, namely, on the bond-slip mechanism.

The results of the experimental tests conducted in the framework of the thesis highlight the key role of the concrete-steel bond properties on the cyclic response of RC elements with plain reinforcing bars. The influence of bond was particularly relevant on the damage distribution in the tested specimens. Regarding, in particular, the results of the cyclic tests on the joint specimens, the strength was conditioned by the poor bond properties of plain bars. The Eurocode 2 expressions did not provide a good estimate of the elements' strength hence underlining the need for specific formulations to properly estimate the strength capacity of RC elements with plain bars.

The results of the numerical analyses carried out to simulate the response of the tested specimens confirm the need of taking into account the effects of the bond-slip mechanism towards a more accurate simulation of the cyclic response of RC structural elements with plain reinforcing bars. Concerning, in particular, the numerical analysis of the joint specimens, the results underline the inadequacy of current models established for elements with deformed bars to simulate the response of elements with plain bars. It is therefore

highlighted the need for specific models to account for the effects of bar slippage in the presence of plain bars.

The results obtained in the framework of this thesis contribute to the advance of knowledge about the cyclic behaviour of RC elements with plain reinforcing bars. Besides contributing to expand and improve the available experimental database on the subject, the data provided by the experimental tests can be used to calibrate and upgrade available models for simulating the behaviour of this type of elements, or to develop new ones.

7.2 - FUTURE RESEARCH

Considering the recognized lack of information regarding the cyclic behaviour of RC structural elements with plain reinforcing bars, and bond performance itself between concrete and plain bars, the research needs regarding this type of elements are vast. In addition to being scarce, the experimental data available in the literature presents some discrepancies. In this way, there is a marked need for more experimental evidence in order to understand more comprehensively the cyclic behaviour of RC elements with plain reinforcing bars. The experimental work presented in this thesis contributed only to a small part of the identified needs. As future research work, it would be interesting to:

i) Extend the experimental programme to other beam-column joint typologies, namely exterior tee-joints, and also to RC columns. This would imply some modifications to the current test setup.

ii) Investigate the influence of other important parameters, like: presence and amount of joint transverse reinforcement, anchorage of the longitudinal reinforcing bars in beam-column joints (namely in exterior joints) and column footings, presence and detailing of lap-splices, and presence of transverse beams and slabs.

iii) Investigate the influence of varying axial load and of bi-directional loading.

iv) Test RC structural elements with plain reinforcing bars collected from existing structures.

v) Calibrate and improve available numerical models, based on the data provided by the experimental tests.

vi) Propose new analytical expressions adequate to estimate the strength capacity of RC elements with plain reinforcing bars, based on a comprehensive analysis of test results concerning this type of elements.

vii) Collect and analyse information about the models available in the literature that include bond-slip effects; assess their inadequacy to simulate the cyclic behaviour of RC elements with plain reinforcing bars; identify the major shortcomings of these models; and, propose solutions for upgrading these models and/or new developments.

REFERENCES

CHAPTER 2 – SEISMIC VULNERABILITY OF EXISTING RC BUILDING STRUCTURES WITH PLAIN REINFORCING BARS: STATE OF THE ART

1. Paulay, T. and Priestley, M.N.J., *Seismic design of reinforced concrete and masonry buildings*. 1992: John Wiley & Sons, Inc.

2. Varum, H., *Seismic assessment, strengthening and repair of existing buildings*. PhD Thesis. 2003, University of Aveiro: Aveiro, Portugal.

3. *RSCCS. Regulamento de Segurança das Construções Contra os Sismos. Decreto nº 41 658*. 1958, Imprensa Nacional: Lisboa.

4. RSA, *Regulamento de Segurança e Acções para Estruturas de Edifícios e Pontes. Decreto de Lei n.º 235/83*. 2000, Porto Editora.

5. Ricci, P., De Luca, F., and Verderame, G.M., *6th April 2009 L'Aquila earthquake, Italy: reinforced concrete building performance.* Bulletin of Earthquake Engineering, 2011. **9**(1): p. 285-305.

6. CEN, *NP EN 1992-1-1. Eurocode 2 - Design of concrete structures. Part 1-1: General rules and rules for buildings*. 2010, European Committee for Standardization: Brussels, Belgium.

7. CEN, *NP EN 1998-1. Eurocode 8 - Design of structures for earthquake resistance. Part 1: General rules, seismic actions and rules for buildings*. 2010, European Committee for Standardization: Brussels, Belgium.

8. Pampanin, S., Calvi, G.M., and Moratti, M., *Seismic behavior of RC beam-column Joints designed for gravity loads* in *12th European Conference on Earthquake Engineering*. 2002: London, UK.

9. LNEC, *Levantamento do parque habitacional de Portugal continental para o estudo da sua vulnerabilidade sísmica com base nos CENSOS-91 - Relatório 260/00*. 2000, C3ES, LNEC: Lisbon.

10. Fardis, M.N., *Seismic design, assessment and retrofitting of concrete buildings. Based on EN-Eurocode8*. Geotechnical, Geological and Earthquake Engineering, ed. A. Ansal. Vol. 8. 2009, New York: Springer.

11. Verderame, G.M., Ricci, P., Manfredi, G., and Cosenza, E., *Ultimate chord rotation of RC columns with smooth bars: Some considerations about EC8 prescriptions.* Bulletin of Earthquake Engineering, 2010. **8**(6): p. 1351-1373.

12. Hertanto, E., *Seismic assessment of pre-1970s reinforced concrete structure*. Master of Engineering. 2005, University of Canterbury: Christchurch, New Zealand.

13. Cosenza, E., Manfredi, G., and Verderame, G.M., *Seismic assessment of gravity load designed RC frames: Critical issues in structural modelling.* Journal of Earthquake Engineering, 2002. **6**(1 (special issue)): p. 101-122.

14. NISEE. *The Earthquake Engineering Online Archive - (Nisee e-library).* Available from: http://nisee.berkeley.edu/elibrary/.

15. Rodrigues, H., Romão, X., Costa, A.G., Arêde, A., Varum, H., Guedes, J., Vicente, R., Costa, A.A., and Paupério, E., *Sismo de L'Aquila de 6 de Abril de 2009. Ensinamentos para Portugal*, in *SISMICA 2010, 8º Congresso Nacional de Sismologia e Engenharia Sísmica*. 2010: Aveiro, Portugal.

16. CEB, *RC elements under cyclic loading. State of the art report*. 1996, Comite Euro-Internatinal du Beton.

17. CEB-FIP, *Bond of reinforcement in concrete. CEB-FIP Task Group Bond Models, Bulletin No. 10*. 2000, International Federation for Structural Concrete, Comité Euro-International du Béton.

18. Berra, M., Castellani, A., Ciccotelli, S., and Coronelli, D., *Bond-slip effects on reinforced concrete elements under earthquake loading.* European Earthquake Engineering, 1994. **3**: p. 3-10.

19. Abrams, D.A., *Tests on bond between concrete and steel*, in *University of Illinois Bulletin No. 71*. 1913, University of Illinois.

20. Feldman, L.R. and Bartlett, F.M., *Bond strength variability in pullout specimens with plain reinforcement.* ACI Structural Journal, 2005. **102**(6): p. 860-867.

21. Fabbrocino, G., Verderame, G.M., and Manfredi, G., *Experimental behaviour of anchored smooth rebars in old type reinforced concrete buildings.* Engineering Structures, 2005. **27**(10): p. 1575-1585.

22. Fabbrocino, G., Verderame, G.M., Manfredi, G., and Cosenza, E., *Structural models of critical regions in old-type R.C. frames with smooth rebars.* Engineering Structures, 2004. **26**(14): p. 2137-2148.

23. Sezen, H., *Seismic behavior and modeling of reinforced concrete building columns.* PhD Thesis. 2002, University of California: Berkeley, California, U.S.A.

24. Verderame, G.M., Fabbrocino, G., and Manfredi, G., *Seismic response of R.C. columns with smooth reinforcement. Part I: Monotonic tests.* Engineering Structures, 2008. **30**(9): p. 2277-2288.

25. Verderame, G.M., Fabbrocino, G., and Manfredi, G., *Seismic response of R.C. columns with smooth reinforcement. Part II: Cyclic tests.* Engineering Structures, 2008. **30**(9): p. 2289–2300.

26. Sezen, H. and Setzler, E.J., *Reinforcement slip in reinforced concrete columns.* ACI Structural Journal, 2008. **105**(3): p. 280-289.

27. Limkatanyu, S. and Spacone, E., *Reinforced concrete frame element with bond interfaces. I: Displacement-based, force-based and mixed formulations.* Journal of Structural Engineering, 2002. **128**(3): p. 346-355.

28. Limkatanyu, S. and Spacone, E., *Effects of reinforcement slippage on non-linear response under cyclic loadings of RC frame structures.* Earthquake Engineering and Structural Dynamics, 2003. **32**(15): p. 2407–2424.

29. Filippou, F.C. and Issa, A., *Nonlinear analysis of reinforced concrete frames under cyclic load reversals*. 1988, Earthquake Engineering Research Center, College of Engineering, University of California, Berkeley, California, U.S.A.

30. Filippou, F.C., D'Ambrisi, A., and Issa, A., *Effects of reinforcement slip on hysteretic behavior of reinforced concrete frame members.* ACI Structural Journal, 1999. **96**(3): p. 327-335.

31. Manfredi, G. and Pecce, M., *A refined RC beam element including bond-slip relationship for the analysis of continuous beams.* Computers and Structures, 1998. **69**(1): p. 53-62.

32. Monti, G. and Spacone, E., *Reinforced concrete fiber beam element with bond-slip.* Journal of Structural Engineering, 2000. **126**(6): p. 654-661.

33. Spacone, E., Filippou, F.C., and Taucer, F.F., *Fibre beam-column model for nonlinear analysis of R/C frames. Part I: Formulation.* Earthquake Engineering and Structural Dynamics, 1996. **25**: p. 711-725.

34. Monti, G., Filippou, F.C., and Spacone, E., *Finite element for anchored bars under cyclic load reversals.* Journal of Structural Engineering, 1997. **123**(5): p. 614–623.

35. Limkatanyu, S., *Reinforced concrete models with bond-interfaces for the nonlinear static and dynamic analysis of reinforced concrete frame structures*. PhD. 2002, University of Colorado, Boulder: Boulder, Colorado.

36. Fernandes, C., Varum, H., and Costa, A., *Concrete-steel bond characterization of RC structural elements built with smooth plain reinforcement bars*, in *2nd International Symposium on Connections between Steel and Concrete*, R. Eligehausen, et al., Editors. 2007, ibidem-Verlag: Stuttgart, Germany. p. 1171-1180.

37. Millard, A., *CASTEM 2000 – Guide d'utilisation*, in *Rapport CEA 93/007*. 1993: Saclay, France.

38. CEB-FIP, *CEB-FIP MC-90 Model Code 90 (MC-90)*, C.E.-I.d.B. (CEB), Editor. 1993, Thomas Telford Ltd.: London, U.K.

39. OpenSees. *Open System for Earthquake Engineering Simulation*. Available from: http://opensees.berkeley.edu/.

40. Zhao, J. and Sritharan, S., *Modelling of strain penetration effects in fibre-based analysis of reinforced concrete structures.* ACI Structural Journal, 2007. **104**(2): p. 133-141.

41. Lowes, L. and Altoontash, A., *Modeling reinforced-concrete beam-column joints subjected to cyclic loading.* Journal of Structural Engineering, 2003. **129**(12): p. 1686-1697.

42. Cervenka, J. and Jendele, L., *Atena user's manual – Part 1-7*. 2000-2002, Cervenka Consulting Ltd.: Prague, Czech Republic.

43. Bigaj, A.J., *Structural dependence of rotation capacity of plastic hinges in beams and slabs*. PhD Thesis. 1999, Delft University of Technology: The Netherlands.

44. Jendele, L. and Cervenka, J., *Finite element modelling of reinforcement with bond.* Computer and Structures, 2006. **84**(28): p. 1780-1791.

45. Pantelides, C.P., Hansen, J., Nadaul, J., and Reaveley, L.D., *Assessment of reinforced concrete building exterior joints with substandard details*. 2002, Pacific Earthquake Engineering Research Center.

46. Hakuto, S., Park, R., and Tanaka, H., *Seismic load tests on interior and exterior beam-column joints with substandard reinforcing details.* ACI Structural Journal, 2000. **97**(1): p. 11-24.

47. Paulay, T., *Equilibrium criteria for reinforced concrete beam-column joints.* ACI Structural Journal, 1989. **86**(6): p. 635-643.

48. Liu, A. and Park, R., *Seismic behaviour and retrofit of pre-1970's as-built exterior beam-column joints reinforced by plain round bars.* Bulletin of the New Zealand Society for Earthquake Engineering, 2001. **34**(1): p. 68-81.

49. Pampanin, S., Magenes, G., and Carr, A., *Modelling of shear hinge mechanism in poorly detailed RC beam columns joints*, in *fib 2003 Symposium "Concrete Structures in Seismic Regions"*. 2003: Athens, Greece.

50. Calvi, G.M., Magenes, G., and Pampanin, S., *Relevance of beam-column joint damage and collapse in RC frame assessment.* Journal of Earthquake Engineering, 2002. **6**(1): p. 75-100.

51. Pagni, C. and Lowes, L., *Predicting earthquake damage in older reinforced concrete beam-column joints*. 2004, Pacific Earthquake Engineering Research Center.

52. Favvata, M.J., Izzuddin, B.A., and Karayannis, C.G., *Modelling exterior beam–column joints for seismic analysis of RC frame structures.* Earthquake Engineering and Structural Dynamics, 2008. **37**(13): p. 1527–1548.

53. Shiohara, H., *New model for shear failure of RC interior beam-column connections.* Journal of Structural Engineering, 2001. **127**(2): p. 152-160.

54. Mitra, N. and Lowes, N.L., *Evaluation, calibration, and verification of a reinforced concrete beam–column joint model.* Journal of Structural Engineering, 2007. **133**(1): p. 105-120.

55. Celik, O.C. and Ellingwood, B.R., *Modeling beam-column joints in fragility assessment of gravity load designed reinforced concrete frames.* Journal of Earthquake Engineering, 2008. **12**(3): p. 357-381.

56. Giberson, M., *Two nonlinear beams with definition of ductility.* Journal of the Structural Division, 1969. **95**(2): p. 137-157.

57. Alath, S. and Kunnath, S.K., *Modeling inelastic shear deformation in reinforced-concrete beam-column joints engineering mechanics*, in *Engineering Mechanics: Proceedings of the 10th Conference, University of Colorado at Boulder, Boulder, Colorado*, S. Sture, Editor. 1995, ASCE: New York. p. 822–825.

58. Biddah, A. and Ghobarah, A., *Modelling of shear deformation and bond slip in reinforced concrete joints.* Journal of Structural Engineering and Mechanics, 1999. **7**(4): p. 413–432.

59. Elmorsi, M., Kianoush, M.R., and Tso, W.K., *Modeling bond-slip deformations in reinforced concrete beam column.* Canadian Journal of Civil Engineering, 2000. **27**: p. 490-505.

60. Youssef, M. and Ghobarah, A., *Modelling of RC beam-column joints and structural walls.* Journal of Earthquake Engineering, 2001. **5**(1): p. 93-111.

61. Mitra, N. and Lowes, N.L., *Evaluation and advancement of a reinforced concrete beam-column joint model*, in *13th World Conference on Earthquake Engineering*. 2004: Vancouver, Canada.

62. Altoontash, A., *Simulation and damage models for performance assessment of reinforced concrete beam-column joints*. PhD. 2004, Stanford University: Stanford.

63. Shin, M. and LaFave, J.M., *Testing and modeling for cyclic joint shear deformations in RC beam-column connections*, in *13th World Conference on Earthquake Engineering*. 2004: Vancouver, Canada.

64. Kwak H.-G., Kim S.-P., and J.-E., K., *Nonlinear dynamic analysis of RC frames using cyclic moment–curvature relation.* Journal of Structural Engineering and Mechanics, 2004. **17**(3-4): p. 357–378.

65. Bing, L., Yiming, W., and Tso-Chien, P., *Seismic behavior of nonseismically detailed interior beam-wide column joints - Part II: Theoretical comparisons and analytical studies.* ACI Structural Journal, 2003. **100**(1): p. 56-65.

66. Eligehausen, R., Genesio, G., Ožbolt, J., and Pampanin, S., *3D analysis of seismic response of RC beam-column exterior joints before and after retrofit*, in *2nd International Conference on Concrete Repair, Rehabilitation and Retrofitting*, M.G. Alexander, et al., Editors. 2008, Taylor & Francis Group: Cape Town, South Africa.

67. Sagbas, G., Vecchio, F.J., and Christopoulos, C., *Computational modeling of the seismic performance of beam-column subassemblies.* Journal of Earthquake Engineering, 2011. **15**(4): p. 640–663.

68. CEB, *CEB-217 - Bulletin d'Information N. 217 - Selected Justification Notes*. 1993, Euro-International du Béton.

69. Verderame, G.M., Ricci, P., De Carlo, D., and Manfredi, G., *Cyclic bond behaviour of plain bars. Part I: Experimental investigation.* Construction and Building Materials, 2009. **23**(12): p. 3499-3511.

70. Verderame, G.M., De Carlo, D., Ricci, P., and Fabbrocino, G., *Cyclic bond behaviour of plain bars. Part II: Analytical investigation.* Construction and Building Materials, 2009. **23**(12): p. 3512-3522.

71. Cosenza, E. and Prota, A., *Experimental behaviour and numerical modeling of smooth steel bars under compression.* Journal of Earthquake Engineering, 2006. **10**(3): p. 313-329.

72. Prota, A., De Cicco, F., and Cosenza, E., *Cyclic behavior of smooth steel reinforcing bars: experimental analysis and modeling issues.* Journal of Earthquake Engineering, 2009. **13**(4): p. 500–519.

73. Xiao, J. and Falkner, H., *Bond behaviour between recycled aggregate concrete and steel rebars.* Construction and Building Materials, 2007. **21**(2): p. 395-401

74. Feldman, L.R. and Bartlett, F.M., *Bond in flexural members with plain steel reinforcement.* ACI Structural Journal, 2008. **105**(5): p. 552-560.

75. Giuffrè, A. and Pinto, P.E., *Il comportamento del cemento armato per sollecitazioni cicliche di forte intensita.* Giornale del Genio Civile, 1970.

76. Menegotto, M. and Pinto, P., *Method of analysis for cyclically loaded reinforced concrete plane frames including changes in geometry and non-elastic behaviour of elements under combined normal force and bending*, in *IABSE Symposium: Resistance and Ultimate Deformability of Structures Acted on by Well Defined Repeated Loads*. 1973: Lisbon, Portugal.

77. Monti, G. and Nuti, C., *Nonlinear cyclic behaviour of reinforcing bars including buckling*. Journal of Structural Engineering, 1992. **118**(12): p. 3268–3285.

78. Monti, G., Nuti, C., and Santini, S., *CYRUS: CYclic Response of Upgraded Sections. A program for the analysis of retrofitted or repaired sections under biaxial cyclic loading including buckling of rebars*, in *Report DSSAR No. 2/96 Materiali*. 1996, Università degli Studi G. D'Annunzio: Chieti, Italy.

79. Eligehausen, R., Popov, E.P., and Bertero, V.V., *Local bond stress-slip relationships of deformed bars under generalized excitations*. 1983, Earthquake Engineering Research Center, College of Engineering, University of California, Berkeley, California, U.S.A.

80. Rehm, G., *Über die grundlagen des verbundes zwischen stahl und beton*. 1961: Deutscher Ausschuβ für Stahlbeton, Heft 138 (in German).

81. Feldman, L.R. and Bartlett, F.M., *Bond stresses along plain steel reinforcing bars in pullout specimens.* ACI Structural Journal, 2007. **104**(6): p. 685-692.

82. Cosenza, E., Manfredi, G., and Realfonzo, R., *Behavior and modeling of bond of FRP rebars to concrete.* Journal of Composites for Construction, 1997. **1**(2): p. 40-51.

83. Filippou, F.C., Popov, E.P., and Bertero, V.V., *Effects of bond deterioration on hysteretic behavior of reinforced concrete joints*. 1983, Earthquake Engineering Research Center, University of California Berkeley.

84. Tassios, T.P. *Properties of bond between concrete and steel under load cycles idealizing seismic actions*. in *AICAP-CEB Symposium, Structural Concrete Under Seismic Actions*. 1979. Rome, Italy: Comité Euro-International du Béton.

85. Morita, S. and Kaku, T. *Local bond stress-slip relationship under repeated loading*. in *IABSE Symposium, Resistance and Ultimate Deformability od Structures Acted on by Well Defined Repeated Loads*. 1973. Lisbon, Portugal.

86. Viwathanatepa, S., Popov, E.P., and Bertero, V.V., *Effects of generalised loadings on bond of reinforcing bars embedded in confined concrete blocks*. 1979, Earthquake Engineering Research Center.

87. Hawkins, N.M., Lin, I.J., and Jeang, F.L., *Local bond strength of concrete for cyclic reversed loadings*, in *Bond in Concrete*, P. Bartos, Editor. 1982, Applied Science Publishers: London, U.K. p. 151-161.

88. Marefat, M.S., Shirazi, S.M.H., Rostamshirazi, R., and Khanmohammadi, M., *Cyclic response of concrete beams reinforced by plain bars.* Journal of Earthquake Engineering, 2009. **13**(4): p. 463-481.

89. CEN, *BS EN 1998-3:2005. Eurocode 8 - Design of structures for earthquake resistance. Part 3: Strengthening and repair of buildings*. 2005, European Committee for Standardization: Brussels, Belgium.

90. Di Ludovico, M., Verderame, G.M., Prota, A., Manfredi, G., and Cosenza, E., *Experimental investigation on non-conforming full scale RC columns*, in *XIII ANIDIS 2009 - XIII Conference ANIDIS "L' ingegneria Sismica in Italia"*. 2009: Bologna, Italy.

91. Bousias, S.N., Fardis, M.N., and Biskinis, D., *Retrofitting of RC columns with deficient lap splices*, in *fib symposium "keep concrete attractive"*. 2005: Budapest, Hungary. p. 885–890.

92. Fardis, M.N., *Design rules for FRP retrofitting according to Eurocode 8 and their background*, in *Lecture to Fib Course 2006 "Retrofitting of concrete structures through externally bonded FRPs with emphasis on seismic applications"*. 2006: Mexico.

93. Faella, C., Napoli, A., and Realfonzo, R., *Cyclic flexural behavior of FRP-confined concrete columns under high axial loading*, in *ReLUIS congress "Valutazione e riduzione della vulnerabilità sismica di edifici esistenti in c.a."*. 2008: Rome, Italy. p. 510–520.

94. Fabbrocino, G., Verderame, G.M., and Manfredi, G., *Rotation capacity of old type RC columns*, in *fib symposium "keep concrete attractive"*. 2005: Budapest, Hungary. p. 891–896.

95. Di Ludovico, M., Verderame, G.M., Prota, A., Manfredi, G., and Cosenza, E., *Experimental investigation on non-conforming RC columns with plain and deformed bars.* ACI Structural Journal (submitted), 2010.

96. Bousias, S., Spathis, A.-L., and Fardis, M.N., *Seismic retrofitting of columns with lap spliced smooth bars through FRP or concrete jackets.* Journal of Earthquake Engineering, 2007. **11**(5): p. 653-674.

97. Park, R., *A summary of results of simulated seismic loads on reinforced concrete beam-column joints, beams and columns with substandard reinforcing details.* Journal of Earthquake Engineering, 2002. **6**(2): p. 147-174.

98. Liu, A. and Park, R., *Seismic load tests on two interior beam-column joints reinforced by plain bars designed to pre-1970s seismic codes.* Bulletin of the New Zealand Society for Earthquake Engineering, 1998. **31**(3): p. 164-176.

99. Hakuto, S., Park, R., and Tanaka, H., *Retrofitting of reinforced concrete moment resisting frames. Research Report 95-4*. 1995, Department of Civil Engineering, University of Canterbury: New Zealand.

100. Bedirhanoglu, I., Ilki, A., Pujol, S., and Kumbasar, N., *Behavior of deficient joints with plain bars and low-strength concrete.* ACI Structural Journal, 2010. **107**(3): p. 300-310.

101. Liu, A. and Carr, A.J., *Seismic assessment of a pre-1970s reinforced concrete frame building with plain round reinforcing bars*, in *The 14th World Conference on Earthquake Engineering*. 2008: Beijing, China.

102. Liu, A. and Park, R., *Seismic assessment and retrofit of pre-1970sreinforced concrete frame structures. Research Report 2002-1*. 2002, Department of Civil Engineering, University of Canterbury: New Zealand.

103. Akguzel, U. and Pampanin, S., *Seismic upgrading of exterior beam-column joints using GFRP*, in *14th European Conference on Eartquake Enginnering*. 2010: Ohrid, Republic of Macedonia.

104. Genesio, G., Eligehausen, R., Akguzel, U., and Pampanin, S., *Application of post-installed anchors for seismic retrofit of RC frames*, in *14th European Conference on Earthquake Engineering*. 2010: Ohrid, Republic of Macedonia.

105. Kam, W.Y. and Pampanin, S., *Selective weakening and post-tensioning for retrofit of non-ductile R.C. exterior beam-column joints*, in *14th European Conference on Earthquake Engineering*. 2010: Ohrid, Republica of Macedonia.

106. Akguzel, U. and Pampanin, S., *Effects of variation of axial load and bidirectional loading on seismic performance of GFRP retrofitted reinforced concrete exterior beam-column joints.* Journal of Composites for Construction, 2010. **14**(1): p. 94-104.

107. Calvi, G.M., Magenes, G., and Pampanin, S., *Experimental test on a three storey RC frame designed for gravity only*, in *12th European Conference on Earthquake Engineering*. 2002: London, U.K.

108. Pinto, A., Verzeletti, G., Molina, J., Varum, H., Coelho, E., and Pinho, R., *Pseudo-dynamic tests on non-seismic resisting RC frames (bare and selective retrofit frames).* 2002, Report EUR, EC, Joint Research Centre: Ispra, Italy.

109. Pinto, A.V., Varum, H., and Molina, J., *Experimental assessment and retrofit of full-scale models of existing RC frames*, in *12th European Conference on Earthquake Engineering*. 2002: London, U.K.

110. Negro, P., Mola, E., Molina, F.J., and Magonette, G.E., *Full-scale PsD testing of a torsionally unbalanced three-storey non-seismic RC frame*, in *13th World Conference on Earthquake Engineering*. 2004: Vancouver, Canada.

111. Molina, F.J., Buchet, P., Magonette, G.E., Hubert, O., and Negro, P., *Bidirectional pseudodynamic technique for testing a three-storey reinforced concrete building*, in *13th World Conference on Earthquake Engineering*. 2004: Vancouver, Canada.

CHAPTER 3 – CYCLIC TESTING OF INTERIOR RC BEAM-COLUMN JOINTS

1. Fernandes, C., Melo, J., Varum, H., and Costa, A., *Comparative analysis of the cyclic behaviour of beam-column joints with plain and deformed reinforcing bars.* IBRACON Structures and Materials Journal, 2011. **4**(1): p. 147-172.

2. Fernandes, C., Melo, J., Varum, H., and Costa, A., *Cyclic behavior of substandard RC beam-column joints with plain bars.* ACI Structural Journal, 2011. **(paper accepted for publication)**.

3. CEN, *NP EN 1992-1-1. Eurocode 2 - Design of concrete structures. Part 1-1: General rules and rules for buildings*. 2010, European Committee for Standardization: Brussels, Belgium.

4. IPQ, *NP EN 12390-3. Testing hardened concrete. Part 3: Compressive strength of test specimens*. 2009, Instituto Português da Qualidade: Lisbon, Portugal.

5. IPQ, *NP EN 206-1. Concrete. Part 1: Specification, performance, production and conformity*. 2007, Instituto Português da Qualidades: Lisbon, Portugal.

6. IPQ, *EN ISO 6892-1. Tensile testing of metallic materials. Method of test at ambient temperature*. 2009, Instituto Português da Qualidade: Lisbon, Portugal.

7. Verderame, G.M., Stella, A., and Cosenza, E., *Le proprieta` meccaniche degli acciai impiegati nelle strutture in c.a. realizzate negli anni '60*, in *10th National Proceedings ''L'ingegneria Sismica in Italia*. 2001: Potenza-Matera, Italy.

8. REBAP, *Regulamento Estruturas de Betão Armado e Pré-Esforçado. Decreto de Lei n.º 349-C/83*. 2001, Porto Editora.

9. CEN, *NP EN 1998-1. Eurocode 8 - Design of structures for earthquake resistance. Part 1: General rules, seismic actions and rules for buildings*. 2010, European Committee for Standardization: Brussels, Belgium.

10. Genesio, G., Eligehausen, R., and Pampanin, S. *Seismic assessment of pre-1970s RC beam-column joints*. in *14th European Conference on Earthquake Engineering*. 2010. Ohrid, Republic of Macedonia.

11. Hakuto, S., Park, R., and Tanaka, H., *Seismic load tests on interior and exterior beam-column joints with substandard reinforcing details.* ACI Structural Journal, 2000. **97**(1): p. 11-24.

12. Fardis, M.N., *Seismic design, assessment and retrofitting of concrete buildings. Based on EN-Eurocode8*. Geotechnical, Geological and Earthquake Engineering, ed. A. Ansal. Vol. 8. 2009, New York: Springer.

13. CEN, *BS EN 1998-3:2005. Eurocode 8 - Design of structures for earthquake resistance. Part 3: Strengthening and repair of buildings*. 2005, European Committee for Standardization: Brussels, Belgium.

14. Verderame, G.M., Ricci, P., Manfredi, G., and Cosenza, E., *Ultimate chord rotation of RC columns with smooth bars: Some considerations about EC8 prescriptions.* Bulletin of Earthquake Engineering, 2010. **8**(6): p. 1351-1373.

15. CEN, *Corrigenda to EN 1998-3, document CEN/TC250/SC8/N437A*. 2009, European Committee for Standardization: Brussels, Belgium.

16. Di Ludovico, M., Verderame, G.M., Prota, A., Manfredi, G., and Cosenza, E., *Experimental investigation on non-conforming full scale RC columns*, in *XIII ANIDIS 2009 - XIII Conference ANIDIS "L' ingegneria Sismica in Italia"*. 2009: Bologna, Italy.

17. Blandon, C. and Priestley, M.N.J., *Equivalent viscous damping equations for direct displacement based design.* Journal of Earthquake Engineering, 2005. **9**(2, Special Issue): p. 257–278.

18. Varum, H., *Seismic assessment, strengthening and repair of existing buildings*. PhD Thesis. 2003, University of Aveiro: Aveiro, Portugal.

19. Priestley, M.N.J., *Myths and fallacies in earthquake engineering, revisited. The Mallet-Milne lecture*. 2003, Pavia, Italy: IUSS Press.

20. Gulkan, P. and Sozen, M.A., *Inelastic responses of reinforced concrete structures to earthquakes motions*, in *ACI Journal Proceedings*. 1974. p. 604-610.

21. Priestley, M.J.N. and Grant, D.N., *Viscous damping in seismic design and analysis.* Journal of Earthquake Engineering, 2005. **9**(2): p. 229-255.

22. Park, Y.-J. and Ang, A.H.-S., *Mechanistic seismic damage model for reinforced concrete.* Journal of Structural Engineering, 1985. **111**(4): p. 722-739.

23. Kunnath, S.K., Reinhorn, A.M., and Park, Y.-J., *Analytical modelling of inelastic seismic response of RC structures.* Journal of Structural Engineering, 1990. **116**(4): p. 996-1017.

24. Arêde, A., *Seismic assessment of reinforced concrete frame structures with a new flexibility based element*. PhD. 1997, FEUP: Porto, Portugal.

25. Park, Y.-J., Ang, A.H.-S., and Wen, Y.K., *Damage-limiting aseismic design of buildings.* Earthquake Spectra, 1987. **3**(1): p. 1-26.

26. Bedirhanoglu, I., Ilki, A., Pujol, S., and Kumbasar, N., *Behavior of deficient joints with plain bars and low-strength concrete.* ACI Structural Journal, 2010. **107**(3): p. 300-310.

27. Marefat, M.S., Shirazi, S.M.H., Rostamshirazi, R., and Khanmohammadi, M., *Cyclic response of concrete beams reinforced by plain bars.* Journal of Earthquake Engineering, 2009. **13**(4): p. 463-481.

28. Hertanto, E., *Seismic assessment of pre-1970s reinforced concrete structure*. Master of Engineering. 2005, University of Canterbury: Christchurch, New Zealand.

CHAPTER 4 – NUMERICAL MODELLING OF THE BEAM-COLUMN JOINTS

1. SeismoStruct. Available from: http://www.seismosoft.com/en/SeismoStruct.aspx.

2. Mander, J.B., Priestley, M.J.N., and Park, R., *Theoretical stress-strain model for confined concrete.* Journal of Structural Engineering, 1988. **114**(8): p. 1804-1826.

3. Martínez-Rueda, J.E. and Elnashai, A.S., *Confined concrete model under cyclic loads.* Materials and Structures, 1997. **30**(3): p. 139-147.

4. Priestley, M.J.N., Seible, F., and Calvi, G.M., *Seismic design and retrofit of bridges*. 1996, New York: John Wiley & Sons Inc.

5. Menegotto, M. and Pinto, P., *Method of analysis for cyclically loaded reinforced concrete plane frames including changes in geometry and non-elastic behaviour of elements under combined normal force and bending*, in *IABSE Symposium: Resistance and Ultimate Deformability of Structures Acted on by Well Defined Repeated Loads*. 1973: Lisbon, Portugal.

6. Filippou, F.C., Popov, E.P., and Bertero, V.V., *Effects of bond deterioration on hysteretic behavior of reinforced concrete joints*. 1983, Earthquake Engineering Research Center, University of California Berkeley.

7. Lowes, L. and Altoontash, A., *Modeling reinforced-concrete beam-column joints subjected to cyclic loading.* Journal of Structural Engineering, 2003. **129**(12): p. 1686-1697.

8. Yu, W., *Inelastic modeling of reinforcing bars and blind analysis of the benchmarks tests on beam-column joints under cyclic loading*. Master Thesis. 2006, Rose School - European School for Advanced Studies in Reduction of Seismic Risk: Pavia.

9. OpenSees. *Open System for Earthquake Engineering Simulation*. Available from: http://opensees.berkeley.edu/.

10. Takeda, T., Sozen, M.A. and Nielsen, N.N., *Reinforced concrete response to simulated earthquakes.* Journal of Structural Division, ASCE, 1970. **96**(ST12): p. 2557-2573.

11. Emori, K. and Schnobrich, W.C., *Analysis of Reinforced Concrete Frame-Wall Structures for Strong Motion Earthquakes, Structural Research Series No. 434, Civil Engineering Studies.* 1978, University of Illinois at Urbana-Champaign, USA.

12. Otani, S., *SAKE, A Computer Program for Inelastic Response of R/C Frames to Earthquakes. Report UILU-Eng-74-2029, Civil Engineering Studies*. 1974, University of Illinois at Urbana-Champaign, USA.

CHAPTER 5 – CYCLIC TESTING OF A RC BEAM COLLECTED FROM AN EXISTING BUILDING STRUCTURE

1. Fernandes, C., Melo, J., Varum, H., and Costa, A., *Cyclic behavior of a two-span RC beam built with plain reinforcing bars.* Periodica Polytechnica Civil Engineering, 2011. **55**(1): p. 21-29.

2. CEN, *NP EN 1992-1-1. Eurocode 2 - Design of concrete structures. Part 1-1: General rules and rules for buildings*. 2010, European Committee for Standardization: Brussels, Belgium.

3. IPQ, *NP EN 12504-1. Testing concrete in structures. Part 1: Cored specimens. Taking, examining and testing in compre*. 2003, Instituto Português da Qualidade: Lisbon, Portugal.

4. AASHTO, *ASTM C42/C42M - Standard test method for obtaining and testing drilled cores and sawed beams of concrete*. 1999, American Association of State Highway and Transportation Officials.

5. IPQ, *NP EN 206-1. Concrete. Part 1: Specification, performance, production and conformity*. 2007, Instituto Português da Qualidades: Lisbon, Portugal.

6. CEN, *NP EN 1998-1. Eurocode 8 - Design of structures for earthquake resistance. Part 1: General rules, seismic actions and rules for buildings*. 2010, European Committee for Standardization: Brussels, Belgium.

CHAPTER 6 – NUMERICAL MODELLING OF THE BEAM

1. OpenSees. *Open System for Earthquake Engineering Simulation*. Available from: http://opensees.berkeley.edu/.

2. Melo, J., Fernandes, C., Varum, H., Rodrigues, H., Costa, A., and Arêde, A., *Numerical modelling of the cyclic behaviour of RC elements built with plain reinforcing bars.* Engineering Structures, 2011. **33**(2): p. 273-286.

3. Melo, J., *Influência do escorregamento na resposta cíclica de elementos de B.A.* MSc. Thesis 2009, University of Aveiro: Aveiro, Portugal.

4. Mazzoni, S., McKenna, F., Scott, M., and Fenves, G.L., *OpenSees Command Language Manual*. 2007, Pacific Earthquake Engineering Research Center, University of California, Berkeley: U.S.A.

5. Zhao, J. and Sritharan, S., *Modelling of strain penetration effects in fibre-based analysis of reinforced concrete structures.* ACI Structural Journal, 2007. **104**(2): p. 133-141.

6. Guedes, J.M., *Seismic behaviour of reinforced concrete bridges. Modelling, numerical analysis and experimental assessment*. 1997, Faculty of Engineering of the University of Porto: Porto, Portugal.

7. *RBA. Regulamento do betão armado. Decreto n.º 25948*. 1935, Imprensa Nacional: Lisboa.

8. Menegotto, M. and Pinto, P., *Method of analysis for cyclically loaded reinforced concrete plane frames including changes in geometry and non-elastic behaviour of elements under combined normal force and bending*, in *IABSE Symposium: Resistance and Ultimate Deformability of Structures Acted on by Well Defined Repeated Loads*. 1973: Lisbon, Portugal.

9. CEB-FIP, *CEB-FIP MC-90 Model Code 90 (MC-90)*, C.E.-I.d.B. (CEB), Editor. 1993, Thomas Telford Ltd.: London, U.K.

10. CEN, *BS EN 1998-3:2005. Eurocode 8 - Design of structures for earthquake resistance. Part 3: Strengthening and repair of buildings*. 2005, European Committee for Standardization: Brussels, Belgium.

11. Verderame, G.M., Ricci, P., Manfredi, G., and Cosenza, E., *Ultimate chord rotation of RC columns with smooth bars: Some considerations about EC8 prescriptions.* Bulletin of Earthquake Engineering, 2010. **8**(6): p. 1351-1373.

12. CEN, *NP EN 1992-1-1. Eurocode 2 - Design of concrete structures. Part 1-1: General rules and rules for buildings*. 2010, European Committee for Standardization: Brussels, Belgium.

APPENDIX

This appendix lists the references of the papers published in journals and articles presented in conferences, in the framework of the PhD thesis.

PAPERS IN INTERNATIONAL JOURNALS WITH SCIENTIFIC REFEREE

Fernandes, C.; Melo, J.; Varum, H.; Costa, A. (2011) – *Cyclic behavior of substandard RC beam-column joints with plain bars* – ACI Structural Journal (paper submitted and accepted for publication).

Fernandes, C.; Melo, J.; Varum, H.; Costa, A. (2011) – *Cyclic behavior of a two-spans RC beam built with plain reinforcing bars* – Periodica Polytechnica Civil Engineering, Vol. 55, No. 1, p. 21-29.

Fernandes, C.; Melo, J.; Varum, H.; Costa, A. (2011) – *Comparative analysis of the cyclic behavior of beam-column joints with plain and deformed reinforcing bars* – IBRACON Structures and Materials Journal, Vol. 4, No. 1, p. 147-172.

Melo, J.; Fernandes, C.; Varum, H.; Rodrigues, H.; Costa, A.; Arêde, A. (2011) – *Numerical modelling of the cyclic behaviour of RC elements built with plain reinforcing bars* – Engineering Structures, Vol. 33, No. 2, p. 273-286.

PAPERS IN INTERNATIONAL CONFERENCES

Fernandes, C.; Melo, J.; Varum, H.; Costa, A.; (2012) – *Experimental and numerical analysis of the cyclic behaviour of RC beam-column connections with plain reinforcing bars* – 15WCEE, 15th World Conference on Earthquake Engineering, to be held in Lisbon, Portugal, September 24-28 (abstract accepted).

Fernandes, C.; Melo, J.; Rodrigues, H.; Varum, H.; Costa, A.; Arêde, A. (2010) – *Cyclic behaviour analysis of RC elements with plain reinforcing bars* – 14ECEE, 14th European

Conference on Earthquake Engineering, Ohrid, Republic of Macedonia, August 30 - September 3.

Fernandes, C.; Melo, J.; Varum, H.; Costa, A. (2010) – *Comportamento cíclico de nós viga-pilar com armadura lisa* – CINPAR 2010, 6th International Conference on Structural Defects and Repair - Paper Ref. 042, Córdoba, Argentina, June 2-4.

Fernandes, C.; Varum, H.; Costa, A. (2007) – *Concrete-steel bond characterization of RC structural elements built with smooth plain reinforcement bars* – Proceedings of the 2nd International Symposium on Connections between Steel and Concrete, Stuttgart, Germany, September 4-7, Vol. 2, p. 1171-1179.

PAPERS IN NATIONAL CONFERENCES

Fernandes, C.; Melo, J.; Varum, H.; Costa, A. (2010) – *Análise do comportamento de nós viga-pilar com armadura lisa sujeitos a cargas horizontais cíclicas* – Encontro Nacional Betão Estrutural 2010, Lisbon, Portugal, November 10-12.

Fernandes, C.; Melo, J.; Varum, H.; Rodrigues, H.; Costa, A.; Arêde, A. (2010) – *Caracterização do comportamento cíclico em flexão de elementos de BA com armadura lisa* – Encontro Nacional Betão Estrutural 2010, Lisbon, Portugal, November 10-12.

Fernandes, C.; Melo, J.; Varum, H.; Costa, A. (2010) – *Análise do comportamento cíclico de uma viga de B.A. com armadura lisa* – SÍSMICA 2010, 8º Congresso Nacional de Sismologia e Engenharia Sísmica – University of Aveiro, Aveiro, Portugal, October 20-23.

Fernandes, C.; Melo, J.; Varum, H.; Costa, A. (2010) – *Análise do comportamento cíclico de nós viga-pilar representativos de estruturas de B.A. com armadura lisa* - SÍSMICA 2010, 8º Congresso Nacional de Sismologia e Engenharia Sísmica – University of Aveiro, Aveiro, Portugal, October 20-23.

Fernandes, C.; Rodrigues, H.; Costa, A.A.; Arêde, A.; Varum, H.; Costa, A. (2008) – *Influência do mecanismo de aderência aço-betão no comportamento de elementos de betão armado com armadura lisa sujeitos a cargas cíclicas* – CD de Actas do 4º CINPAR - Congresso Internacional sobre Patologia e Reabilitação de Estruturas, University of Aveiro, Aveiro, Portugal, June 25-28, ISBN 978-989-95695-3-9.

Varum, H; Costa, A.; Rodrigues, H.; Fernandes, C. (2007) – *Concrete-steel bond influence in the cyclic response of RC structural elements* (abstract) – XIII Conference of Sociedade Portuguesa de Materiais and IV International Materials Symposium - Global Materials for the XXI Century: Challenges to Academia and Industry, Faculdade de Engenharia da Universidade do Porto, Porto, Portugal, April 1-4, p. 487.